



VNIVERSITAT
DE VALÈNCIA

1

2 **Search for associated production of a Higgs**
3 **boson and a single top quark in the $2\ell + \tau_{had}$**
4 **final state using proton-proton collisions**
5 **at $\sqrt{s} = 13$ TeV with the ATLAS detector**

6

PhD Thesis

7

Pablo Martínez Agulló

8

Instituto de Física Corpuscular (IFIC)
Departament de Física Atòmica, Molecular i Nuclear
Programa de Doctorat en Física

9

10

Under the supervision of

11

Carlos Escobar Ibáñez
and
Susana Cabrera Urbán

12

13

14

15

València, 10th January 2023

¹⁶ **Carlos Escobar Ibáñez,**
¹⁷ investigador científico del Consejo Superior de Investigaciones Científicas, y
¹⁸

¹⁹ **Susana Cabrera Urbán,**
²⁰ científica titular del Consejo Superior de Investigaciones Científicas,

²¹ **Certifican:**

²² Que la presente memoria, **Search for associated production of a**
Higgs boson and a single top quark in the $2\ell + \tau_{had}$ final state
using proton-proton collisions at $\sqrt{s} = 13$ TeV with the ATLAS
detector, ha sido realizada bajo su dirección en el Instituto de Física
Corpuscular, centro mixto de la Universitat de València y del CSIC, por
Pablo Martínez Agulló, y constituye su Tesis para optar al grado de
Doctor en Física.

²⁹ Y para que así conste, en cumplimiento de la legislación vigente, presenta
³⁰ en el Departamento de Física Atómica, Molecular y Nuclear de la Univer-
³¹ sidad de Valencia la referida Tesis Doctoral, y firman el presente certificado.

³²

³³ València, a DD de MES de 2023,

³⁴

³⁵ Carlos Escobar Ibáñez

Susana Cabrera Urbán

36

37

38

39

C'est quoi ce bordel ???

—DANIEL BOSSON,

⁴⁰ Preface

⁴¹ The Standard Model of particle physics is both incredibly successful and
⁴² glaringly incomplete theory. It brings together all elementary particles that
⁴³ make up the known universe in a single theory. Among these, the top quark
⁴⁴ and the Higgs boson are of special interest because they can help to answer
⁴⁵ some of the open questions. The object of study of this thesis focusses in
⁴⁶ these two singular particles and its interplay.

⁴⁷ The studies presented at this dissertation have been carried using an
⁴⁸ integrated luminosity of 139 fb^{-1} of proton-proton collision data at center-
⁴⁹ of-mass energy of 13 TeV collected by the ATLAS detector during the Large
⁵⁰ Hadron Collider (LHC) Run 2. Located at the European Organization
⁵¹ for Nuclear Research, the LHC is the most powerful particle accelerator
⁵² in the world and ATLAS one of its largest detectors. The experimental
⁵³ setup in which this work is contextualised is described in Chapter 3. The
⁵⁴ data and generation of Monte Carlo simulations within ATLAS is described
⁵⁵ in Chapter 4. The reconstruction and identification of physical objects is
⁵⁶ explained in Chapter 5.

⁵⁷ The discovery of a Higgs boson by the ATLAS [1] and CMS [2] exper-
⁵⁸ iments in 2012 opened a new field for exploration in the realm of particle
⁵⁹ physics. In order to better understand Standard Model, it is of promi-
⁶⁰ nent interest to determine the Yukawa coupling of the Higgs boson to the
⁶¹ top quark (y_t), being the latter the most massive fundamental particle and,
⁶² consequently, the one with the largest coupling to the Higgs boson.

⁶³ The direct measurement of y_t is only possible at the LHC via two asso-
⁶⁴ ciated Higgs productions: with a top-quark-antiquark pair ($t\bar{t}H$) and with
⁶⁵ a single-top quark with an additional parton (tHq). While the $t\bar{t}H$ just
⁶⁶ permits the determination of the magnitude of y_t , the only way of simultan-
⁶⁷ eously measuring its sign and magnitude is through the tH production [3].
⁶⁸ The possible observation of an excess of signal events with respect to the
⁶⁹ Standard Model prediction, would be an evidence of new physics in terms
⁷⁰ of CP-violating y_t coupling.

71 In this work it is presented a search for the tHq production in a final
72 state with two light-flavoured-charged leptons (electrons or muons) and one
73 hadronically-decaying τ lepton (named $2\ell + 1\tau_{\text{had}}$ channel). This search is
74 exceptionally challenging due to the extremely small cross-section of the tHq
75 process (70 fb [4]), and of the $2\ell + 1\tau_{\text{had}}$ final-state channel, in particular,
76 which only accounts for a 3.5% of the total tHq production.

77 Therefore, to distinguish the tHq signal events from background events,
78 machine-learning techniques are used. Particularly, boosted-decision trees
79 are employed to define signal-enriched regions as well as control regions
80 that constrain the most important background processes. The most relev-
81 ant backgrounds are those related to top-quark-antiquark-pair production
82 without and with an additional boson ($t\bar{t}$, $t\bar{t}H$, $t\bar{t}W$ and $t\bar{t}Z$) and Z boson
83 plus jets.

84 Additionally, to help identifying signal events within the data, the re-
85 construction of the event plays an important role. Different tools are used
86 to retrieve the four momentum of the top quark and Higgs boson from the
87 reconstructed objects. This information can be later used to build variables
88 that help separating the signal events from the processes that mimic the
89 $2\ell + 1\tau_{\text{had}}$ signature. The reconstruction of the events is also enhanced by
90 similar machine-learning methods since in the scenario in which the light-
91 flavour leptons have the same sign, a priori, it is not possible to determine
92 which lepton is originated from the Higgs boson and which from the top
93 quark.

94 Significant suppression of the background events with jets wrongly selec-
95 ted as leptons or non-prompt leptons originating from heavy-flavour decays
96 is achieved by demanding electrons and muons to pass strict identification
97 and isolation requirements. Simultaneously, hadronic- τ leptons are deman-
98 ded to pass the requirement of a recurrent-neural-network-based discrimin-
99 ator to reduce misidentifications from jets.

100 The tools and methods developed for the associated tHq production
101 search are described in Chapter 6.

¹⁰² Acknowledgements

¹⁰³ This work would not have been possible without the invaluable assist-
¹⁰⁴ ance of a large number of people, whom I have been fortunate to meet. I
¹⁰⁵ would like to thank them all and dedicate this thesis to them.

¹⁰⁶ Special mention to Stack Overflow, this thesis is as much yours as it is
¹⁰⁷ mine. Thanks.

¹⁰⁸ Gracias gracias

¹⁰⁹ Contents

¹¹⁰	Preface	v
¹¹¹	Acknowledgements	vii
¹¹²	1 Theoretical Framework	1
¹¹³	1.1 The Standard Model of particle physics	1
¹¹⁴	1.1.1 Introduction to the SM and its elementary particles	2
¹¹⁵	1.1.2 Quantum electrodynamics	6
¹¹⁶	1.1.3 Electroweak interactions	8
¹¹⁷	1.1.4 Quantum chromodynamics	15
¹¹⁸	1.1.5 Particle masses	18
¹¹⁹	1.1.6 Wrap up	25
¹²⁰	2 Top quark and Higgs boson physics	31
¹²¹	2.1 Top quark	31
¹²²	2.1.1 Top-quark discovery	32
¹²³	2.1.2 Top quark production at LHC	33
¹²⁴	2.1.3 Top-quark decay	42
¹²⁵	2.1.4 Top quark polarisation	43
¹²⁶	2.2 Higgs boson	46
¹²⁷	2.2.1 Higgs-boson discovery	46
¹²⁸	2.2.2 Higgs boson production at LHC	46
¹²⁹	2.2.3 Higgs-boson decay	48

130	2.3	Top quark and Higgs boson interplay	51
131	2.3.1	\mathcal{CP} properties in top-Higgs interactions	51
132	2.3.2	$t\bar{t}H$	52
133	2.3.3	tHq	53
134	3	The ATLAS experiment at the Large Hadron Collider of CERN laboratory	57
135	3.1	CERN	57
136	3.2	Large Hadron Collider	59
137	3.2.1	Machine design	60
138	3.2.2	Accelerator complex	62
139	3.2.3	LHC Experiments	63
140	3.2.4	LHC Computing grid	65
141	3.2.5	Energy, Luminosity and Cross-section	67
142	3.2.6	The Pile-up effect	73
143	3.2.7	Phenomenology of proton-proton collisions	74
144	3.3	ATLAS	77
145	3.3.1	Coordinate system	80
146	3.3.2	Inner Detector	81
147	3.3.3	Calorimeters	86
148	3.3.4	Muon Spectrometer	91
149	3.3.5	Magnet system	93
150	3.3.6	Trigger and Data Acquisition System	96
151	3.4	Alignment of the inner detector	97
152	3.4.1	Track based alignment	100
153	3.4.2	Web-based display for alignment monitoring	102
154	3.4.3	Alignment results during Run-2	105
155	4	Recording data and simulating events in ATLAS	107
156	4.1	Data	108
157			

158	4.2 Monte Carlo	108
159	4.2.1 MC simulations	110
160	4.2.2 MC generators	110
161	5 Object reconstruction and identification	113
162	5.1 Tracking	113
163	5.1.1 Sagitta method	114
164	5.2 Vertices	114
165	5.3 Electrons and photons	114
166	5.4 Muons	114
167	5.5 Jets	114
168	5.5.1 Jet energy calibration and resolution	115
169	5.5.2 Bottom quark induced jets	116
170	5.6 Missing transverse energy	116
171	5.7 Overlap removal	116
172	6 Search for rare associate tHq production	117
173	6.1 Introduction	117
174	6.2 Data and simulated events	118
175	6.2.1 Single lepton triggers	119
176	6.3 Object definition	119
177	6.4 Signal	119
178	6.4.1 Signal generation and validation	119
179	6.4.2 Parton-level truth validation	119
180	6.4.3 Lepton assignment	120
181	6.4.4 Top quark and Higgs boson reconstruction	124
182	6.5 Background estimation	124
183	6.5.1 Fakes estimation	125
184	6.5.2 Reducible backgrounds	126
185	6.6 Event selection	127

186	6.6.1	Preselection	128
187	6.6.2	Discriminant variables	129
188	6.6.3	BDT	129
189	6.6.4	Signal Region	130
190	6.6.5	Control Regions	130
191	6.7	Systematic uncertainties	131
192	6.7.1	Theoretical uncertainties	131
193	6.7.2	Modelling uncertainties	131
194	6.7.3	Experimental uncertainties	131
195	6.8	Fit results	131
196	6.8.1	Likelihood fit	131
197	6.8.2	Strategy	133
198	6.8.3	Fit with Asimov data	133
199	6.8.4	Fit to data	133
200	6.8.5	Results	133
201	6.8.6	Data fit	134
202	6.9	Combination results	134
203	6.10	Conclusions	134
204	7	Conclusion	135
205	A	Effect of negative weights	137
206	A.1	Negative weights uncertainties	137
207	A.2	Statistical uncertainty of negative weights	137
208	A.2.1	Errors in binned histograms	139
209	A.3	Negative weights in MVA methods	140
210	Appendices		137
211	B	Boosted Decision Trees	141
212	B.1	How does a BDT work?	141

213	B.1.1	Training	143
214	B.1.2	Evaluation / Validation	147
215	B.1.3	Application	147
216	B.2	Treatment of negative weights	147
217	B.3	Cross validation and k -folding	147
218	B.4	Other considerations about BDTs	148
219	B.4.1	Hyperparameters	149
220	Abbreviations		154
221	Bibliography		157
222	Summary of the results		171
223	Resum de la tesi		173
224	1	Marc teòric	173
225	1.1	El Model Estàndard	173
226	1.2	La física del quark top	173
227	1.3	La física del bosó de Higgs	173
228	2	Dispositiu experimental	173
229	3	L'experiment ATLAS del LHC al CERN	174
230	3.1	El gran col·lisionador d'hadrons	174
231	3.2	El detector ATLAS	174
232	4	Mesura de la polarització del quark top al canal- t	174
233	4.1	Selecció d'esdeveniments	174
234	4.2	Estimació del fons	174
235	4.3	Fonts d'incertesa	174
236	4.4	Resultats	174
237	5	Recerca de processos tH amb un estat final $2\ell + 1\tau_{\text{had}}$	174
238	5.1	Selecció d'esdeveniments	174
239	5.2	Estimació del fons	174

240	5.3	Fonts d'incertesa	174
241	5.4	Resultats	174
242	6	Conclusions	174

²⁴³ **Chapter 1**

²⁴⁴ **Theoretical Framework**

²⁴⁵
²⁴⁶
²⁴⁷
²⁴⁸
²⁴⁹

L'essentiel est invisible pour les yeux.
—ANTOINE DE SAINT-EXUPÉRY,
LE PETIT PRINCE (1943)

²⁵⁰ **1.1 The Standard Model of particle physics**

²⁵¹ Since the very first moment of our history, the humankind has pursued
²⁵² the knowledge of nature, has tried to understand and describe how the
²⁵³ universe works at a fundamental level. In fact, the word physics comes
²⁵⁴ from the Greek “*φύσικη*” which means “nature” [5][6]. Most of the enquires
²⁵⁵ regarding this, can be boiled down to two basic questions: What are the
²⁵⁶ ultimate building blocks of reality? and which are the rules that govern
²⁵⁷ them?

²⁵⁸ In the 7th century BCE, the pre-Socratic philosopher Thales of Miletus
²⁵⁹ already proclaimed that every event had a natural cause [7]. Later, to un-
²⁶⁰ derstand how the basic components of the matter were formed, the ancient

261 Indian philosophers such as Kanada and Dignaga on the 6th century BCE
 262 and Greeks Democritus and Leucippus on the 5th century BCE, developed
 263 the atomism, which comes from “*ατομον*” meaning uncuttable or indivisible
 264 [8][9].

265 From then to our days, the search for the minute fragments that comprise
 266 the matter and its interactions has led us to the Standard Model (SM) of
 267 particle physics, one of the most successful scientific theories cultivated
 268 so far. This understanding of the universe can explain phenomena from
 269 behaviour of atoms to how stars burn.

270 1.1.1 Introduction to the SM and its elementary 271 particles

272 Based on Quantum Field Theory (QFT), the SM of particle physics
 273 provides the theoretical framework that constitutes what is currently ac-
 274 cepted as the best description of particles physics. It aims to explain both
 275 all particles of matter and their interactions. The completion of the SM
 276 was a collaborative effort of several scientists during the second half of the
 277 20th, being the current formulation finalised in the decade of 1970. A rep-
 278 resentation of the fundamental particles, i.e. particles that are not made
 279 of anything else, that compose the SM is presented in Figure 1.1. Most of
 280 these particles are unstable and decay to lighter particles within fractions
 281 of a second. As the scheme in Figure 1.1 indicates, the 12 fermions have
 282 their corresponding 12 anti-fermions and the quarks and gluons carry colour
 283 charge.

284 The SM is a gauge theory based on the symmetry group
 285 $SU(3)_C \otimes SU(2)_L \otimes U(1)_Y$, which describes all fundamental interactions
 286 except from the gravitational force¹. This theory provides an explana-
 287 tion to strong, weak and electromagnetic interactions via the exchange of
 288 the corresponding vector² bosons (spin-1 gauge fields). The mediation for
 289 the electromagnetic interaction (explicated in 1.1.2) is done by one mass-
 290 less photon (γ), this force is invariant under the $U(1)$ symmetry group.
 291 While for the weak interactions, guided by $SU(2)$, three massive bosons,
 292 W^+ , W^- and Z , act as mediators ($m_{W^\pm} = 80.385 \pm 0.015$ GeV [12] and
 293 $m_Z = 91.1876 \pm 0.02$ GeV [13]). Although the electromagnetic and weak in-
 294 teractions seem completely different at low energies, they are two aspects of
 295 the same force and can be described simultaneously by the $SU(2)_L \otimes U(1)_Y$

¹The gravitational interaction is described by Einstein’s General Relativity (GR) [11].

²“Vector bosons” refer to all particles that have spin 1 in contrast to the “scalar boson’s” which have spin 0.

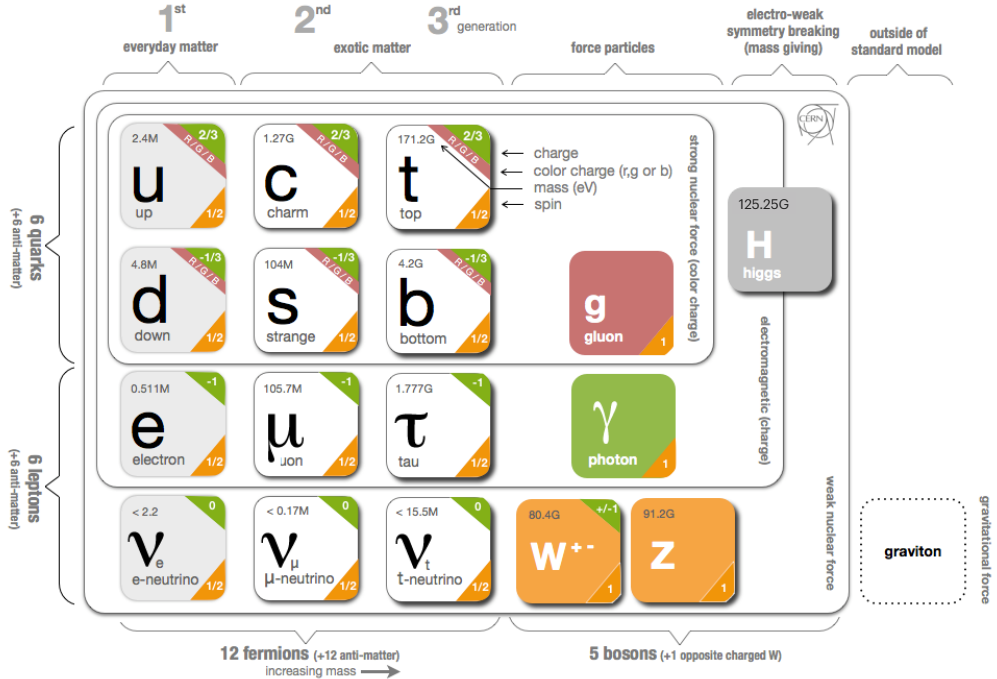


Figure 1.1: Fundamental particles of the Standard Model (image modified from [10]).

symmetry group, which represents the so called Electro-Weak (EW) sector (detailed in Section 1.1.3). The strong force, with its eight massless gluons (g), is described by the $SU(3)_C$ colour group (see Section 1.1.4). All these interactions differ in their magnitude, range and the physical phenomena that describe. These features are summarised in Table 1.1, where not only the interactions of the SM are included but the gravitation is as well.

Apart from the vector bosons, there is one massive scalar boson, the Higgs boson ($m_H = 125.25 \pm 0.17$ GeV). Through the interaction with this particle, all massive particles of Figure 1.1 gain their mass via the EW spontaneous symmetry breaking. This mechanism was first described by Englert, Brout [14] and Higgs [15], and its summarised in Section 1.1.5.1.

Before describing the fundamental interactions of the SM in the QFT formalism, let's introduce the main two types of particles according to their spin, i.e. intrinsic angular momentum: fermions and bosons.

310 Fermions

The fermions are the particles that follow the Fermi-Dirac statistics, i.e. obey the Pauli exclusion principle [16], resulting in a distribution of particles over energy levels in which two elements with the same quantum numbers

Interaction	Theory	Mediator	Relative strength	Range (m)
Strong	QCD	g	1	10^{-15}
Electromagnetic	QED/EW	γ	1/137	∞
Weak	EW	W^\pm, Z	10^{-6}	10^{18}
Gravitational	GR	-	6×10^{-39}	∞

Table 1.1: Typical strength of the fundamental interactions with respect to the strong interaction. Here the strength is understood as the coupling constant or gauge coupling parameter. In GR the gravitational interaction is not a force but the effect of the four-dimensional spacetime curvature and, hence, it has no mediator in this formalism.

cannot occupy the same states. The fermions include all particles with half-integer spin: quarks, leptons and baryons. A baryon is a non-fundamental particle composed of an odd number of valence quarks may be encountered or experienced in everyday life is baryonic matter. Some examples of baryons are³ the proton ($u u d$), the neutron ($d d u$), Λ ($u d s$), Λ_c^+ ($u d c$) and Σ^+ ($u u s$). Apart from the 3-quark baryons, an exotic pentaquark state has been observed at LHCb experiment of the LHC [17].

The fundamental fermionic matter (Table 1.2) is organised in the three families of leptons and quarks:

$$\begin{bmatrix} \nu_e & u \\ e^- & d \end{bmatrix}, \begin{bmatrix} \nu_\mu & c \\ \mu^- & s \end{bmatrix}, \begin{bmatrix} \nu_\tau & t \\ \tau^- & b \end{bmatrix}$$

.

These three generations, which are defined as the columns in Figure 1.1, exhibit the same kind of gauge interactions and they only differ in their mass [18]. According to the EW symmetry, each family can be classified as:

$$\begin{bmatrix} \nu_\ell & q_u \\ \ell^- & q_d \end{bmatrix} \equiv \begin{pmatrix} \nu_\ell \\ \ell^- \end{pmatrix}_L, \begin{pmatrix} q_u \\ q_d \end{pmatrix}_L, \ell^-_R, q_{uR}, q_{dR}$$

(plus the corresponding antiparticles) where the subindices L and R stand from left and right handed particles respectively. This structure responds to the fact that left-handed particles convert different than right-handed ones under $SU(2)$ transformations. The left-handed fields are $SU(2)_L$ doublets and the right-handed ones $SU(2)_L$ singlets. This difference is explained with more detail in Section 1.1.3.

The fundamental representation of $SU(3)$ is a triplet, this is why each quark can appear in three different colours, whereas each antiquark can exhibit one of the corresponding “anticolours”.

³Between round brackets, the valence quarks are shown.

Family	Name	Mass	Q
Quarks	Up (u)	$2.16^{+0.49}_{-0.26}$ MeV	$2/3$
	Down (d)	$4.67^{+0.48}_{-0.17}$ MeV	$-1/3$
	Charm (c)	1.27 ± 0.02 GeV	$2/3$
	Strange (s)	93^{+11}_{-5} MeV	$-1/3$
	Top (t)	172.76 ± 0.30 GeV	$2/3$
	Bottom (b)	$4.18^{+0.03}_{-0.02}$ GeV	$-1/3$
Leptons	Electron (e^-)	$0.5109989461 \pm 0.0000000031$ MeV	-1
	Muon (μ)	$105.6583745 \pm 0.0000024$ MeV	-1
	Tau (τ)	776.86 ± 0.12 MeV	-1
	Electron neutrino (ν_e)	ν_e, ν_μ, ν_e	0
	Muon neutrino (ν_μ)	\neq	0
	Tau neutrino (ν_τ)	ν_1, ν_2, ν_3	0

Table 1.2: Properties of the quarks and leptons. The electric charge, represented by Q, is presented in units of elementary charge (1.602×10^{-19} C). The ν_1, ν_2, ν_3 are the neutrino mass eigenstates.

338 The SM fermions properties are summarised in Table 1.2. As can be seen
 339 in its last rows, the neutrino flavour states do no correspond to the mass
 340 states (ν_1, ν_2, ν_3). What happens is that each flavour state is a quantum
 341 mechanical combination of neutrinos of different masses and viceversa. More
 342 details about the neutrino masses can be found in a dedicated text in Section
 343 1.1.6.2

344 The fundamental fermions are usually understood as the fundamental
 345 building blocks of matter. However, while the building blocks are important,
 346 there is a point that also has to be taken into account, the force. Without
 347 force these fermions would not interact which each other. The particles that
 348 mediate these interactions are the gauge bosons.

349 Bosons

350 Bosons differ from fermions by obeying the Bose-Einstein statistics, thus,
 351 bosons are not limited to single occupancy for a determined state. In other
 352 words, the Pauli exclusion principle is not applied. All particles with integer
 353 spin are bosons; from the particles shown on the right columns of Figure 1.1
 354 to the mesons. Mesons, along with baryons, are part of the hadron family,
 355 i.e. particles composed of quarks (see Section 1.1.4). The particularity
 356 of mesons is that they are formed from an equal number of quarks and
 357 antiquarks (usually one of each) bound together by strong interactions.
 358 Some examples of mesons are π^+ ($u \bar{d}$), π^0 ($\frac{u\bar{u}-d\bar{d}}{\sqrt{2}}$), K^+ ($u \bar{s}$) and J/ψ
 359 ($c \bar{c}$).

360 The elementary vector bosons are the force carriers and presented in
361 Table 1.1 while the Higgs boson is a fundamental particle as well.

362 **Gauge Invariance**

363 Constituting one of the most successful theories of Physics, the SM is able
364 to provide an elegant mathematical framework to describe the experimental
365 physics results with great precision. Another key element to understand the
366 SM is the concept of gauge invariance. As it is illustrated during the rest
367 of the Section 1.1, by demanding that the Lagrange density (also denoted
368 as Lagrangian) invariant under local gauge transformations, the existence
369 of the SM force-carrier bosons (γ , W^+ , W^- , Z and g).

370 **1.1.2 Quantum electrodynamics**

371 The gauge invariance refers to the invariance of a theory under trans-
372 formations which the theory is said to posses internal symmetry. The trans-
373 formations which are applied in all space-time locations simultaneously are
374 known as “global” transformations while the ones that vary from one point
375 to another are “local”. Each local symmetry is the basis of a gauge theory
376 and requires the introduction of its own gauge bosons as it is discussed in
377 the following pages.

In QFT, particles are described as excitations of quantum fields that satisfy the corresponding mechanical field equations. The Lagrangians in QFT are used analogous to those of classical mechanics, where the equation of motion can be derived from the Lagrangian density function (\mathcal{L}) and the Euler-Lagrange equations for fields:

$$\frac{\partial \mathcal{L}}{\partial \phi} - \partial_\mu \frac{\partial \mathcal{L}}{\partial (\partial_\mu \phi)} = 0,$$

378 where $\partial_\mu = \frac{\partial}{\partial x^\mu}$ denotes the partial derivatives with respect to the four-
379 vector x^μ and $\phi = \phi(\vec{x}, t)$ is the quantum field of a fermion or boson. The
380 Lagrangian is used to express the dynamics of the quantum field. In QFT,
381 Noether’s theorem [19] relates a symmetry in the \mathcal{L} to a conserved current.

382 The Dirac equation, $(i\gamma^\mu \partial_\mu - m)\Psi(x) = 0$, is one of the simplest relativistic
383 field equations. Its Lagrangian describes a free Dirac fermion:

$$\mathcal{L}_0 = i\bar{\Psi}(x)\gamma^\mu \partial_\mu \Psi(x) - m\bar{\Psi}(x)\Psi(x), \quad (1.1)$$

384 being Ψ the wave function (spinor represented by four complex-valued
385 components) of the particle, γ^μ are the Dirac or gamma matrices,

³⁸⁶ $\{\gamma^0, \gamma^1, \gamma^2, \gamma^3\}$, m the rest-mass of the fermion and $\bar{\Psi} = \Psi^\dagger \gamma^0$, the hermitic conjugate of the wave function. The gamma matrices build a set of
³⁸⁷ orthogonal basis vectors for covariant vectors in a Minkowski space. The
³⁸⁸ first term of \mathcal{L}_0 is the kinetic term while the second is the mass term.
³⁸⁹

This Lagrangian is invariant under $U(1)$ global transformations such as:

$$\Psi(x) \xrightarrow{U(1)} \Psi'(x) \equiv \exp\{iQ\theta\}\Psi(x), \quad (1.2)$$

³⁹⁰ where $Q\theta$ is a real constant. The phase of $\Psi(x)$ is a pure convention-
³⁹¹ dependent quantity without a physical meaning since the observables de-
³⁹² pend on $|\Psi(x)|^2$.

However, if θ was x dependent, the transformation 1.2 would be:

$$\Psi(x) \xrightarrow{U(1)} \Psi'(x) \equiv \exp\{iQ\theta(x)\}\Psi(x), \quad (1.3)$$

which is not longer a global transformation but a local transformation instead. The transformation in 1.3 would not let the \mathcal{L}_0 in 1.1 invariant because the derivative in the kinetic term would go as:

$$\partial_\mu \Psi(x) \xrightarrow{U(1)} \exp\{iQ\theta\}(\partial_\mu + iQ\partial_\mu\theta)\Psi(x). \quad (1.4)$$

The gauge principle is the requirement that the $U(1)$ phase invariance should hold locally. In order to do so, it is necessary to introduce an additional term to the Lagrangian so that when one applies $\Psi'(x) \equiv \exp\{iQ\theta(x)\}\Psi(x)$, the $\partial_\mu\theta$ term is canceled in 1.4. To achieve this invariance, a term with the vector gauge field A_μ is inserted. This field transforms as

$$A_\mu(x) \xrightarrow{U(1)} A'_\mu(x) \equiv A_\mu(x) + \frac{1}{e}\partial_\mu\theta \quad (1.5)$$

with a new D_μ , which acts as follows:

$$D_\mu\Psi(x) \equiv [\partial_\mu + ieQA_\mu(x)]\Psi(x) \quad (1.6)$$

which transforms like the field:

$$D_\mu\Psi(x) \xrightarrow{U(1)} (D_\mu\Psi)'(x) \equiv \exp\{iQ\theta\}D_\mu\Psi(x).$$

The Lagrangian density can be defined by replacing the partial derivatives in \mathcal{L}_0 (1.1) by the covariant derivative in 1.6:

$$\begin{aligned} \mathcal{L}_{QED} &\equiv i\bar{\Psi}(x)\gamma^\mu D_\mu\Psi(x) - m\bar{\Psi}(x)\Psi(x) \\ &= i\bar{\Psi}(x)\gamma^\mu[\partial_\mu + ieQA_\mu(x)]\Psi(x) - m\bar{\Psi}(x)\Psi(x) \\ &= i\bar{\Psi}(x)\gamma^\mu\partial_\mu\Psi(x) - \bar{\Psi}(x)\gamma^\mu eQA_\mu\Psi(x) - m\bar{\Psi}(x)\Psi(x) \\ &= \mathcal{L}_0 - eQA_\mu\bar{\Psi}(x)\gamma^\mu\Psi(x). \end{aligned} \quad (1.7)$$

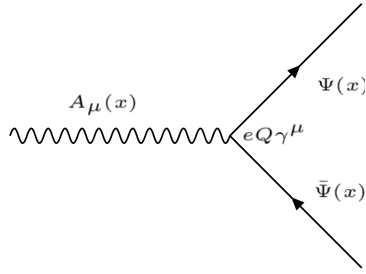


Figure 1.2: Three-point interaction vertex of QED.

393 The resulting Lagrangian is invariant under $U(1)$ local transformation.
 394 When the conversions 1.3 and 1.5 take place, the effects of the transformation
 395 are canceled out. Along with the original Lagrangian (\mathcal{L}_0), the \mathcal{L}_{QED}
 396 has an additional term describing the interaction between the fermion Ψ
 397 and the gauge field A_μ with a strength proportional to the charge eQ . This
 398 term, $eQA_\mu\bar{\Psi}\gamma^\mu\Psi$, that has been generated only by demanding the gauge
 399 invariance under $U(1)$, is not other than the vertex of QED (Figure 1.2).

This new A_μ term is the electromagnetic field and its quanta is the photon. A mass term containing $A^\mu A_\mu$ is forbidden because it would violate the $U(1)$ local invariance. In consequence, the mediator of the new A_μ field, the photon, is predicted to be a massless particle. To make A_μ a propagating field it is necessary to add the kinetic term of the field A_μ :

$$\mathcal{L}_{kin} \equiv -\frac{1}{4}F_{\mu\nu}(x)F^{\mu\nu}(x), \quad (1.8)$$

where $F^{\mu\nu} \equiv \partial_\mu A_\nu - \partial_\nu A_\mu$. The kinetic term $F_{\mu\nu}F_{\mu\nu}F^{\mu\nu}$ is already invariant under local $U(1)$ phase transformations. From the QED Lagrangian in 1.7 and the kinetic term in 1.8, the Maxwell equations can be derived to describe electromagnetism, the infinite range⁴ interaction that occurs between particles with electrical charge. The \mathcal{L}_{QED} with this kinetic term is written as:

$$\mathcal{L}_{QED} = \bar{\Psi}(x)(i\gamma^\mu\partial_\mu - m)\Psi(x) - eQ\bar{\Psi}(x)\gamma^\mu A_\mu\Psi(x) - \frac{1}{4}F_{\mu\nu}(x)F^{\mu\nu}(x). \quad (1.9)$$

400 1.1.3 Electroweak interactions

401 1.1.3.1 Weak interactions and Symmetries

402 The weak interaction is mediated by the W^+ , W^- and Z massive gauge
 403 bosons. Due their large mass, the range of the interactions is within a scale

⁴Since the photon is (predicted to be) massless, the electromagnetic interaction has an infinite range.

⁴⁰⁴ of $\sim 10^{-18}$ m. It is responsible for radioactive decays and flavour changing⁵
⁴⁰⁵ decays of fermions such as the decay of the muon ($\mu^- \rightarrow e^- \bar{\nu}_e \nu_\mu$).

⁴⁰⁶ Another particularity of this interaction is that it is the only interaction
⁴⁰⁷ that violates several fundamental symmetries. There is a relation between
⁴⁰⁸ symmetries and conservations laws which is known as Noether's theorem.
⁴⁰⁹ Classical physics examples of how the symmetries leads to conserved quanti-
⁴¹⁰ ties are:

- ⁴¹¹ • Invariance under change of time \rightarrow Conservation of energy
- ⁴¹² • Invariance under translation in space \rightarrow Conservation of momentum
- ⁴¹³ • Invariance under rotation \rightarrow Conservation of angular momentum

⁴¹⁴ The three discrete symmetries that are fundamental for the SM formu-
⁴¹⁵ lation and are always hold for electromagnetic and strong interactions are:

- **Charge conjugation (\mathcal{C}):** Replace positive quantum charges by neg-
 ative charges and vice versa. It does not affect mass, energy, mo-
 mentum or spin. Essentially, it is a transformation that switches all
 particles with their corresponding antiparticles.

$$\mathcal{C}\Psi(\vec{r}, t) = \bar{\Psi}(\vec{r}, t)$$

- **Parity (\mathcal{P}):** Parity involves a transformation that changes the alge-
 braic sign of the spatial coordinate system. It does not reverse time,
 mass, energy or other scalar quantities.

$$\mathcal{P} : \begin{pmatrix} x \\ y \\ z \end{pmatrix} \rightarrow \begin{pmatrix} -x \\ -y \\ -z \end{pmatrix} \quad \mathcal{P}\Psi(\vec{r}, t) = \Psi(-\vec{r}, t)$$

- **Time reversal (\mathcal{T}):** Consists in flipping the sign of the time

$$\mathcal{T} : t \rightarrow -t \quad \mathcal{T}\Psi(\vec{r}, t) = \Psi(\vec{r}, -t)$$

⁴¹⁶ The simultaneous combination of this three symmetries mentioned above
⁴¹⁷ results in the \mathcal{CPT} symmetry, a profound symmetry of QFT which is
⁴¹⁸ consistent through all experimental observations [20]. Meanwhile, the \mathcal{P} -
⁴¹⁹ symmetry and the \mathcal{C} -symmetry can be combined to create the \mathcal{CP} -symmetry,
⁴²⁰ the product of the two transformations. The weak interaction violates \mathcal{P}
⁴²¹ and \mathcal{C} symmetries. It also violates the combined \mathcal{CP} -symmetry. Therefore,
⁴²² through the CPT theorem [21], if the \mathcal{CP} is violated, \mathcal{T} is violated as well
⁴²³ to preserve the \mathcal{CPT} invariance [22].

⁵The leptonic charges are conserved.

424 **Parity violation**

425 Previously theorised by Lee and Yang [23], the confirmation of the non-
 426 conservation of \mathcal{P} in weak interactions arrived with the Wu experiment in
 427 1957 [24]. Studying the beta decay of the Cobalt-60, Wu and collaborators
 428 found that the neutrino and the antineutrino have the relative orientations
 429 of spin and linear momentum fixed. The neutrino spin is always opposite
 430 to the linear momentum, this is called left-handed particles. Meanwhile, for
 431 the antineutrinos, the momentum is always aligned in the same direction as
 432 the spin (right-handed particles). This causes the weak interactions which
 433 emit neutrinos or antineutrinos to violate the conservation of parity.

Only left-handed particles and right-handed antiparticles are sensitive to the weak force. Dirac fermion fields, ψ , exhibit chiral symmetry and the right and left handed chiral states can be expressed as:

$$\psi_L(x) = \frac{1}{2}(1 - \gamma_5)\psi(x) \equiv P_L\psi(x) \quad (1.10)$$

$$\psi_R(x) = \frac{1}{2}(1 + \gamma_5)\psi(x) \equiv P_R\psi(x) \quad (1.11)$$

with

$$\gamma^5 \equiv \gamma_5 \equiv \gamma^0\gamma^1\gamma^2\gamma^3 = \begin{pmatrix} 1 & 0 \\ 0 & 1 \end{pmatrix}$$

434 where P_L and P_R are known as projection operators. The last equality is
 435 valid in the Dirac representation.

436 **\mathcal{CP} violation**

437 While \mathcal{P} and \mathcal{C} are violated in a maximal way by the weak interactions,
 438 the product of these two discrete transformations, \mathcal{CP} , is still a good sym-
 439 metry (left-handed fermions \leftrightarrow right-handed fermions). Experiences such
 440 as the Wu experiment respect the \mathcal{CP} symmetry and, in fact, in the \mathcal{CP} is a
 441 symmetry of nearly all the observed phenomena. However, in 1964 Cronin
 442 and Fitch discovered a slight (2%) violation of the \mathcal{CP} symmetry in the
 443 decays of neutral kaons [25]. The \mathcal{CP} violation plays a fundamental role to
 444 explain the dominance of matter over antimatter in the present universe.
 445 More information about the matter-antimatter asymmetry can be found in
 446 the dedicated text in Section 1.1.6.2.

447 Direct \mathcal{CP} violation is allowed in the SM if a complex phase is present
 448 in the CKM matrix (described below). The “direct” \mathcal{CP} violation is a phe-
 449 nomenon where the same decay process has a different probability for a
 450 particle than for an antiparticle. An example of strong global \mathcal{CP} asym-
 451 metry observed corresponds to the decay into two kaons and one pion. The
 452 probability of $B^+ \rightarrow \pi^+ K^+ K^-$ is 20% higher than for $B^- \rightarrow \pi^- K^+ K^-$.

CKM matrix

The eigenstates that interact through weak interactions, known as “weak eigenstates” (d' , s' , u'), are different from the the physically observed mass eigenstates (d , s , u). This make possible the charged-flavour-changing-weak decays trough the Cabibbo-Kobayashi-Maskawa (CKM) matrix. The CKM matrix, V_{CKM} , describes the mixing between the three generations of quarks in the SM. The coupling of two quarks i and j to a W boson is proportional to the CKM matrix element V_{ij} .

$$\begin{pmatrix} d' \\ s' \\ u' \end{pmatrix} = \begin{pmatrix} V_{ud} & V_{us} & V_{ub} \\ V_{cd} & V_{cs} & V_{cb} \\ V_{td} & V_{ts} & V_{tb} \end{pmatrix} \begin{pmatrix} d \\ s \\ u \end{pmatrix} \quad (1.12)$$

453 It is a 3×3 unitary matrix described by four independent parameters:
454 three angles (θ_{ij}) and one phase (δ_{13}). Different equivalent representations
455 of the CKM matrix can be found in literature but the Particle Data Group
456 recommends the standard CKM parameterisation:

$$V_{CKM} = \begin{pmatrix} c_{12}c_{13} & -s_{12}c_{13} & s_{13}e^{-i\delta_{13}} \\ -s_{12}c_{23} - c_{12}s_{23}s_{13}e^{i\delta_{13}} & -c_{12}c_{23} - s_{12}s_{23}s_{13}e^{i\delta_{13}} & s_{23}c_{13} \\ s_{12}s_{23} - c_{12}c_{23}s_{13}e^{i\delta_{13}} & -c_{12}s_{23} - s_{12}c_{23}s_{13}e^{i\delta_{13}} & c_{23}c_{13} \end{pmatrix} \quad (1.13)$$

457 where $c_{ij} \equiv \cos \theta_{ij}$ and $s_{ij} \equiv \sin \theta_{ij}$, with i and j labelling the generations
458 ($i, j \in \{1, 2, 3\}$). The angles θ_{12} , θ_{23} and θ_{13} are known as Euler angles.
459 The complex phase δ_{13} allows the \mathcal{CP} violation [26].

460 The different elements of the CKM matrix are determined experiment-
461 ally and are summarised in Table 1.3. As can be seen in this table, the
462 largest values correspond to the diagonal elements of the CKM matrix.
463 This implies that the processes that do not change the flavour are strongly
464 preferred over the family-changing charged currents. For instance, for the
465 top quark, the decay to any of the three down-type quarks is allowed but
466 only $|V_{td}|^2 \times 100\% = 0.0064\%$ of times will decay to a down quark and
467 $|V_{ts}|^2 \times 100\% = 0.14\%$ to a strange quark.

468 1.1.3.2 Electroweak unification

469 At energies above the scale of the mass of the weak vector bosons
470 ($E_{EW} \sim m_Z \sim m_W \sim 100$ GeV), the electromagnetic and weak interactions
471 are unified into the Electroweak (EW) force. In other words, electromagnet-
472 ism and weak interactions are simultaneously described by the symmetry
473 group $SU(2)_L \otimes U(1)_Y$. The subindex L refers to left-handed fields and Y

CKM element	Value
V_{ud}	0.9740 ± 0.00011
V_{us}	0.22650 ± 0.00048
V_{cd}	0.22636 ± 0.0048
V_{cs}	0.97340 ± 0.011
V_{cb}	$0.04053^{+0.00083}_{-0.00061}$
V_{ub}	$0.00361^{+0.00011}_{-0.00009}$
V_{td}	$0.00854^{+0.00023}_{-0.00016}$
V_{ts}	$0.03978^{+0.00082}_{-0.00060}$
V_{tb}	$0.999172^{+0.000024}_{-0.000035}$

Table 1.3: Magnitude of the nine elements of the CKM matrix. The mean for the different measurements has been done by [27]. Note how the elements that refer to quarks of the same generation are favoured over the flavour-changing currents.

474 to the weak hypercharge. In contrast, at low energies, this interactions are
 475 treated as independent phenomena, the electromagnetism is described QED
 476 and the weak interaction by Fermi's theory.

In the EW model (Glashow-Salam-Weinberg model), two new quantum numbers are assigned to the particles of the SM: the weak isospin (\vec{T}) and Y . Here, the left-handed chiral states of fermions form isospin doublets (χ_L) with $T_3 = \pm 1/2$ and the right-handed form chiral states are composed of isospin singlets (χ_R) with $T_3 = 0$. For a particle, T_3 is the third component of the \vec{T} , which is related to the electric charge (Q) and the $U(1)$ hypercharge by Gell-Mann-Nishijima relation:

$$Q = T_3 + \frac{1}{2}Y \quad (1.14)$$

477 With this expression, the electromagnetic coupling and the electroweak
 478 couplings are connected. Having χ_L with $T_3 = \pm 1/2$ and χ_R with $T_3 = 0$
 479 implies that a $SU(2)$ weak interaction can rotate left-handed particles (i.e.
 480 convert a left-handed e^- into a left-handed ν_e emitting a W^-) but cannot
 481 do the same with right-handed.

482 Using the gauge invariance principle it is possible to find the QED and
 483 QCD Lagrangians, as it is described in Sections 1.1.2 and 1.1.4 respectively.

The free Lagrangian, as in the case of QED and QCD is:

$$\begin{aligned} \mathcal{L} &= i \sum_{j=1}^3 \bar{\Psi}(x) \gamma^\mu \partial_\mu \Psi(x) \\ &= i \sum_{j=1}^3 \bar{\chi}_L(x) \gamma^\mu \partial_\mu \chi_L(x) + i \sum_{k=1}^3 \bar{\chi}_R(x) \gamma^\mu \partial_\mu \chi_R(x) \end{aligned} \quad (1.15)$$

where the wave function Ψ has been spited into the left isospin doublets χ_L and and right isospin singlets χ_R . The indices j and k run over the three generations of the SM. This Lagrangian should be invariant when a gauge transformation under the $SU(2)_L \times U(1)_Y$ symmetry group in the flavour space is applied:

$$\chi_L(x) \xrightarrow{SU(2)_L \times U(1)_Y} \chi'_L(x) = \exp\{i\alpha^n \tau_n\} \exp\{i\beta y\} \chi_L(x) \quad (1.16)$$

$$\chi_R(x) \xrightarrow{SU(2)_L \times U(1)_Y} \chi'_R(x) = \exp\{i\beta y\} \chi_R(x) \quad (1.17)$$

with $\alpha, \beta \in \mathbb{R}$ and $n \in \{1, 2, 3\}$. This transformation is given by the generators of $SU(2)_L \times U(1)_Y$, i.e. the Pauli matrices (τ_n) and the weak hypercharge y . Note that $SU(2)_L$ transformation, $\exp\{i\alpha^n \tau_{nu}\}$, only acts on the doublet fields. This term containing the Pauli matrices is non-abelian like in QCD and, like in QCD, this leads to self-interacting terms.

To ensure invariance under $SU(2)_L \times U(1)_Y$, four different gauge fields have to be added (three from $SU(2)$ and one from $U(1)$). Four is also the correct number of gauge bosons needed to describe EW interactions: W^+ , W^- , Z and γ . While the three weak isospin currents couple to the triplet of vector bosons W_μ^n with $n \in \{1, 2, 3\}$, the weak hypercharge couples to an isosinglet B_μ . The fields W_μ^1 and W_μ^2 are electrically charged whereas W_μ^3 and B_μ are neutral fields. The EW covariant derivative is defined as:

$$D^\mu \chi_{L_j}(x) = [\partial_\mu - ig \frac{\tau_i}{2} W_\mu^i(x) - ig' \frac{y_j}{2} B_\mu(x)] \chi_{L_j}(x) \quad i \in [1, 2, 3] \quad (1.18)$$

$$D^\mu \chi_{R_j}(x) = [\partial_\mu - ig' \frac{y_j}{2} B_\mu(x)] \chi_{R_j}(x), \quad (1.19)$$

where g and g' are the interaction couplings to W_μ^i isotriplet and the B_μ isosinglet.

Using the derivatives in Equations 1.18 and 1.19, the Lagrangian in 1.20 is already invariant under local $SU(2)_L \times U(1)_Y$ transformations:

$$\mathcal{L} = i \sum_{j=1}^3 \bar{\chi}_L^j(x) \gamma^\mu D_\mu \chi_L^j(x) + i \sum_{k=1}^3 \bar{\chi}_R^k(x) \gamma^\mu D_\mu \chi_R^k(x) \quad (1.20)$$

Finally, if kinetic terms for the gauge bosons are included in 1.20, the EW SM Lagrangian is obtained:

$$\begin{aligned} \mathcal{L}_{EW} = & i \sum_{j=1}^3 \bar{\chi}_L^j(x) \gamma^\mu D_\mu \chi_L^j(x) + i \sum_{k=1}^3 \bar{\chi}_R^k(x) \gamma^\mu D_\mu \chi_R^k(x) \\ & - \frac{1}{4} W_{\mu\nu}^n(x) W_n^{\mu\nu}(x) - \frac{1}{4} B_{\mu\nu}(x) B^{\mu\nu}(x) \end{aligned} \quad (1.21)$$

Where the addition of kinetic terms gives rise to cubic and quadratic self-interactions among the gauge fields. Note that the mass terms of the fields are forbidden in order to ensure local gauge invariance and since the observed W^+ , W^- and Z bosons have masses different from zero, for the moment let's assume that something breaks the symmetry generating the observed masses.

The in \mathcal{L}_{EW} in 1.21 can be divided in two different parts according to the charge of the bosons: charged currents and neutral currents. Relating the charged currents (W_μ^1 and W_μ^2) to the W^+ and W^- bosons of the SM and the neutral (W_μ^3 and B_μ) ones with the Z and γ , it is possible to build linear combinations fo the original gauge fields that define the SM bosons.

Therefore, from the charged-current interactions, the W^+ and W^- bosons are:

$$W^\pm \equiv \frac{1}{\sqrt{2}}(W_\mu^1 \mp i W_\mu^2) \quad (1.22)$$

While for the neutral-current these combinations can be defined as a rotation of the so called Weinberg (or weak mixing) angle θ_W :

$$\begin{pmatrix} W_\mu^3 \\ B_\mu \end{pmatrix} \equiv \begin{pmatrix} \cos \theta_W & \sin \theta_W \\ -\sin \theta_W & \cos \theta_W \end{pmatrix} \begin{pmatrix} Z_\mu \\ A_\mu \end{pmatrix}$$

Rewriting this equation, the photon and Z -boson fields are

$$A_\mu = B_\mu \cos \theta_W + W_\mu^3 \sin \theta_W \quad Z_\mu = -B_\mu \cos \theta_W + W_\mu^3 \sin \theta_W \quad (1.23)$$

In order to ensure that this A_μ is the one of QED, apart from the Gell-Mann-Nishijima relation (Equation 1.14), it is requiered that the couplings of the γ , W^\pm and Z satisfy the relation:

$$g \sin \theta_W = g' \cos \theta_W = e \quad (1.24)$$

502 .

Within the unified EW model, once θ_W is known, the mass of Z is specified. Current measurements of θ_W give a value of $\sin^2 \theta_W = 0.2310 \pm 0.0005$ [28].

There is no mass term for the bosons in the EW Lagrangian that has been obtained in 1.21 by demanding the $SU(2)_L \times U(1)_Y$ local invariance, which enters in contradiction with the experimental observations for the W and Z bosons ($m_{Z,W} \sim 80$ GeV). The introduction of such a mass term would break the symmetry, however, the it is possible to add the mass for the W and Z bosons without loosing the properties of the symmetry. The method to do so is known as Englert–Brout–Higgs–Guralnik–Hagen–Kibble mechanism or, more commonly, just as Higgs mechanism. This mechanism is described in Section 1.1.5.



(a) Quark colours combine to be colourless. (b) Antiquark colours also combine to be colourless.

Figure 1.3: Colour charge combinations for quarks and antiquarks. Due to the confinement, the hadrons are colourless.

515 1.1.4 Quantum chromodynamics

516 1.1.4.1 Quarks and colour

517 QCD is QFT-based theory for describing the strong interactions between
518 quarks and gluons (partons). This type of interaction is the responsible
519 of the nuclear force, the one that acts between the protons and neutrons
520 of atoms binding them together. Without the strong force, the protons
521 inside the nucleus would push each other apart due to the electromagnetic
522 repulsion. It also holds the quarks within a hadron together.

QCD is based in the $SU(3)$ symmetry group and its name derives from the “colour” charge, an analogous to the electric charge of QED but for strong interactions. The colour charge was introduced in 1964 [29] to explain how quarks could coexist within some hadrons apparently having the same quantum state without violating the Pauli exclusion principle. To satisfy the Fermi-Dirac statistics it is necessary to add an additional quantum number, the colour, to the theory. Each species of quark (q) may have three different colours (q^α , $\alpha = 1, 2, 3$): red, green, blue. Baryons and mesons are described then by the colour singlet combinations:

$$B = \frac{1}{\sqrt{6}} \epsilon^{\alpha\beta\gamma} |q_\alpha q_\beta q_\gamma\rangle \quad M = \frac{1}{\sqrt{3}} \epsilon^{\alpha\beta} |q_\alpha \bar{q}_\beta\rangle$$

523 .

524 Additionally, it is postulated that all hadrons must have a global neutral
525 colour charge, i.e. the hadrons must be “colourless”. This assumption
526 is known as confinement hypothesis and it is made to avoid the existence
527 of non-observed extra states with non-zero colour. It is called colour con-
528 finement because it implies that it is not possible to observe free quarks
529 since they carry colour charge and, hence, they have to be confined within
530 colour-singlet combinations. Figure 1.3 depicts how different colours and
531 anticolours combine to create the “colourless” state.

⁵³² **1.1.4.2 Gauge invariance for $SU(3)$**

The dynamics of the quarks and gluons are controlled by the QCD Lagrangian. Using the power of the gauge invariance principle it is possible to deduce \mathcal{L}_{QCD} similarly to the reasoning developed in Section 1.1.2. Firstly, let's denote a quark field of colour α and flavour f by q_f^α . The vector $q_f^T \equiv (q_f^1, q_f^2, q_f^3)$ is defined under the $SU(3)$ colour space, meaning that each dimension corresponds to a colour. The Lagrangian

$$\mathcal{L}_0 = \sum_f \bar{q}_f (i\gamma^\mu \partial_\mu - m_f) q_f \quad (1.25)$$

is invariant under global $SU(3)$ transformation in the colour space,

$$q_f^\alpha \rightarrow (q_f^\alpha)' = U_\beta^\alpha q_\beta^\beta, \quad UU^\dagger = U^\dagger U = 1, \quad \det U = 1. \quad (1.26)$$

In the $SU(N)$ algebra, $SU(N)$ is the group of $N \times N$ unitary matrices (U) which can be written in the form $U = \exp\{i(\lambda^a/2)\theta_a\}$ with $a = 1, 2, \dots, N^2 - 1$. Therefore, the $SU(3)$ matrices can be written as

$$U = \exp\left\{i\frac{\lambda^a}{2}\theta_a\right\} \quad (1.27)$$

where the index a goes from 1 to 8 for the arbitrary parameter θ_a and $\frac{\lambda^a}{2}$, which denotes the fundamental representation of the $SU(3)$ algebra. The Einstein notation for summation over repeated indices is implied. The matrices λ^a are traceless and satisfy the commutation relations [18]:

$$\left[\frac{\lambda^a}{2}, \frac{\lambda^b}{2}\right] = if^{abc}\frac{\lambda^c}{2} \quad (1.28)$$

⁵³³, being f^{abc} the $SU(3)_C$ structure constants, which are real and totally ⁵³⁴ antisymmetric.

To satisfy the gauge invariance requirement, the Lagrangian has to be invariant under $SU(3)$ local transformations, i.e, transformations in which the phase is dependent of the space-time location, $\theta_a = \theta_a(x)$. To fulfil the condition, the quark derivatives in the Lagrangian in 1.25 have to be substituted by covariant objects. Since there are eight independent gauge parameters, eight different gauge bosons $G_a^\mu(x)$ are needed⁶. This bosons are the eight gluons and the new covariant objects are:

$$D^\mu q_f \equiv \left[\partial_\mu + ig_s \frac{\lambda^a}{2} G_a^\mu(x) \right] q_f \equiv [\partial_\mu + ig_s G^\mu(x)] q_f$$

⁶The eightfold multiplicity of gluons is labeled by a combination of color and anticolor charge (e.g. red–antigreen)

- 535 The compact matrix notation is used $[G^\mu(x)]_{\alpha\beta} \equiv \left(\frac{\lambda^a}{2}\right)_{\alpha\beta} G_a^\mu(x)$.

To ensure that the covariant derivative $(D^\mu q_f)$ transforms like the q_f , the transformation of the gauge fields are:

$$D^\mu \rightarrow (D^\mu)' = UD^\mu U^\dagger \quad G^\mu \rightarrow (G^\mu)' = UG^\mu U^\dagger + \frac{i}{g_s}(\partial_\mu U)U^\dagger \quad (1.29)$$

. The quark and gluon fields transform under an infinitesimal local transformation, i.e. $\theta_a(x) = \delta\theta_a(x) \approx 0$, the $SU(3)_C$ unitary matrices (eq. 1.27) can be expressed as their first order expansion:

$$U = \exp\left\{i\frac{\lambda^a}{2}\theta_a(x)\right\} \approx 1 + i\left(\frac{\lambda^a}{2}\right)\delta\theta_a(x)$$

and, consequently, the transformations for the colour-vector field (eq. 1.26) and gluon field (eq. 1.29) become:

$$\begin{aligned} q_f^\alpha \rightarrow (q_f^\alpha)' &= q_f^\alpha + \left(\frac{\lambda^a}{2}\right)_{\alpha\beta}\delta\theta_a q_f^\beta \\ G_a^\mu \rightarrow (G_a^\mu)' &= G_a^\mu - i\frac{i}{g_s}\partial_\mu(\delta\theta_a) - f^{abc}\delta\theta_b G_c^\mu. \end{aligned}$$

- 536 In contrast to the transformation for the photon field in QED (Equation 1.5), the non-commutativity⁷ of the $SU(3)_C$ matrices give rise to an
 537 additional term involving the gluon fields themselves $(-f^{abc}\delta\theta_b G_c^\mu)$, as the
 538 relation 1.28 expresses. For constant $\delta\theta_a$, the transformation rule for the
 539 gauge fields is expressed in terms of the structure constants f^{abc} ; thus, the
 540 gluon fields belong to the adjoint representation for the colour group. There
 541 is a unique coupling at $SU(3)_C$, g_s . All the colour-triplet flavours couple to
 542 the gluon fields with exactly the same interaction strength.

It is necessary to introduce the corresponding fields strengths to build a gauge-invariant kinetic terms for the gluon fields.

$$\begin{aligned} G^{\mu\nu} &\equiv -i\frac{-i}{g_s}[D^\mu, D^\nu] = \partial_\mu G^\nu - \partial_\nu G^\mu + ig_s[G^\mu, G^\nu] \equiv \frac{\lambda^a}{2}G_a^{\mu\nu}(x) \\ G_a^{\mu\nu} &\equiv \partial_\mu G_a^\nu - \partial_\nu G_a^\mu - g_s f^{abc}G_b^\mu G_c^\nu \end{aligned}$$

Under a $SU(3)_C$ transformation,

$$G^{\mu\nu} \rightarrow (G^{\mu\nu})' = UG^{\mu\nu}U^\dagger \quad (1.30)$$

⁷Because the generators of $SU(3)$ do not commute, QCD is known as non-Abelian gauge theory.

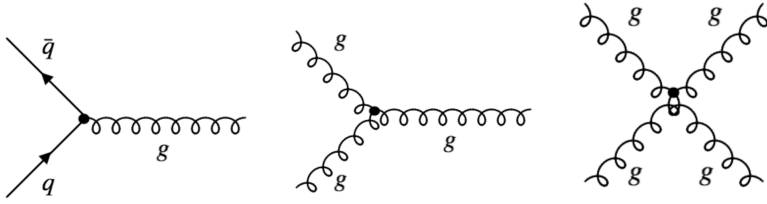


Figure 1.4: The predicted QCD interaction vertices arising from the requirement of $SU(3)_C$ local gauge invariance. The presence of the triples and quadruple gluon vertices is possible to the Non-Abelian nature of $SU(3)_C$.

and the colour trace $\text{Tr}(G^{\mu\nu}G_{\mu\nu}) = \frac{1}{2}G^{\mu\nu}G_{\mu\nu}$ remains invariant. Normalising the gluon kinetic term, the $SU(3)_C$ invariant QCD Lagrangian is obtained:

$$\mathcal{L}_{QCD} \equiv -\frac{1}{4}G_a^{\mu\nu}G_{\mu\nu}^a + \sum_f \bar{q}_f(i\gamma^\mu D_\mu - m_f)q_f \quad (1.31)$$

544 Note how the gluon-gluon vertex is find by demanding the gauge invari-
 545 ance under local $SU(3)_C$ transformation. A mass term is forbidden for the
 546 gluon fields by the $SU(3)_C$ gauge symmetry because a something of the form
 547 $\frac{1}{2}m_G^2 G_a^\mu G_\mu^a$ would not be invariant under the transformation in 1.29. The
 548 gluons are, then, predicted by the theory to be spin-1 massless particles.

549 Thanks to the colour symmetry properties, this Lagrangian looks very
 550 simple and all its interactions depend on the strong coupling constant, g_s .
 551 In contrast to the Lagrangian derived for QED (eq 1.7), in \mathcal{L}_{QCD} the boson
 552 field have a self-interacting term. This gluon self-interactions give rise to the
 553 triple and quadratic gluon vertex (center and right diagrams in Figure 1.4).
 554 This self-interactions among the gluon fields can explain features the asymp-
 555 totic freedom and confinement, properties that were not present in QED.
 556 The asymptotic freedom causes interactions between particles to become
 557 asymptotically weaker as the energy scale increases and the corresponding
 558 length scale decreases. The confinement implies that the strong forces in-
 559 crease with the distance, therefore, as two colour charges are separated,
 560 at some point it becomes energetically favorable for a new quark-antiquark
 561 pair to appear rather than keep getting further. This new quarks bond with
 562 the previous two, preventing single quarks to be isolated. This mechanism,
 563 depicted in Figure 1.5, explains why the strong interaction is responsable
 564 for keeping the quarks together forming hadrons.

565 1.1.5 Particle masses

For the QED Lagrangian, \mathcal{L}_{QED} (eq. 1.9), it is clear how the mass of the photon must be zero in order to satisfy the $U(1)$ local gauge symmetry



Figure 1.5: The QCD colour confinement explains the inseparability of quarks inside a hadron in spite of investing ever more energy. In this example, the mechanism is shown for a meson.

because, if a mass term for the vector gauge field A_μ is included, the \mathcal{L}_{QED} would be:

$$\mathcal{L}_{QED} = \bar{\Psi}(x)(i\gamma^\mu \partial_\mu - m)\Psi(x) - eQ\bar{\Psi}(x)\gamma^\mu A_\mu\Psi(x) - \frac{1}{4}F_{\mu\nu}(x)F^{\mu\nu}(x) + \frac{1}{2}m_\gamma^2 A_\mu A^\mu$$

and, with the $U(1)$ transformation in Equation 1.5, the new mass term becomes:

$$\frac{1}{2}m_\gamma^2 A_\mu A^\mu \rightarrow \frac{1}{2}m_\gamma^2 (A_\mu + \frac{1}{e}\partial_\mu \theta)(A^\mu + \frac{1}{e}\partial^\mu \theta) \neq \frac{1}{2}m_\gamma^2 A_\mu A^\mu$$

566 Confirming that the photon mass term is not invariant under local $U(1)$
 567 and, consequently, that the photon must be massless to satisfy the gauge
 568 invariance. Experimental efforts to measure the mass of the photon have
 569 set an upper limit of $m_\gamma \leq 1 \times 10^{-18}$ eV [30].

570 With the Lagrangian of QCD in Equation 1.31 happens the same, the
 571 mass term for the gluon fields are forbidden by the $SU(3)_C$ gauge symmetry.
 572 Therefore, the mediating bosons for the strong interactions are massless as
 573 well (experimentally, a mass as large as upper limits of a few MeV have
 574 been set, see [31]).

575 While the prohibition of mass terms for the bosons of QED and QCD is
 576 not a problem, this requirement also applies to the $SU(2)_L$. This condition
 577 enters into open contradiction with the measurements of large masses for
 578 the W and Z bosons of weak interactions.

579 For weak interactions, the problem of massless particles do not only
 580 affect the bosons. Since under the $SU(2)_L$ transformations left-handed
 581 particles transform as weak isospin doubles and right-handed particles as
 582 isospin singlets, the mass term of a spinor field Ψ written as chiral states
 583 also breaks the required gauge invariance: $-m\bar{\Psi}(x)\Psi(x) = -m\bar{\Psi}(x)(P_R +$
 584 $P_L)\Psi(x) = -m(\bar{\Psi}_R(x)\Psi_L(x) + \bar{\Psi}_L(x)\Psi_R(x))$

585 The Higgs mechanism describes how both the W and Z bosons and the
 586 fermions acquire mass without breaking the local gauge symmetry of the
 587 SM.

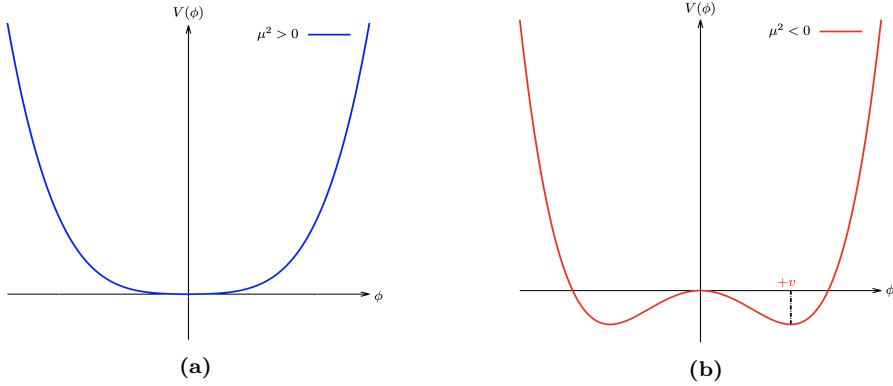


Figure 1.6: The potential $V(\phi)$ of Lagrangian 1.32 for (a) μ^2 positive and (b) negative.

588 1.1.5.1 The Higgs mechanism

Goldstone theorem and spontaneous symmetry breaking

For a scalar field ϕ with a Lagrangian of the form:

$$\mathcal{L} = \frac{1}{2} \partial_\mu \phi_i \partial^\mu \phi_i - V(\phi) \text{ where } V(\phi) = \frac{1}{2} \mu^2 \phi_i \phi_i + \frac{1}{4} \lambda (\phi_i \phi_i)^2 \quad (1.32)$$

This Lagrangian is invariant under $\phi_i \rightarrow \phi'_i = R_{ij} \phi_j$, where R_{ij} are rotational matrices in 4-dimensions. The mass term is the one with $\phi_i \phi_i$ and the parameter λ has to be positive for \mathcal{L} to describe a physical system, if $\lambda < 0$ the potential is unbounded from below. Contrary, the parameter μ^2 can be either positive or negative. As depicted in Figure 1.6a, if $\mu^2 > 0$, the vacuum expectation value (i.e. minimum of potential) is located at the origin ϕ_0 and this \mathcal{L} would describe a spin-0 particle of mass μ . However, if $\mu^2 < 0$, the potential $V(\phi)$ has the form of Figure 1.6a and \mathcal{L} would not represent anymore the Lagrangian of a particle of mass μ . The vacuum expectation value is now multivalued:

$$\phi_0 = \pm \sqrt{-\frac{\mu^2}{\lambda}} \equiv \pm v$$

Expanding the field around the minima at $\phi_i = (0, 0, 0, v)$, the \mathcal{L} becomes:

$$\begin{aligned} \mathcal{L} = & \frac{1}{2} \partial_\mu \sigma \partial^\mu \sigma + \mu^2 \sigma^2 - \sqrt{\mu^2 \lambda} \sigma^3 - \frac{1}{4} \lambda^4 \\ & + \frac{1}{2} \partial_\mu \pi_i \partial^\mu \pi_i - \frac{1}{4} \lambda (\pi_i \pi_i)^4 - \lambda v \pi_i \pi_i \sigma - \frac{1}{2} \pi_i \pi_i \sigma^2 \end{aligned} \quad (1.33)$$

589 where i runs from 1 to 3. Here $\sigma = \phi_4 - v$ and $\pi_i = \phi_i$ are new boson fields,
590 being the latter massless and the former with a mass of $m_\sigma^2 = -2\mu^2$. The

new terms break the original symmetry because the symmetry of the Lagrangian is not longer a symmetry of the vacuum, it has been spontaneously broken. One massive σ boson and three massless π_i bosons with a residual $O(3)$ symmetry have appeared. This is a consequence of the Goldstone theorem which states that “for a continuous symmetry group \mathcal{G} spontaneously broken down to a subgroup \mathcal{H} , the number of broken generators is equal to the number of massless scalars that appear in the theory” [32]. Therefore, since the $O(N)$ group has $N(N - 1)/2$ generators, the $O(N - 1)$ has $(N - 1)(N - 2)/2$ and, hence, $N - 1$ Goldstone bosons appear. The example shown is for $N = 4$.

The Higgs mechanism in the SM - Bosons

To apply this mechanism to the SM, it is necessary to generate mass for the W^+ , W^- and Z bosons while keeping the photon massless. In order to do so, the EW symmetry group $SU(2)_L \times U(1)_Y$ has to be broken into a $U(1)$ subgroup describing electromagnetism. A gauge-invariant interaction that gives masses to fermions without mixing chiral components is introduced by defining a $SU(2)$ isospin doublet of complex scalar field with hypercharge $Y = 1$:

$$\Phi = \begin{pmatrix} \phi^+ \\ \phi_0 \end{pmatrix}$$

Being ϕ^+ positively charged and ϕ^0 neutral. The Lagrangian \mathcal{L}_{Higgs} has to be added to the \mathcal{L}_{EW} in 1.21.

$$\mathcal{L}_{Higgs} = (D_\mu \Phi)^\dagger (D^\mu \Phi) - V(\Phi) \text{ where } V(\Phi) = \mu^2 \Phi^\dagger \Phi + \lambda (\Phi^\dagger \Phi)^2$$

with $\lambda > 0$ required for vacuum stability. When $\mu^2 > 0$, the minimum of the potential occurs when both fields (ϕ^+ and ϕ^0) are at zero. If $\mu^2 < 0$, the minimum of the potential has an infinite number of degenerate states that satisfy $\Phi^\dagger \Phi = \mu^2/2\lambda$ and the physical vacuum state will correspond to any particular point on the circle of Figure 1.7. Having to chose a particular point breaks the global $U(1)$ symmetry of the Lagrangian. Without loss of generality, in this scenario, the ground state Φ_0 can be chosen to be:

$$\Phi_0 = \frac{1}{\sqrt{2}} \begin{pmatrix} 0 \\ v \end{pmatrix} \text{ where } v = 2\sqrt{\frac{\mu^2}{\lambda}}$$

being v the vacuum expectation value. This defines the already mentioned circle in the minimum of $V(\Phi)$ in the $\mu^2 < 0$ scenario.

The Lagrangian density must be formulated in terms of deviations from one of these ground states. This can be done by introducing an excitation, $h(x)$, that can be understood as a small deviation of the field from the

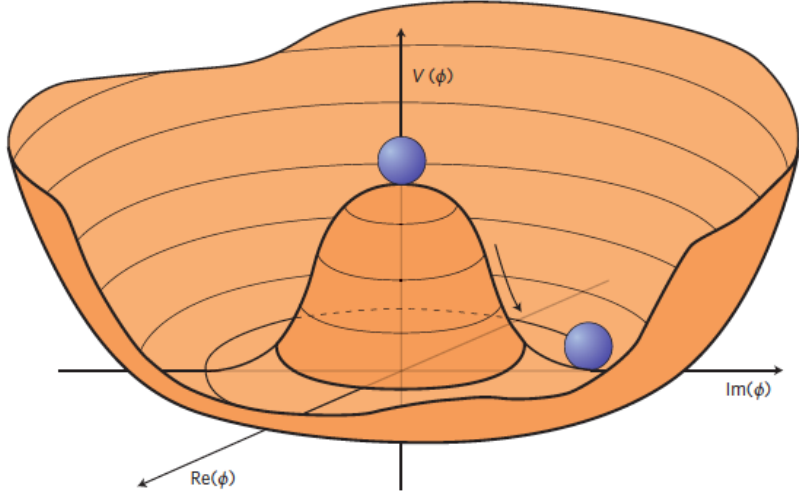


Figure 1.7: An illustration of the Higgs potential $V(\Phi)$ in the case of $\mu^2 < 0$. Choosing any particular point in the circle defined by v spontaneously breaks the $U(1)$ rotational symmetry. This type of potential is frequently called “Mexican hat”.

ground state. Accordingly, the fields can be expanded around the minimum as:

$$\Phi = \frac{1}{\sqrt{2}} \begin{pmatrix} 0 \\ v + h(x) \end{pmatrix} \exp\{i\chi(x)\}$$

The new field $\chi(x)$ can be set to zero in the so called “unitary gauge”.

$$\Phi = \frac{1}{\sqrt{2}} \begin{pmatrix} 0 \\ v + h(x) \end{pmatrix} \quad (1.34)$$

Expanding the covariant derivative of the \mathcal{L}_{Higgs} :

$$\begin{aligned} (D_\mu \Phi)^\dagger (D^\mu \Phi) &= \left| \left(\partial_\mu + ig \frac{\tau^k}{2} W_\mu^k(x) + ig' \frac{y}{2} B_\mu \right) \right|^2 \\ &= \frac{1}{2} \left| \begin{pmatrix} \partial_\mu + i\frac{1}{2}(gW_\mu^3 + g'\frac{y}{2}B_\mu) & i\frac{g}{2}(W_\mu^1 - iW_\mu^2) \\ i\frac{g}{2}(W_\mu^1 - iW_\mu^2) & \partial_\mu - i\frac{1}{2}(gW_\mu^3 - g'\frac{y}{2}B_\mu) \end{pmatrix} \begin{pmatrix} 0 \\ v + h \end{pmatrix} \right|^2 \\ &= \frac{1}{2} (\partial_\mu h)^2 + \frac{1}{8} (v + h)^2 |W_\mu^1 - iW_\mu^2|^2 \\ &\quad + \frac{1}{8} (v + h)^2 |gW_\mu^3 - g'B_\mu| + (\text{interaction terms}) \end{aligned}$$

Where the τ_k with $k = 1, 2, 3$ are the Pauli Matrices. In this equation there are terms mixing the W^3 and the B_μ fields that, by using the physical fields defined in Equation 1.1.3.2, should disappear since the physical bosons do not mix. Applying the Relation 1.1.3.2 into the covariant derivative,

$$(D_\mu \Phi)^\dagger (D^\mu \Phi) = \frac{1}{2} + \frac{g^2 v^2}{4} W_\mu^+ W^{-\mu} + \frac{g^2 v^2}{8 \cos^2 \theta_W} Z_\mu Z^\mu + 0 A_\mu A^\mu$$

, the W^+ , W^- and Z bosons have finally acquired mass. Through the Higgs mechanism, their masses within the SM are:

$$M_W = \frac{1}{2}gv \quad M_Z = \frac{1}{2} \frac{gv}{\cos \theta_W}$$

603 Additionally, a new scalar field $h(x)$ has appeared with its correspondent
 604 mass term, the Higgs field. Note that the $h(x)$ was introduced as a perturba-
 605 tion from the ground state of the Higgs potential $V(\Phi)$, so the Higgs boson
 606 can be understood as an excitation of the Higgs potential. Apart from cou-
 607 plings to the electroweak gauge fields, the Higgs field has also self-interaction
 608 vertices. The mass of this boson is $m_H = \sqrt{2}\mu$.

With this covariant term, the Higgs Lagrangian density of the system is obtained:

$$\begin{aligned} \mathcal{L}_{Higgs} = & \frac{1}{2}(\partial_\mu h)(\partial^\mu h) + \frac{g}{4}(v+h)^4 W_\mu W^\mu + \frac{g^2}{8\cos^2 \theta_W}(v+h)^2 Z_\mu Z^\mu \\ & + \frac{\mu^2}{2}(v+h)^2 - \frac{\lambda}{16}(v+h)^4 \end{aligned}$$

and expressing it in terms of the boson masses and coupling parameters, it can be written as:

$$\begin{aligned} \mathcal{L}_{Higgs} = & \frac{1}{2}(\partial_\mu h)(\partial^\mu h) - \frac{1}{2}m_H^2 h^2 + \frac{1}{2}m_W W_\mu W^\mu + \frac{1}{2}m_Z Z_\mu Z^\mu + g m_W h W_\mu W^\mu \\ & + \frac{g^2}{4} W_\mu W^\mu + g \frac{m_Z}{2\cos \theta_W} h Z_\mu Z^\mu - g^2 \frac{1}{4\cos^2 \theta_W} h^2 Z_\mu Z^\mu - g \frac{m_H^2}{4m_W} h^3 \\ & - g^2 \frac{m_H^2}{32m_W^2} h^4 + \text{const.} \end{aligned} \tag{1.35}$$

609 As can be seen in the Lagrangian 1.35, the coupling strengths of the W and
 610 Z fields to the Higgs are proportional to m_W and m_Z respectively.

The Higgs mechanism in the SM - Fermions

The Higgs mechanism for spontaneous symmetry breaking of the $SU(2)_L \times U(1)_Y$ gauge group of the SM generates the masses of the W^\pm and Z bosons. For originating the mass of the fermions without violating the EW gauge symmetry a similar procedure is carried but taking into account that the left-handed particles transform different than the right-handed. To do so, additional terms including the Yukawa couplings are added into the Lagrangian. These terms are of the form:

$$-y_f (\bar{\chi}_L^f \Phi \chi_R^f + \bar{\chi}_R^f \Phi^\dagger \chi_L^f)$$

where the f superindex runs over all quarks and charged leptons. It is usual to express the second part of the sum just as “plus hermitic conjugate” (“+ h.c.”). Note that the hermitic conjugate part is necessary to ensure that expression fulfils the requirement for a hermitian operator to be self-adjoint in a complex Hilbert space. The different y_f constants are known as Yukawa couplings of the particle f to the Higgs field. The Higgs doublet is denoted by Φ . For the electron $SU(2)$ doublet, the element with this coupling can be written as:

$$\mathcal{L}_e = -y_e \left[(\bar{\nu}_e \bar{e})_L \begin{pmatrix} \phi^+ \\ \phi^0 \end{pmatrix} e_R + \bar{e}_R (\phi^{+*} \phi^{0*}) \begin{pmatrix} \nu_e \\ e \end{pmatrix}_L \right] \quad (1.36)$$

Here, y_e is the Yukawa coupling of the electron to the Higgs boson. After spontaneously breaking the symmetry as it is done in eq. 1.34, the Lagrangian in 1.36 becomes:

$$\mathcal{L}_e = \frac{-y_e}{\sqrt{2}} v (\bar{e}_L e_R + \bar{e}_R e_L) + \frac{-y_e}{\sqrt{2}} h (\bar{e}_L e_R + \bar{e}_R e_L) \quad (1.37)$$

The y_e is not predicted by the Higgs mechanism, but can be chosen to be consistent with the observed electron mass (m_e) so that $y_e = \sqrt{2} m_e / v$. Using this relation, the Lagrangian in 1.37 becomes:

$$\mathcal{L}_e = -m_e \bar{e} e - \frac{m_e}{v} \bar{e} e h \quad (1.38)$$

611 The first element of the Lagrangian in 1.38 gives mass to the electron and
 612 gives rise to the coupling of the electron to the Higgs fields in its non-
 613 zero vacuum expectation. The second term represents the coupling of the
 614 electron and the Higgs boson itself.

615 The non-zero vacuum expectation value occurs only in the neutral part
 616 of the Higgs doublet (the lower in $\Phi = \begin{pmatrix} \phi^+ \\ \phi^0 \end{pmatrix}$) due to the form in the
 617 ground state in 1.34. This implies that the combination $\bar{\chi}_L^f \Phi \chi_R^f + \bar{\chi}_R^f \Phi^\dagger \chi_L^f$
 618 can only generate masses for the fermions in the lower component of an
 619 $SU(2)$ doublet, i.e. the charged leptons and the down type quarks. Putting
 620 aside the procedure to give mass to the up-type quarks, this explains why
 621 the neutrinos do not get mass through the Higgs mechanism.

For the up-type quarks, a gauge invariant term can be constructed from $\bar{\chi}_L^f \Phi_c \chi_R^f + \bar{\chi}_R^f \Phi_c^\dagger \chi_L^f$:

$$\mathcal{L}_u = y_u (\bar{u} \bar{d})_L \begin{pmatrix} -\phi^{0*} \\ \phi^- \end{pmatrix} u_R + \text{h.c.}$$

Applying the symmetry breaking:

$$\mathcal{L}_u = \frac{-y_u}{\sqrt{2}} v (\bar{u}_L u_R + \bar{u}_R u_L) + \frac{-y_u}{\sqrt{2}} h (\bar{u}_L u_R + \bar{u}_R u_L)$$

with a Yukawa coupling between the up quark and the boson $y_u = \sqrt{2} m_u/v$, resulting in:

$$\mathcal{L}_u = -m_u \bar{u} u - \frac{m_u}{v} \bar{u} u h.$$

Therefore, for Dirac fermions, mass terms that let the Lagrangian invariant under local gauge transformations can be constructed from

$$\mathcal{L} = -y_f [\bar{\chi}_L^f \Phi \chi_R^f + (\bar{\chi}_R^f \Phi \chi_L^f)^\dagger] \quad \text{or} \quad \mathcal{L} = y_f [\bar{\chi}_L^f \Phi_c \chi_R^f + (\bar{\chi}_R^f \Phi_c \chi_L^f)^\dagger].$$

The left Lagrangian is used for the leptons and down-type quarks, while the right one is used for the up-type quarks. These elements give rise not only to the mass of the fermions but also to the interaction strengths between these fermions and the Higgs boson. The Yukawa coupling of the fermions to the Higgs field is given by:

$$y_f = \sqrt{2} \frac{m_f}{v} \tag{1.39}$$

where the Higgs vacuum expectation value is fixed by the Fermi coupling G_F and is measured to be $v = \sqrt{2} G_F \approx 246.22 \text{ GeV}$. The G_F is measured from the μ^+ lifetime [33]. The G_F is also used to determine the magnitude of the elements in the CKM matrix.

The value of fermionic masses is not predicted by the SM but obtained through experimental observations. Given the $m_{top} = 172.76 \pm 0.30 \text{ GeV}$, it is of particular interest the Yukawa coupling of the top quark to the Higgs field, y_t , which is almost exactly equal to one. It is important to verify this because deviation of the measured y_t from the SM prediction would be a proof of new physics.

1.1.6 Wrap up

Perhaps the ultimate and definitive (if talking about definitive makes any sense) theory of particle physics is a simple equation with a small number of free parameters. Meanwhile, the SM is here, and while it is not the ultimate theory, it is unquestionably one of modern physics' greatest successes. Despite its achievements, many questions remain unsolved.

1.1.6.1 The parameters of the Standard Model

The SM contains 25 free parameters that must be determined through observation and experimentation. These are the masses of the twelve fermions (assuming color variations and antiparticles are not viewed as separate

642 fermions) or, more precisely, the twelve Yukawa couplings to the Higgs field
 643 ($m_{\nu_1}, m_{\nu_2}, m_{\nu_3}, m_e, m_\mu, m_\tau, m_u, m_d, m_c, m_s, m_t$ and m_b):

644 The three coupling constants of describing the strength of the gauge
 645 interactions (g, g' and g_s). and the two parameters describing the Higgs po-
 646 tential (μ and λ) or, equivalently, its vacuum expectation value v and the
 647 Higgs mass m_h . The three mixing angles and the complex phase of the CKM
 648 matrix and the four of the PMNS matrix ($\theta_{12}, \theta_{13}, \theta_{23}, \rho_{13}, \theta'_a, \theta'_b, \theta'_c$ and θ'_d),
 649 which mixing of neutrino-mass eigenstates with neutrino-flavour eigen-
 650 states):

651 From the 25 free parameters of the SM, 14 are associated to the Higgs
 652 field, eight with the flavour sector and only three with the gauge interac-
 653 tions.

654 1.1.6.2 Problems with the Standard Model

655 While the SM is very good theory that has passed rigorous testing, this
 656 is not the ending of the story, there are several limitations of the SM and
 657 a variety phenomena that it does not explain. The SM does not cover all
 658 questions in the universe and, hence, physicist continue looking for better
 659 theories to explain more. There is a long list of small and minor issues with
 660 the SM in the following pages only the most relevant ones are described.

661 Gravity

662 Gravity is the first force that any person learns about and the one known
 663 by the humankind for the most time. The SM describes all the other fun-
 664 damental interactions but this one. In the Table 1.1, the four forces are
 665 presented along with the theories to describe them. While QCD, QED and
 666 EW interactions are part of the SM, the GR is not. GR is a geometric the-
 667 ory that currently describes the gravitation in modern physics. Some of the
 668 suggested solutions to integrate gravitational interactions in the SM consist
 669 in postulating a new force carrier particle, the “graviton”, that mediates
 670 this interaction in a similar way to how the gauge bosons were proposed.
 671 Other explanations state that the gravity can only be described by a deeper
 672 theory in which the time-space structure is not flat like it is in the SM but
 673 dynamic.

674 Neutrino masses

675 According to the SM the neutrinos are massless, nevertheless, many ex-
 676 periments confirm that this is not true [34]. This is due to a property of
 677 neutrinos that allows them to change their flavour while traveling through

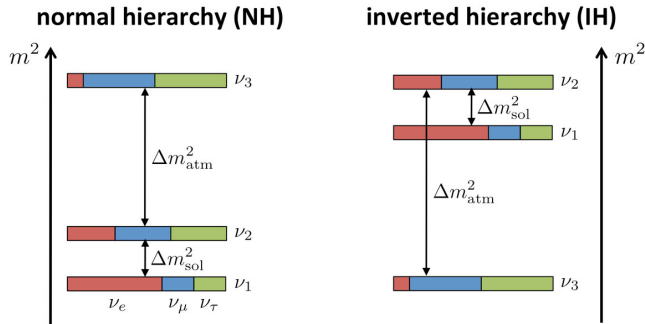


Figure 1.8: Two potential mass orderings of neutrinos are the normal ordering (normal hierarchy) and the inverted ordering (inverted hierarchy).

the space, this feature is known as “neutrino oscillations”. Each of the three neutrino flavours (ν_e , ν_μ , ν_τ) is a linear combination of three discrete neutrino-mass eigenstates (ν_i with $i \in \{1, 2, 3\}$) with mass eigenvalues (m_i). While the neutrino oscillation experiments could probe the squared neutrino-mass eigenvalues (Δm_{ij}^2), both the total scale of the masses and the sign of Δm_{ij} remains as some the most relevant open questions in particle physics. Regarding to the sign of Δm_{ij} , it is known that the mass of ν_2 is slightly higher than ν_1 ($\Delta m_{21}^2 \equiv m_2^2 - m_1^2 \sim 10^{-4}$ eV) but for the third mass eigenstate it has not been measured yet whether it is greater (normal ordering) or lower (inverted ordering) than the other two, as it is depicted in Figure 1.8. Nevertheless, the absolute square difference is known ($\Delta m_{31}^2 \equiv |m_3^2 - m_1^2| \sim 10^{-3}$ eV).

Non-zero neutrino masses opened an interesting portal on beyond SM physics and, even though neutrinos are very elusive when it comes to detect them, some next-generation experiments such as Dune are very promising when it comes to set competitive and model independent limits on neutrino masses.

Regarding to the nature of this mass, one could add mass terms to the SM as it is done in Section 1.1.5.1 for the up-type quarks but the origin of the neutrino masses is still not known. Also, if neutrinos gained mass through Yukawa interaction, it would imply the presence of right-handed neutrinos, which has not been observed.

700 Matter-antimatter asymmetry

In principle, the Big Bang should have produced an equal amount of matter and antimatter which would all have then annihilated, leaving behind an empty Universe filled with EM radiation. However, everything we see now is essentially totally constituted of matter, from the tiniest life forms on

705 Earth to the greatest celestial objects. In comparison, there isn't a lot of
 706 antimatter around.

707 By looking at the CMB radiation, which contain the residual photons
 708 of the Big Bang, researchers have determined that there was a symmetry
 709 between the matter and antimatter content in the early universe. For every
 710 3×10^9 antimatter particles, there were 3×10^9 and 1 matter particles. The
 711 matter and antimatter annihilate and produced the CMB and the remaining
 712 1 part turned into all the stars and galaxies that are seen. The field of
 713 cosmology that studies the processes that produced an asymmetry between
 714 leptons and antileptons in the very early universe is called leptogenesis.

715 Researches carried during the last few decades have revealed that the
 716 laws of nature do not equally apply to matter and antimatter. So far, the
 717 only non-trivial difference between matter and antimatter found is the \mathcal{CP}
 718 asymmetry (or \mathcal{CP} violation, which has been introduced in Section 1.1.3).
 719 Alas, the quantity of \mathcal{CP} asymmetry included in the SM is insufficient to
 720 explain the composition of the observable universe and, hence, extensive
 721 searches of new sources of \mathcal{CP} violation are being carried.

722 In this context, the studies described in this thesis are part of the seek
 723 of new \mathcal{CP} -violation sources. As Section 2.3.3 details, the observation of a
 724 cross-section greater than the one predicted by the SM would imply that
 725 Higgs-single-top-quark associated production does not conserve \mathcal{CP} .

726 **Dark energy**

727 According to cosmological observations, the matter described by the SM
 728 only makes up around 5% of the universe. It turns out that roughly 68% of
 729 the universe is dark energy, which is not considered by the SM.

730 Dark energy is an unknown type of energy postulated to explain the
 731 observed accelerated expansion of the universe as Figure 1.9. This expansion
 732 is dominated by a spatially smooth component with negative pressure
 733 called dark energy. Modern cosmological measurements are based in super-
 734 novae, cosmic microwave background fluctuations, galaxy clustering and
 735 weak gravitational lensing, and methods agree with a spatially flat universe
 736 with about 30% matter (visible and dark) and 70% dark energy [35].

737 **Dark matter**

738 The rest of the energy content in the universe is the matter. Dark matter
 739 (DM) adds up for approximately 85% of all matter and 27% of all energy.
 740 This matter is called dark because it does not interact with the electromagnetic
 741 field, so maybe a name such us invisible matter would have been more
 742 appropriate since rather than being dark it just does not emit or reflect

743 light. The only way to interact with DM is via gravitational interaction,
 744 which is about 25 orders of magnitude weaker than the weak force (as Table
 745 1.1 shows). This is why DM is so difficult to detect. The SM does not
 746 provide a proper explanation but searches are being carried and candidates
 747 such as weakly interacting massive particles (WIMPs) or axions⁸ have been
 748 proposed.

749 The existence of DM has been
 750 inferred through gravitational ef-
 751 fects in astrophysical and cosmolo-
 752 gical observations. The rotational
 753 speed of the galaxies [38], the grav-
 754 itational lensing [39] and the CMB
 755 angular spectrum [40] are some ex-
 756 amples of phenomena that cannot
 757 be explained with general relativity
 758 unless there is more present matter
 759 what it is seen.

760 Although the vast majority of
 761 scientific community accepts dark
 762 matter existence, alternative ex-
 763 planations for the observed phe-
 764 nomena have suggested. Most of
 765 these model consists in modifica-
 766 tions of GR. The search of DM at
 767 particle colliders, which is focussed on large missing transverse energy sig-
 768 natures, have not result in any observation. Nevertheless, the existence of a
 769 particle is never discarded, only its presence within the detector sensitivity
 770 limits.

771 Others

772 (**quizás, esto the "others" sobra ya**) The different problems mentioned
 773 hitherto are just some of the most relevant open questions that fundamental
 774 physics has not being able to answer yet. Nonetheless, there are many other
 775 issues whose discussion would need many pages and are outside the scope
 776 of this work. Even so, it won't harm to list a few of them:

- 777 • Hierarchy problem: It is caused by the enormous distance between
 778 two fundamental physics scales: the EW scale ($\sim 10^2$ GeV) and the
 779 Planck scale ($\sim 10^{19}$ GeV).

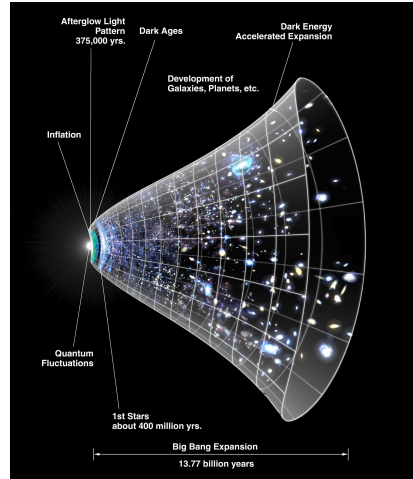


Figure 1.9: The universe's expansion over time. The dark-energy existence has been suggested to explain this expansion.

⁸An axion is a hypothetical elementary particle postulated to resolve the strong CP problem [36] [37].

- Strong \mathcal{CP} problem: It refers to the fact that, while QCD does not explicitly prohibit \mathcal{CP} violation in strong interactions, it has yet to be observed in experiments.
- Naturalness: It is the property that the dimensionless ratios between free parameters or physical constants appearing in a physical theory should take values of order unity. By looking at the parameters of the SM described in Section 1.1.6.1, it can be seen that the naturalness principle is not satisfied. For instance, the masses of the first generation of fermions are in the range of 1 MeV while the top quark has a mass of 172-173 GeV. Though this is not a flaw in the theory itself, it is frequently seen as a sign of undiscovered principles hidden behind a more comprehensive theory.
- Composite Higgs models:
- Majorana neutrinos: It is not clear yet if neutrinos are Majorana particles, i.e. they are their own antiparticles ($\nu = \bar{\nu} = \nu_M$). Current experiments trying to solve this question are focused on neutrino-less double- β decay, which can occur only if neutrinos are Majorana particles.

Most of theoretical concepts of the SM were in place by the end of the 1960s. With the discovery of the W [41] and Z [42] bosons at CERN in the mid 1980s and the Higgs boson in 2012, the SM has established itself as one of the major pillars of modern physics. The understanding of the universe at the most fundamental level is based in this theory, which has been tried to be summarised through the entire Section 1.1.

Despite its brilliance and success, the SM is not the ending of the story. As exposed above, there are far too many unanswered questions and loose ends. The HL-LHC [43] and the next generation of experiments will look for evidence of physics outside the SM in the next years.

Among the open questions, unresolved concerns and measurements to be completed, this research is focused on the top quark⁹. On one hand, contributions to the measurement of the polarisation of this quark are presented and, on the other hand, the study of the associated production of a single-top quark with a Higgs boson is present as well. Now that the basics of the SM have been settled, in the sections to come, the context of these two topics is being discussed.

⁹Here and in the following, the usage of the term top quark includes the top antiquark.

815 **Chapter 2**

816 **Top quark and Higgs boson
817 physics**

818 **2.1 Top quark**

819 The top quark (t) or, for simplicity, just top is the up-type quark of
820 the third generation of fermions. Its most distinctive feature is its huge
821 mass, which is the largest among all fundamental particle particles. The
822 left-handed top is the $Q = 2/3$ and $T_3 = +1/2$ member of the weak isospin
823 doublet that also contains the bottom quark. The right-handed top quark is
824 the $SU(2)_L$ weak isospin singlet ($Q = 2/3$ and $T_3 = 0$). Its phenomenology
825 is driven by its large mass. The top quark is often regarded as a
826 window for new physics since it provides a unique laboratory where to test
827 the understanding of the SM.

828 Due to being so massive, its life time is very short ($\tau_t = 5 \times 10^{-25}$ s [39]).
829 Actually, it is shorter than the hadronisation timescale ($1/\Lambda_{QCD} \sim 10^{-24}$ s),
830 this represents a unique opportunity to study quarks in free state, something
831 that is quite exceptional due to colour confinement, as explained in Section
832 1.1.4. In fact, the top quark is the only quark that can be investigated
833 unbonded. Its lifetime also is smaller than the spin decorrelation timescale
834 ($m_{top}/\Lambda_{QCD}^2 \sim 10^{-24}$ s), implying that the top-quark states conserve their
835 spin state from its production to its decay. Thanks to this, the top-quark
836 properties, such as the spin information, can be accessed through its decay
837 products and, consequently, be measured.

838 Another consequence of its large mass is that the top quark is the only
839 quark with a Yukawa coupling (y_t) to the Higgs boson of the order of one;
840 hence, a thorough understanding of its properties (mass, couplings, decay
841 branching ratios, production cross section, etc.) can reveal crucial informa-

tion on basic interactions at the electroweak symmetry-breaking scale and beyond. The main objective of this thesis is, precisely, the study of the top quark and Higgs boson interplay to, ultimately, help to determine if the y_t is that predicted by the SM or there is some \mathcal{CP} -violating phase that would affect the sign of the Higgs-top Yukawa coupling. The theoretical base for the understanding the associated production of a top quark and a Higgs boson given in Section 2.3 and the analysis investigating this matter is presented in Chapter 6.

2.1.1 Top-quark discovery

In 1973, Kobayashi and Maskawa postulated the possibility of a third generation of quarks to explain \mathcal{CP} violations in kaon decays [44]. To match the names of the up and down quarks, the new generation's quarks were given the names top and bottom. The GIM¹ mechanism[45], which predicted the existence of the yet-to-be-discovered charm quark, was used to make this prediction. When the charm was observed [46], the GIM was integrated into the SM and the postulation of the third family, and thus the top quark, gained acceptance. Shortly after the charm, the bottom quark was discovered in the E288 experiment at Fermilab [47], reinforcing the idea of the existence of the top quark. However, due to its large mass, it took 18 years to confirm the existence of the top.

The top quark was observed for the first time at Tevatron with the CDF [48] and D \emptyset [49] detectors via flavour-conservating strong interaction in 1995. Back then and until the start of LHC Run 1, Tevatron was the only accelerator powerful enough to produce top quarks.

Top quark mass

As discussed in Section 1.1.6.1, m_{top} is a free parameter of the SM. The theory does not predict its value, hence it must be determined experimentally. To derive the m_{top} from hadron collision data, two approaches are explored:

- Direct measurements (also known as template methods) [50]: The m_{top} is determined by reconstructing (fully or partially) the decay products of one or more top quarks in a $t\bar{t}$ or single-top event². A comparison

¹Standing for Glashow–Iliopoulos–Maiani, its the mechanism to describe the flavour-changing neutral currents.

²In particle physics, an event is the result of a collision.

875 of the detector-level distribution with templates created with a MC
 876 generator is used to determine the mass. Analysing $t\bar{t}$ events with
 877 lepton-plus-jets and dilepton topologies provides the most precise re-
 878 ults.

- 879 • Indirect measurements [50]: Performed from measurements of cross-
 880 section. These methods rely on the dependence on the value of the
 881 m_{top} for the total or differential production cross sections for processes
 882 involving top quarks.

883 Among the top quark's properties, its mass is the one that has received
 884 the most attention so far. The most recent studies for the top quark mass
 885 measurements result in $m_{top} = 172.76 \pm 0.30$ GeV [51]. This number is an
 886 average of the measurements at LHC with ATLAS (172.69 ± 66 GeV [52])
 887 and CMS (172.6 ± 3.5 GeV at CMS [53]) and at Tevatron with CDF and D \emptyset
 888 (combined result: 174.30 ± 0.89 GeV [54]). These values are measured from
 889 the kinematics of $t\bar{t}$ events³.

890 Figure 2.1 summarises the measurements of ATLAS and CMS for m_{top}
 891 from direct-top-quark decay.

892 2.1.2 Top quark production at LHC

893 The LHC is sometimes referred as a top quark factory due to its ability
 894 to produce such particles. In this collider, at pp collisions, the top quark
 895 is mainly produced via two mechanisms: through QCD in top and anti-top
 896 pairs ($t\bar{t}$), and by means of the Wtb vertex of EW in single-top quarks
 897 associated with other particles. Apart from the $t\bar{t}$ (Section 2.1.2.1) and
 898 single-top (Section 2.1.2.2) productions, the associated $t\bar{t} + X$ and four-top-
 899 quark productions (Sections 2.1.2.4 and 2.1.2.3 respectively) are presented
 900 as well.

901 Since the top quarks often constitute a main background in other physics
 902 analysis, a better understanding of this particle's properties will directly
 903 translate into improvements in those searches.

904 2.1.2.1 Top pairs

905 The production top and anti-top pair of quarks is the largest source of
 906 production of top quarks in hadron collisions. This process is one of the

³This m_{top} results are sensitive to the top quark mass used in the MC generator that is usually interpreted as the pole mass.

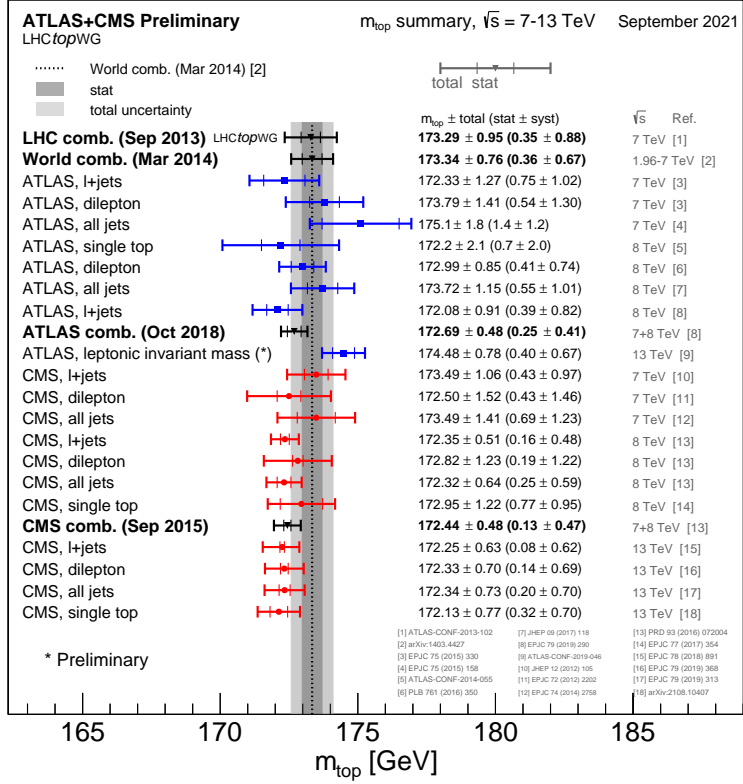


Figure 2.1: Summary of the ATLAS and CMS measurements from top-quark decay. Results compared to LHC m_{top} combination [55] **Can be updated with the June 2022 plot (+ Ref). Maybe there will be even a new one after TOP2022.**

most important at LHC because it allows to precisely study the properties of the top quark. Additionally, due to the dominance of this production mode, the top-quark-pair production is also a major background in many searches for rare processes. Including the one carried in this thesis, where $t\bar{t}$ is the main background in the both of the analysed decay channels (see Section 6.5).

For the $p\bar{p}$ collisions at Tevatron or pp at LHC, the $t\bar{t}$ production is described by perturbative QCD. In this approach, a hard scattering process between the two hadrons is the result of an interaction between the quarks and gluons that constitute these hadrons. This model is described with detail in Section 3.2.7.

At LHC, the gluon fusion (Figures 2.2 (a)-(c)) dominates with a 90% of the $t\bar{t}$ production. It is followed by the quark and antiquark annihilation (Figure 2.2d), which accounts for a 10% of the the total top-quark-pair production. The theoretical calculations for the $t\bar{t}$ production are done to an accuracy of next-to-next-to-leading order (NNLO) in QCD [56] and measured by ATLAS and CMS. Figure 2.3 shows the measurements for the

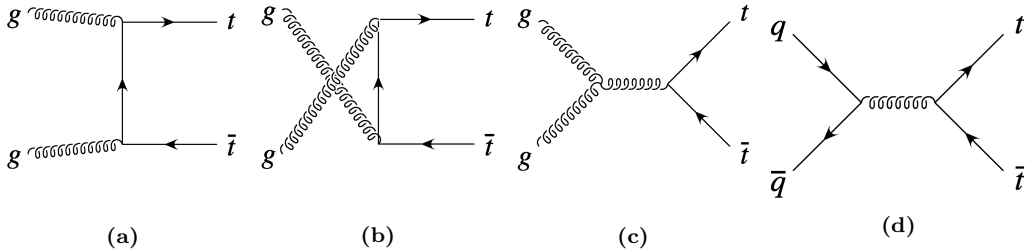


Figure 2.2: Representative Feynman diagrams of the LO processes contributing to the $t\bar{t}$ production. Subfigures (a), (b) and (c) correspond to the production through gluon fusion and Subfigure (d) to the production via quark and antiquark annihilation.

924 $t\bar{t}$ production cross section ($\sigma_{t\bar{t}}$) at $\sqrt{s} = 13$ TeV. The measurements and
 925 the theory calculations are quoted at $m_{top} = 172.5$ GeV.

926 2.1.2.2 Single top

927 In addition to the top-quark-antiquark-pair production, the single-top-
 928 quark processes are of great importance to the study of the top quark prop-
 929 erties at the LHC. This mechanism has a cross section three times smaller
 930 than that of $t\bar{t}$ and it's almost exclusively produced through the EW Wtb
 931 vertex. This is precisely the reason why single-top-quark production is es-
 932 sential to gather information the Wtb interaction and to directly measure
 933 $|V_{tb}|$ at hadron colliders. The reason why the single-top quark is produced
 934 and decays via a b -quark and not from strange or down quarks is because
 935 the CKM elements V_{ts} and V_{td} are smaller than V_{tb} by several orders of
 936 magnitude as Table 1.3 shows.

937 At LO, there are three production modes for single top, being the t -
 938 channel the dominant mechanism at the LHC with, approximately 70% of
 939 the single top quark cross section at a $\sqrt{s} = 13$ TeV. The other processes
 940 are the s -channel and the associated production tW production. Only t -
 941 channel and tW productions are relevant to the EW single-top production
 942 at LHC.

943 **t -channel**

944 This production mode involves the scattering of a light quark and a gluon
 945 from the proton sea as shown in Figure 2.4. Note that additional diagrams
 946 to those in Figure 2.4 are obtained by either replacing the u and d by a c and
 947 s quarks or by switching the light quarks in the fermion line. The diagrams
 948 for antitop production are the charge conjugate of the ones presented.

The measurements cross sections at 13 TeV for single-top ($\sigma_{t-channel,t}$) and single-anti-top ($\sigma_{t-channel,\bar{t}}$) quarks in the t -channel production are

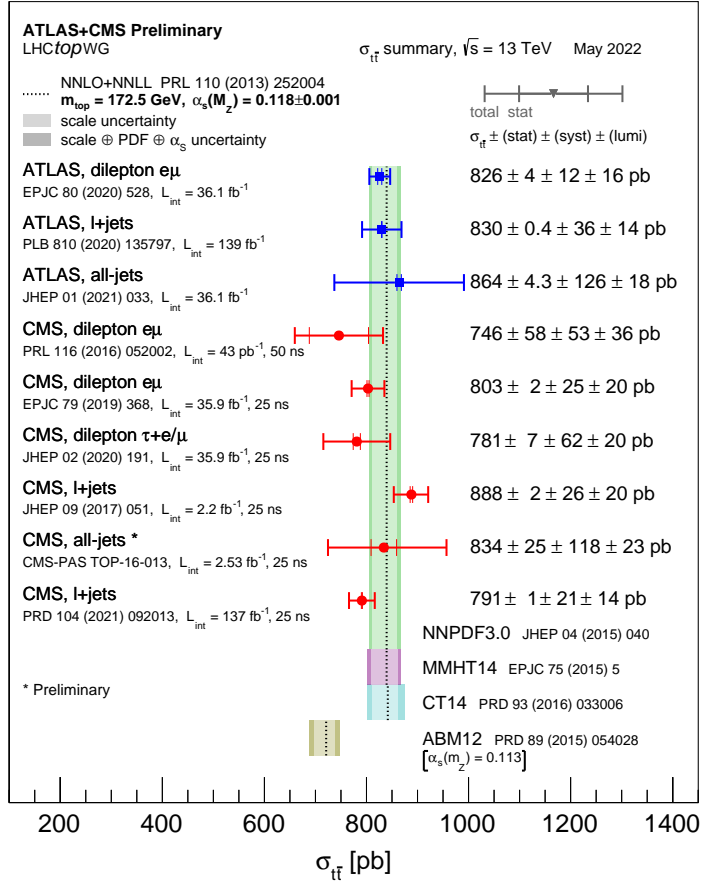


Figure 2.3: Summary of measurements $\sigma_{t\bar{t}}$ at 13 TeV compared to the exact NNLO QCD calculation complemented with NNLL resummation.

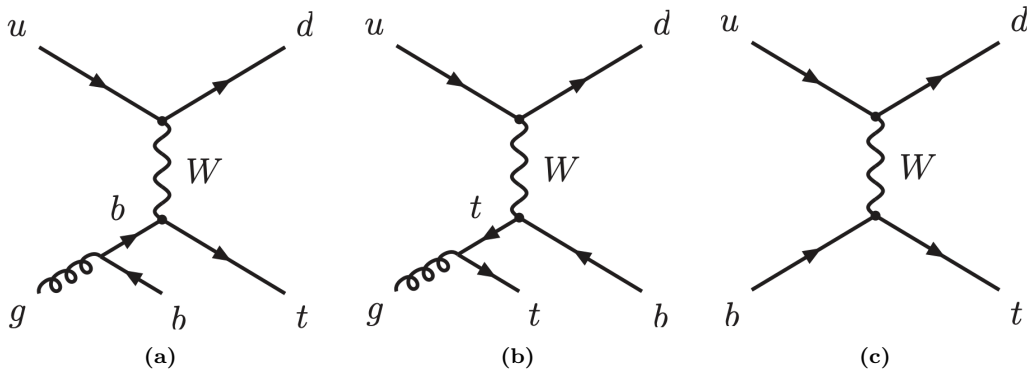


Figure 2.4: Representative Feynman diagrams for the single-top-quark production in the t -channel process. Observe that the u and d quarks could be substituted by c and s quarks.

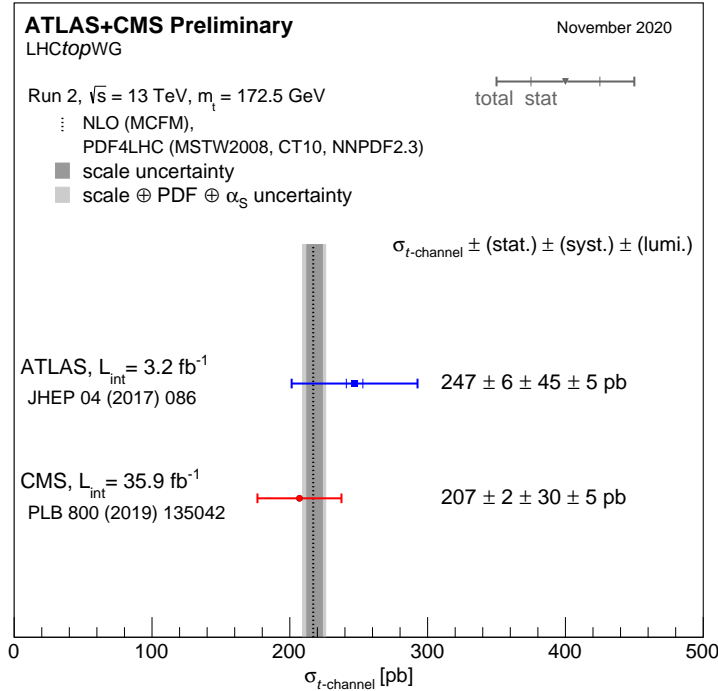


Figure 2.5: Summary of the ATLAS and CMS measurements of the single top production cross-sections in the t -channel at 13 TeV.

shown in Figure 2.5. The theoretical calculations at NLO for $\sigma_{t\text{-channel}, t+t\bar{t}}$ at 13 TeV are:

$$\begin{aligned}\sigma_{t\text{-channel}, t} &= 136^{+4.1}_{-2.9}(\text{scale}) \pm 3.5(\text{PDF} + \alpha_s) \text{ pb}, \\ \sigma_{t\text{-channel}, t\bar{t}} &= 81.0^{+2.5}_{-1.7}(\text{scale}) \pm 3.2(\text{PDF} + \alpha_s) \text{ pb}, \\ \sigma_{t\text{-channel}, t+t\bar{t}} &= 217^{+6.6}_{-4.6}(\text{scale}) \pm 6.5(\text{PDF} + \alpha_s) \text{ pb}.\end{aligned}$$

949 These numbers have been obtained using HATHOR 2.1 [57][58].

950 The dominant process in the SM is the one in diagram 2.4a, while the one
 951 in 2.4b is included in order to form a gauge invariant set but its contribution
 952 is not very significative since for the gluon is easier to decay to $b\bar{b}$ pair than
 953 to a $t\bar{t}$ pair. These two $3 \rightarrow 2$ production modes are known as 4 Flavour
 954 Scheme (FS) because the proton is considered to be composed by five quark
 955 flavours (u, d, c and s) and is characterised by having a b quark in the final
 956 state. This final state b quark is sometimes referred as second b and it has a
 957 transverse momentum (p_T) distribution peaking around 2 or 3 GeV as can
 958 be seen in Figure 2.6. This is the reason why the final b quark from the
 959 gluon splitting frequently goes undetected, because it does not pass the p_T
 960 threshold of the detector. This is why, at detector level, whenever only jet
 961 is identified as originated from a b quark, it is assumed to be the b from the

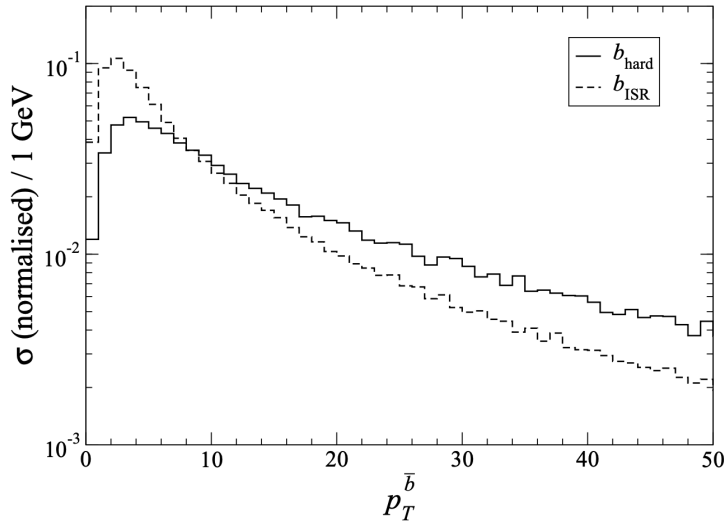


Figure 2.6: Normalised p_T distribution of the second b quark in the t -channel process, generated by Monte Carlo (MC) simulation [59].

the top-quark decay. This particularity becomes more important in Chapter 6.

The $2 \rightarrow 2$ process in 2.4c is known as 5FS because the proton is considered to be composed by five flavours of quarks (u, d, c and s) and it is characterised by having a b quark in the initial state. The simulations for the 4FS and 5FS diagrams are produced separately and merged afterwards. When adding the two contributions, some double-counting may appear due to the overlap in the phase space so one has to be careful. The naming 4FS and 5FS is later used again for the associated tHq production.

971 s-channel

972 The s -channel process for single-top is the one with less impact among
 973 single-top production channels. It is depicted in Figure 2.7a. This produc-
 974 tion mode is also referred as the quark-antiquark annihilation or W^* process
 975 and it is very similar to the Drell-Yann.

According to the LHC cross section group, at 13 TeV of center-of-mass energy, the cross sections for the single top and single anti-top production in the s -channel ($\sigma_{s\text{-channel}}$) are:

$$\begin{aligned}\sigma_{s\text{-channel},t} &= 6.35^{+0.18}_{-0.15}(\text{scale}) \pm 0.9(\text{PDF} + \alpha_s) \text{ pb}, \\ \sigma_{s\text{-channel},\bar{t}} &= 3.97^{+0.11}_{-0.09}(\text{scale}) \pm 0.15(\text{PDF} + \alpha_s) \text{ pb}, \\ \sigma_{s\text{-channel},t+\bar{t}} &= 10.32^{+0.29}_{-0.34}(\text{scale}) \pm 0.27(\text{PDF} + \alpha_s) \text{ pb}.\end{aligned}$$

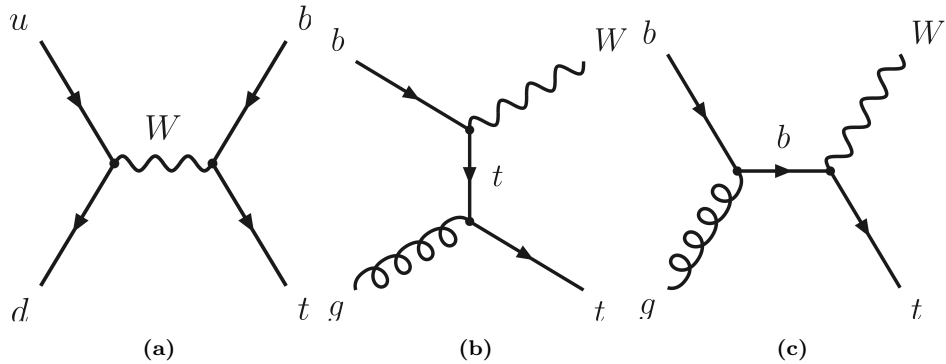


Figure 2.7: Representative Feynman diagrams for the single-top-quark production in (a) the s -channel and with (b) and associated W boson. While the first one is not observed, the tW is one the backgrounds in the tHq analysis.

976 Note that while at LHC the s -channel production has not been observed
977 at LHC, for Tevatron it was a significant part of the total single-top cross-
978 section.

Associated tW

Finally, the associated production of a single top quark with a W boson (sometimes referred as tW -channel) is represented by two the Feynman diagrams in Figures 2.7b and 2.7c. To these two diagrams, the charge conjugate processes could be added to complete the tW mechanisms. The predicted cross section for the associated tW is:

$$\sigma_{tW,t+\bar{t}} = 71.7 \pm 1.80(\text{scale}) \pm 3.40(\text{PDF} + \alpha_s) \text{ pb.}$$

979 This and all σ in the section are calculated for a top mass of $m_{top} =$
980 172.5 GeV and NLO in QCD with HATHOR v.2.1. The PDF and α_s un-
981 certainties are calculated using the PDF4LHC prescription [60] with the
982 MSTW2008 68% CL NLO [61][62], CT10 NLO [63] and NNPDF2.3 [64]
983 PDF sets, added in quadrature to the scale uncertainty.

984 2.1.2.3 Four tops

985 Figure 2.10

986 2.1.2.4 Associated $t\bar{t} + X$ production

987 The associated top productions are important processes to measure the
988 coupling of the top to the other particles of the SM. When a pair of tops
989 is produced along other particle it is referred as $t\bar{t}X$. The most relevant

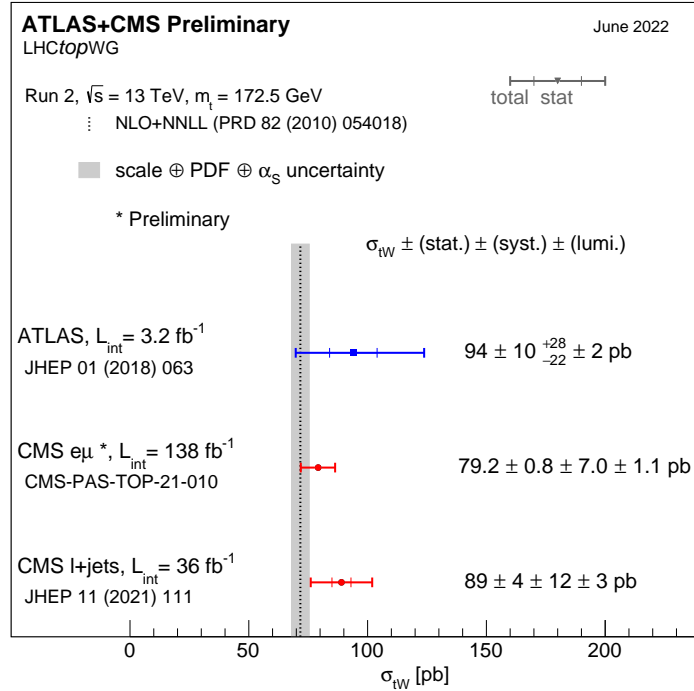


Figure 2.8: Cross-section measurements for the associated tW production boson performed by ATLAS and CMS at 13 TeV, and combined result compared with the NLO+NNLL prediction.

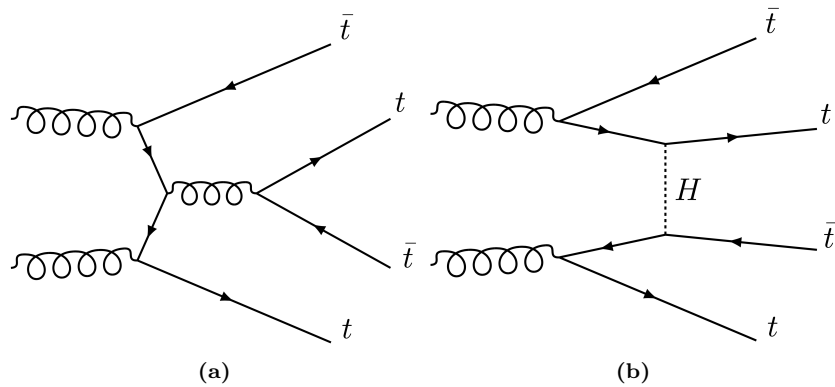


Figure 2.9: Representative Feynman diagrams for the $gg \rightarrow t\bar{t}t\bar{t}$ production.

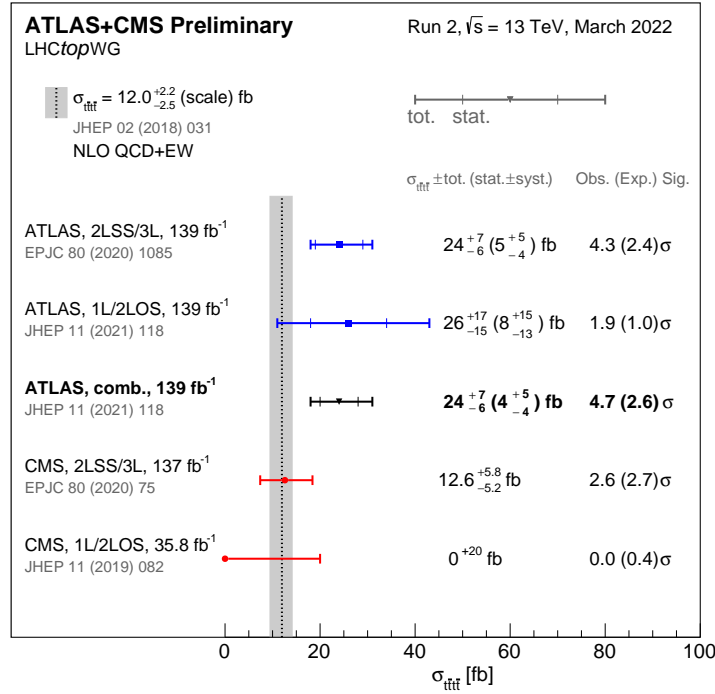


Figure 2.10: Summary of the ATLAS and CMS measurements of the $t\bar{t}t\bar{t}$ production cross-sections at 13 TeV in various channels

990 $t\bar{t}X$ productions are those in which the pair is created with W , Z or γ
991 boson. From these, $t\bar{t}W$ and $t\bar{t}Z$ play an important role as backgrounds
992 in the 2ℓ OS + $1\tau_{\text{had}}$ channel of the tHq production, being the second and
993 third most important after $t\bar{t}$. The different production diagrams for $t\bar{t}W$
994 are shown in Figure 2.11. **igual tampoco hace falta enseñar estos**
995 **diagramas**

996 The cross sections for the $t\bar{t}W$, $t\bar{t}\gamma$ and $t\bar{t}Z$ productions are presented
997 in Figure 2.12. The associated production of a $t\bar{t}$ pair with a Higgs boson
998 is described in Section 2.3.2.

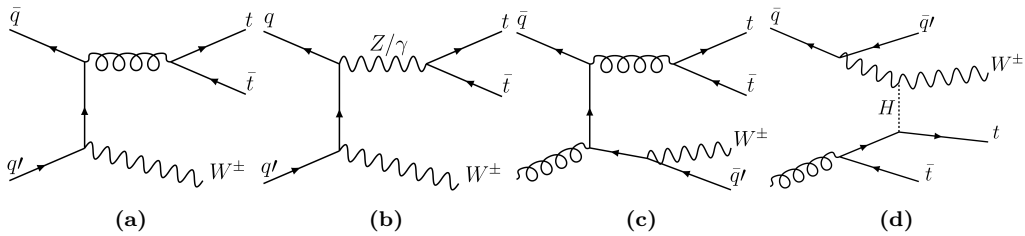


Figure 2.11: Representative Feynman diagrams for $t\bar{t}W$ production. Left diagrams show the $\bar{q}q' \rightarrow t\bar{t}W$ processes and right ones the $\bar{q}g \rightarrow t\bar{t}Wq'$ production.

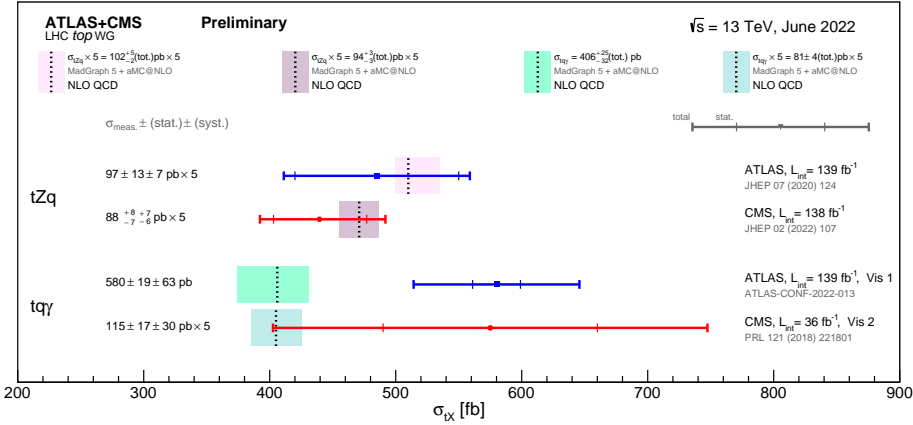


Figure 2.12: Summary of the ATLAS and CMS measurements of the $t\bar{t}X$ production cross-sections at 13 TeV. Here $X = W, Z$ and γ .

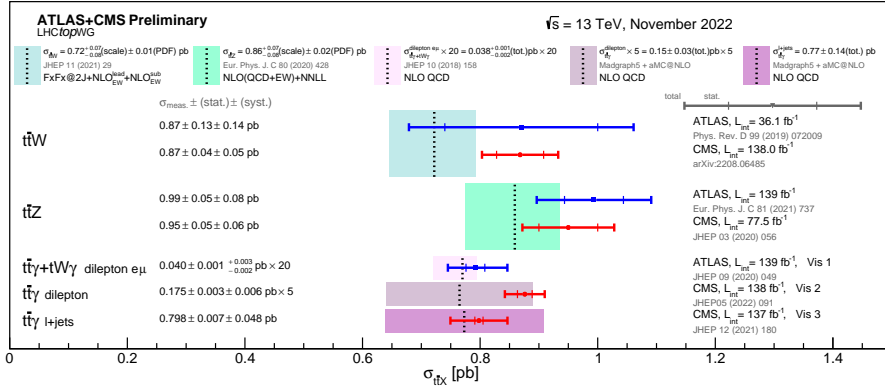


Figure 2.13: Summary of the ATLAS and CMS measurements of the tX production cross-sections at 13 TeV. Here $X = Z$ and γ .

2.1.2.5 Associated $t + X$ production

Not only the top pairs but also the single-top quark can be produced in association with other particles (tX). This type of production play an important role in the tHq searches since the tZq process is one of the backgrounds in the more difficult to separate in the 2ℓ OS + $1\tau_{\text{had}}$ channel. The

Section 2.3.3

2.1.3 Top-quark decay

As advanced in the Section 2.1.2.2, due to the large V_{tb} element of the CKM matrix, the top quark decays almost entirely ($\sim 99.8\%$) through the

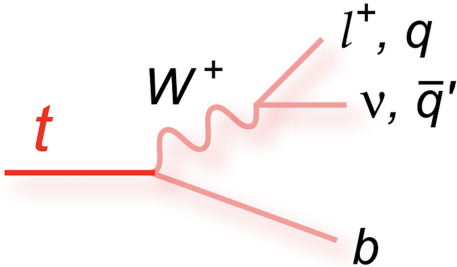


Figure 2.14: Decay of a top quark to a b quark and a W boson. The W boson can decay either leptוניתly to a neutrino and a lepton or hadronically to a pair of light-flavour quarks. In the hadronic W decay, a jet triplet is formed along with the b quark.

medium of the Wtb vertex to a b quark and a W boson. The final state decay is classified according to the subsequent decay of the W boson. As W are massive vector bosons, its lifetime is very short ($\tau_W \approx 3 \times 10^{-25}$ s). For the W^+ , the decay modes are:

$W^+ \rightarrow e^+ \nu_e$	$(10.71 \pm 0.16)\%$
$W^+ \rightarrow \mu^+ \nu_\mu$	$(10.63 \pm 0.15)\%$
$W^+ \rightarrow \tau^+ \nu_\tau$	$(11.38 \pm 0.21)\%$
$W^+ \rightarrow q\bar{q}$ (hadrons)	$(67.41 \pm 0.27)\%$
$W^+ \rightarrow$ invisible	$(1.4 \pm 2.9)\%$

1007 For the conjugate processes involving the W^- , the branching ratios (BR)
 1008 are the same. Therefore, the W decay and consequently the t decay can be
 1009 classified either as leptonic or hadronic. The decay chain of the top quark is
 1010 represented in Figure 2.14. Due to its large mass, the W can decay to any
 1011 quark except the top quark. For a certain decay mode, the BR is defined
 1012 as the fraction times that the particle decays in that particular mode with
 1013 respect to total possible decays.

1014 2.1.4 Top quark polarisation

1015 As mentioned previously, the lifetime of the top quark is shorter than
 1016 the depolarisation scale and, hence, the top-quark spin information can be
 1017 transferred into its decay products. This allows to measure the top-quark
 1018 polarisation from its child particles. The polarisation refers to the alignment
 1019 between the momentum and the spin of the top quark and antiquarks. The
 1020 polarisation of t and \bar{t} are important quantities because they are sensitive to
 1021 many BSM effects and can also provide useful input for the MC generators
 1022 which are described in Section 4.2.

At LHC, the single-top-quark production is the only source of highly polarised top quarks. Specifically, in the t -channel (see Section 2.1.2.2) the top quark is created with a high degree of polarisation in the direction of the spectator quark momentum [65]. As a consequence of the vector and axial-vector form of the coupling of the top quark to the W boson and bottom quark in the t -channel ($t \rightarrow Wb$ vertex), specific values of the polarisation vectors $\{P_x', P_y', P_z'\}$ of top quarks/antiquarks are expected in the SM.

Even though it is not described with detail in this manuscript, during the development of my thesis I have also been involved in the first measurement of the top-(anti)quark-polarisation vectors. My contribution is an extension of the work done in reference [66] and the results of these measurements are published in reference [67]. In this work, the three components of the polarisation vector for the top quark and antiquark have been measured in the single-top t -channel production. Using the entire Run 2 dataset recorded by ATLAS and demanding events with exactly one light lepton, I defined a set of stringent selection requirements to discriminate the t -channel signal from the background contributions. This signal-region⁴ definition used specific cuts in several variables such as the lepton p_T or the invariant masses of several particles. I have also developed the so called trapezoidal cut, which is described in the published paper.

The polarisation vectors are later obtained from the distributions of the direction cosines of the charged-lepton momentum in the top-quark rest frame: $\cos(\theta_{lx'})$, $\cos(\theta_{ly'})$ and $\cos(\theta_{lz'})$. Figure 2.15 shows the distributions for these angular variables.

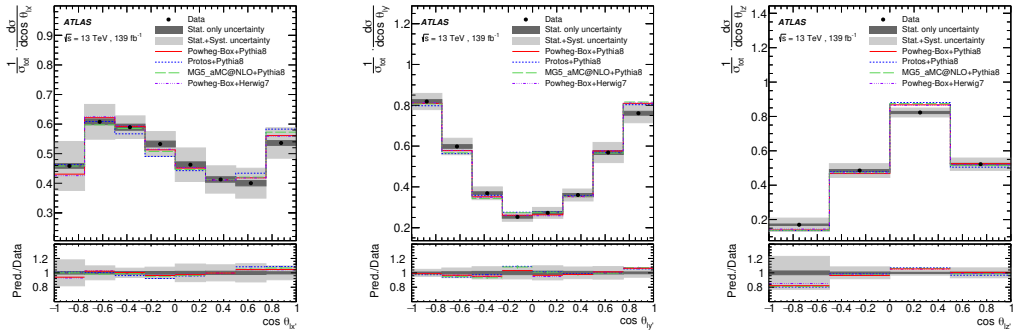


Figure 2.15: Normalised differential cross-sections as a function of $\cos(\theta_{lx'})$, $\cos(\theta_{ly'})$ and $\cos(\theta_{lz'})$. The data is shown as black points with statistical uncertainties compared to the predictions of the MC generators, which are shown as lines. The ratio between the predictions and data is shown on the lower panel. These plots are inclusive for top quark and top antiquark.

⁴The signal region is a region of the phase space enriched with events of the signal process.

1047 Limits on the two of the components of the polarisation vector of the top
 1048 quark and antiquark have been set and Figure 2.16 presents the observed
 1049 best-fit polarisation measurements for $P_{x'}$ and $P_{z'}$ in the two dimensional
 1050 parameter space. The components of polarisation are measured to be:

1051 For top quarks

- $P_{x'}^t = 0.01 \pm 0.18$
- $P_{y'}^t = -0.029 \pm 0.027$
- $P_{z'}^t = 0.91 \pm 0.10$

For top antiquarks

- $P_{x'}^{\bar{t}} = -0.02 \pm 0.20$
- $P_{y'}^{\bar{t}} = -0.007 \pm 0.051$
- $P_{z'}^{\bar{t}} = -0.79 \pm 0.16$

1052 Data measurements of the polarisation-vector components and differ-
 1053 ential cross sections show good agreement with SM predictions. The
 1054 results are consistent with NNLO QCD predictions and expectation of
 1055 $P_{y'}^t = P_{y'}^{\bar{t}} = 0$ from the hypothesis of \mathcal{CP} symmetry in the top-quark and
 1056 top-antiquark decay.

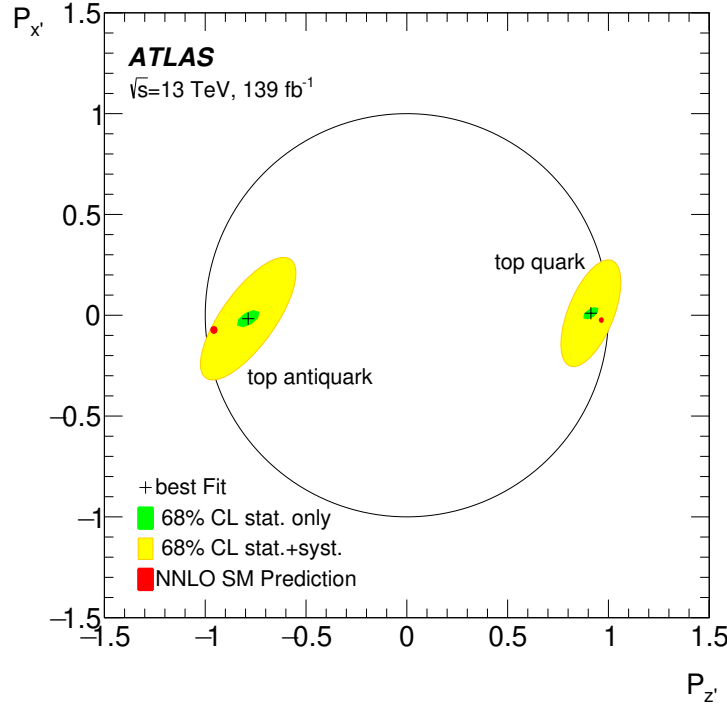


Figure 2.16: Observed best-fit limit on two-dimensional top quark polarisation parameter space $\{P_{z'}, P_{x'}\}$. The statistical-only (green) and the statistical+systematic uncertainty contours have a 68% CL. The physically allowed values for $P_{x'}$ and $P_{z'}$ are lay inside the black circle. The red point indicates the parton-level prediction at NNLO.

1057 2.2 Higgs boson

1058 Following the top quark, the Englert-Brout-Higgs-Guralnik-Hagen-
 1059 Kibble-Higgs boson or, for simplicity, Higgs boson (H) or just Higgs is
 1060 the most massive particle in the SM with a mass of $m_H = 125.25 \pm 0.17$
 1061 GeV [68]. The value provided by [68] is an average of the ATLAS com-
 1062 bined measurement ($m_H = 124.86 \pm 0.27$ GeV [69]) and the CMS results
 1063 ($m_H = 125.46 \pm 0.16$ [70]).

1064 The Higgs boson existence was theorised in 1964 by three independent
 1065 groups: Englert-Brout [71], Higgs [72] and Guralnik-Hagen-Kibble [73], and
 1066 its discovery meant one of the greatest successes of the SM. This theory was
 1067 not only able to calculate with great precision the physics but also predicted
 1068 the existence of a particle that was found later (see 2.2.1).

1069 2.2.1 Higgs-boson discovery

1070 Any particle physicist enthusiast remembers July 4th of 2012 pretty
 1071 well, it was LHC experiments ATLAS [1] and CMS [2] who announced the
 1072 discovery of a massive state H with the properties expected for the Higgs
 1073 boson.

1074 Both the ATLAS and CMS Collaborations reported excesses of events
 1075 for 2011 ($\sqrt{s} = 7$ TeV and $\mathcal{L} = 4.8 \text{ fb}^{-1}$) and 2012 ($\sqrt{s} = 8$ TeV and $\mathcal{L} = 458$
 1076 fb^{-1}) datasets of proton-proton (pp) collisions. This surplus of events was
 1077 compatible in its production and decay with the SM Higgs boson in the mass
 1078 region $m_H \in [124, 135]$ GeV with significances of 2.9σ for ATLAS and 3.1
 1079 σ for CMS. At Tevatron (circular proton-antiproton collider at Fermilab),
 1080 the experiments CDF [74] and D \emptyset [75] also reported an excess in the mass
 1081 region $m_H \in [120, 135]$ GeV.

1082 2.2.2 Higgs boson production at LHC

1083 One of the reasons why the Higgs boson was found the latest among
 1084 SM fundamental particles is because it is a fairly heavy particle and, hence,
 1085 it was necessary a lot of energy to produce it. Even though that colliders
 1086 such as SLAC or LEP had enough energy, they were colliding electrons and
 1087 positrons and, since the coupling of the Higgs to fermions is proportional to
 1088 the fermions mass, the process $e^- e^+ \rightarrow H$ processes is highly suppressed⁵

⁵The dominant Higgs production in $e^- e^+$ annihilation is the so called Higgsstrahlung, an s -channel process in which the H is produced in association to a Z boson similarly to Figure 2.17c.

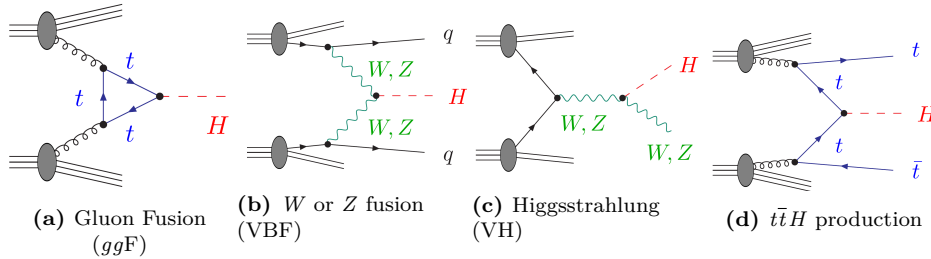


Figure 2.17: Lowest-order Feynman diagrams for the dominant production mechanisms of a Higgs boson at hadron colliders.

and, for this reason, there were not enough statistics of events with a Higgs boson. The most favoured way of producing a Higgs boson is through the mediation of the heaviest fundamental particles in the SM because these have the strongest couplings with the Higgs and, consequently, the greater cross section.

The four most dominant processes for Higgs boson production at LHC are summarised in Figure 2.17:

- **Gluon-gluon Fusion (ggF):** This channel is depicted in Figure 2.17a and, as the diagram shows, the process $gg \rightarrow H$ has to be mediated by a massive fermion loop. This due to the fact that there is no direct gluon-Higgs coupling within the SM. Although in principle all quarks should be included in the loop, in practise it is the top quark the one doing so because its coupling to the Higgs boson is 35 times stronger than the next-heaviest fermion, the bottom quark.

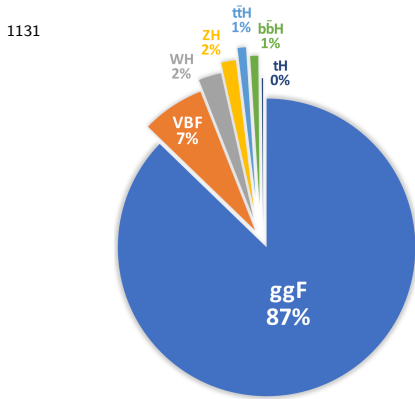
Due to the abundance of gluons in pp collisions, the ggF is very favoured at LHC.

- **Vector Boson Fusion (VBF):** The second most important is the radiation by the incoming quarks of a W or Z vector bosons that fuse to form a Higgs as Figure 2.17b illustrates. The vector bosons of the process $V\bar{V} \rightarrow H$ are originated from initial state quarks which scatter thorough the final state (changing its flavours in the case of W fusion) producing two forward jets.
- **Higgsstrahlung (VH):** There is another significant contribution involving the W or Z bosons, the Higgsstrahlung or associated WH or ZH production. Here, a, off-shell W or Z (formed from the annihilation of two quarks) radiate a Higgs boson via $V^* \rightarrow VH$. Figure 2.17c depicts the VH associated production.
- **Quark-pair associated production ($q\bar{q}H$):** In this mode, the Higgs is produced from a $q\bar{q}$ pair via $q\bar{q} \rightarrow H$ with a $q\bar{q}H$ final state. Typ-

1118 ically, the involved quark pair is either a $b\bar{b}$ or $t\bar{t}$. In the case of $t\bar{t}$
 1119 (Figure 2.17d), the top quarks decay before hadronising, leading to
 1120 final states with a high number of physics objects.

- 1121 • **Associated Higgs boson and single-top quark (tHX):** This sub-
 1122 dominant contribution can be either a tHq or a tWH . The former
 1123 constitutes the central topic developed in this thesis, where this pro-
 1124 cess is searched. Details about this production modes are further
 1125 discussed in Section 2.3.3 .

1126 The cross section of the different procedures for Higgs boson produc-
 1127 tion at $\sqrt{s} = 13$ TeV are shown in Figure 2.18 as a function of m_H . For
 1128 Figure 2.18a, the σ_{tH} accounts for the t -channel and s -channel but not the
 1129 tW -channel. Assuming a $m_H = 125.2$ GeV, the cross-sections for Higgs
 1130 production are [4]:



$$\begin{aligned}\sigma_{ggF} &= 48.5^{+2.2}_{-3.3} \text{ pb} \\ \sigma_{VBF} &= 3.78 \pm 0.05 \text{ pb} \\ \sigma_{WH} &= 1.37 \pm 0.03 \text{ pb} \\ \sigma_{ZH} &= 0.89^{+0.04}_{-0.03} \text{ pb} \\ \sigma_{t\bar{t}H} &= 0.5^{+0.03}_{-0.05} \text{ pb} \\ \sigma_{b\bar{b}H} &= 0.49^{+0.10}_{-0.11} \text{ pb} \\ \sigma_{tHX} &= 0.09 \pm 0.01 \text{ pb}\end{aligned}$$

1132 2.2.3 Higgs-boson decay

1133 The Higgs boson has a very short lifetime ($\tau_H = 1.6 \times 10^{-22}$ s [4]) and,
 1134 hence, is always detected through its decay products. Figure 2.19 shows the
 1135 branching ratio⁶ (BR) for the Higgs boson.

1136 Despite the expected large Yukawa coupling between the Higgs boson
 1137 and the top quark, the $H \rightarrow t\bar{t}$ is forbidden because the $m_H < 2m_{top}$.
 1138 Consequently, the most prominent decay mode is the $H \rightarrow b\bar{b}$ followed by
 1139 the $H \rightarrow W^+ W^-$. For the rest fermionic decays, the decay rates are ordered
 1140 by the fermion masses. Regardless of the expected large coupling between

⁶The fraction of particles which decay by an individual decay mode with respect to the total number of particles which decay.

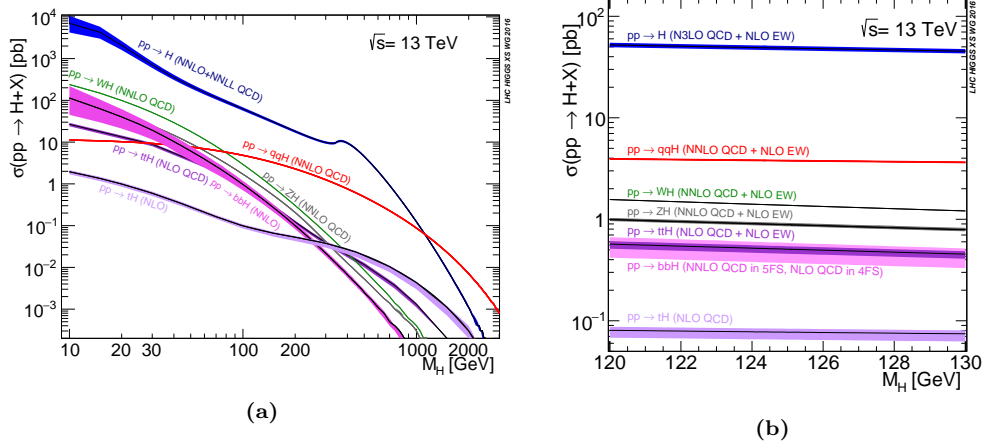


Figure 2.18: Higgs boson production cross sections as function of m_H at $\sqrt{s} = 13$ TeV [4]. A wide range of m_H values is showed in (a). In (b) is shown the result zooming around the measured Higgs mass value. Looking at (a) it can be seen that if the Higgs weighted just about 60 GeV more there would have been only two relevant decay modes, $H \rightarrow WW$ and $H \rightarrow ZZ$. On the other hand, if had Higgs been just 30 GeV lighter, these two channels would have been very difficult to observe.

the weak force bosons and the Higgs, the $H \rightarrow VV^*$ is suppressed due to the requirement that one vector boson has to be produced off-shell⁷.

Higgs to tau tau is the most relevant Higgs to fermions decay that can be observed Add some diagrams of the Higgs decay modes

For the analysis carried in this thesis, are of particular the decays $H \rightarrow W^+W^-$, $H \rightarrow ZZ$ and $H \rightarrow \tau^-\tau^+$. Sorted by its importance and assuming a $m_H = 125.2$ GeV, the BR for the Higgs are [76]:

⁷Off-shell means that the particle is produced virtually and it does not satisfy the energy-momentum relation.

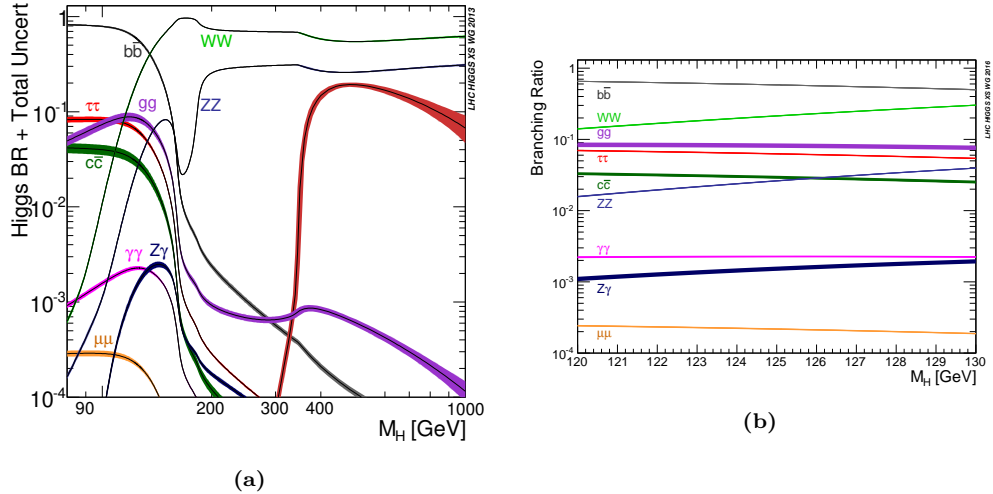
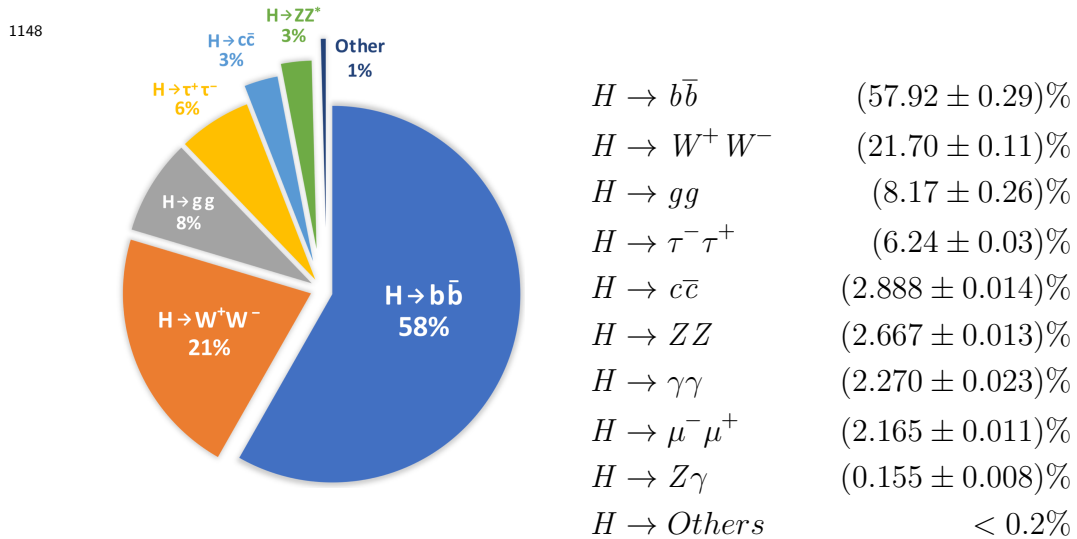


Figure 2.19: Standard Model Higgs-boson-decay branching ratios as function of m_H at $\sqrt{s} = 13$ TeV [4]. In (a) the BR are shown in a Higgs mass range $m_H \in (90, 10^3)$ GeV. In (b) only values of m_H around the measured one are shown. Looking at (a) it can be seen that if the Higgs weighed just about 50 GeV more there would have been only two relevant decay modes, $H \rightarrow WW$ and $H \rightarrow ZZ$. On the other hand, if had Higgs been just 10 GeV lighter, these two channels would have been very difficult to observe.



1152 2.3 Top quark and Higgs boson interplay

So far, the couplings of the Higgs boson to the SM particles have been found to be proportional to the masses of these particles. Since the top quark is the most massive particle and the coupling of Higgs to SM particles is uniquely determined by the mass of these particles, the Yukawa coupling between the top quark and the Higgs boson (y_t) is expected to be the strongest among all fermions and, hence, its study is of crucial importance, as it is discussed in references [77][78] and developed in the succeeding sections. The Yukawa coupling is expected to be of the order of the unity:

$$y_t = \frac{\sqrt{2}m_{top}}{v} = 2^{3/4}G_F^{1/2}m_{top} = 0.995 \simeq 1.$$

1153 This value is quite larger than the couplings of the other quarks. For com-
1154 parison $y_b \simeq 0.025$ and $y_c \simeq 0.007 \gg y_{s,d,u}$.

1155 The production of a pair of top quarks along with a Higgs boson ($t\bar{t}H$)
1156 allows possible to measure the absolute value of y_t . This process has the
1157 advantage of being the leading mechanism to produce the Higgs together
1158 with the quark top. At $\sqrt{s} = 13$ TeV it has a cross section of **poner cálculos**
1159 **del SM para $\sigma_{t\bar{t}H}$** (the definition of cross section can be found in Section
1160 3.2.5).

1161 Having a very much lower cross section than $t\bar{t}H$ (**poner $\sigma_{t\bar{t}H}$**), the
1162 Higgs boson production alongside a single top quark (tH) brings valuable
1163 information, specially regarding the sign of the Yukawa coupling. Note that
1164 the sign of y_t is not a well-defined physical property by itself but the relative
1165 sign compared to the coupling of the Higgs to weak⁸ boson is indeed physical
1166 [77]. This is explored with more detail in 2.3.3.

1167 A change in the Yukawa sign and/or absolute value with respect to its
1168 SM value would signal an origin of the fermion masses different from the
1169 described by the EWSB because the relative sign of the Higgs coupling to
1170 fermions and gauge vector bosons is crucial for recovering the unitarity and
1171 renormalisability of the theory [79].

1172 2.3.1 \mathcal{CP} properties in top-Higgs interactions

1173 The \mathcal{CP} properties of the Yukawa coupling of the Higgs boson to the
1174 top quark can be probed through the associated production of these two
1175 particles. While SM predicts the Higgs to be a scalar boson ($J^{\mathcal{CP}} = 0^{++}$),
1176 the presence of a $J^{\mathcal{CP}} = 0^{+-}$ pseudoscalar admixture has not been excluded

⁸The coupling of the Higgs to the gauge bosons is taken as positive.

yet. This pseudoscalar would introduce a second coupling to the top quark. Finding a \mathcal{CP} -odd contribution would be a sign of physics beyond the SM and could account for the imbalance between matter antimatter in the universe.

The production rates of $t\bar{t}H$ and tH depend on the y_t coupling. The former is specially sensible to y_t deviations from the SM as it is described in Section 2.3.3. The presence of a \mathcal{CP} -mixing in y_t would also affect the ggF production and $H \rightarrow \gamma\gamma$ decay rates.

Higgs characterisation

The Higgs characterisation model used in the thesis is the one described in reference [3]. Let's consider a spin-0 particle with a \mathcal{CP} -violating Yukawa interaction with the top quark, X_0 . This X_0 particle couples to both scalar and pseudoscalar fermionic densities, and its interaction with the W boson is the one described by the SM. The reason to call this particle X_0 instead of H is because its description does not correspond to the typical realisation of the Higgs but, in practise, we are referring to the Higgs. Within this model, the term in the effective Lagrangian that describes the Higgs-top Yukawa coupling below the EWSB scale is:

$$\mathcal{L} = -\bar{\psi}_t [\cos(\alpha)\kappa_{Htt}g_{Htt} + i\text{sen}(\alpha)\kappa_{Att}g_{Att}\gamma^5]\psi_t X_0, \quad (2.1)$$

where ψ_t and X_0 represent the top quark and the Higgs boson respectively and α is the \mathcal{CP} mixing phase. The κ_{Htt} and κ_{Att} are real-dimensionless rescaling parameters. Finally, $g_{Htt} = g_{Att} = \frac{m_{top}}{v} = \frac{y_t}{\sqrt{2}}$. The Lagrangian 2.1 can be rewritten as:

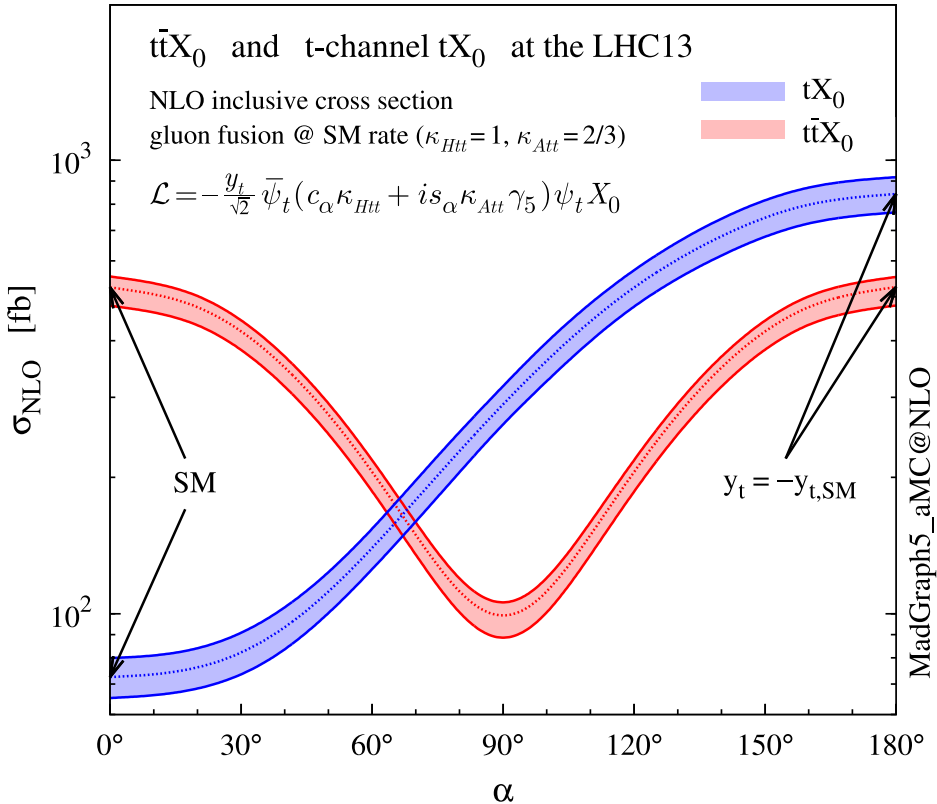
$$\mathcal{L} = -\frac{y_t}{\sqrt{2}}\bar{\psi}_t [\cos(\alpha)\kappa_{Htt} + i\text{sen}(\alpha)\kappa_{Att}\gamma^5]\psi_t X_0. \quad (2.2)$$

The advantage of this top-Higgs parametrisation is that is simple to interpolate between the \mathcal{CP} -even ($\cos(\alpha) = 1$ and $\text{sen}(\alpha) = 0$) and the \mathcal{CP} -odd ($\cos(\alpha) = 0$ and $\text{sen}(\alpha) = 1$) scenarios. The SM coupling corresponds to the \mathcal{CP} -even: $\mathcal{L} = -\frac{y_t}{\sqrt{2}}\bar{\psi}_t\psi_t X_0$.

Figure 2.20 shows the buena movida clave para la tesis [<- continuar por aquí](#)

2.3.2 $t\bar{t}H$

The first associated production of a Higgs boson with a pair of top quarks was observed in 2008 by ATLAS [80] and CMS [81]. This process marked a significant milestone for the field of high-energy physics because

**Figure 2.20:** blablabla

it helped establishing the first direct measurement of the tree-level coupling of the Higgs boson to the top quark, which was in agreement with the SM expectation.

The associated production of H with top quark pair has been studied by ATLAS and CMS previously during Run 1 at $\sqrt{s} = 7$ TeV and 8 TeV [82] [83] and Run-2 [[buscar \$t\bar{t}H\$ en Run-2](#)]

2.3.2.1 $t\bar{t}H$ Standard Model

2.3.2.2 $t\bar{t}H$ Charge-Parity

2.3.3 tHq

The associated tH production takes place either via the t -channel, where the Higgs boson couples to a top quark or W boson (Figures 2.21a and 2.21b respectively), or through the tW process, in which the Higgs couples to the top quark (Figure 2.21c). Both these processes are sensible the the sign of y_t .

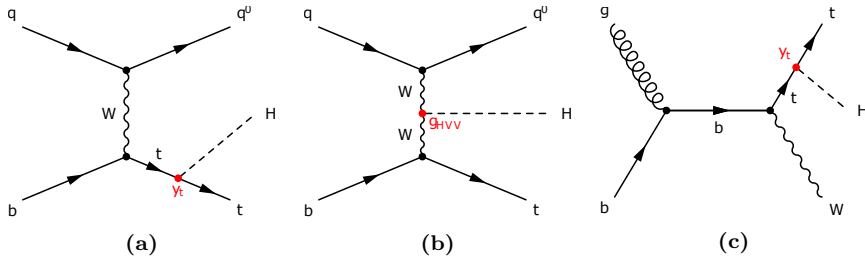


Figure 2.21: Representative LO Feynman diagrams for the t -channel tHq associated production, where the Higgs boson couples either to the top quark (a) or the W boson (b). Here g_{HVV} is the coupling of the Higgs boson to the vector bosons. On (c) an example of the tWH production is presented.

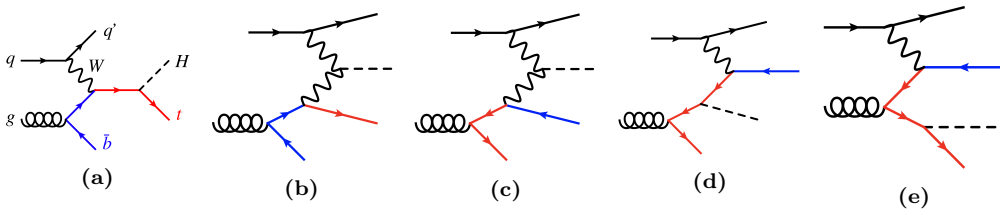


Figure 2.22: LO Feynman diagrams for t -channel tH production in the 4FS. The red line represents the top quark while the blue is the b quark.

1209 **tHq production modes**

1210 At LO, the production of a Higgs boson in association with a single top
 1211 quark and additional parton (tHq) in pp collisions is classified in three
 1212 groups according to the virtuality of the W boson. These groups are: t -
 1213 channel production, s -channel production and associated production with
 1214 and on-shell W boson. This categorisation is the same as for the single-
 1215 top-quark (Section 2.1.2.2), which makes sense since the tHq production
 1216 is, basically, a single-top-quark process in which a Higgs boson is radiated
 1217 either from the W or the top.

1218 In the t -channel production modes are classified in 4FS and 5FS as it
 1219 is done for the single-top case. The 4FS and the 5FS modes are shown in
 1220 Figures 2.22 and 2.22 respectively. For the 4FS modes, the diagrams in
 1221 which the gluon decays to a top pair (2.22c, 2.22d and 2.22e) contribute
 1222 less than the the ones in which it does to a $b\bar{b}$ (2.22a and 2.22b).

1223 Poner las tablas para las cross section de Demartin [3] para 1224 **t -channel y s -channel**

1225 Since the s -channel contribution is so small to the total cross section of
 1226 the tHq process,

1227 For tH and single-top-quark production at colliders, the 5FS calculations
 1228 are easier than the 4FS due to the lesser final state-multiplicity and smaller
 1229 phase space. This is why in the 5FS the single-top production is known

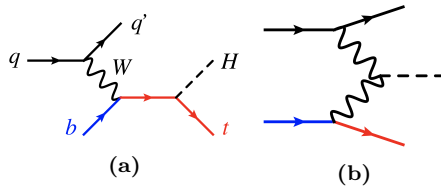


Figure 2.23: LO Feynman diagrams for t -channel tH production in the 5FS.

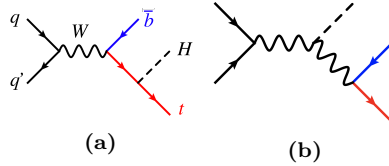


Figure 2.24: LO Feynman diagrams for s -channel tH production in the 5FS.

at NNLO while the 4FS this is done only for NLO. Another advantage of the 5FS is that the t -channel, s -channel and associated tWH production do not interfere until NNLO. Contrary, the in 4FS, the t -channel at NLO and s -channel at NNLO can interfere. Nevertheless, this interferences are very small and can be neglected [3].

Poner algo in información del tWH production mode para tH
y The tWH production is a background in the tHq analysis.

In reference [3] is shown that the shapes of the distributions of most observables in the s -channel differ significantly from those of the t -channel. So, even though the total cross section of the tHq production with the s -channel is much more smaller than the one for t -channel, one could think that including the s -channel in the analysis would increase the precision. This is not the case because the LHC is not sensible for to the tHq production via the s -channel. In fact, not event the s -channel-single-top production (without any associated Higgs boson) has been found at LHC.

Summarise production modes described in [3]

tHq sensibility to y_t

As already commented in the introduction of the Section 2.3, the main interest of the tHq process is that it is among the few processes in the LHC that are sensible to the relative size and phase between the couplings of the Higgs top and the Higgs to the gauge bosons. The other mechanisms to determine this relative sign are $H \rightarrow \gamma\gamma$ and $gg \rightarrow ZZ$. This is due to the fact that in the SM the tHq production of the where the H couples to the W (Figure 2.21 right) interfere destructively with those in which the H is radiated from the top (Figure 2.21 left). As it is later explained in Section 3.2.5, the cross section is proportional to the square of the matrix element,

\mathcal{M} and if there are several diagrams for a same process, the matrix elements have to be summed before squaring leading to interference terms. For the tHq production

$$\sigma_{tHq} \propto |\mathcal{M}_{qq \rightarrow tHq}|^2 = |\mathcal{M}_{qq \rightarrow tHq_{WH}} + \mathcal{M}_{qq \rightarrow tHq_{tH}}|^2 \quad (2.3)$$

When squaring the scattering amplitude, the destructive interference⁹ term decreases the σ_{tHq} . This behaviour makes the tHq cross section exceptionally sensible to the departures of y_t from the SM predictions. Typically, the destructive interference yields a reduction in the rate as compared to the contribution from each individual diagram by about an order of magnitude [84]. Therefore, in the presence of non-SM new physics, a positive relative sign between the tH and the WH couplings would imply that the amount of tHq events recorded should increase a factor of ~ 13 over the SM expectations, surpassing the number of events from $t\bar{t}H$ production [85].

The tHq production has been studied at LHC Run 1 by CMS [86]

[Usar los papers the \$tHq\$ de CMS la sección 5 de Demartin \[3\]](#)

2.3.3.1 tH Standard Model

2.3.3.2 tH Charge-Parity

2.3.3.3 ATLAS and CMS results

In order to gather the necessary information, the widest campaign of measurements has to be undertaken, including as many possible decay modes. In this context, the scope of this thesis is the study of the production tH with a final state characterised by two light leptons (ℓ), i.e. electrons (e^\pm) or muons (μ^\pm), and one hadronically decaying tau lepton (τ_{had}). This signature is usually referred as dileptau or lep-had channel and is denoted by $2\ell + 1\tau_{\text{had}}$.

⁹By destructive interference is meant that the relative sign between $\mathcal{M}_{qq \rightarrow tHq_{WH}}$ and $\mathcal{M}_{qq \rightarrow tHq_{tH}}$ is negative.

¹²⁶⁷ Chapter 3

¹²⁶⁸ ¹²⁶⁹ ¹²⁷⁰ The ATLAS experiment at the Large Hadron Collider of CERN laboratory

¹²⁷¹ The work developed in this thesis is framed in the context of the AT-
¹²⁷² LAS detector [87], a general-purpose particle physics detector registering
¹²⁷³ the events originated from the collisions produced by the largest and most
¹²⁷⁴ powerful particle accelerator built up to this date, the LHC. This experi-
¹²⁷⁵ mental setup is located in one of the largest and most renowned centres for
¹²⁷⁶ scientific research in the world, the CERN.

¹²⁷⁷ This chapter is devoted to the introduction of the CERN laboratory and
¹²⁷⁸ a description of the technical design of LHC and ATLAS. The CERN or-
¹²⁷⁹ ganisation is presented through an overview of its history, its achievements
¹²⁸⁰ and some of the most relevant research projects carried out currently. The
¹²⁸¹ essential technical aspects of the LHC machine design are covered. The
¹²⁸² distribution and functioning of the accelerator complex and the main exper-
¹²⁸³ iments conducted at LHC are summarised as well. Finally, a full overview
¹²⁸⁴ of the different components of the ATLAS detector is exposed, presenting
¹²⁸⁵ the specific features of each of its parts.

¹²⁸⁶ 3.1 CERN

¹²⁸⁷ The European Organization for Nuclear Research, known as CERN, is
¹²⁸⁸ the largest particle physics laboratory in the world. The convention estab-
¹²⁸⁹ lishing CERN was ratified in 1954. Its name is derived from the French
¹²⁹⁰ acronym *Conseil Européen pour la Recherche Nucléaire*, which was the pro-
¹²⁹¹ visional body designated in 1952 to foster the fundamental physics research

1292 in Europe, and the acronym has been maintained until CERN’s foundation.
1293 Initially formed by 12 member states, now it has 23 member states and
1294 many non-European countries involved in different ways such as associate
1295 members, partners and observers [88].

1296 The main site of the laboratory is located at Meyrin, a municipality of
1297 the Canton of Geneva (Switzerland), at the Franco–Swiss border. There
1298 are other sites in the vicinity of the Meyrin site, being the most relevant the
1299 Prévessin Site, the CERN’s second-largest site, straddling the communes of
1300 Prévessin-Moën (France).

1301 Since its beginning, CERN’s objective has been helping to uncover what
1302 the universe is made of and how it works. CERN started its first accelerator,
1303 the Synchrocyclotron, on 1957 and rapidly observed the electron decay of
1304 the pion for the very first time [89]. Thereafter, the laboratory has con-
1305 tinued contributing to not only particle and nuclear physics but also more
1306 technical fields. For instance, one of the most important achievements made
1307 through CERN experiments is the discovery in 1973 of neutral currents in
1308 the Gargamelle bubble chamber installed in the Proton Synchrotron (PS)
1309 [90]. This observation was an indirect evidence for the existence of the Z
1310 boson and ten years later, in 1983, CERN announced the discovery of the
1311 Z and W bosons [91]. This finding was done at the UA1 and UA2 ex-
1312 periments, located within the Super Proton Synchrotron (SPS), and it was
1313 awarded with the laboratory first Nobel Prize in 1984. Other major suc-
1314 cesses of CERN were the determination of the number of light neutrino
1315 families at the Large Electron-Positron Collider (LEP) on 1995 [92] and the
1316 creation for the very first time of antihydrogen atoms in 1995 at the PS210
1317 experiment [93]. More crucial accomplishment followed such as the discov-
1318 ery during the 1990’s of \mathcal{CP} violation by NA31 [94] and NA48 experiments
1319 [95]. And, in 2012, the Higgs boson discovery by ATLAS and CMS[1] [2], a
1320 fundamental test for the robustness of the SM as described in Section 2.2.1.
1321 More recently, in 2015, a state consistent with a pentaquark was observed
1322 at LHCb [96].

1323 Currently, a wide diversity of projects are carried at CERN being the
1324 most renowned of them the LHC and its experiments which are described in
1325 more detail in Section 3.2. In addition, fixed-target experiments, antimatter
1326 experiments and experimental facilities make use of the LHC injector chain.
1327 The main fixed-target experiments at CERN are the Antiproton Decelerator
1328 (AD) [97] for slowing antiprotons for the antimatter factory [98] and the
1329 On-Line Isotope Mass Separator (ISOLDE) facility for short-lived ions [99].
1330 The world’s first proton-driven plasma wakefield acceleration experiment is
1331 also at CERN, the Advanced Proton Driven Plasma Wakefield Acceleration
1332 Experiment (AWAKE) [100]. In the International Space Station (ISS), the

Parameter	Design	Run-1	Run-2	Run-3	HL-LHC
Beam energy	7	3.5 - 4	6.5	7	7
Center-of-mass energy (\sqrt{s}) [TeV]	14	7 - 8	13	13.6	14
Bunch spacing [ns]	25	50	25	25	25
Bunch Intensity [10^{11} ppb]	1.15	1.6	1.2	up to 1.8	2.2
Number of bunches (n_b)	2800	1400	2500	2800	2800
Transverse emittance (ϵ) [μm]	3.5	2.2	2.2	2.5	2.5
Amplitude function at the interaction point (β^*)[cm]	55	80	30→25	30→25	down to 15
Crossing angle [μrad]	285	-	300→260	300→260	TBD
Peak Luminosity [$10^{34} \text{ cm}^2 \text{ s}^{-1}$]	1.0	0.8	2.0	2.0	5.0
Peak pileup	25	45	60	55	150
Nominal magnetic field (B) [T]	8.73	4.16 - 7.76	7.73	8.73	8.73
Injection energy [GeV]				450	
Circumference length [km]				26.7	
Radius [km]				4.24	
Number of dipole magnets				1232	
Length of dipole magnets [m]				14.3	
Number of quadrupole magnets				395	
Total mass [tons]				27.5	

Table 3.1: Summary of main accelerator parameters for the LHC, showing the design values, and those used during Run-1 and Run-2, as well as the expected parameters for Run-3 and the HL-LHC.

1333 Alpha Magnetic Spectrometer (AMS) tries to observe dark matter [101].
 1334 The research programme at CERN covers topics from the basic structure
 1335 of matter to cosmic rays, and from the SM to supersymmetry.

1336 3.2 Large Hadron Collider

1337 In the mid of the decade of 1980, the plans for building the Large Hadron
 1338 Collider (LHC) were started. At several high-energy physics workshops
 1339 and conferences, the idea of assembling a machine able to reach multi-TeV
 1340 energies was discussed. This instrument would allow physicists to search for
 1341 the Higgs boson at all possible masses. In 1991 the Long-Range Planning
 1342 Committee of CERN proposed the construction of the LHC as the best step
 1343 forward in CERN’s future [102]. The approval of the LHC project arrived
 1344 in 1994 and in 1995 the Conceptual Design Report was published [103].
 1345 Finally, on 10 September 2008, a beam of protons was successfully directed
 1346 into the LHC pipes for the first time.

1347 A summary of the main parameters of LHC for pp collisions is presented
 1348 in Table 3.1. These parameters are shown for how the machine was
 1349 designed, for Run-1 (2011-2012) and Run-2 (2015-2018) as well as the ex-
 1350 pected parameters for Run-3 (2025-2027). The forecasted values for the
 1351 High Luminosity (HL) LHC upgrade (after 2027) are exposed too.

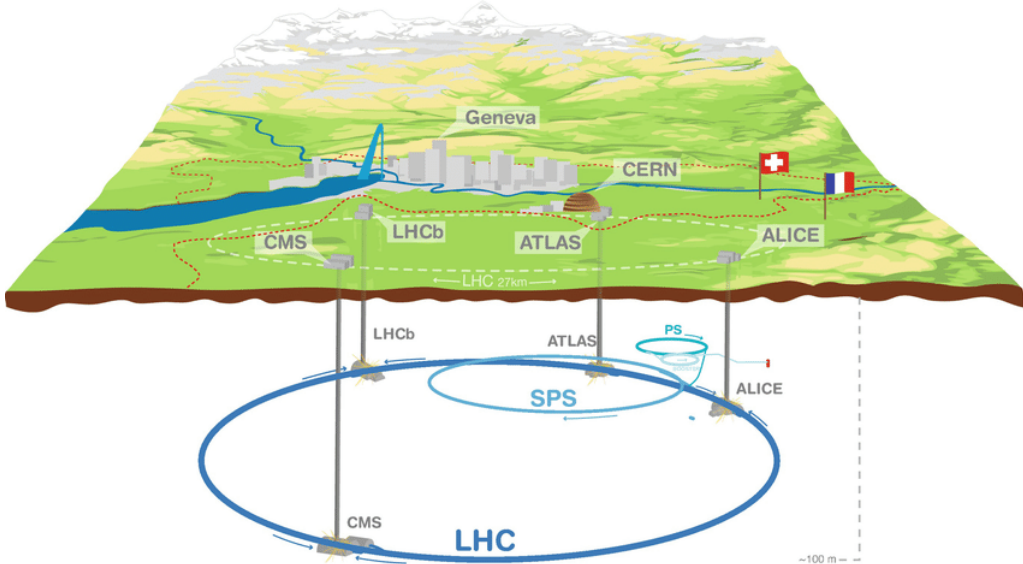


Figure 3.1: Overall view of the LHC including the ATLAS, CMS, ALICE and LHCb experiments. [This image duplicates the information of Figure 3.4](#)

1352 3.2.1 Machine design

1353 The LHC is a circular hadron accelerator with a circumference of 27 km.
 1354 Located where once was the LEP collider, the accelerator used by CERN
 1355 from 1999 to 2000 [104], the LHC tunnels are almost entirely outside the
 1356 main site, being mainly on french territory. An overall schematic view of
 1357 the LHC is shown in Figure 3.1.

1358 The LHC has two rings with ultra-high vacuum (to prevent collisions
 1359 with gas molecules while moving through the accelerator) inside of which
 1360 particle beams travel in opposite directions. It was designed to accelerate
 1361 and collide proton beams with a center-of-mass energy (\sqrt{s}) up to 14 TeV at
 1362 a luminosity (\mathcal{L}) of $10^{34} \text{ cm}^2 \text{ s}^{-1}$ (see Section 3.2.5 for details about luminosity).
 1363 As well as protons, it can collide heavy ions, in particular lead nuclei,
 1364 at $\sqrt{s} = 2.3 \text{ TeV}$ per nucleon and a peak luminosity of $\mathcal{L} = 10^{27} \text{ cm}^2 \text{ s}^{-1}$
 1365 [105]. These specifications make the LHC the accelerator with higher collision energy [106].

1367 The beams in the LHC are made up of bunches of protons that are spaced
 1368 7 m apart and collide every 25 ns. Each bunch contains around 1.1×10^{11}
 1369 hadrons, being 2556 the maximum possible number of bunches that can be
 1370 reached with the beam preparation method currently used [107]. The size
 1371 of each bunch is approximately 25 cm [108].

1372 The LEP tunnel lies between 45 m and 170 m below the surface on a
 1373 plane inclined at 1.4% sloping towards the Léman lake. The underground

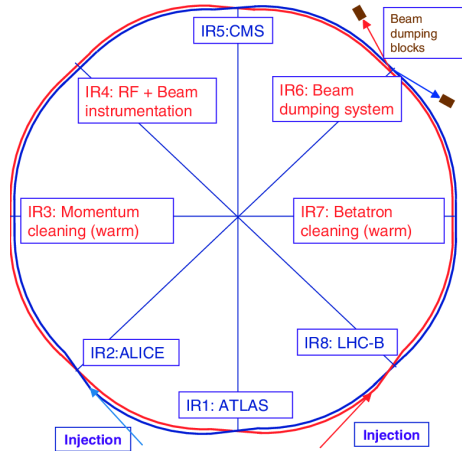


Figure 3.2: Schematic layout of the LHC (Beam 1clockwise, Beam 2 anti-clockwise).

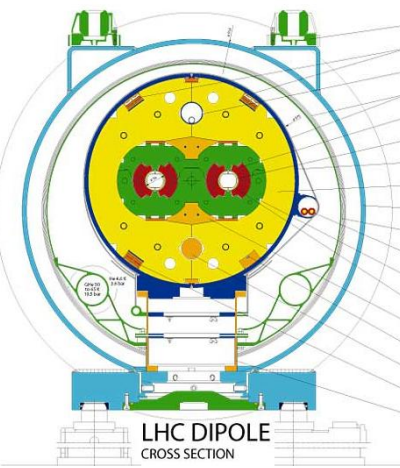


Figure 3.3: LHC dipole cross section.

construction adds some shielding from outside interferences that could interact with the detectors and cause anomalous readings. Even 100 m underground, the cosmic rays can reach the detectors, so these are used to help to calibrate them. The tunnel has an internal diameter of 3.7 m, which makes it extremely difficult to install two completely separate proton rings [109] as in the Superconducting Super Collider (SSC). Therefore, the counter-rotating rings are built under the *two-in-one* twin-bore superconducting magnet design. These twin bore configurations have the disadvantage of having the rings magnetically coupled, which adversely affects flexibility [110]. Figure 3.3 shows an example of the LHC twin-bore dipole magnet.

The LHC is not a perfect circle. Approximately 22 km of the LHC ring consists of 8 curved sections. The remaining 5 km of the tunnel are made of 8 straight sections, denominated insertion regions (IR), that provide space for the experiments. Figure 3.2 shows the distribution of IR and crossing points for the LHC. This layout follows that of the LEP tunnel. The number of crossing points where the beams pass from one ring to the other for colliding was decreased from the original eight at LEP to four in the LHC in order to reduce costs and optimise the utility insertions containing Radio Frequency (RF), the collimation and the beam dump systems [103].

The arcs contain the dipole bending magnets, which are shown in Section 3.3. The 1232 twin-bore magnets curve the trajectory of the particle beam that would, otherwise, follow a straight line. Dipoles are also equipped with additional multipole lattice magnets (sextupole, octupole and decapole), which correct for small imperfections in the magnetic field at the extremities of the dipoles.

1399 Each of the eight straight sections is approximately 528 m long. The RF
1400 cavities delivering 2 MV (an accelerating field of 5 MV/m) at 400 MHz are
1401 located in the IR4. The 16 RF cavities compensate the synchrotron radi-
1402 ation losses (the electromagnetic radiation emitted when charged particles
1403 travel in curved paths) that take place at the arcs of LHC. The energy ra-
1404 diated per particle by synchrotron radiation is proportional to the inverse
1405 of the mass of the particle: $\Delta E \propto 1/m^4$. This radiation is, thus, smaller
1406 for protons than for electrons. That is why the LHC machine has much less
1407 synchrotron radiation losses than the LEP and its design would ideally have
1408 longer arcs and shorter straight sections for the same circumference. But
1409 using the tunnel as built for LEP was the cost-effective solution. During
1410 the 20 minutes that are needed to reach the beams maximum energy, the
1411 bunches have passed the RF cavities more than 10 million times [103].

1412 The RF cavities (also known as resonators) are metallic chambers spaced
1413 at intervals along the accelerator shaped to resonate at specific frequencies,
1414 allowing radio waves to interact with passing particle bunches. The main
1415 role of the RF cavities is to keep the proton bunches tightly packed to
1416 ensure the required luminosity at the interaction point. They also transfer
1417 RF power to the beam to accelerate it to the top energy [111].

1418 At the insertion of the arc and straight sections, quadrupole magnets
1419 are installed to suppress the dispersion of particles. Acting as focal lenses,
1420 quadrupole magnets gather the particles together. This system not only
1421 cancels the horizontal dispersion arising in the arc but also adapts the LHC
1422 reference orbit to the geometry of the LEP tunnel. Before entering the
1423 detectors, the inner triplets (which are made mostly from quadrupoles)
1424 tighten the beam, from 0.2×10^{-3} m down to 16×10^{-6} m. These are known
1425 as insertion magnets.

1426 In total there are more than 9000 magnets all over the LHC and more
1427 than 50 types of magnets are needed to make the particles circulate in
1428 their path without losing speed. The coils are made of niobium-titanium
1429 (NbTi) which is cooled to less than 2 K with superfluid helium to reach
1430 superconductivity.

1431 **3.2.2 Accelerator complex**

1432 To accelerate the proton beams, the existing CERN accelerator complex
1433 is used. These accelerators were, back in the day, the state of the art
1434 colliders and now they serve as injection system for the LHC. The path
1435 followed by the particle beams is presented in Figure 3.4. The accelerator
1436 complex consists in several machines interconnected with higher and higher
1437 capabilities, i.e. the beams are injected from one accelerator to the next in

1438 sequence, boosting the particles to higher energies in each step until they
1439 enter into the LHC.

1440 The proton bunches are produced ionising a gas of hydrogen atoms and
1441 then they are accelerated to a momentum of 50 MeV by the linear accelerator
1442 (LINAC2). Starting from Run-3, the LINAC2 is being replaced by the
1443 LINAC4. After being produced, the beams enter into the first circular
1444 accelerator, the Proton Synchrotron Booster (PSB) which has 630 m radius
1445 and increases the energy of the protons until 1.4 GeV.

1446 The main advantage of circular accelerators compared to linear ones is
1447 that they can speed up particles with much less physical space. Circular
1448 accelerators ramp up two different beams with opposite charges at the same
1449 time with a single magnetic field. The maximum energy transferred to the
1450 beams in a circular accelerator is given by p_T [GeV] = $0.3qB[T]r[m]$, being
1451 p_T the transverse momentum of the particles, q the charge of the particles
1452 ($q = 1$ for protons), B the magnetic field applied and r the radius of the
1453 circular accelerator.

1454 Right after the PSB, the Proton Synchrotron brings the particles 25 GeV.
1455 The next step in the chain raises the energy to 450 GeV. This is done by the
1456 SPS, which is 6.9 km long. Once the protons have 450 GeV, the minimum
1457 energy at which the LHC can maintain a stable beam, they are injected
1458 into the LHC by two different 2 km-long Transfer Injection (TI) lines [112].
1459 Protons will circulate in the LHC for 20 minutes until reaching the maximum
1460 speed and energy (650 GeV per beam) [110].

1461 Heavy-ion collisions were included in the conceptual design of the LHC
1462 from an early stage. Lead ions for the LHC are extracted from a source
1463 of vaporised lead and enter LINAC3 before being collected and accelerated
1464 in the Low Energy Ion Ring (LEIR). They, then, follow the same route to
1465 maximum acceleration as the protons [110].

1466 3.2.3 LHC Experiments

1467 In the LHC four major experiments are carried, each of them with its own
1468 detector (Figure 3.5). These particle detectors measure particles produced
1469 as debris from the pp collisions through the interaction with the material
1470 of the sub-detectors. Distributed along the collider as is shown in Figures
1471 3.1, 3.2 and 3.4, these highly sophisticated experiments are:

- 1472 • **A Toroidal LHC ApparatuS (ATLAS)** [113]: Located in the IR1,
1473 it is a generic multi-purpose experiment for high luminosity (up to \mathcal{L}
1474 = $10^{34} \text{ cm}^2 \text{ s}^{-1}$). It studies pp collisions and investigates a wide range

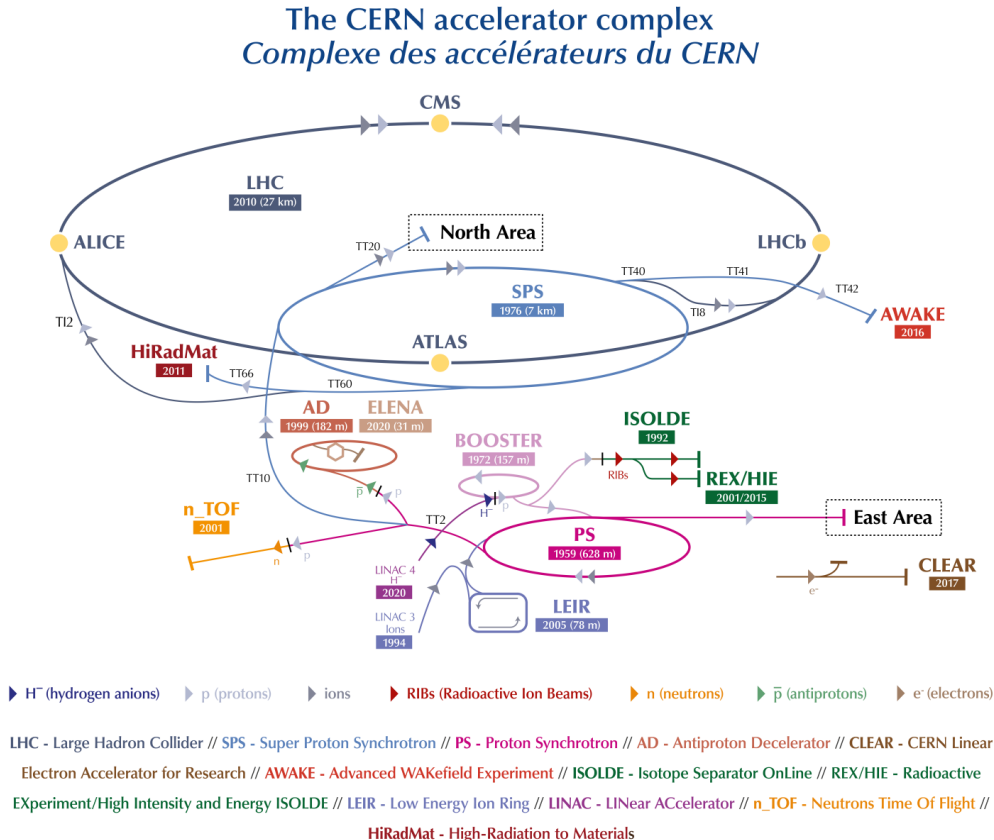


Figure 3.4: Scheme of CERN accelerator complex. Protons are injected from the LINAC2 into the PS Booster, then the PS, followed by the SPS, before finally reaching the LHC.

of physics, from the SM to the search for extra dimensions or dark matter. It has the dimensions of a cylinder, 46 m long, 25 m in diameter. The ATLAS detector weighs 7×10^3 tonnes. The design of the ATLAS detector features excellent jet and E_T^{miss} resolution, particle identification and flavour tagging and standalone muon measurements. A scheme of this detector is shown in Figure 3.5a. ATLAS will be covered in detail in Section 3.3.

- **Compact Muon Solenoid (CMS)** [114]: Built inside the IR5, it's the other general-purpose experiment for high luminosity (same \mathcal{L} as ATLAS). CMS has the same objectives and goals as ATLAS but both its hardware and software designs are different. Even though CMS is smaller than ATLAS (21 m long, 15 m in diameter) it is much heavier, weighting 14×10^3 tonnes. The bulk of its weight is the steel yoke that confines the 4 T magnetic field of its superconducting solenoid.

1489 The design of CMS emphasises magnificent electron/photon energy
1490 and momentum resolution. Figure 3.5b illustrates this device. The
1491 role of coexistence of CMS and ATLAS is fundamental so that one
1492 can verify and confirm the experiments of the other independently.

- 1493 • **Large Hadron Collider beauty (LHCb)** [115]: Hosted at IR2, it
1494 is a lower luminosity experiment designed to study the small asymmetries
1495 between matter and antimatter through \mathcal{CP} violation using rare decays of b -quark based hadrons. The detector is arranged as a
1496 succession of planar sub-detectors (as can be seen in Figure 3.5c) since most of the b -flavoured mesons follow the beam pipe direction when
1497 created in the pp collision. LHCb delivers remarkable low-momentum track reconstruction and particle identification.
- 1498 • **A Large Ion Collider Experiment (ALICE)** [116]: It is a low
1499 luminosity experiment in IR8 that focuses on QCD. The main feature
1500 of ALICE is a general-purpose detector that it uses heavy-ion collisions to study matter interacting at extreme densities and temperatures, thus reproducing the quark-gluon plasma. This detector is shown in Figure 3.5d and it provides highly efficient track reconstruction in an environment full of heavy ions. Besides running with Pb ions, the physics programme includes collisions with lighter ions, lower energy collisions and a dedicated proton-nucleus run.

1510 Along the LHC machine, there are other experiments much more smaller than ATLAS, CMS, LHCb and ALICE, typically sharing the cavern
1511 with the major projects. The most relevant among the minor experiments are LHCf [117], MATHUSLA [118], MilliQan [119], MoEDAL [120],
1512 TOTEM [121] and FASER [122].

1515 3.2.4 LHC Computing grid

1516 The data collected by the different LHC experiments is stored, processed
1517 and, then, made available for all the researchers of each collaboration¹. This
1518 is possible thanks to the last piece of the LHC, its computing model and
1519 infrastructure: the LHC Computing Grid (LCG). It consists of several computing farms distributed around the world and interconnected. Figure 3.6
1520 shows the geographical distribution of the different facilities that comprise
1521 the LCG. Just as the WWW enables access to information, the Grid enables
1522 access to computer resources. Employing a grid certificate, is possible
1523 for any user to run jobs on the grid and to access the data stored. The

¹Within the grid context, each collaboration is known as Virtual Organisation (VO).

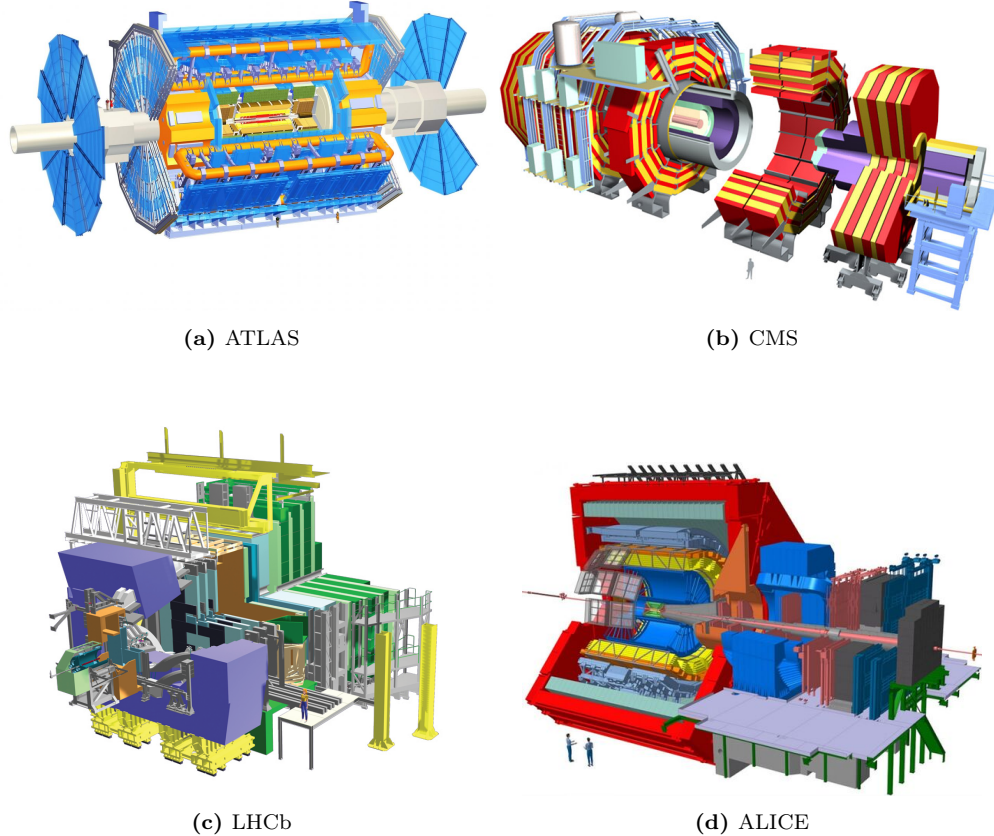


Figure 3.5: Scheme of LHC main experiments. Note that the images are not equally scaled.

1525 implementation of the grid model implies an effective coordination among
1526 all LHC collaboration centres [123].

1527 Different types of computing centres have been defined and classified in
1528 Tiers [125]:

- 1529 • **Tier-0:** This facility is located at CERN and it is responsible for
1530 archiving (first copy) and distributing the raw data received from the
1531 Event Filter, i.e., the data emerging from the Data Acquisition sys-
1532 tems (DAQ) after the trigger. It provides prompt reconstruction and
1533 distributes a copy of the raw data to the Tier-1 centres.
- 1534 • **Tier-1:** These facilities archive the raw data permanently and provide
1535 the computational capacity for reprocessing and for physical analysis.
1536 It also stores the simulated and reprocessed data. Currently, there
1537 are thirteen large computer centres serving as Tier-1 (see Figure 3.7).
1538 These make data available to their Tier-2 centres [126].

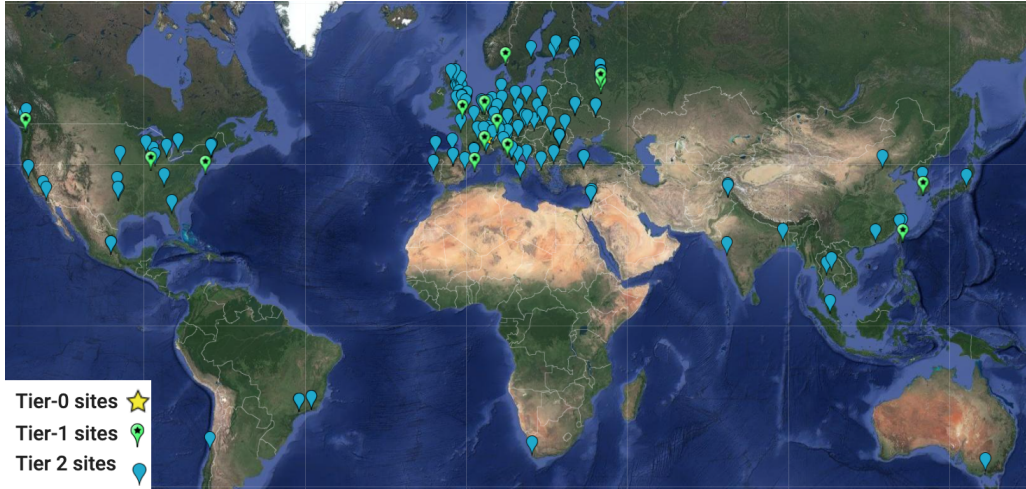


Figure 3.6: Worldwide LHC Computing Grid geolocalisation of sites [124].

- **Tier-2:** Typically located at universities and other scientific institutes, there are more than 150 Tier-2 sites. The derived datasets produced by the physics groups are copied to the Tier-2 facilities for further analysis. The MC simulations for event production are executed at this level.
- **Tier-3:** The local computing resources, from local clusters to even just an individual PC are referred to as Tier-3. There is no formal engagement between worldwide LCG and the Tier-3.

This system provides near real-time access to LHC data. The LCG collaboration spreads out over 42 countries with 170 computing centres and 1 million computer cores, being the world's largest computer grid. It deals with over two million tasks daily. These specifications make the LCG the most sophisticated system for data taking and analysis ever built for science.

3.2.5 Energy, Luminosity and Cross-section

Energy

Another name to refer to the field of Particle Physics is “high energy physics”. Particles such as the Higgs boson or the top quark are more than 100 times heavier than the proton so, in order to produce them, huge energies are required. The center-of-mass energy, \sqrt{s} , allows the production of physical effects. The greater the energy is, the bigger is the range of the different processes that can be produced by the accelerator.

The four-vector, $\mathbf{p} = (E, \vec{p})$, of a particle of mass m describes its kinematics with its energy E and \vec{p} . The square of the four-vector, \mathbf{p}^2 , cor-

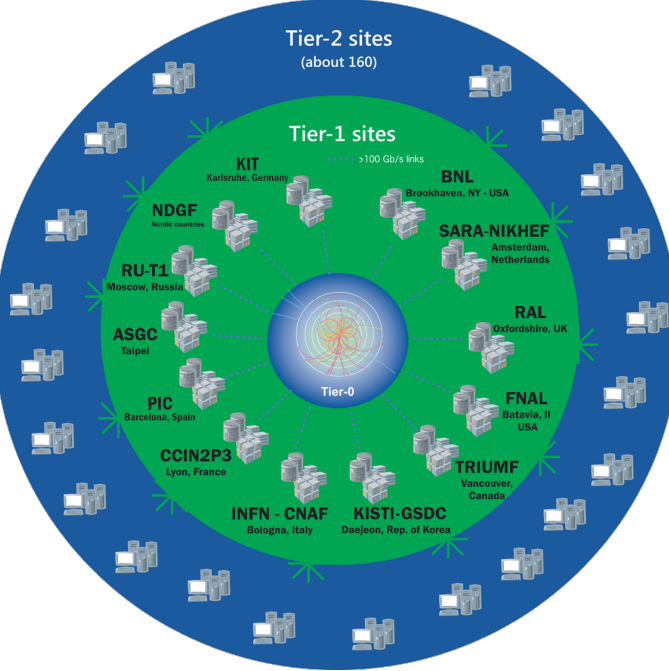


Figure 3.7: Distribution by Tiers of the LCG [126]. This project provides global computing resources to store, distribute and analyse the data recorded at the LHC.

responds to the particle mass:

$$p^2 = E^2 - \vec{p}^2 = m^2 \quad (3.1)$$

When two particles of mass m_1 and m_2 and momenta \vec{p}_1 and \vec{p}_2 respectively collide, the center of mass energy, \sqrt{s} , can be expressed as:

$$s = E_{CM}^2 = (p_1 + p_2)^2 = (E_1 + E_2)^2 - (\vec{p}_1 + \vec{p}_2)^2 \quad (3.2)$$

For symmetric colliding beams, such those of LHC, the collision point is at rest in the laboratory frame ($\vec{p}_1 = -\vec{p}_2$) and, hence, the energy is

$$s = E_{CM}^2 = (E_1 + E_2)^2 \quad (3.3)$$

1560 Since the energy of each beam is 650 GeV during Run-2, the center of mass
1561 energy of LHC collisions is

$$\sqrt{s} = E_{CM} = (E_{beam1} + E_{beam2}) = 650 \text{ GeV} + 650 \text{ GeV} = 13 \text{ TeV} \quad (3.4)$$

1562 **Luminosity**

1563 Besides \sqrt{s} , the luminosity is the most relevant parameter in an experiment,

especially in searches for events with small cross-section. It measures the ability of the particle accelerator to produce enough events of the desired type.

The luminosity, \mathcal{L} , is the ratio of events detected in a certain period of time for a given cross-section (σ):

$$\mathcal{L} = \frac{1}{\sigma} \frac{dN}{dt} = \frac{1}{\sigma} R \quad (3.5)$$

where N is the number of the events and t the time. $R = \frac{dN}{dt}$ is known as reaction rate. It can be understood as number of particle collision per unit area (typically expressed in cm^2) and per second, therefore it is measured in $\text{cm}^2 \text{s}^{-1}$ [127]. For instance, for LEP was $\mathcal{L}_{LEP} = 1.0 \times 10^{32} \text{ cm}^2 \text{s}^{-1}$ and the LHC is designed to achieve $\mathcal{L}_{LHC_{pp}} = 2.1 \times 10^{34} \text{ cm}^2 \text{s}^{-1}$ in pp collisions and $\mathcal{L}_{LHC_{PbPb}} = 6.1 \times 10^{27} \text{ cm}^2 \text{s}^{-1}$ for heavy ion collisions.

For two beams colliding, the instantaneous luminosity is proportional to the number of bunches per beam (n_1 and n_2), the revolution frequency (f) with which the bunches are crossing and the number of proton bunches in the machine (n_b), and it is and inversely proportional to the beams effective transverse area in which the collision takes places (Area = $4\pi\sigma_x\sigma_y$)

$$\mathcal{L} = f \cdot \frac{n_1 n_2 n_b}{4\pi\sigma_x\sigma_y} \cdot F(\theta_c, \sigma_x, \sigma_z) \quad (3.6)$$

where $F(\theta_c, \sigma_x, \sigma_z)$ is a factor accounting for the luminosity reduction due to the beam crossing angle (θ_c). At the LHC, assuming that the particles travel at the speed of light, for its 27 km, the bunch crossing frequency is $f = 11245.5 \text{ Hz}$. The maximum number of proton bunches in the machine with 25 ns slots is² $n_b = 2808$. In each bunch there are $n_1 \approx n_2 \approx 1.15 \times 10^{11}$ particles. Finally, characterising the optics of the collision at the interaction point (IP), the RMS transverse beam width in the horizontal and vertical directions are $\sigma_x \approx \sigma_y \approx 12, \dots, 50 \mu\text{m}$. The expression 3.6 assumes that the particles in the beam are Gaussian distributed. According to equation 3.6 the instantaneous luminosity only depends on the machine and its beam parameters [128][129].

The integrated luminosity over time is given by

$$L = \int \mathcal{L} dt \quad (3.7)$$

and it is used to determine the number of events, N , that have taken place during that time: $N = \sigma \times L$. The ability to observe low cross-section

²The theoretical maximum of 3564 bunches cannot be reached due to space needed between bunch trains and for the beam dump kicker magnets.

events is

$$N_{events}^{obs} = \sigma_{process} \times \text{efficiency} \times L \quad (3.8)$$

, where the efficiency of the detection is to be optimised by the experimental physicist, the integrated luminosity (L) is delivered by LHC and the cross-section of the process ($\sigma_{process}$) is given by nature.

On one hand, several factors can limit the maximum luminosity that can be achieved at LHC [127]:

- **Beam-beam effect:** The bunches of two beams or the particles in the same bunch can interact electromagnetically, this leads to distortions from the orbit and results in an increase of the emittance, ϵ .
- **Crossing angle:** Often used to avoid unwanted collisions in machines with many bunches, due to the crossing angle θ_c , the luminosity is reduced by a factor $F(\theta_c, \sigma_x, \sigma_z) = \sqrt{1 + (\theta_c \sigma_z / 2\sigma x)^2}$.
- **Beam offset:** Originated from the beam-beam effects or misalignments in the quadrupole magnets, the beams can collide with small transverse offset. Such beams' offsets induce a loss of \mathcal{L} at the interaction point.
- **Hourglass effect:** Appears when beams collide in a point away from the IP.

On the other hand, there are diverse strategies to maximise the luminosity delivered by a machine [128]:

- **Maximise the total beam current:** Improvements in beam collimation, cryogenics vacuum and background protection could extend the limit on the maximum beam current.
- **Compensate reduction factor:** The hourglass effect may be reduced by shorter bunches at the expense of a higher longitudinal pileup density (see Section 3.2.6).

The cumulative luminosity delivered by LHC to ATLAS during the Run-2 per year is shown in Figure 3.8. In Figure 3.9, the total Run-2 cumulative luminosity is presented differentiating between the delivered and recorded luminosity and showing that almost all delivered events are considered to be good data quality. The delivered luminosity accounts for the luminosity given from the start of stable beams until the LHC requests ATLAS to put the detector in a safe standby mode to allow a beam dump or beam studies. The recorded luminosity reflects the DAQ inefficiency, as well as

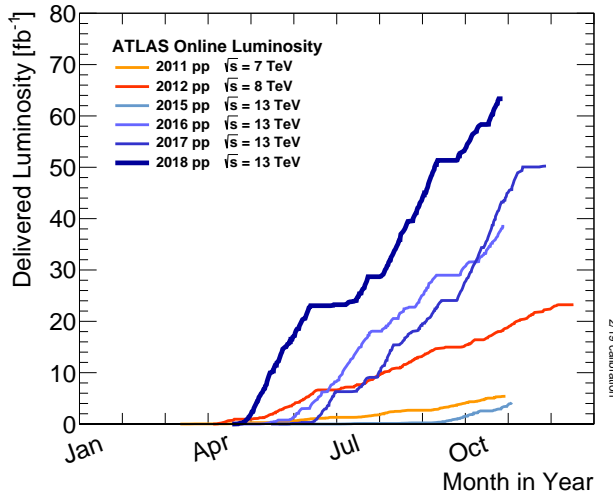


Figure 3.8: Cumulative luminosity versus day delivered to ATLAS during stable beams and for high energy pp collisions **Maybe it is not a good idea to put an ATLAS plot before introducing ATLAS. Move figure to section 4.2.1.5.**

Year	2015	2016	2017	2018
Peak instantaneous luminosity ($\times 10^{33} \text{ cm}^2 \text{ s}^{-1}$)	5	13	16	19
Total delivered integrated luminosity (fb ⁻¹)	4.0	38.5	50.2	63.4

Table 3.2: Peak luminosity and total integrated luminosity delivered by the LHC at $\sqrt{s} = 13 \text{ TeV}$ in Run-2 per year [131].

the inefficiency of the so-called “warm start”: when the stable beam flag is raised, the tracking detectors undergo a ramp of the high-voltage and, for the pixel system, turning on the preamplifiers. The All Good Data Quality criteria require all reconstructed physics objects to be of good data quality [130].

1622 Cross-section

1623 The cross-section is a metric of the likely is a particular reaction to occur.
 1624 The higher the cross section is for a process, the more probable is for it to
 1625 take place. Denoted by σ , it is measured in units of area named barns: 1
 1626 barn = b = 10^{-24} cm^2 . For instance, for the LHC energy:

- 1627 • $\sigma(pp \rightarrow X) \approx 0.1 \text{ b}$
- 1628 • $\sigma(pp \rightarrow X + H) \approx 1 \times 10^{-11} \text{ b}$
- 1629 • $\sigma(pp \rightarrow X + H; H \rightarrow \gamma\gamma) \approx 50 \times 10^{-15} \text{ b}$

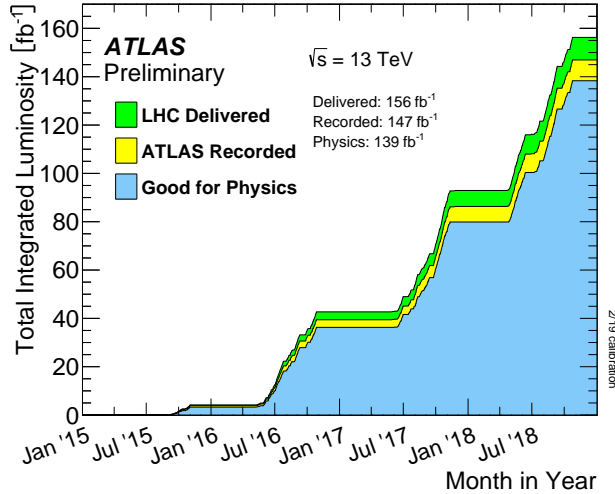


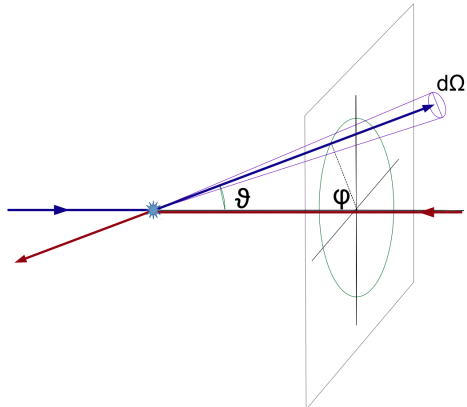
Figure 3.9: Total cumulative luminosity versus time delivered to ATLAS (green), recorded by ATLAS (yellow) and certified to be good quality data (blue) during stable beams for pp collisions at $\sqrt{s} = 13$ TeV.

1630 In experiments with rotational symmetry, such as ATLAS, it is usual to
 1631 define the differential cross-section ($\frac{d\sigma}{d\Omega}$) as the cross-section per solid angle.
 1632 If the differential cross-section is integrated over corresponding the angular
 1633 range, the cross-section for a specific region (σ_ϑ) is obtained:

1634

$$\sigma_\vartheta = \int_0^\vartheta \int_0^{2\pi} \frac{d\sigma}{d\Omega} \sin(\vartheta) d\phi d\vartheta$$

with $\vartheta \in [0, \pi]$ is the coverage of the scattering angle.



The total cross-section is determined by the amplitude of the scattering matrix \mathcal{M} , which is independent of the experimental setup. The \mathcal{M} , also known as scattering amplitude, relates the initial state and the final state of a physical system undergoing a scattering process. Using \mathcal{M} , the total cross-section for a process is determined by:

$$\sigma_{tot} = \int \frac{d\sigma}{d\Omega} d\Omega = \int \frac{1}{\Phi} |\mathcal{M}|^2 dQ$$

1635 being Φ the incident particle flux in the process and the parameter dQ
 1636 describes the kinematic phase space.

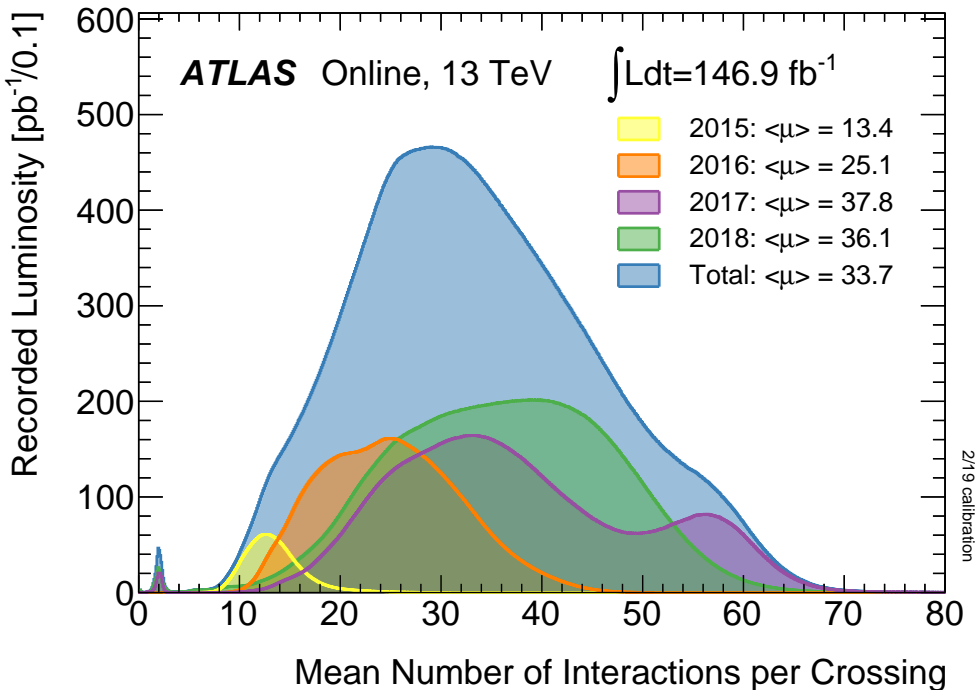


Figure 3.10: Luminosity-weighted distribution of the mean number of interactions per crossing $\langle \mu \rangle$ for Run-2 with pp collisions data.

3.2.6 The Pile-up effect

Pile-up is a challenging matter among detectors and for the acquisition and analysis of the data. In particle physics, pile-up is called to the situation where the detector is being affected by several events at the same time.

Even though the bunches are composed by $\sim 10^{11}$ protons, there are only around 30 collisions per crossing with nominal beam currents. The mean number of interactions per bunch crossing is presented in Figure 3.10 for each year of Run-2. The data shown in Figure 3.10 is recorded by ATLAS during stable beams at $\sqrt{s} = 13$ TeV. The mean number of interactions per crossing corresponds to the mean of the poisson distribution of the number of interactions per crossing calculated for each bunch. It is calculated from the instantaneous per bunch luminosity as $\langle \mu \rangle = \mathcal{L}_{bunch} \times \sigma_{inel} / f_r$ where \mathcal{L}_{bunch} is the instantaneous luminosity per bunch, $\sigma_{inel} = 80$ mb is the inelastic cross section of pp collisions at 13 TeV and $f_r = 11.245$ kHz is the LHC revolution frequency.

Work in progress

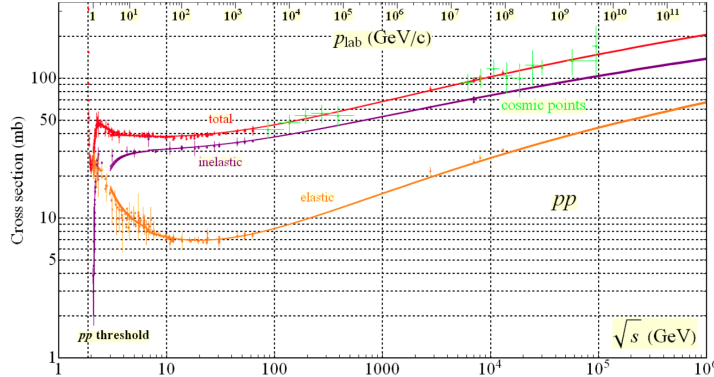


Figure 3.11: Total and elastic cross-section for pp collisions as a function of the laboratory momentum and the \sqrt{s} [133].

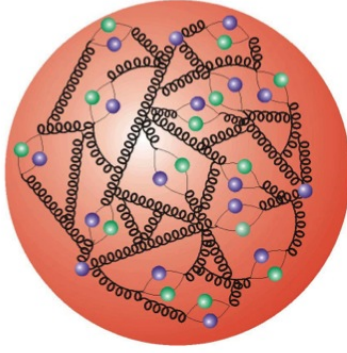
1653 3.2.7 Phenomenology of proton-proton collisions

1654 During LHC Run-2 data taking period, the protons were colliding at
 1655 $\sqrt{s} = 13$ TeV. The pp total cross-section at this energy is measured to be
 1656 $\sigma_{tot} = (110.6 \pm 3.4)$ mb [132]. The luminosity-independent method used
 1657 to measure σ_{tot} allows to split the cross-section into elastic and inelastic
 1658 cross-sections, $\sigma_{el} = (31.9 \pm 1.7)$ mb and $\sigma_{inel} = (79.5 \pm 1.8)$ mb respectively.
 1659 However, only inelastic scattering generates particles with an sufficient angle
 1660 with respect to the beam axis so that these particles enter into the geo-
 1661 metrical acceptance of the detector. Figure 3.11 shows the cross-section
 1662 (elastic, inelastic and total) for pp collisions depending on \sqrt{s} (**Why the**
 1663 **values of the Figure 3.11 do not match the: $\sigma_{tot} = (110.6 \pm 3.4)$,**
 1664 **$\sigma_{el} = (31.9 \pm 1.7)$ and $\sigma_{inel} = (79.5 \pm 1.8)$**). The shown cross-section
 1665 can be computed as the convolution of parton density functions (PDFs)
 1666 with the parton scattering matrix element \mathcal{M} .

1667 Unlike leptons, protons are composite objects since they are made of
 1668 quarks and gluons. Therefore and specially at LHC energy regime, the pp
 1669 collisions cannot be described as a point-like interactions, here is where the
 1670 PDFs come into play. The PDFs are functions containing the long distance
 1671 structure of the hadron in terms of valence and sea quarks and gluons. This
 1672 description is known as “parton model”.

1673 **3.2.7.1 Proton structure and parton model for collisions**

1674



The parton model for hadrons describes these non-fundamental particles as a composite of a number of point-like constituents named partons. The proton is not only simply made of three quarks (uud , the so called “valence” quarks) but also, there is a “sea” of gluons and short-lived quark and anti-quark pairs. The partons in the sea are continuously interacting with each other and can have any flavour.

1675 The PDFs describe the distribution of the hadron’s momentum among
1676 its constituents. The PDFs are essential to describe the $p\bar{p}$ interactions be-
1677 cause these collisions cannot be understood as point-like particles crashing.
1678 Instead, all the constituents of the protons are taken into account [60].

1679 Due to the fact that inside of hadrons the quarks are continuously in-
1680 teracting with each other via the exchange of gluons, it is not possible to
1681 calculate PDFs using non-perturbative QCD. Instead, the momentum dis-
1682 tribution function of the partons within the proton is obtained by a fit on
1683 a large number of cross-section data points over a grid of x and Q^2 values
1684 obtained from many experiments (deep inelastic scattering, Drell-Yan and
1685 jet measurements). There are various global fitting collaborations (ABM,
1686 CT, MMHT, NNPDF, MSTW, CTEQ), each taking different approaches
1687 to this fitting procedure. These fits are later extrapolated to new energy
1688 scales.

1689 Formally, the PDF $f_{a/A}(x, Q^2)$ is defined as the probability of finding
1690 a parton a within the hadron A carrying a fraction $x = p_a/p_A$ of its mo-
1691 mentum at Q^2 energy scale. The energy scale Q characterises the hard
1692 scattering and typically corresponds to the momentum transfer in the given
1693 process. As an example, several PDFs at two different scale energies are
1694 presented in Figure 3.12 as a function of x .

1695 The momentum of the proton is distributed among its constituents and,
1696 while at lower energies ($Q \sim 1$ GeV) it is shared mainly between the valence
1697 quarks, at higher energies ($1 < Q \lesssim 1$ GeV) the emission of gluons carrying
1698 a some of the initial momentum of the quark is more probable. Within the
1699 QCD theory, these interactions can be classified in two main groups: “hard”
1700 and “soft”. The hard processes are those involving large momentum trans-
1701 fer. This type of processes are well understood and their cross-section can
1702 be predicted with good precision using perturbation theory. In contrast,

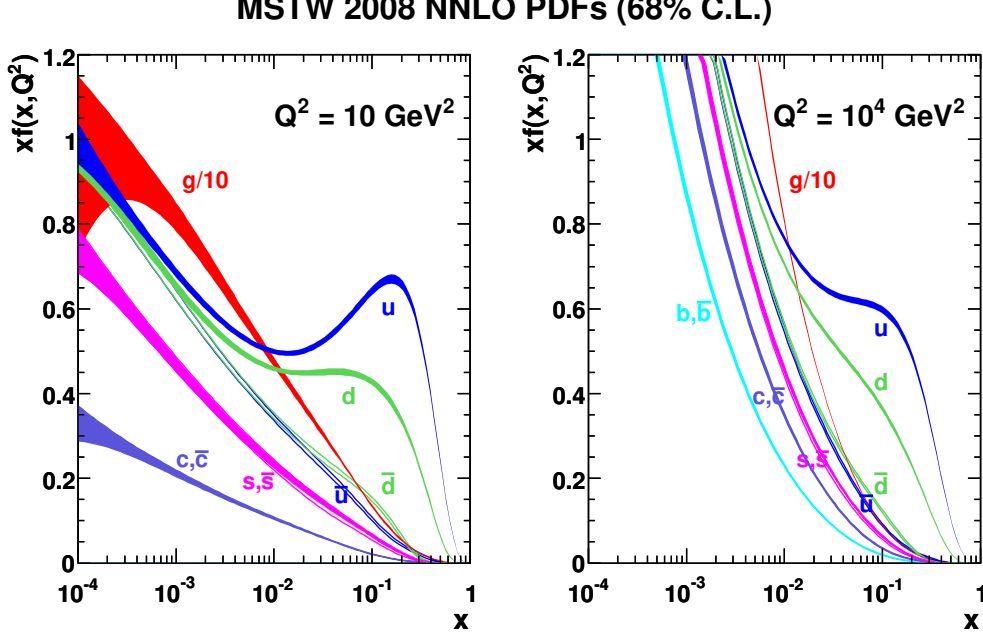


Figure 3.12: Parton distribution functions $xf(x, q^2)$ plotted against x for gluons different quark flavours at $Q^2 = 10 \text{ GeV}^2$ and $Q^2 = 10^4 \text{ GeV}^2$ using MSTW 2008 NNLO [61].

1703 the low momentum transfer of soft interactions leads to a much more dominant impact of non-perturbative QCD, which makes much more difficult to
 1704 calculate the cross-section.
 1705

1706 When two protons (A and B) collide, what actually happens is that the
 1707 partons of one proton can interact with partons of the other via a hard
 1708 scattering process. Each of the interactions between the partons pairs (let a
 1709 be a parton from A interacting with b , a parton from B) is independent from
 1710 the interactions of other partons. The remaining partons also contribute to
 1711 the final state as “underlying events”.

In a pp or, more generally, in a hadron-hadron (A and B) hard scattering process, the total cross section is given by:

$$\sigma_{AB \rightarrow X} = \sum_{a,b} \iint dx_a dx_b f_a(x_a, Q^2) f_b(x_b, Q^2) \times \hat{\sigma}_{ab \rightarrow X} \quad (3.9)$$

1712 where a and b denote the parton constituents of the hadrons A and B
 1713 respectively and $f_i(x_i, Q^2)$ their PDF. Here, the Q is chosen to be the factorisation scale (μ_F). The contribution of the individual partons a and b is
 1714 denoted by $\hat{\sigma}_{ab \rightarrow X}$. With this equation, all process in pp collisions can be
 1715 computed.
 1716

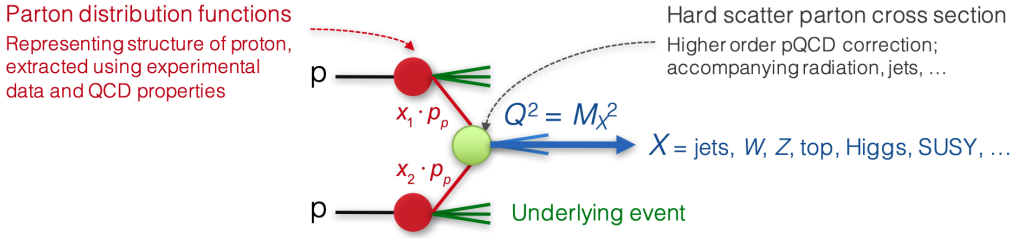


Figure 3.13: Simplified view of a pp collision [128].

Depending on the order achieved in perturbation theory (LO, NLO, NNLO, ...), the cross-section of the individual partons to give the final state of interest ($ab \rightarrow X$) is calculated as

$$\begin{aligned}\hat{\sigma}_{ab \rightarrow X} &= \sum_{i=0}^{\infty} \alpha_s^i(\mu_R) \sigma_n(x_a, x_b, \mu_F^2) \\ &= [\sigma_{LO}(x_a, x_b, \mu_F^2) + \alpha_s(\mu_R) \sigma_{NLO}(x_a, x_b, \mu_F^2) \\ &\quad + \alpha_s(\mu_R)^2 \sigma_{NNLO}(x_a, x_b, \mu_F^2) + \dots]_{ab \rightarrow X}\end{aligned}$$

where $\alpha_s^i(\mu_R)$ is the coupling constant derived for a specific renormalization scale (μ_R).

Work in progress

3.2.7.2 Underlying event

3.3 ATLAS

Installed in its experimental cavern at point 1, ATLAS is the largest detector ever constructed for a particle collider with its 46 m long and 25 m in diameter. It is designed to record events of high-energy colliding particles at high luminosities. The thousands of millions of interactions that take place at the centre of the ATLAS detector are recorded and processed by the different sub-detectors, which are composed by more than 100 million sensitive electronic channels. Each ATLAS sub-detector is sensible to a different type of particle and to different properties. Therefore, the layered structure allows for effective particle identification, as well as enables accurate measurements of energy and momentum. Figure 3.14 shows an overall layout of the ATLAS detector and identifies its different sub-detectors. In the picture can be appreciated that the cylindrical shape of ATLAS is divided into two parts: the “barrel” (curved parts) and the two “end-caps” (bases). In the barrel region, the sub-detectors are built as coaxial layers around the beam pipe (see memo 3.15). As one moves away from the axis,

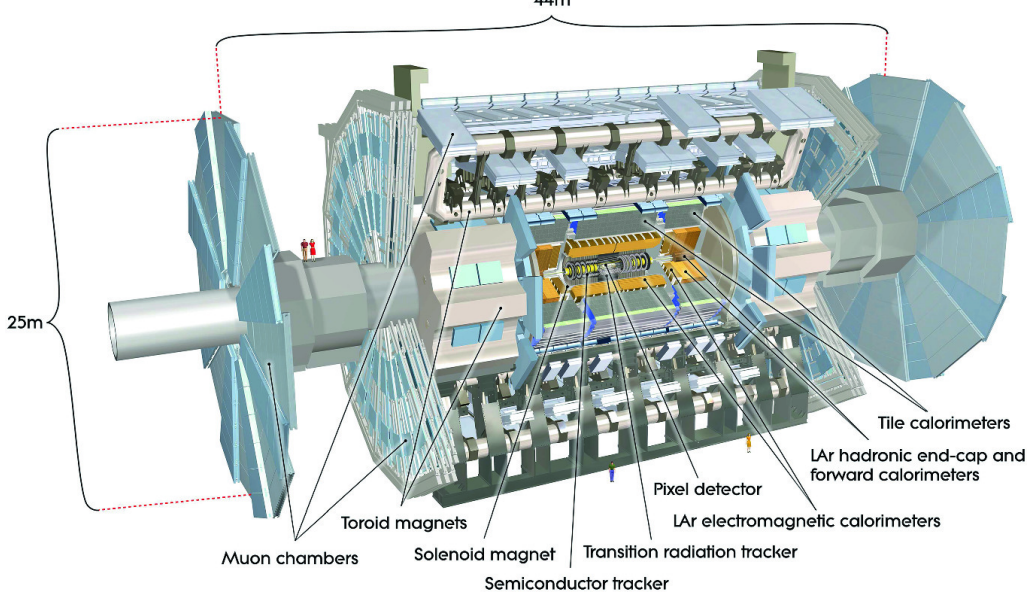


Figure 3.14: Simulated schematic view of the ATLAS detector.

1737 it finds the Inner Detector (ID), the solenoid magnet, the Electromagnetic
 1738 (ECAL) and Hadronic (HCAL) Calorimeters, and the Muon Spectrometer
 1739 (MS) in the outermost layer. The technical details of these sub-detectors
 1740 are presented in the coming sections.

1741 ATLAS is able to explore a wide range of phenomena with high pre-
 1742 cision, including new physics events. Even though it is a general-purpose
 1743 experiment, it was designed taking into account the Higgs and BSM phe-
 1744 nomena searches that were carried out at LHC. This is why, since the mass of
 1745 the Higgs was not known at that time, its performance requirements cover
 1746 a large mass range for the Higgs decay products.

1747 One of the most important milestones for ATLAS (and for all science in
 1748 the last decades) was the observation of a particle consistent with the Higgs
 1749 boson in July 2012 (see 2.2.1). In 2016, the combination of ATLAS and
 1750 CMS measurements for Higgs boson production on decay rates with Run-
 1751 1 data was published [135]. After that, the physics programme at 13 TeV
 1752 allowed precision studies of the Higgs boson and other SM particles, as well
 1753 as the search for new particles with other masses.

1754 Other relevant items in ATLAS timeline are the observation and rate
 1755 measurement of $t\bar{t}$ events [136] or the evidence for rare electroweak $W^\pm W^\pm$
 1756 production [137]. The first evidence of light-by-light scattering at high
 1757 energy was also found with ATLAS [138]. The first $t\bar{t}H$ associate production
 1758 [139] and $H \rightarrow b\bar{b}$ decays [140] were observed for first time by ATLAS too.



Figure 3.15: Due to its coaxial-layered structure ATLAS can be understood as cylindric onion: “*ATLAS have layers, onions have layers*” [134].

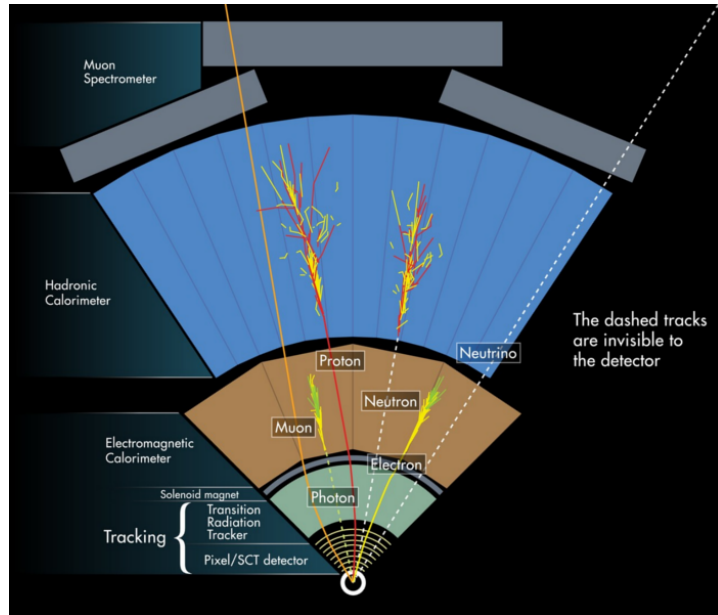


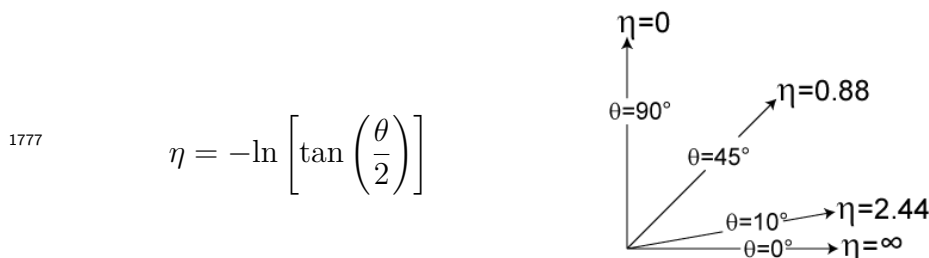
Figure 3.16: Fraction of the transversal plane of ATLAS. Each particle leaves a different signature in each layer. By signature is meant the particular distribution of energy deposition. This scheme is fundamental to understand the object reconstruction in the next chapter.

The physics programme of ATLAS include precise measurements of the SM [141], super-symmetry studies [142], sources of \mathcal{CP} -violation [143], large E_T^{miss} dark-matter searches [144], astroparticle physics [145], extra dimensions [146] and others.

ATLAS is not only a detector but also a collaboration of people composed of more than 5000 members including physicists, engineers, technicians, doctoral students and support staff. Working at CERN or at any of the 181 institutions that constitute ATLAS, the different teams work collaboratively to achieve success.

3.3.1 Coordinate system

Due to its cylindrical structure, ATLAS uses a right-handed system with its origin at the IP where the collisions take place. On one side, there are the (x, y, z) Cartesian coordinates. The x -axis is pointing towards the centre of the ring circumference, the y -axis is perpendicular to the plane defined by the LHC ring and it points to the surface, and the z -axis is defined by the direction of the beam. On the other side, it is more frequent to employ the cylindrical coordinates (r, ϕ, z) or the system defined by the azimuthal angle (ϕ) and the pseudorapidity (η):



where θ is the polar angle³. As the polar angle approaches zero, pseudorapidity tends towards infinity. The change in pseudorapidity $\Delta\eta$ is Lorentz invariant under boosts along the beam axis. The use of η is preferred over θ because the distribution of events typically looks flat with respect to η . In terms of the momentum, the above equation can be expressed as:

$$\eta = -\ln \left(\frac{|\vec{p}| + p_z}{|\vec{p}| - p_z} \right)$$

being p_z the momentum along the beam direction. The rapidity is used when dealing with massive particles and it can be expressed as $y = \frac{1}{2}\log[(E + p_z)(E - p_z)]$, being E the energy projection of the momentum in the z -axis.

³Defined as the angle between the particle three-momentum, \vec{p} and the positive direction of the beam axis.

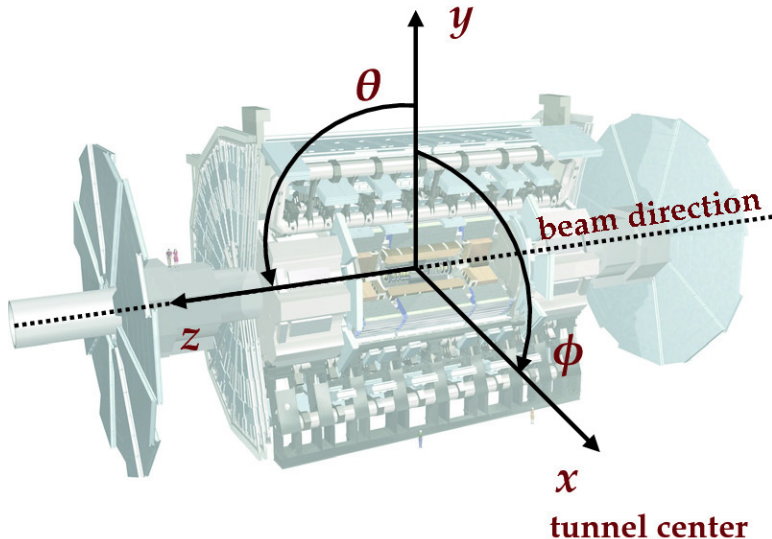


Figure 3.17: Coordinate system of the ATLAS detector.

1781 Note that when the particles approach the speed of light, they are in the
 1782 limit $E \approx |\vec{p}|$ and the values for rapidity and pseudorapidity converge. The
 1783 angular distance is measured in units of $\Delta R = \sqrt{(\Delta\eta)^2 + (\Delta\phi)^2}$, which is
 1784 invariant under a boost along the z -axis⁴. Figure 3.17 shows the coordinate
 1785 system of ATLAS for both Cartesian and cylindrical coordinates.

The transverse magnitudes such as the transverse momentum (p_T) and transverse energy (E_T) are defined in the x - y plane. Knowing the p_T , and the η and ϕ angles, the cartesian momentum (p_x, p_y, p_z) can be derived from:

$$\begin{aligned} p_x &= p_T \cos(\phi) & p_y &= p_T \sin(\phi) \\ p_z &= p_T \sinh(\phi) & |\vec{p}| &= p_T \cosh(\phi) \end{aligned}$$

1786 3.3.2 Inner Detector

1787 The ATLAS ID [147][148][113] is the closest sub-detector to the beam
 1788 pipe. Its layout is shown in Figures 3.18 and 3.19. The charged particles
 1789 follow a curved trajectory inside the ID due to the magnetic field of the
 1790 ATLAS bending magnet (see 3.3.5). The different pieces that comprise the
 1791 ID can reconstruct the traces of these particles with great accuracy allowing,
 1792 thus, to measure its momentum (this is done using the sagitta method
 1793 described in Section 5.1.1). For particles coming from the IP, the geometric
 1794 acceptance of the ID is $|\eta| < 2.5$ for pseudorapidity and full ϕ coverage in
 1795 the azimuthal angle. The ID provides p_T resolution of $\sigma_{p_T}/p_T = 0.05\%$ GeV

⁴ $\Delta\eta = \eta_2 - \eta_1$ and $\Delta\phi = \phi_2 - \phi_1$.

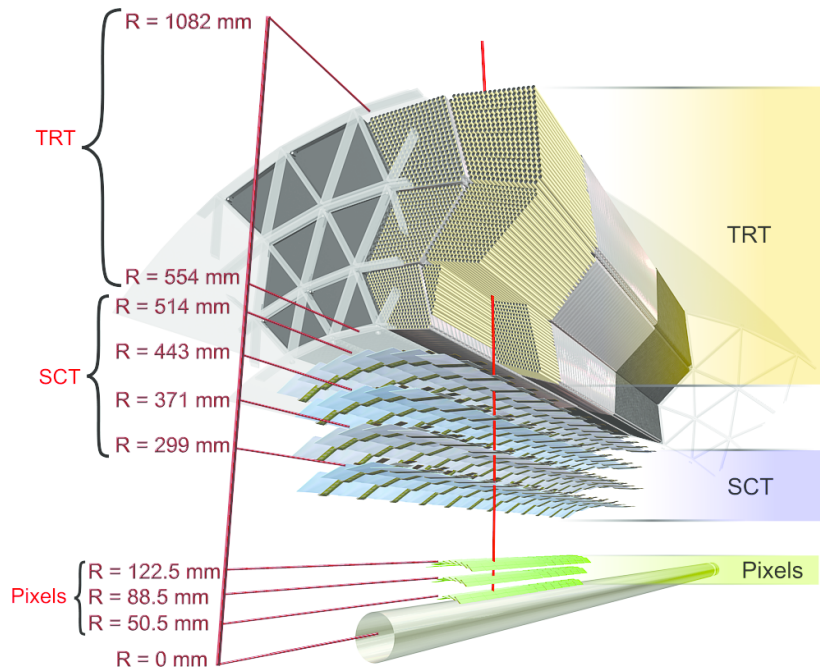


Figure 3.18: Barrel part of ID of the ATLAS experiment with the Pixel, SCT and TRT sub-detectors. The IBL is not shown here.

1796 $\oplus 1\%$ and a transverse impact parameter resolution⁵ of $10 \mu\text{m}$ for particles in
 1797 the central η region. It is designed to provide excellent momentum reso-
 1798 lution, pattern recognition and measurements of both primary and secondary
 1799 vertex for charged particles above the p_T threshold (nominally 0.5 GeV).

1800 The ID is composed of four complementary sub-detectors: The Insert-
 1801 able B-Layer (IBL), the Pixel Detector, the Semiconductor Tracker (SCT)
 1802 and the Transition Radiation Tracker (TRT). In the sections that follow, a
 1803 description of each sub-system is provided.

1804 Depending on the η that a particle has, it will interact with some ele-
 1805 ments of the detector. Figure 3.19 shows the end-cap elements transversed
 1806 by two charged particles with $\eta = 2.2$ and 1.4 . The track with $\eta = 1.4$
 1807 traverses first the beryllium beam-pipe, then the three cylindrical silicon
 1808 pixels and the four disks with double layers of the SCT. Finally, this particle
 1809 travels across approximately 40 tubes in the TRT wheels. In contrast, the
 1810 particle with $\eta = 2.2$ encounter the first of the cylindrical silicon-pixel layers
 1811 after leaving the beryllium pipe. Then, the two end-cap pixel disks and the
 1812 four last disks of the end-cap SCT.

⁵The impact parameter determine the distance of a reconstructed track from a charged particle to the perigee (the closest point of the track to the global z -axis)

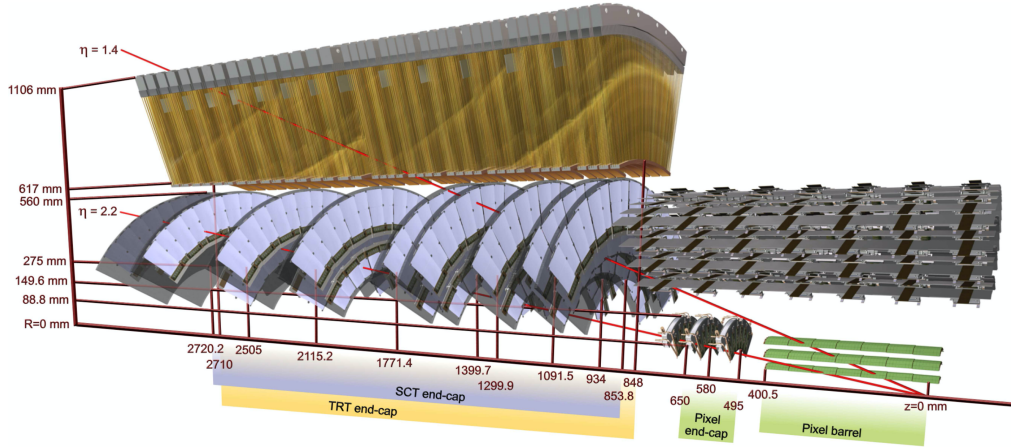


Figure 3.19: End-cap of the ID.

1813 Silicon semiconductors

1814 When a charged particle traverses a doped silicon semiconductor, it creates
 1815 a pair electron-hole by ionisation. An electric field is applied to the active
 1816 part of the detector module so that the electron drifts in oposite direction
 1817 of the electric field and the hole in the field direction. Then, both charges
 1818 are collected by the p-n junctions. The silicon sensors can be shaped either
 1819 as pixels, providing precies 2D space point, or as strips, giving a single
 1820 dimension positioning. On the order of 10^5 electron-hole pairs are liberated
 1821 when a particle crosses the silicon wafer and, with appropriate electronics,
 1822 a clear signal is obtained in the pixel or strip in which the charged was
 1823 collected.

1824 3.3.2.1 Insertable B-Layer

1825 The IBL [149] is the innermost component of the ID. It is located
 1826 between the beam pipe and the pixel detector. Added after Run-1, it
 1827 provides the closest-to-IP measurements. This improves the robustness and
 1828 performance of the ATLAS tracking system. It plays a fundamental role
 1829 for b -tagging efficiency because this tagging relies on precise vertex recon-
 1830 struction. The IBL provides redundancy in the measurements of tracks in
 1831 order to control the fake rate arising from random combinations of clusters
 1832 in events with a high pile-up background.

1833 With a hit resolution of $8 \mu\text{m}$ in $r-\phi$ and $40 \mu\text{m}$ along z , the IBL covers
 1834 the $|\eta| < 2.7$ and the entire ϕ range.

1835 The barrel structure if the IBL has a radius of 3.2 cm and is composed
 1836 by 14 carbon fibre staves as it is shown in Figure 3.20. Each stave has

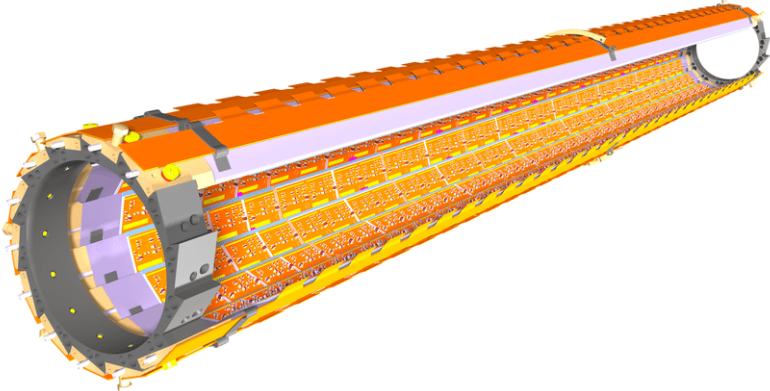


Figure 3.20: Schematic drawing of the ATLAS IBL Detector [149].

1837 incorporated cooling CO₂ circuits, has 32 or 16 modules and uses two types
1838 of photodetectors: ATLAS pixel planar sensors and 3D pixel sensors. The
1839 used pixels have a size of $50 \times 400 \mu\text{m}^2$. Due to the high luminosity of the
1840 LHC, the IBL is built with radiation-tolerant sensors.

1841 3.3.2.2 Pixel Detector

1842 The ATLAS Pixel Detector [150] consists of a strip detector in the out-
1843 ermost layers and a pixel detector in the region which is closer to the IBL.
1844 Along with the IBL, it aims to reconstruct the trajectories of the particles
1845 traversing it. It provides a full coverage of the azimuthal angle ϕ and a
1846 pseudorapidity range of $|\eta| < 2.5$ as well as a resolution of $10 \mu\text{m}$ in $r\text{-}\phi$ and
1847 $115 \mu\text{m}$ in the z .

1848 The Pixel Detector and the IBL combined contain 92×10^6 pixels with its
1849 respective electronic channels, which cover an area of approximately 1.9 m^2
1850 of silicon consuming 15 kW. The barrel region consists of four concentric
1851 layers equipped with 1736 sensor modules and each of the two end-caps
1852 has three disks with 2888 modules [151]. Figure 3.22 shows the assembly
1853 view and cross section of a module of the ATLAS ID Pixel Detector. Each
1854 of these modules consists on a silicon pixel sensor bonded to the front-end
1855 electronic chips.

1856 Hits in a pixel are read out if the signal exceeds a tunable threshold. The
1857 pulse height is measured using the Time-over-Threshold (ToT) technique.

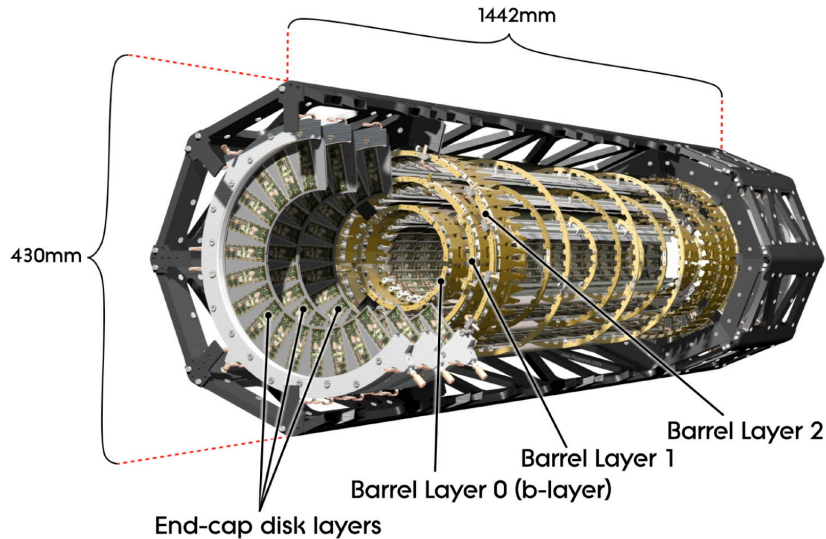


Figure 3.21: Schematic view of the ATLAS pixel detector consisting of individual barrel and end-cap layers [113].

1858 3.3.2.3 Semiconductor Tracker

1859 The SCT consists of 4088 modules tiling four coaxial cylindrical layers
 1860 in the barrel region and two end-caps each containing nine disk layers, all
 1861 of this surrounding the Pixel Detector and providing additional precision
 1862 tracking. The main difference with the Pixel Detector is that the SCT uses
 1863 microstrip sensor technology, which is very similar to that of a pixel but
 1864 being much larger (6 cm). The reason to use microstrips instead of pixels
 1865 is that the strips are more cost-effective than traditional pixels and a good
 1866 spatial resolution can be obtained as well if the strips are arranged with an
 1867 angular offset. Therefore, each SCT detector unit consists on two back-to-
 1868 back silicon-microstrip planes with a relative angle of 40 mrad. Eight strip
 1869 layers (i.e. four space points) are crossed by each track in the SCT providing
 1870 valuable tracking information with resolution of $17 \mu\text{m}$ in $r\phi$ and $580 \mu\text{m}$
 1871 in the z coordinate. The SCT covers the entire ϕ range and up to 2.5 in η .

1872 Figure 3.23 shows an exploded view of the different components of an
 1873 SCT module, including the high thermal conductivity spine, the polyimide
 1874 hybrids and readout chips.

1875 3.3.2.4 Transition Radiation Tracker

1876 The TRT is used in conjunction with the Pixel Detector and silicon micro
 1877 strip (SCT) to extend the η range in which the tracks can be reconstructed to
 1878 $|\eta| = 2$. This part of the ID is formed by a large number of 4 mm straw tubes

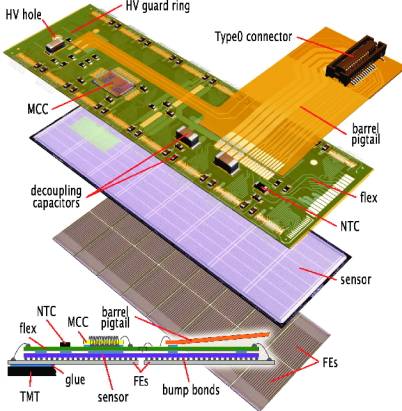


Figure 3.22: Pixel Detector module [150].

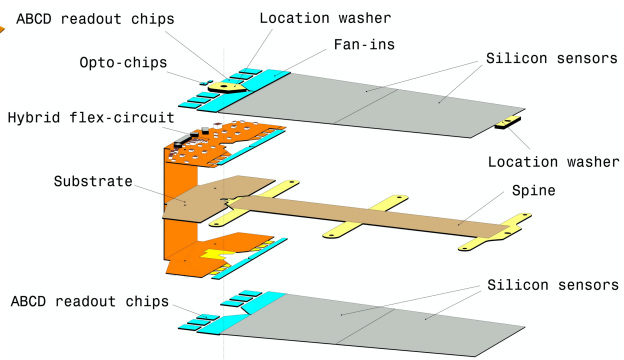


Figure 3.23: SCT detector module [113].

1879 filled with gas. This part of the ID relies both on the collection of primary
 1880 ionisation charge and the collection of secondary ionisation charge arising
 1881 from the transition radiation to measure the track of charged particles. The
 1882 tube surface functions as a cathode while the wire in the center as a cathode.
 1883 When a charged particle passes through the gas in the tube, it ionises the
 1884 gas and the freed electrons drift towards the anode, generating an electrical
 1885 current. This detector provides a single hit resolution of $170\ \mu\text{m}$ in $r\text{-}\phi$
 1886 but does not have sensitivity in z . The TRT also provides discrimination
 1887 between electrons and pions since the latter generate a much smaller signal
 1888 than the former. When the electrons pass, they produce x-ray photons that
 1889 lead to strong avalanches within the tubes and, thus, a great signal.

1890 3.3.3 Calorimeters

1891 After the ID, the next layer of detectors in ATLAS correspond to the
 1892 calorimeters (Figure 3.24) [152]. Their purpose is to measure the energy
 1893 of the particles (neutral or charged), as well as to help to reconstruct the
 1894 path followed by them. Most particles initiate a shower (Section 3.3.3.1)
 1895 when they enter into the calorimeter. Part of the energy of these particles is
 1896 deposited in the device, then collected and measured by it. Most of calorim-
 1897 eters in particle physics are segmented transversely to provide information
 1898 about the direction of the particles. Based on how the particle shower devel-
 1899 ops, the longitudinal segmentation can provide information for identifying
 1900 the particle (a more detailed discussion of how particles are reconstructed
 1901 within the ATLAS detector is presented in Chapter 5).

1902 In general, calorimeters can be classified as sampling, when are made of
 1903 two types of materials, or homogeneous, built with just one type of material.

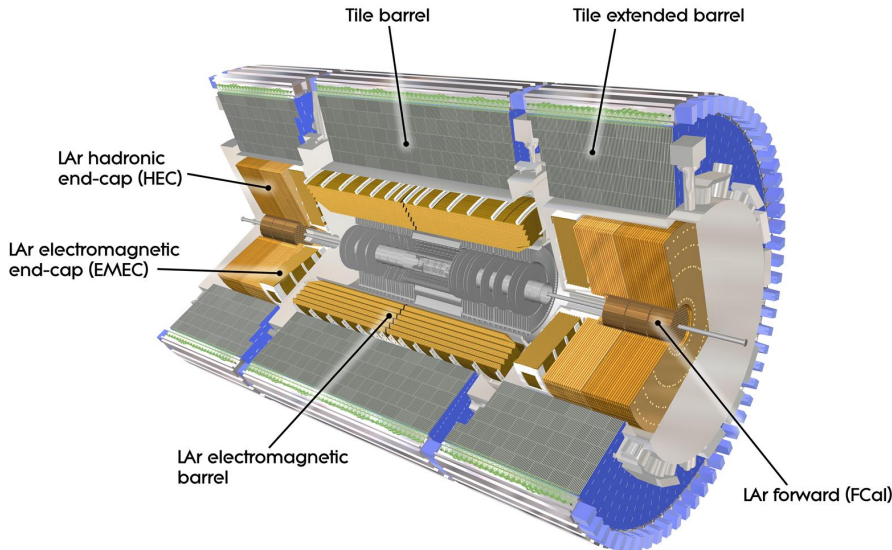


Figure 3.24: Computer generated image of the ATLAS calorimeter [151].

1904 ATLAS uses sampling calorimeters, which consist of alternating layers of
 1905 different materials:

- 1906 • **Passive material:** Also known as absorber, it is a denser material to
 1907 full stop the traversing particles. When a particle interacts with the
 1908 passive material it produces the shower (Figures 3.25 and 3.26). For
 1909 the absorber layers in ATLAS, lead is used for the ECAL and steel
 1910 for the HCAL.
- 1911 • **Active material:** This material detects the particles from the shower
 1912 originated in the absorber. The liquid Argon (LAr) is used as active
 1913 material for ECAL and plastic scintillator for HCAL.

1914 In the homogeneous calorimeters, the material used combines the features
 1915 of an absorber and a detector, performing both tasks.

1916 Since each type of particle interacts differently, there are two main types
 1917 of calorimeters: the electromagnetic calorimeter (ECAL), which measures
 1918 the energy of electrons/positrons and photons, and the hadronic calorim-
 1919 eters (HCAL), which registers the energy of the strongly-interacting particles.
 1920 Both classes are covered in the next sections.

1921 **Scintillator**

1922 The particles from the shower leave some of the molecules of the plastic

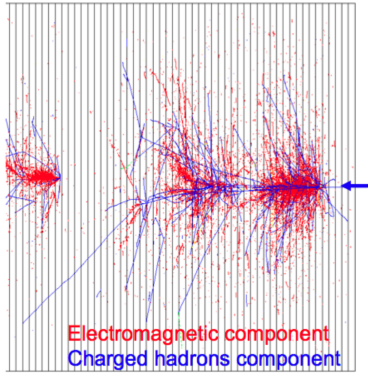


Figure 3.25: EM and hadronic cascades.

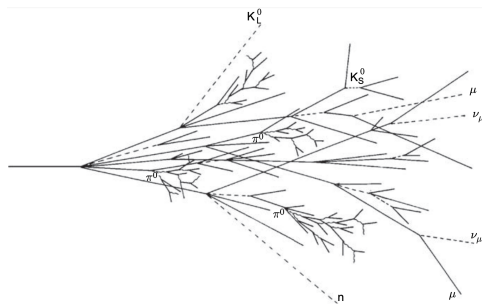


Figure 3.26: Sketch of a hadronic cascade [153].

1923 scintillator in an excited state. The subsequent decay of these molecules
1924 produces the emission of photons in the ultraviolet energy region. This
1925 light is collected by photomultiplier tubes at the edge of the tiles
1926 and converted into a current pulse whose amplitude is proportional to the
1927 energy deposited by transversing particle.

1928 3.3.3.1 Particle showering

1929 A particle shower is a cascade of secondary particles produced when
1930 a high-energy particle interacts with matter. The first particle interacts
1931 with the passive material producing a secondary particle with less energy
1932 than the first one. The second particle does the same and, in each step,
1933 the particles produced are less and less energetic. For a single incoming
1934 particle, this iterative process can continue for thousands of periods [153].
1935 An illustration of the EM and hadronic particle cascades is shown in Figure
1936 3.25.

1937 Electromagnetic shower

1938 The electromagnetic (EM) shower is initiated by a e^- , e^+ or γ , these
1939 three particles are the sole components of this type of shower. At energies
1940 higher than 100 MeV, the EM showering is based on two main processes:
1941 Bremsstrahlung and pair creation. The electrons lose their energy almost
1942 exclusively by bremsstrahlung radiation, a process in which the lepton ra-
1943 diates thousands of soft photons because of its interaction with another
1944 charged particle. The photons lose their energy by the production of an
1945 $e^- - e^+$ pair. At lower energy scales, other processes contribute. In the MeV

range, the Compton scattering⁶ and photoelectric effect⁷ are the dominant interactions for energy loss for photons, while the ionisation and excitation are for the charged particles (e^- and e^+).

Hadronic shower

When a hadron interacts with the passive material, this shower is initialised. Both strong and EM interactions are involved in the development of this type of shower and they present a larger variety of particle components. Therefore, the hadronic showers are significantly more complex than the EM. Figure 3.26 shows the processes leading to a hadronic cascade.

The production of neutral pions represents about a third of the energy loss of hadronic interactions. These pions decay 98.8% of times to two photons [154] that are starting the EM showers. The rest of hadronic interactions consist of the production of charged mesons, nuclear fragments and protons, soft neutrons and photons or unpredictable loss through undetectable processes.

3.3.3.2 Electromagnetic calorimeter

The ECAL [152] absorbs the energy of the e^- , e^+ or a γ covering a pseudorapidity range of $|\eta| < 1.475$ in the barrel. It is made of a lead absorber and LAr detector following an accordion shape, as can be seen in Figure 3.27a, where the different layers are clearly visible. The shower originated at the absorber layer ionise the LAr producing a measurable current proportional to the energy of the original particle. The LAr layer operates at 87 K.

The barrel part is split into two identical half-barrels separated by a small gap at $z = 0$. Each end-cap calorimeter is composed of two coaxial wheels that cover $|\eta| < 1.475$.

The total amount of material in the ECAL corresponds to 25-35 radiation lengths, X_0 , and 2-4 nuclear interaction lengths, λ , over the entire η range. Characteristic of each material, the ration length is the mean distance over which a high-energy electron lose all but $1/e$ of its energy by bremsstrahlung. The radiation length is the mean free path between interactions required to reduce the number of relativistic charged particles by the factor $1/e = 0.37$ as they pass through matter.

⁶Scattering of a photon after interacting with a charged particle, usually an electron.

⁷Emission of photoelectrons when the EM radiation interacts with matter.

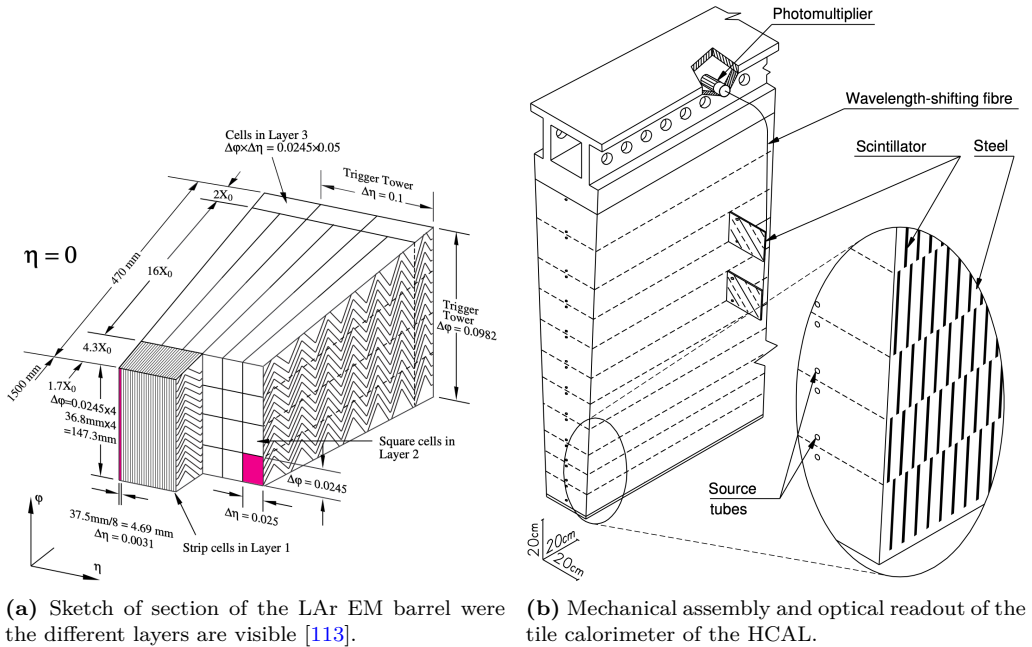


Figure 3.27: Sketch of a section of the ATLAS (a) ECAL and (b) HCAL [113].

The energy resolution of a calorimeter can be parametrised as:

$$\frac{\sigma_E}{E} = \frac{a}{\sqrt{e}} \oplus \frac{b}{E} \oplus c = \frac{10\%}{\sqrt{e}} \oplus \frac{170 \text{ MeV}}{E} \oplus 0.7\%$$

1979 Where a is the stochastic term, b the electronic noise and c a constant that
1980 includes detector instabilities and increases with E [155].

1981 **3.3.3.3 Hadronic calorimeter**

1982 The ATLAS HCAL [152] is made of a sampling calorimeter of steel and
1983 plastic scintillator tiles covering the pseudorapidity region of $|\eta| < 1.7$ in
1984 the barrels. The end-caps are made of copper and LAr, covering $1.5 < |\eta| <$
1985 3.2, and are emended in the end-caps of the ECAL. This calorimeter uses
1986 9800 electronic channels in the barrel and 5600 in the end-cap. With 2900
1987 tones, the HCAL is the heaviest part of the ATLAS detector. It has 420000
1988 scintillator tiles and 9500 photomultiplier tubes [151]. All these elements are
1989 shown in Figure 3.27b, where the tiles, the fibres and the photomultipliers
1990 are visible.

The contribution of the electronic noise is negligible, therefore, the energy resolution for the tile calorimeter is [152]:

$$\frac{\sigma_E}{E} = \frac{5.9\%}{\sqrt{e}} \oplus 5.7\%$$

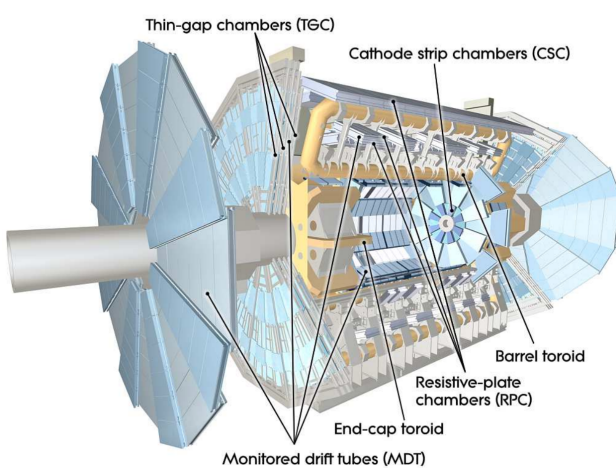


Figure 3.28: Conceptual layout of the MS (blue). The magnet system (yellow) is also shown [113].

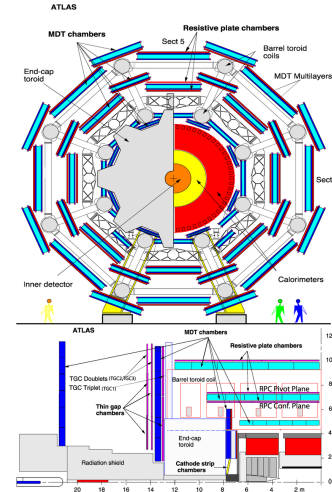


Figure 3.29: ATLAS Muon detectors.

1991 3.3.3.4 Forward calorimeter

1992 In addition to the ECAL and HCAL, a smaller calorimeter is placed
 1993 in the end-caps surrounding the beam pipe in order to cover the forward
 1994 region ($3.1 < |\eta| < 4.9$), the forward calorimeter (FCAL). This coverage is
 1995 required for many physics tasks such as the reconstruction of the E_T^{miss} of
 1996 the forward-jet tagging.

1997 This calorimeter is a sampling calorimeter based on LAr as active medium
 1998 and copper as absorber. The thickness of the FCAL is optimised to
 1999 achieve high absorption, approximately, $10 X_0$ [155].

This detector has a resolution of:

$$\frac{\sigma_E}{E} = \frac{100\%}{\sqrt{e}} \oplus 10\%$$

2000 3.3.4 Muon Spectrometer

2001 The muons can penetrate through calorimeters and reach the last layer
 2002 of the ATLAS detector, the MS [156]. Figure 3.28 shows a schematic cut-
 2003 away view of the ATLAS muon system.

2004 The MS surrounds the calorimeters and its aim is to measure the trajectories
 2005 of muons to determine their direction and momentum with excellent
 2006 tracking precision as well as their electric charge in a pseudorapidity cover-
 2007 age of $|\eta| < 2.7$. To bend the particle tracks after they exit the HCAL, the
 2008 MS uses eight large superconducting air-core toroid magnets in $|\eta| < 1.4$

Type	Purpose	Location	Coverage
MDT	Tracking	Barrel + end-cap	$0.0 < \eta < 2.7$
CSC	Tracking	End-cap layer 1	$2.0 < \eta < 2.7$
RPC	Trigger	Barrel	$0.0 < \eta < 1.0$
TGC	Trigger	End-cap	$1.0 < \eta < 2.4$

Table 3.3: ATLAS MS sub-detectors [157].

region. For the $1.6 < |\eta| < 2.7$, the tracks are bent by magnets inserted in the end-caps. In the transition region, $1.4 < |\eta| < 1.6$, the magnetic field responsible of bending the particles is provided by both the air-core toroid magnets and the smaller end-cap magnets. These fields are perpendicular to the trajectory of the muons originated in the IP. More details about the magnet systems of the MS can be found in Section 3.3.5.

The MS instrumentation is based, on one hand, on precision chambers for the coordinate measurements in the bending plane: Monitored Drift Tube chambers (MDT) and Cathode-Strip Chambers (CSC), and, on the other hand, on trigger chambers: Resistive Plate Chambers (RPC) and Thin Gap Chambers (TGC). Table 3.3 gives a summary of the MS detector components. In Figure 3.29 the distribution of the MS detectors is described.

- **Monitored Drift Tube chambers (MDTs)** [158]: The MDT chambers provide precise momentum measurements by determining with high accuracy the curve of the tracks. This part of the MS cover a pseudorapidity range of $|\eta| < 2$. The MDTs are designed to have stand-alone measurement capability in order to safeguard against any unanticipated background and to ensure good discovery potential in the scenario of unexpected topologies. In the barrel region, the MDTs are arranged in three cylindrical stations coaxial to the beam axis and in the end-cal, the MDTs are vertically installed in three layers. An MTD chamber consists of six layers of drift tubes (as depicted in Figure 3.30), each of them with 3 cm of diameter, filled with gas. A tube can achieve a single wire resolution of 80 μm [157]. In the entire MDT system, there are 1 171 chambers with a total of 354 240 tubes.
- **Cathode-Strip Chambers (CSC)**: It is the innermost tracking layer of the MS. Due to its higher rate capability and time resolution, it is located close to the beam axis, where the particle fluxes are higher. This component of the muon detector system covers the η range $2.0 < |\eta| < 2.7$. It measures with precision the coordinates at

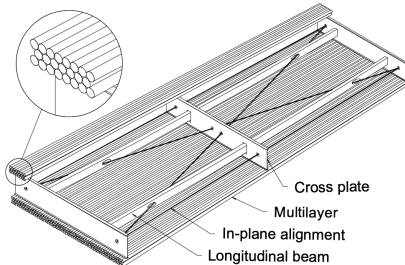


Figure 3.30: Schematic view of an MDT chamber.

the ends of the detector. With its 70 000 electric channel, provides a resolution around 60 μm .

- **Resistive Plate Chambers (RPC)** [159]: This is the barrel element of the trigger system. These chambers are located on both sides of the central CSC and inside the outermost CSC station. The RPCs are gaseous detectors used for triggering and for measuring the second coordinate in the barrel region. RCPs provide a time-space resolution of 1 cm \times 1 ns. The gas gap is of the order of 2 mm and the plate external surfaces are coated by thin layers of graphite painting. This part of the MS is composed of 3 800 electric channels.
- **Thin Gap Chambers (TGC)** [160]: As a first-level trigger, they have to provide high efficiency and excellent time resolution for bunch-crossing tagging in a high-background environment. The particle flux received by the TCG is higher than that of the RPC. The three TGCs are located near the middle end-cap MDT station, in the forward regions. TGCs measure the second coordinate in the non-bending direction with its circa 440 000 electrical channels.

3.3.5 Magnet system

The curvature in the track of the particles is fundamental to measure the transverse momentum and the charge of the particles. To bend the path of charged particles, these are immersed in a homogeneous magnetic field which is produced by the both the toroidal and solenoid magnets. The bending power is proportional to $\int B dl$, where B is the magnetic field component orthogonal to the charged direction.

ATLAS magnetic system is divided into three subsystems: the central solenoid magnet, the barrel toroids (BT) and the end-cap toroid (ECT).

2066 **3.3.5.1 Central solenoid magnet**

2067 The ATLAS solenoid surrounds the ID providing a 2 T magnetic at
2068 the centre of the tracking volume. This magnet is very thin, having only
2069 4.5 cm thickness, which minimises the interaction of the particles with the
2070 magnet material. It is important to not use a lot of material here because,
2071 otherwise, the interaction of the particles with the solenoid magnet would
2072 impact negatively in the performance of the calorimeters. To achieve such
2073 a field within a small thickness, 9 km of niobium-titanium superconductor
2074 wires into strengthened, pure aluminium strips and cooled down to 4.5 K are
2075 used. The central solenoid magnet has a cylindrical shape with a diameter
2076 of 5.6 m and a length of 2.56 m, and it weights 5 tonnes.

2077 **3.3.5.2 Toroid magnets**

2078 Three large air-core toroids (one barrel and two end-caps) generate the
2079 magnetic field in the MS. Each toroid consists of eight coils assembled with
2080 cylindrical symmetry (see the yellow elements in Figure 3.28). The coils are
2081 based on an aluminium stabilised Niobium-Titanium alloy (Al/NbTi/Cu)
2082 superconductor operating at 4.5 K. The main difference between the barrel
2083 and end-cap toroids for the cold mass is that the latter has a higher critical
2084 current and less aluminium than the former [161].

2085 **Barrel Toroid**

2086 The Barrel Toroid magnet is the largest component of the ATLAS magnet
2087 system. It generates a toroidal magnetic field which, as introduced in Sec-
2088 tion 3.3.4, is almost completely perpendicular to the track of the particles.
2089 In order to minimise the impact (i.e. reduce any interaction apart from
2090 applying magnetic field) of the magnet system with the particles, the barrel
2091 toroid is designed as an open and light structure. The barrel toroid coils
2092 are housed in eight individual cryostats, with the linking elements between
2093 them providing the overall mechanical stability. A view of the coils of the
2094 barrel toroid in their cryostats is in Figure 3.31.

2095 The magnetic flux density delivered by this magnet is 3.9 T on the su-
2096 perconductor. For the toroid barrel, the bending power ($\int B dl$) is in the
2097 interval 1.5 Tm to 5.5 Tm in $0 < |\eta| < 1.4$. It is the largest toroidal magnet
2098 ever built (25.3 m in length), being probably the most iconic and character-
2099 istic element of ATLAS. It weights 830 tonnes and uses more than 56 km of
2100 superconducting wire [151].

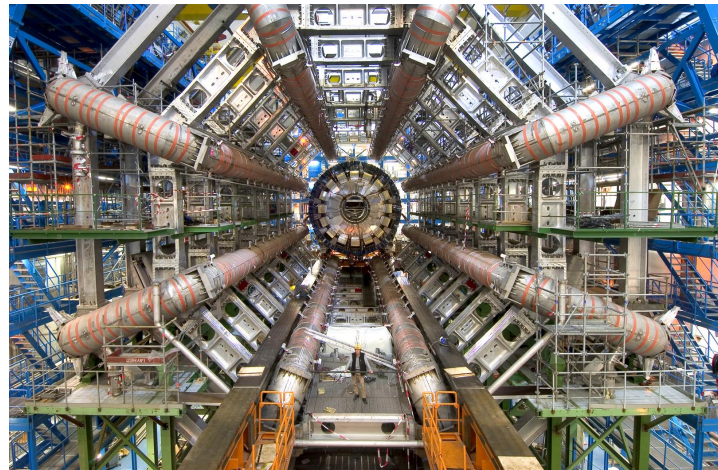


Figure 3.31: Very cool picture of the installation ATLAS calorimeters. The eight coils that compose the ATLAS barrel toroid magnets are already installed in the cryostats. Thus view is one of the most iconic of the ATLAS detector.

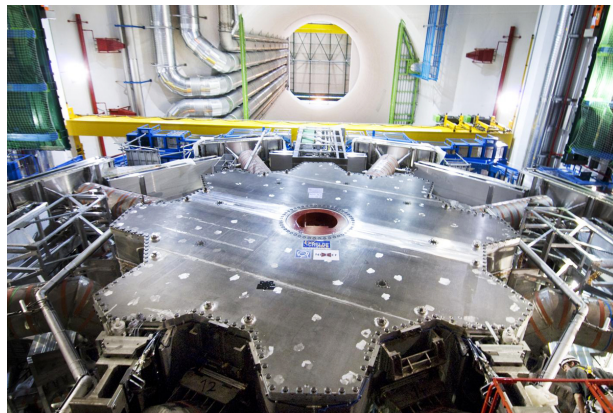


Figure 3.32: One of the two end-cap toroidal magnets. Each is made by eight superconducting coils with a magnetic field peaking at 4.1 T.

2101 **End-cap Toroid**

2102 The end-caps extend the magnetic field of the barrel toroid to the beam pipe.
 2103 These magnets are constrained by the inner radius of the barrel toroid and
 2104 the axial length of the experiment.

2105 As well as in the barrel toroid, it has a 4.1 T magnetic field on the
 2106 superconductor. For the end-cap toroid, the $\int B dl \in [4, 8]$ Tm in the
 2107 pseudorapidity range $1.6 < |\eta| < 2.7$ [161]. In the transition region where
 2108 the end-cap and barrel toroids overlap ($1.4 < |\eta| < 1.6$), the bending power
 2109 is lower. Each end-cap magnet (Figure 3.32) has a diameter 10.7 m and
 2110 weights 240 tonnes [151].

2111 **3.3.6 Trigger and Data Acquisition System**

2112 The proton bunches cross at the center of the ATLAS detector 40 million
2113 times per second, resulting in approximately (using Run-2 mean pile-up
2114 $\langle\mu\rangle = 33.7$) 1 200 million proton collisions per second. Reading out and
2115 storing all the information from this interactions is not feasible since it has a
2116 combined data volume of more than 60 million megabytes per second. Only
2117 some of these events are of interest to physics studies and, consequently,
2118 only this subset need to be saved into permanent storage for later analysis.
2119 In order to select only interesting data, ATLAS uses a complex and highly
2120 distributed Trigger and Data Acquisition System (TDAQ) [162] that reduces
2121 the rate of recorded data from the initial 1 200 MHz of interactions to just
2122 an average of 1 kHz. The reduction through the trigger is carried in two
2123 steps: The electronic performs an initial selection and, afterwards, a large
2124 computer farm analyses the data that pass the initial filter.

2125 The TDAQ system is an essential component of ATLAS in charge of
2126 processing the events online, selecting the relevant ones and storing them.
2127 To do so, the TDAQ verifies for each bunch crossing if at least one among the
2128 hundred conditions is satisfied. These conditions, also known as “triggers”,
2129 are based on identifying both combinations of candidate physics objects
2130 (“signatures”) and global properties of the events [163]. Figure 3.33 shows
2131 a diagram of the TDAQ system, in this figure can be seen the different
2132 components as well as the detector read-out and data flow.

2133 The first-level trigger (LVL1) is a hardware-based filter performed by
2134 ATLAS sub-detectors. The LVL1 uses the information of the Calorimeters
2135 and the MS to select events up to the maximum-readout rate of the detector
2136 (100 kHz) within a latency of $2.5 \mu\text{s}$. Additionally, the LVL1 identify the
2137 regions of interest (RoI), which includes the position and the p_T of the
2138 candidate objects.

2139 For each event accepted by the LVL1, the Front-End (FE) detector elec-
2140 tronics read the detectors data and pass it to the ReadOut Drivers (ROD).
2141 The ROD performs the initial processing and formatting and the ReadOut
2142 Systems (ROS) buffers this data.

2143 The data from the different sub-detectors is sent from the ROS to the
2144 software-based trigger, the so called “High Level Trigger” (HLT), when is
2145 requested by the HLT. This system is comprised by the second-level trig-
2146 ger (LVL2) and the Event Filter (EF or third-level), both made of several
2147 farms of computers (about 40 000 CPU cores) interconnected by Ethernet
2148 networks. Using modest computing power, LVL2 provides high rejection
2149 power with fast and limited precision algorithms. With higher computing
2150 power, the EF features lower rejection power with slower but higher preci-

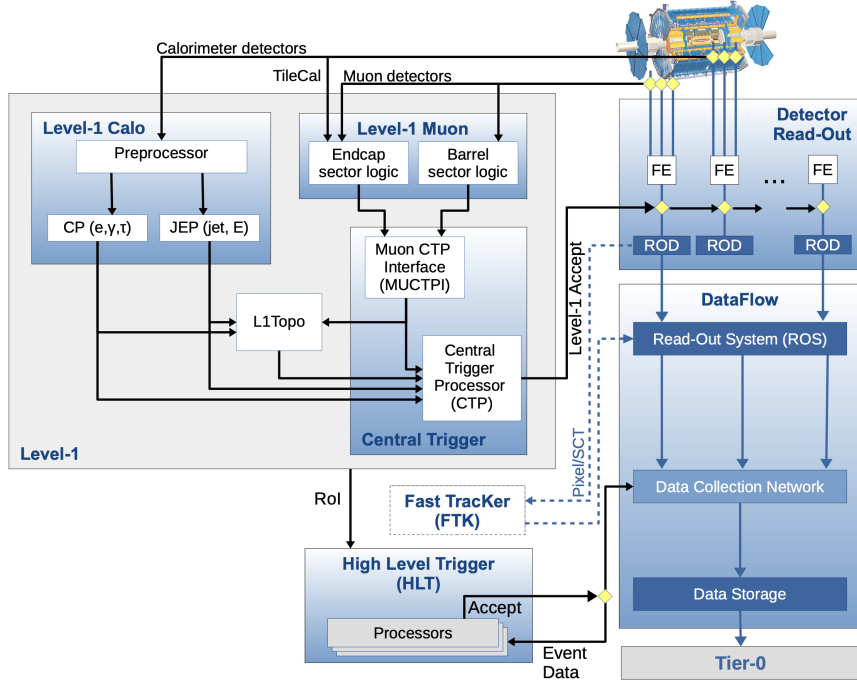


Figure 3.33: The ATLAS TDAQ system in Run-2.

sion algorithms [162]. This combination is a cost-effective and flexible way of implementing the HLT. The ID, which was not used by the LVL1, is of key importance for the HLT because on, one hand, the LVL2 reconstruction algorithms are specifically designed to meet strict timing requirements and, on the other hand, the track reconstruction on the EF is less time constrained. This is done by the ID's Fast TracKer (FTK) as the Figure 3.33 shows.

An average 1.2 kHz output rare for Run-2 pass the HLT (with a latency of just $200\ \mu\text{s}$) and is sent by the Sub-Farm Output (SFO) to the Tier-0 facilities for permanent storage and later offline physics analysis. It is important to highlight that the decisions performed by trigger about whether or not to store an event are irrevocable. If an event does not pass the trigger requirements, it is not stored.

2164 3.4 Alignment of the inner detector

2165 A fundamental part for the correct operation of the ATLAS detector
 2166 is its alignment [164]. The goal of the detector alignment is to determine
 2167 the detector geometry as accurately as possible in order to correct the ef-
 2168 fects of the time-dependent displacements. In this section, the need of an

2169 adequate alignment is motivated, its principles discussed and my contribu-
2170 tions presented.

2171 As commented in Section 3.3.2, the ID is used to reconstruct the trajec-
2172 tories of the charged particles by combining into tracks the energy deposits
2173 (hits) of the particles as well as identifying primary and secondary vertices.
2174 These functionalities are essential for some tasks such as the lepton recon-
2175 struction or the b -jet tagging.

2176 To be able to have proper tracking, the full resolution of the ID has to be
2177 exploited and to do so it is crucial to know the geometry of the detector, i.e.
2178 the location and orientation of each of its elements. Due to several factors
2179 such as thermal expansion/contraction, the detector is constantly experien-
2180 cing small movements that affect to its geometry. With the alignment it is
2181 possible to account online for this displacements, re-calibrate and correct
2182 its effects. The alignment algorithm's accuracy is such that the position of
2183 the various detector parts may be established with a few microns of accu-
2184 racy [87]. This accuracy is superior to that attained by directly measuring
2185 the module placements. Any missalignment of the different elements of the
2186 ID will degrade the quality of the track reconstruction, which is vital to
2187 perform any physics analysis. During the development of this thesis, I have
2188 contributed to the alignment of the ID through the refurbishment of the soft-
2189 ware package for monitoring the track-based ID alignment results obtained
2190 at the calibration loop and show them as a web-based service.

2191 **3.4.0.1 Local coordinate frame**

2192 In Section 3.3.1 the global (x , y , z) Cartesian coordinate system of AT-
2193 LAS was introduced. The local coordinate frame of an individual sensor of
2194 the detector (x' , y' , z') is also a Cartesian system. The local system is a
2195 right-handed frame with the origin placed at the geometrical centre of the
2196 module. According to the convention, the x' -axis and y' -axis are within the
2197 plane of the component and the z' -axis points outside of this plane. The
2198 x' -axis points to the most sensitive direction of the module. For the Pixel
2199 and IBL modules this is the shorter pitch side and, for the SCT, the perpen-
2200 dicular to the strip orientation. In the case of the TRT the y' -axis points
2201 along the wire while the x' -axis remains perpendicular to both the wire and
2202 the radial direction. The local coordinates are represented schematically in
2203 Figure 3.34.

2204 The hits are reconstructed in the local coordinate frame of the different
2205 modules.

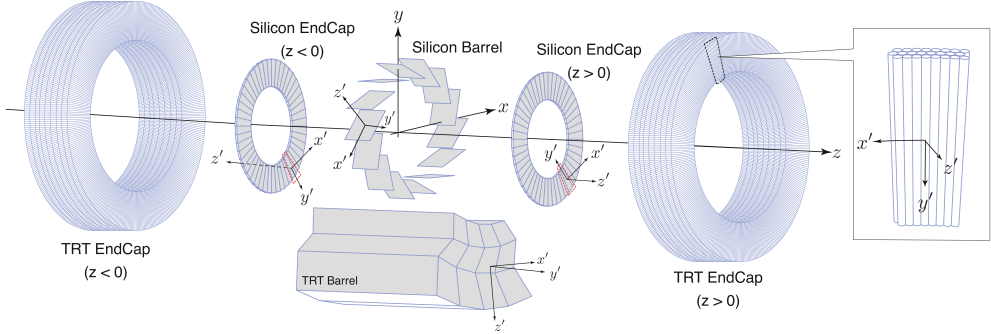


Figure 3.34: Schematic representation of the ATLAS global (x , y , z) and local (x' , y' , z') reference frames [164]. The local coordinates are shown for the Pixel, IBL, SCT and TRT.

2206 3.4.0.2 Track parameters

2207 The trajectory followed by a charged particle within a magnetic field
 2208 B is an helix that can be fully parametrised by the five track parameters:
 2209 $\boldsymbol{\tau} = (d_0, z_0, \phi_0, \theta_0, q/p)$, where d_0 and z_0 are the transverse and longitudinal
 2210 impact parameters; ϕ_0 and θ_0 the azimuthal and polar angles of the track.
 2211 Lastly, the q/p is ratio between the particles charge and momentum and it
 2212 measures the curvature of the tracks.

2213 3.4.0.3 Alignment levels and degrees of freedom

2214 The orientation of a rigid body can be described by a total of six degrees
 2215 of freedom. This is translated into what are known as alignment parameters
 2216 $\boldsymbol{\alpha} = (T_x, T_y, T_z, r_x, R_y, R_z)$. These correspond to the three transitions with
 2217 respect to the origin of the local reference frame ($T_{x,y,z}$) and three rotations
 2218 ($R_{x,y,z}$) around the local Cartesian axes.

2219 3.4.0.4 Residuals

In tracking, a residual is the distance between a hit and the intersection point of the extrapolated track in the sensor. The residual vector (\mathbf{r}) is define as:

$$\mathbf{r} = (\mathbf{m} - \mathbf{e}(\boldsymbol{\tau}, \boldsymbol{\alpha}))$$

2220 where \mathbf{m} is the vector to center of the module and $\mathbf{e}(\boldsymbol{\tau}, \boldsymbol{\alpha})$ is the vector to
 2221 the track intersection with the surface. For every track and module there
 2222 is a residual, as it is shown in Figure 3.35.

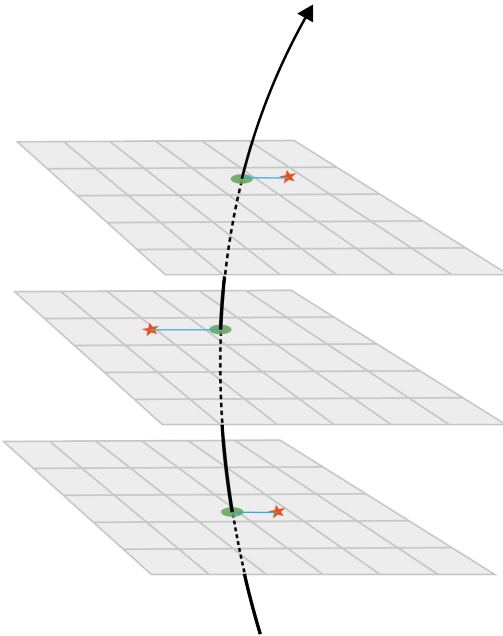


Figure 3.35: Schematic representation of a charged particle crossing detector planes [164]. The red star measures represents the measurement in each layer (m_i). The black line is the fitted trajectory for a given set of track parameters. The position of the intersection of the fitted track with the surface (e_i) on which the i^{th} measurement is made is indicated with a green ellipse. The residuals (r_i) are shown in blue.

2223 3.4.1 Track based alignment

2224 The distance between the hits and the fitted track should be null if
 2225 the detector were perfectly aligned, and the residual distribution would be
 2226 centred at zero and have a width that corresponded to the module resolu-
 2227 tion. Therefore, any deviation from the in the residual distribution would
 2228 indicate a misalignment of the detector.

2229 A schematic description of the alignment chain is illustrated in the three
 2230 panels of Figure 3.36. The blue rectangles on the left panel of Figure 3.36
 2231 represent the true position of the detector modules. A charged particle
 2232 deposits part of its energy in each module producing the hits, which are
 2233 marked with red dots. The track of the particle is marked with a red line.
 2234 The x distance is the deviation of the module from its apparent position.
 2235 In the middle panel, the white rectangles represent the apparent position of
 2236 each module. Here can be seen how the real position and the apparent one
 2237 is not the same by an unknown distance x . This deviation leads to a dis-
 2238 crepancy between the reconstructed tracks and the true ones. The residuals
 2239 in the middle panel are represented by a green line, which corresponds to
 2240 the difference between the recorded track (red dots) and the reconstructed
 2241 one (blue dots). The residual distributions in this panel are displaced from

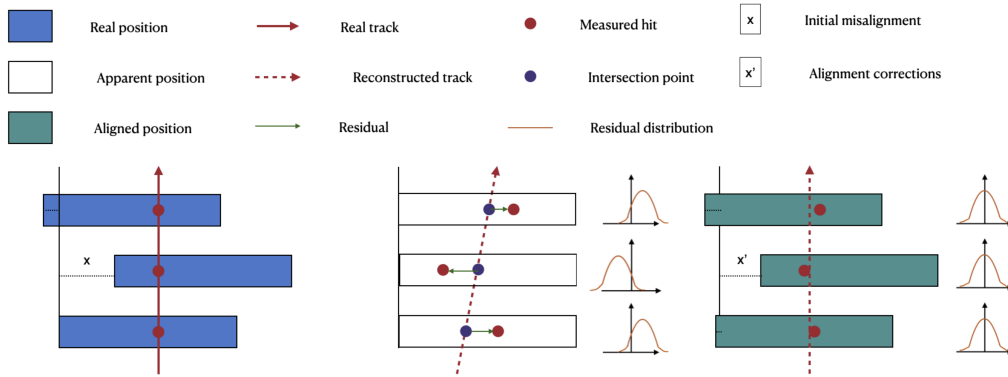


Figure 3.36: Alignment procedure scheme where each rectangle is a detector module. The left panel represents the real position of the detector modules and the charged particle track. The middle panel shows the initially-expected position of the modules and the reconstructed track. The right panel exemplifies how the position of the detectors has been updated to resemble the real one. This update is done by the track-based alignment procedure. **I need to vectorise this image**

2242 zero, indicating a misalignment. The purpose of the alignment algorithm
 2243 is to center this distributions in zero by minimising these residuals. As a
 2244 result of the alignment procedure, the position of the detectors has been
 2245 updated a distance x' for each module. After this, the new expected pos-
 2246 ition of the modules (green rectangles) is much closer to the real one and,
 2247 hence, the residuals are more centred at zero. Anyhow, this is not perfect
 2248 and the different x' are not all equal to x . To improve the precision, the
 2249 alignment procedure is carried iteratively.

2250 3.4.1.1 Global χ^2 algorithm

To correct the position of the the ID, the alignment constants (α) are obtained as result of the minimisation of the χ^2 function. This function is built from the track-hit residuals:

$$\chi^2 = \sum_t \sum_h \left(\frac{r_{t,h}(\boldsymbol{\tau}, \boldsymbol{\alpha})}{\sigma_h} \right)^2,$$

where the index t runs over the reconstructed tracks and the h is the set of hits associated to each track t . The residual of each hit associated to track t is $r_{t,h}$ and σ_h is the hit's uncertainty. In vector notation, the χ^2 function can be expressed as:

$$\chi^2 = \mathbf{r}^T \Omega^{-1} \mathbf{r},$$

where ω is the covariance matrix of the corresponding measurements. The track parameters, $\boldsymbol{\tau}$, are those that minimise the χ^2 and, therefore, first and

second derivatives of χ^2 with respect $\boldsymbol{\tau}$ are used.

$$\frac{d\chi^2}{d\boldsymbol{\tau}} = \sum_t \left[\left(\frac{d\mathbf{r}}{d\boldsymbol{\alpha}} \right)^T \Omega^{-1} \mathbf{r} \right]^T + \sum_t \left[(\mathbf{r}^T \Omega^{-1} \left(\frac{d\mathbf{r}}{d\boldsymbol{\alpha}} \right)) \right] = 0$$

It is worth to remind that \mathbf{r} and Ω are defined for a single track, so the summary will accumulate the residuals from all considered tracks from all the events in the data sample. The last expresión can be simplified taking into account that Ω^{-1} is symmetric and it takes the form:

$$2 \sum_t \left(\frac{d\mathbf{r}}{d\boldsymbol{\alpha}} \right)^T \Omega^{-1} \mathbf{r} = 0 \quad (3.10)$$

Since $\mathbf{r} = \mathbf{r}(\boldsymbol{\tau}, \boldsymbol{\alpha})$, the partial derivatives have to be taken into account:

$$\frac{d\mathbf{r}}{d\boldsymbol{\alpha}} = \frac{\partial \mathbf{r}}{\partial \boldsymbol{\tau}} \frac{d\boldsymbol{\tau}}{d\boldsymbol{\alpha}} + \frac{\partial \mathbf{r}}{\partial \boldsymbol{\alpha}}$$

Inserting this into Eq. 3.10, the condition for minimising the χ^2 turns to be:

$$\sum_t \left(\frac{\partial \mathbf{r}}{\partial \boldsymbol{\tau}} \frac{d\boldsymbol{\tau}}{d\boldsymbol{\alpha}} + \frac{\partial \mathbf{r}}{\partial \boldsymbol{\alpha}} \right)^T \Omega^{-1} \mathbf{r} = 0. \quad (3.11)$$

2251 Here, the term $d\boldsymbol{\tau}/d\boldsymbol{\alpha}$ is of particular importance since its contains the relationship
2252 between the track and alignment parameters, and it will determine
2253 the difference between the *Local* and *Global* χ^2 algorithms.

2254 If the algorithm assumes that track parameters do not depend on the
2255 alignment, i.e. $d\boldsymbol{\tau}/d\boldsymbol{\alpha} = 0$, it is the so-called *Local* χ^2 algorithm. On the
2256 other hand, the *Global* χ^2 is based on the assumption that the track and
2257 alignment parameters are dependent.

2258 The track parameters that satisfy the relation in Eq. 3.11 are found by an
2259 iterative process consisting on evaluating the first and second derivatives of
2260 the χ^2 with respect to the current iteration track parameters, $\boldsymbol{\tau}_0$. Since the
2261 derivative terms of Eq. 3.11 depend on $\boldsymbol{\tau}$ itself, the procedure is repeated
2262 until a convergence criteria is met.

2263 Additionally, the track fit can be further improved by adding additional
2264 terms that account for the effects of multiple Coulomb scatterings of the
2265 particle with the detector.

2266 3.4.2 Web-based display for alignment monitoring

2267 The ID Alignment Monitoring Web Display (Figure 3.37) is an applica-
2268 tion intended for monitoring the track-based alignment results obtained

2269 at the calibration loop for the ID. It helps to evaluate the computed alignment
2270 corrections as well as many graphical distributions related with the
2271 performance (for example, the detector residuals). **I have not explained**
2272 **what the calibration loop is :(**

2273 The web application consists in a server, managed by ATLAS Distributed
2274 Computing, and a collection of scripts to produce distributions, update⁸,
2275 the information and handle the http requests. It is available at Athena⁸,
2276 the software framework for ATLAS [125].

2277 Part of my personal work has consisted in writing the code for both
2278 the frontend and backend of the ID Alignment Monitoring Web Display.
2279 From an outdated set of scripts, the backend of the application has been
2280 remodelled. In the new version all the code duplicities have been suppressed
2281 by defining classes, methods and functions. Several new functionalities have
2282 been added, to name some:

- 2283 • The web uses the standard Athena setup instead of loading a bash
2284 script in which the Athena version had to be hardcoded.
- 2285 • Debug levels using ATLAS printing style methods have been imple-
2286 mented.
- 2287 • Now it is possible to update a single run or list of runs while in the
2288 previous version it was necessary to execute the program over all runs
2289 again.
- 2290 • It is not necessary to hardcode the the year anymore, it is automatic-
2291 ally now.
- 2292 • Depending on which run was decided to plot, it was necessary to
2293 hardcode the year in he scripts. Now the web tool allows to do this
2294 from its interface.
- 2295 • In the new version it is possible to access the ATLAS Metadata In-
2296 terface⁹ information.
- 2297 • The runtime of the code has been speed up by performing the exe-
2298 cution in a single loop in contrast to the two-loops structure of the
2299 previous version.

⁸Athena is a concrete realisation of a component-based architecture (ased on LHCb's Gaudi [165]) which was designed for a wide range of physics data-processing applications.

⁹Known as AMI, it is a generic software ecosystem for retrieving scientific data by metadata criteria. It allows to search for real and simulated data by metadata criteria as well as browse, view, compare and create ATLAS AMI-Tags

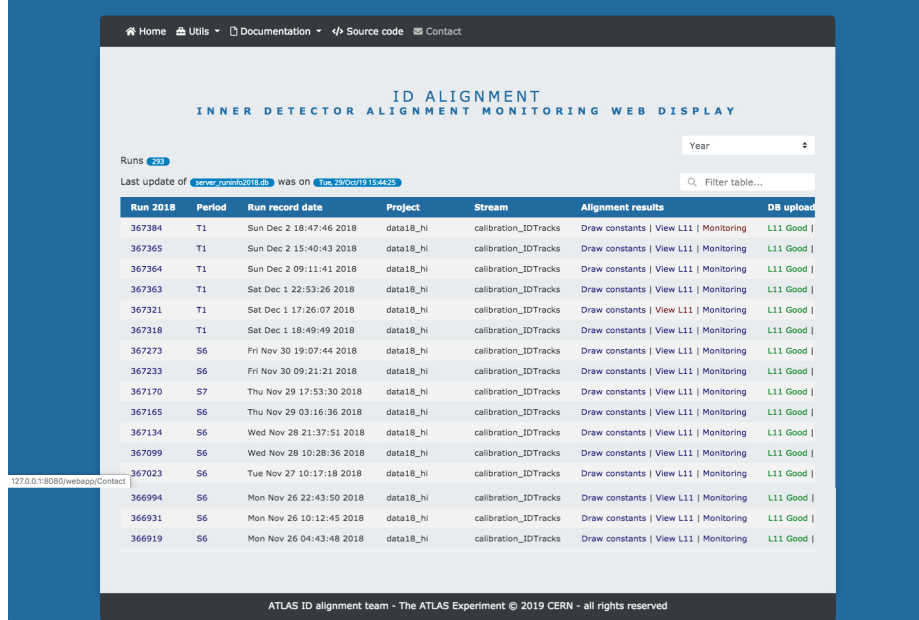


Figure 3.37: Main page of the ID Alignment Monitoring Web Display on wide resolution screen. The monitor presents the runs and allows to access the alignment information and plots. Queries can be used to filter the runs presented.

2300 Regarding the frontend, it has been developed from the scratch. The
 2301 aesthetics of the web page is the most visible change in the monitor dis-
 2302 play. The frontend code is based on CherryPy [166], an object-oriented web
 2303 application framework using the Python programming language, and also
 2304 includes CSS, HTML and Java. The enhanced web display allows to easily
 2305 choose which information is shown. The web has been designed to adapt
 2306 to mobile devices, as Figure 3.38 shows. To do so, it uses Bootstrap, a CSS
 2307 framework directed at responsive, mobile-first frontend web development .

2308 The navigation bar of the web has also being improved, having a better
 2309 organisation, more option and, if the browser screen is narrowed, it collapses
 2310 into a desplegable sidebar. A filter has been added that allows to show only
 2311 the runs that follow the desired specific criteria. A desplegable to select
 2312 the years has been included, the script reads from the available years in the
 2313 database. A year selector presentes the possible years via a script that reads
 2314 the available data. The hoover function highlights the text as the pointer
 2315 goes over it. The plots are presented in a cleaner way using grid view to
 2316 select the plot of interest and light boxes to highlight them. The legends of
 2317 the plots have also been modified to remove duplicated items.

The screenshot shows the 'ID ALIGNMENT INNER DETECTOR ALIGNMENT MONITORING WEB DISPLAY' interface. On the left, a table lists alignment runs from 2018, with columns for Run 2018, Period, Run record date, Project, and Stream. The table includes rows for runs 367384, 367365, 367364, 367363, 367321, 367318, 367273, 367233, 367170, 367023, 366994, and 366931. On the right, detailed logs are shown for runs 367384, 367365, 367363, 367321, 367318, 367273, 367233, 367170, 367023, 366994, and 366931. Each log entry includes a timestamp, project, stream, and various status messages like 'Good' or 'CRONJOB'.

Run 2018	Period	Run record date	Project	Stream
367384	T1	Sun Dec 2 18:47:46 2018	data18_hi	calibration_IDTracks
367365	T1	Sun Dec 2 15:40:43 2018	data18_hi	calibration_IDTracks
367364	T1	Sun Dec 2 09:11:41 2018	data18_hi	calibration_IDTracks
367363	T1	Sat Dec 1 22:53:26 2018	data18_hi	calibration_IDTracks
367321	T1	Sat Dec 1 17:26:07 2018	data18_hi	calibration_IDTracks
367318	T1	Sat Dec 1 18:49:49 2018	data18_hi	calibration_IDTracks
367273	S6	Fri Nov 30 19:07:44 2018	data18_hi	calibration_IDTracks
367233	S6	Fri Nov 30 09:21:21 2018	data18_hi	calibration_IDTracks
367170	S7	Thu Nov 29 17:53:30 2018	data18_hi	calibration_IDTracks
367023	S6	Tue Nov 27 10:17:18 2018	data18_hi	calibration_IDTracks
366994	S6	Mon Nov 26 22:43:50 2018	data18_hi	calibration_IDTracks
366931	S6	Mon Nov 26 10:12:45 2018	data18_hi	calibration_IDTracks

Figure 3.38: Main page of the ID Alignment Monitoring Web Display on narrow screens such as the ones of a mobile device.

2318 3.4.3 Alignment results during Run-2

2319 Here I should find some plot that summarises the results of
 2320 the alignment and I must highlight the importance of alignment
 2321 to perform the analysis.

2322 **Chapter 4**

2323 **Recording data and simulating
2324 events in ATLAS**

2325

2326

In God we trust, all others bring data.

2327

—WILLIAM EDWARDS DEMING (1900-1993)

2328

2329 The word “event” is one of the most commonly used terms in high
2330 energy physics. In the context of LHC experiments there are two types
2331 of events. On side, there are the real events recorded by the detector.
2332 This event is typically a pp collision but it could also be a single particle
2333 such as cosmic ray. On the other side, there the events simulated by the
2334 MC event generator. In ATLAS, both type of events are precessed by a
2335 common software, Athena. For real collision data, the detector response is
2336 evaluated via different algorithms in order to reconstruct the objects in the
2337 final state. For the simulated processes, the MC generated particles undergo
2338 a serie of steps replicating the physics of the collisions, the interaction with
2339 the detector material, the magnetic fields and the response of the detector
2340 electronics. Once this steps have been applied, the simulated events are
2341 evaluated using the same algorithms as the ones from real collisions.

2342 This chapter is divided into two sections that discuss both types of events.
 2343 In Section 4.1 the collection of the data in ATLAS is briefly described and
 2344 in Section 4.2 the MC simulation chain is explained.

2345 **4.1 Data**

- 2346 • How is data collected in ATLAS? DAQ
 2347 • Pileup (differentiate LHC pileup from ATLAS pileup during Run 2)
 2348 • What are triggers

2349 **4.2 Monte Carlo**

2350 In order to study the physics taking place into the ATLAS detector,
 2351 the signals and backgrounds in the analysis are simulated by Monte Carlo
 2352 generators according to the cross sections predicted by the SM. The use of
 2353 the MC simulations is vast and there are many different models generators
 2354 and techniques. As all MC algorithms, these methods rely on repeated
 2355 random sampling to obtain numerical results. In the context of this work,
 2356 the MC generators provide a detailed simulation of the processes from the
 2357 event generation through to output in a format which is identical to that of
 2358 the true detector.

2359 Typically, the simulation chain is divided into these three steps [167]:

- 2360 1. Generation of the events and immediate decays: An event generator
 2361 produces the result of the collisions in terms of particles created and
 2362 stores any stable particle expected to propagate through the detector.
 2363 At this point, the geometry of the detector is not considered because
 2364 only the immediate decays are taken into account.
- 2365 2. Simulation of the detector and physics interactions: At this point, all
 2366 particles from the previous step are propagated through the full ATLAS
 2367 detector using GEANT4. This part simulates all major components
 2368 and materials as well as the interactions of particles such as ionisation
 2369 in trackers, energy deposition in calorimeters, intermediate decays,
 2370 radiation and scattering
- 2371 3. Digitalisation of the energy deposits on the sensitive regions of the
 2372 detector.

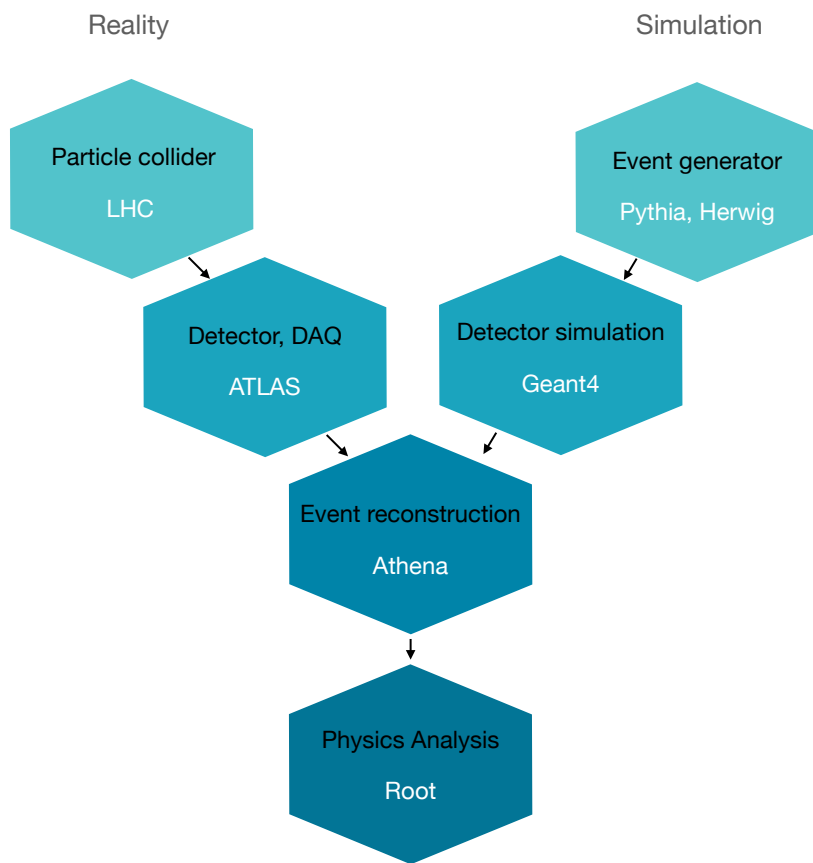


Figure 4.1: Comparison of the paths followed by data recorded by the ATLAS detector and the simulated samples. The format of the simulated data is the same as the recorded at each step.

2373 The output of the full simulation chain is an object with the exact same
 2374 format as a real event registered by the ATLAS DAQ system. The entire
 2375 simulation chain is shown in Figure 4.1 and compared to the path that the
 2376 data follows when it is originated from an actual collision.

2377 The so called “truth” data is kept for each event and particle in both
 2378 event generation and detector simulation. The truth is a history of the
 2379 interactions from the generator. In the analysis presented in Chapter 6, the
 2380 truth information has several uses such us the determination of fake rates
 2381 or the lepton origin assignment. An important part of the work carried
 2382 during the thesis was the proper implementation of the truth information
 2383 at generator level within ATLAS software framework, Athena.

2384 4.2.1 MC simulations

2385 The generation of the simulated event samples includes the effect of
2386 multiple pp interactions per bunch crossing, as well as the effect on the
2387 detector response due to interactions from bunch crossings before or after
2388 the one containing the hard interaction.

2389 4.2.1.1 Parton shower simulation**2390 4.2.1.2 Hadronisation simulation****2391 4.2.1.3 Underlying decay simulation****2392 4.2.1.4 Hadron decay simulation****2393 4.2.1.5 Pile-up simulation****2394 4.2.2 MC generators**

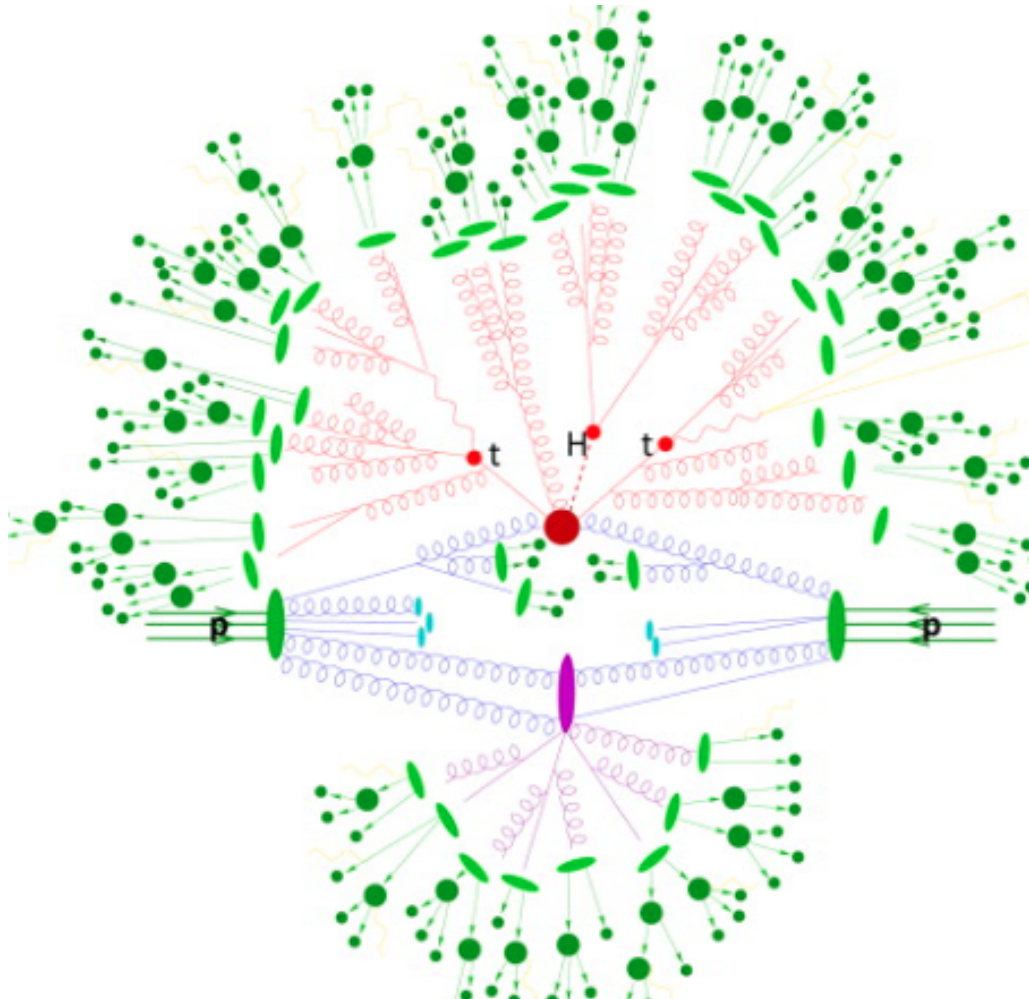


Figure 4.2: Representation of a $t\bar{t}H$ event as produced by an event generator [168]. The big red blob is the hard interaction, which is followed by the decay of the Higgs boson and the two top quarks, represented by the three small red blobs. The additional QCD radiation produced is in red. The secondary interaction, in purple, occurs before the hadronisation of the the final-state partons (light green). In darker green, the hadron decay is presented and in the photon radiation appears in yellow.

2395 **Chapter 5**

2396 **Object reconstruction and
2397 identification**

2398 **Highlight the importance of alignment for the reconstruction**

2399 To reconstruct the physical objects, the information of all the sub-
2400 detectors and systems of ATLAS is employed. A detailed description of
2401 all of them is presented in Section 3. After passing the trigger preselection,
2402 the raw data is analysed to build the physics objects that constitute the
2403 subject of the physical analyses. The process of constructing these elements
2404 is known as reconstruction. Figure 3.16 illustrates how each particle inter-
2405 acts with the different layers of the ATLAS detector. The reconstructed
2406 objects are the particles tracks and vertices, the leptons, the photons, jets
2407 (and their flavour tag) and the missing transverse momentum.

2408 **5.1 Tracking**

2409 The detection and measurement of charged particles moment is an es-
2410 sential aspect of any large particle physics experiment. Regardless of the
2411 medium through which a charged particle travels, it always leaves a trails
2412 of ionised atoms and liberated electrons. By detecting this it is possible to
2413 reconstruct the trajectory of a charged particle. ATLAS does this through
2414 its silicon detectors.

2415 The trajectories followed by particles are referred as “tracks”. For
2416 charged particles, the tracks are reconstructed using, mainly, the informa-
2417 tion of the ID and, in the case of muons, the MS. A charged particle
2418 passing thought the ID will interact with its active sensors, the pixel detector
2419 and SCT (Figures 3.22 and 3.23 respectively) providing a three-dimensional

measurement of space-points. While each hit in the pixel detector is directly translated into a space-point, for the SCT two hits are needed to reconstruct one space-point. These space-points can be given by a single pixel activation or by several neighbouring pixels activated simultaneously. Since the ID is submerged in a solenoidal magnetic field, the charged particles have their trajectories curved by the Lorentz force, this allows to calculate its p_T using the sagitta method. The track reconstruction is performed in two s

Highlight the importance of the alignment for the object definition and its reconstruction. Link this section with 3.4

5.1.1 Sagitta method

5.2 Vertices

5.3 Electrons and photons

5.4 Muons

5.5 Jets

At accelerator based detectors, quarks and gluons are detected by the jets of hadronic particles that they produce in the detector soon after they are created (remember that, as stated in Section 1.1.4, free quarks are suppressed due to color confinement). An exception to this rule are the top quarks, whose lifetime is smaller than the hadronisation time by two orders of magnitude and, hence, they are detected by its decay products. For the gluons and the rest of quarks, hadronisation showers (Section 3.3.3.1) take place and jet clustering algorithms merge the clusters and tracks produced by these jets to reconstruct them. In the majority of ATLAS analyses, the “Anti- k_t ” algorithm is used [165] to analyse the data from hadronic collisions. Modelling the jet as a cone, the algorithm uses a specific choice of radius parameter (R) defining the radial size of the jet. The distance between all pairs of objects i and j (d_{ij}) and the distance between the objects and beam pipe (d_{iB}) are used in:

$$d_{ij} = \min(k_{ti}^{2p}, k_{tj}^{2p}) \frac{\Delta_{ij}^2}{R^2}$$

$$d_{iB} = k_{ti}^{2p}$$

where

$$\Delta_{ij}^2 = (y_i - y_j)^2 - (\phi_i - \phi_j)^2$$

and k_{ti} , y_i and ϕ_i are respectively the transverse momentum, the rapidity and the azimuthal angle of object i . The parameter p accounts for the relative power of the energy versus geometrical (Δ_{ij}) scales. For the Anti- k_t , p is set to -1 . Other clustering algorithms use different choices of p such as $p = 0$ (Cambridge/Aachen algorithm) or $p = 1$ (inclusive k_t algorithm).

The algorithm iterates over the topological-cluster (or, simply, top-clusters) objects of the calorimeter as it follows: First it proceeds to identify the smallest distances with among all the combinations of d_{ij} and d_{iB} . If the distance is a d_{iB} , the entity i is labeled as “jet” and removed from the list of entities. If, on the contrary, it is a d_{ij} , the objects i and j are merged together. This way, before clustering among themselves, soft components (low- p_T) tend to be merged to the hard ones (high- p_T). Then the distances are recalculated and the process repeated. This is done iteratively until all entities are assigned to a particular jet.

If a hard particle has no hard neighbours within a $2R$ distance, all soft particles will be assigned to it, resulting in a perfectly conical jet. But if another hard particle is present in that $2R$ distance, then there will be two hard jets and it will be impossible for both to be perfectly conical.

Work in progress

Typically, the cone size R is selected to be 0.4 or 0.6, though the most standard used in ATLAS is 0.4. If $R = 1$, the jet is labeled a Large- R and if $R = 0.4$ then as Small- R jet.

5.5.1 Jet energy calibration and resolution

The jet calibrations and the associated uncertainties are clearly extremely important in many top analyses. This often makes them the leading experimental uncertainties in Top analyses

2474 5.5.2 Bottom quark induced jets

2475 In general, it is impossible to determine which quark flavour was pro-
2476 duced or even or whether the jet was originated by a quark or a gluon.
2477 However, if a b quark is created, the hadronisation will produce a jet of
2478 hadrons, one of which will be a b -type hadron (B hadron). The B hadrons
2479 turn out to be relatively-long-lived particles (1.5×10^{-12} s). If this larger
2480 longevity is combined with the Lorentz time-dilation that particles exper-
2481 ience when produced in high energy collisions, it results in the B hadron
2482 traveling on average a few mm before disintegrating.

2483 As a result, the experimental signature of a b quark is a jet of particles
2484 emerging from the point of collision (primary vertex) and a secondary vertex
2485 resulting from b -quark decay that is several mm away from the primary
2486 vertex. Therefore, the capacity to resolve secondary vertices from the parent
2487 vertex is crucial for identifying b -quark jets.

2488 5.6 Missing transverse energy**2489 5.7 Overlap removal**

2490 **Chapter 6**

2491 **Search for rare associate tHq
2492 production**

2493 **6.1 Introduction**

2494 **Describe the strategy for the $2\ell + 1\tau_{\text{had}}$ analysis**

2495 The study of the tHq production can be classified attending to the
2496 the number of light-flavour leptons (ℓ), i.e. electrons or muons, and
2497 hadronically-decaying tau leptons (τ_{had}). According to this criteria, the
2498 channels presented in Table 6.1 have been defined. As can be seen in the
2499 table, the study of the 1ℓ channel uses only the $H \rightarrow t\bar{t}$, which is the most
2500 dominant decay mode for the Higgs boson with a 58% BR as is reported in
2501 Section 2.2.3. However, for the multileptonic channels the $H \rightarrow W^+W^-$,
2502 $H \rightarrow \tau^-\tau^+$ and $H \rightarrow ZZ$ are considered. These three Higgs decay channels
2503 combined account for a total 21% BR.

#	0 τ_{had}	1 τ_{had}	2 τ_{had}
1ℓ (e/μ)	$tHq (b\bar{b})$ 1 ℓ		$tHq (WW/ZZ/\tau\tau)$ 1 $\ell + 2\tau_{\text{had}}$
2ℓ (e/μ)	$tHq (WW/ZZ/\tau\tau)$ 2 ℓ SS	$tHq (WW/ZZ/\tau\tau)$ 2 $\ell + 1\tau_{\text{had}}$	
3ℓ (e/μ)	$tHq (WW/ZZ/\tau\tau)$ 3 ℓ		

Table 6.1: Different channels for tHq production according to the presence of light-flavoured leptons and hadronically-decaying taus in the final state.

Moreover, depending on the relative charge between the light charged leptons, the $2\ell + 1\tau_{\text{had}}$ channel is further subdivided in two sub-channels. The so-called $2\ell \text{SS} + 1\tau_{\text{had}}$ channel is defined by the events in which the two light leptons have the same electric charge. In contrast, the one in which they have opposite electric charge is known as $2\ell \text{OS} + 1\tau_{\text{had}}$ channel. For simplicity, through this document, these two sub-channels are usually referred just as SS and OS respectively.

The work of this thesis is focused in the $2\ell + 1\tau_{\text{had}}$ channels. To do so, the $2\ell \text{SS} + 1\tau_{\text{had}}$ and $2\ell \text{OS} + 1\tau_{\text{had}}$ are treated separately since they have different background compositions, being the $2\ell \text{SS} + 1\tau_{\text{had}}$ the one with the lower background contribution.

- different MVAs trained for each channel

When assuming that one of the light-flavoured leptons is originated from the Higgs-boson decay and the other one from the top-quark decay, the determination of which lepton comes from which particle is direct for the $2\ell \text{OS} + 1\tau_{\text{had}}$ but not for the $2\ell \text{SS} + 1\tau_{\text{had}}$. Since knowing the origin of the light-flavoured leptons can be very useful to define variables with the power to discriminate the tHq signal from the background, tools are developed to associate these leptons to its parent particles.

- The fake rate estimates for light leptons and tau leptons are being checked to see if there is anything that has to be treated differently for the two sub-channels.

6.2 Data and simulated events

- the tH samples were done with MADGRAPH5_AMC@NLO +PYTHIA 8 +EVTGEN

The underlying event is generally done with Pythia8 in ATLAS. In the tHq samples we used MADGRAPH5_AMC@NLO for the calculation of the matrix element and PYTHIA 8 for the hadronisation and parton showering. We are also working on alternative samples with HERWIG 7 as parton shower generator. **While in section 3 I describe how the events and samples are generally generated and simulated, in this section I should describe what is specifically used in this analysis**

2536 **6.2.1 Single lepton triggers**

2537 **6.3 Object definition**

2538 **Highlight the importance of alignment**

2539 **6.4 Signal**

2540 In this section, it is discussed how it is find what we know as signal.
2541 In a particular study, the “signal” is the set of events in the dataset that
2542 correspond to the process of interest. Therefore, in this case, the signal
2543 is composed by tHq production events with a $2\ell + 1\tau_{\text{had}}$ final state. In
2544 contrast, the background processes are those which, a priori, look like the
2545 signal process but it is not. A more detailed definition of what a background
2546 is and how it is classified can be found in Section 6.5.

2547 As mentioned already, the cross-section of tHq is very small. One of
2548 the big challenges of LHC is the wide range of cross sections that of the
2549 different process that take place there. When the cross-section is huge, the
2550 process is typically uninteresting. When it is large the process is already
2551 known. The medium cross-sections corresponds to not-so-well studied pro-
2552 cess, and when it is low is for process yet to be discovered. This causes
2553 that the main backgrounds are much larger than the signal, swamping the
2554 interesting physics with known processes. Therefore, in order to produce
2555 some small number of signal events, it is necessary to also produce so many
2556 of uninteresting ones that they even happen in the same crossing (pile-up).
2557 **Maybe this paragraph can be put somewhere else or removed**

2558 **6.4.1 Signal generation and validation**

2559 **rivet**

2560 **6.4.2 Parton-level truth validation**

2561 > Describe what are truth level and reconstruction level.

2562 > The truth information is whatever comes from the generator, the
2563 physics without taking into account the effects of the detector. The truth
2564 level does not include the effects of the interaction with matter. The truth
2565 also includes the parton shower and hadronisation information.

2566 > truth = generator + parton shower + hadronisation
 2567 > The studies I did were done at generator level
 2568 > Particle level is part of truth information
 2569 > Detector level = reconstruction level + calibration +
 2570 > Creo que esto se explica bien en la tesis de florencia
 2571 (**maybe write the calculations of BR_tHq in the Section 6.4.2**
 2572)

2573 6.4.3 Lepton assignment

2574 The two light leptons in the final state of the $2\ell + 1\tau_{\text{had}}$ channel can
 2575 originate either from the Higgs boson or the top quark. The ambiguities
 2576 regarding the origin of these light-flavoured leptons, make the reconstruction
 2577 of the top quark and Higgs boson systems extremely difficult. Nevertheless,
 2578 the electric charge of these leptons could provide us useful information to
 2579 probe their origins.

2580 To have knowledge of whether the light-flavoured leptons in the final
 2581 state are originated from the Higgs boson or the top quark is very beneficial
 2582 in order to both reconstruct the event and design variables at reconstruction
 2583 level with high discriminant power. As is show in Sections 6.6.4 and 6.6.5,
 2584 the variables using the lepton assignment information play a relevant role
 2585 not only in the definition of the signal-enriched section but also the in
 2586 the determination of the control regions to constrain the most important
 2587 background processes.

2588 According to the calculations performed by combining the BR of the
 2589 Higgs boson, the top quark and all its decay products (see Section 6.4.2),
 2590 in the $2\ell + 1\tau_{\text{had}}$ channel of tHq production, the τ_{had} is produced 83.7% of
 2591 times as a product of the Higgs-boson decay in opposition to the 16% in
 2592 which it comes from the top-quark disintegration.

2593 Opposite-sign Leptons

2594 In the dominant scenario (τ_{had} from Higgs) the association of which light-
 2595 flavoured lepton comes from the top-quark decay and which one comes
 2596 from the Higgs-boson decay can be done directly if these two leptons have
 2597 opposite electric charge, i.e. in the $2\ell \text{OS} + 1\tau_{\text{had}}$ channel. Since in Higgs
 2598 boson is neutrally charged, the sum of the charge of its decay products
 2599 should be zero. Therefore, in the OS channel, while the light lepton with
 2600 opposite charge to that of the τ_{had} is the one coming from the Higgs, the

2601 other lepton, i.e. the one with the same charge as τ_{had} , is the one originated
 2602 from the top-quark decay.

2603 **Same-sign Leptons**

2604 In contrast to the the $2\ell \text{OS} + 1\tau_{\text{had}}$ channel, in the case of τ_{had} from Higgs,
 2605 when the two light leptons have the same electric charge (the so called
 2606 $2\ell \text{SS} + 1\tau_{\text{had}}$) it is not possible to know, a priori, which of the leptons
 2607 comes from the top-quark system and which from the Higgs-boson decay.

2608 In order to perform this association for the $2\ell \text{SS} + 1\tau_{\text{had}}$ several methods
 2609 relying in the truth-level information have been tested. **Describir super-**
 2610 **ficialmente los métodos listados en el ítemize**

- 2611 • First method (Cyrus): Assume that the leading lepton was originated
 2612 from the top
- 2613 • Second method (Mathias): Cut in two variables
 - 2614 – Cut 1: $m_{\text{vis},H}(\text{lep}(t)) - m_{\text{vis},H}(\text{lep}(H)) > 57.0 \text{ GeV}$
 - 2615 – Cut 2: $m_{\text{pred},t}(\text{lep}(H)) - m_{\text{pred},t}(\text{lep}(t)) > 0.0 \text{ GeV}$
- 2616 • BDT based method presented in this work

2617 **6.4.3.1 Labelling the $2\ell \text{SS} + 1\tau_{\text{had}}$ with the reconstruction-level
 2618 and truth-level matching**

2619 Even though at reconstruction level it is not known which are the par-
 2620 ents of the particles in the final state, at parton level this informations is
 2621 accesible, in other words, the origin¹ of the light leptons is known. For a
 2622 given event, it is possible to access to both the particle-level and parton-level
 2623 information simultaneously. Having the parton-level leptons, whose parents
 2624 are known, and the reconstruction level leptons, whose parents need to be
 2625 identified, it is possible to compare them to create an association. Specific-
 2626 ally, identify which parton-level lepton correspond to which reconstructed
 2627 lepton. The aim of this relation is to assign the leading (ℓ_1) and sub-leading
 2628 (ℓ_2) light leptons at reconstruction level to the the “lepton from top-quark-
 2629 decay chain” (ℓ_{top}) and “lepton from Higgs-boson-decay chain” (ℓ_{Higgs}) at
 2630 truth level.

2631 In order to link the reconstruction-level light leptons to the parton-
 2632 level light leptons, a $\Delta R < 0.01$ cone around each of the reconstructed

¹By origin of a light lepton is meant whether it comes from the Higgs-boson-decay chain or the top-quark-decay chain.

leptons is built. When inside that cone there is exactly one truth-level light lepton, there is what is called “a match”. Figure 6.1 presents the possible scenarios of the association. In order to identify properly determine the lepton origin in an event, it is required that both leptons at reconstruction level have a match. There are two different cases for this. The first situation is that in which the leading-light lepton is ℓ_{top} and the sub-leading is ℓ_{tHiggs} . For the sake of simplicity, this configuration is named “Type 1” and it is represented in Figure 6.1a. The second double-matching combination is the other way around, the leading-light lepton is ℓ_{Higgs} and the sub-leading is ℓ_{top} . Pictured in Figure 6.1b, this type of events are called “Type 2”. On the contrary, if only one of the two reconstructed light leptons is matched (Figure 6.1c), none of the leptons are classified. If a less strict criteria was used, it would be possible require only one of the two leptons matching in order to classify the event (the unmatched reconstruction-level lepton would be assigned to the unmatched parton-level lepton). The problem of the lax strategy is that while in cases like that on Figure 6.1c it seems clear that unmatched parton correspond to the unmatched reconstructed lepton, for events such as the illustrated in Figure 6.1d the unmatched particle does not necessarily belong to the ℓ_2 cone. For this reason, it is mandatory that both reconstructed light leptons have a match. Finally, in the scenario in which none of the parton-level leptons fall into the cones (Figure 6.1e), no assignation takes place.

To perform this labelling, it has been required that the τ_{had} is originated from the Higgs-boson system. This is imposed in order to guarantee that there are both a ℓ_{top} and a ℓ_{Higgs} . The Higgs-decay channels used for these studies are the $H \rightarrow \tau\tau$ (one τ decaying leptonically and the other hadronically) and the $H \rightarrow WW$. The $H \rightarrow ZZ$ channel has not been included since its impact in the on the $2\ell + 1\tau_{\text{had}}$ production when the τ_{had} comes from the Higgs is very tiny. If the τ_{had} is originated in the Higgs system, only a 2.0% of the events correspond to the $H \rightarrow ZZ$ decay channel, contrasting with the 76.5% of the $H \rightarrow \tau\tau$ and the 21.5% of the $H \rightarrow WW$.

Should add the fraction of events that are labeled from a) the total $2\ell + 1\tau_{\text{had}}$ sample and b) from the total $2\ell SS + 1\tau_{\text{had}}$.

6.4.3.2 BDT-based method for lepton association

- Describe the idea of using reco-level variables to predict (on unlabelled data) whether it is a “Type 1” or “Type 2” event by means of a BDT trained with labeled data (isLep1fromTop)
- Describe with a few words what a BDT is and reference appendix B.

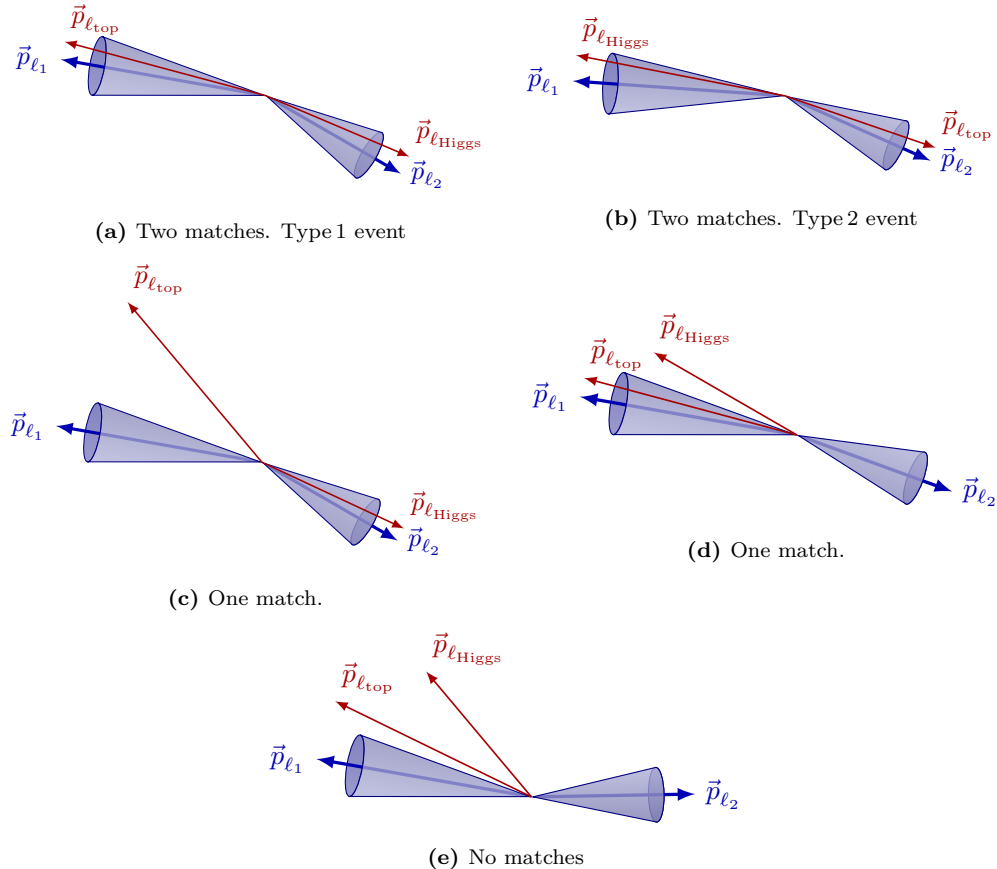


Figure 6.1: Association between reconstruction-level (blue) and parton-level (red) light leptons. Note that the labels ℓ_{top} and ℓ_{Higgs} are only available for the parton-level particles.

- 2671 • Using root.TMVA - Advantages: Nowadays most of ML frameworks
2672 (keras, pyTorch, scikit-learn, XGBoost, etc..) are based on python.
2673 These libraries expect numpy arrays or panda data-frames as input, so
2674 the first thing to do when using the analysis NTuples is to convert the
2675 ROOT data-frame. An advantage of using TMVA library of ROOT
2676 is that this data conversion is not necessary. is that
- 2677 • Describe the particularities of this gradient BDT with detail
- 2678 • One way to reap the benefits of a large training set and large test set
2679 is to use cross validation: k-folding.
 - 2680 – Programmed in an external-to-tHqLoop script
 - 2681 – Trained only over SS signal events. In contrast to the BDT of
2682 SR that trains over all process, this one trains only over signal
2683 because its objective is to determine which lepton comes from

2684 which particle in the signal events and this classification only
 2685 makes sense in signal processes.

- 2686 • Present the feature importance
 - 2687 – Present distributions of used variables and a list with the mean-
 2688 ing of this variables
 - 2689 – Present correlations between pairs of used variables. Note that
 2690 the correlation maps search for bidimensional correlations (i.e.
 2691 between pairs of two variables) and the BDT uses N-dimensional
 2692 relations. (Page 26 of the TMVA guide)
 - 2693 –
- 2694 • Discuss the negative weight strategy: Present used distributions with
 2695 'all weights' and with 'positive weights'
 - 2696 – in contrast to XGboost, ROOT.TMVA can deal with negative
 2697 weights
- 2698 • Hyperparameter optimisation
- 2699 • Present BDT response, ROC curve, ¿something else?
- 2700 • Compare to the results using other MVA methods.
- 2701 • The BDT is integrated in tHqLoop (weights.xml) ¿Where do I describe
 2702 what tHqLoop is?
- 2703 • From tHqLoop, the BTD score can be calculated for all the events
 2704 (signal or not) and then the efficiency of the lepton association can be
 2705 calculated depending on the threshold point which is chosen to define
 2706 whether the event is Type1 or Type2. Note that this efficiency is
 2707 computed only over signal events. → Table of 'efficiency vs cutpoint'

2708 **6.4.4 Top quark and Higgs boson reconstruction**

2709 En aras de que esto es extremadamente complicado y no se
 2710 logró hacer ¿tiene sentido redactar una sección?

2711 **6.5 Background estimation**

2712 The background can be defined as everything in a subset of the data that
 2713 simulates the signal processes without truly being a signal event. In other

2714 words, in this studies, everything that is not signal, is background. In this
 2715 case, whatever that mimics the signature of an associated tHq production
 2716 with $2\ell + 1\tau_{\text{had}}$ final state is referred as background.

2717 In order to perform the physics analysis, it is fundamental to subtract
 2718 the background events from the dataset as much as possible in order to
 2719 achieve higher signal purity. By doing this, the analysed dataset resembles
 2720 more to the process that is desired to study. This procedure is the so called
 2721 “event selection” and its described in Section 6.6

2722 There are two different types of background: “reducible” backgrounds,
 2723 where particles imitate the particles we are looking for (for instance, a
 2724 high-energy electron can mimic a high-energy photon), and “irreducible”
 2725 backgrounds, where particles are the same kind as the ones we are looking
 2726 for.

2727 The main source of background in the $2\ell + 1\tau_{\text{had}}$ channel is due to
 2728 signatures of hadronic tau decays, more specifically, of jets faking τ_{had} .
 2729 [Add Oleh pieCharts](#)

2730 6.5.1 Fakes estimation

2731 τ^- fakes are more important than light lepton fakes

2732 [This is taken from the intNote. I have to reorganise and reph-](#)
 2733 [rase this information](#) The requirements for the objets defined in section
 2734 (ref ref) provide significant suppression of events with jets wrongly selec-
 2735 ted as leptons is achieved by asking electrons and muons to pass the tight
 2736 requirement that combines `tightLH` ID for leptons and `medium` for muons
 2737 and `PLImprovedTight` isolation working points

2738 Similarly, the hadronic taus are required to pass the `medium` require-
 2739 ment of the RNN-based discriminator. Even so, the selected data sample
 2740 is expected to be contaminated with such type of reducible background. It
 2741 is also expected that the simulation of jets faking leptons (electron, muon,
 2742 hadronic tau) in ATLAS detector is imprecise or unreliable. Therefore, an
 2743 important step of the analysis is to estimate this background in data.

2744 **Light-lepton fakes** Particles from the hard scattering process are re-
 2745 ferred as ‘prompt’ . Acceptance, quality and isolation requirements are ap-
 2746 plied to select these leptons Non-prompt leptons and non-leptonic particles
 2747 may satisfy these selection criteria, giving rise to so called ‘non-prompt
 2748 and fake’ lepton backgrounds. Fake electrons/muons will not be explicitly
 2749 distinguished and are referred as fake leptons. The mis-identified lepton

2750 background arises from leptons from heavy-flavour (ℓ_{HF}) hadron decay and
 2751 electrons from γ -conversions. These leptons are mainly produced in $t\bar{t}$,
 2752 $Z + \text{jets}$ and tW events.

2753 The estimation of the fake/non-prompt lepton background is done with
 2754 the template fit method or via the matrix method

2755 The fake and real lepton efficiencies (fake/real rates) are defined as the
 2756 probabilities of a fake or real electron or muon to pass the nominal elec-
 2757 tron/muon requirements. They are given by the tight over loose ratio

2758 - Get some ideas from here: [https://cds.cern.ch/record/1951336/
 2759 files/ATLAS-CONF-2014-058.pdf](https://cds.cern.ch/record/1951336/files/ATLAS-CONF-2014-058.pdf)

2760 **Tau fakes** In the analysis channels involving hadronic taus, all methods
 2761 used for fake background estimation rely on MC-based templates. These
 2762 are splits of simulation according to a type of object mimicking the lepton
 2763 of interest. Construction of MC templates related to the electron and
 2764 muon fakes is based on `TruthClassificationTool` tool. [Describe the
 2765 `TruthClassificationTool`](#)

- 2766 • counting method
- 2767 • template fit method

2768 The extracted SFs are then applied to the simulated background com-
 2769 ponent in the region with taus passing the preselection requirements.

2770 6.5.1.1 $t\bar{t}$

2771 6.5.1.2 $Z + \text{jets}$

2772 6.5.2 Reducible backgrounds

2773 All the processes whose signature is the same as the process of interest
 2774 are known as reducible backgrounds as in contrast to the fake or irredu-
 2775 cible backgrounds described in Section 6.5.1. The objects in the reducible
 2776 backgrounds are prompt. The main reducible backgrounds are:

2777 **6.5.2.1 Diboson**

2778 **6.5.2.2 tW**

2779 **6.5.2.3 $t\bar{t}Z$**

2780 **6.5.2.4 $t\bar{t}H$**

2781 **6.5.2.5 $t\bar{t}W$**

2782 **6.5.2.6 tZq**

2783 **6.6 Event selection**

2784 The event selection

2785 As more and more stringent requirements are made to eliminate these
2786 backgrounds we also lose signal events, so there is a trade off background
2787 rejection against signal acceptance. Since the data is not only limited but
2788 also scarce when it refers to the tHq signal, the event selection is a highly
2789 non-trivial process that requieres a lot of attention.

2790 The signal selection is done in several steps and using different methods.
2791 First of all, it is defined a preselection region (PR) where the physical objects
2792 are selected according to the detector acceptance. The PR is a cut-based
2793 region. Then, discriminant variables are defined and used as input for a
2794 BDT. Finally, the BDT outputs are used to define the signal region (SR)
2795 and control regions (CR).

2796 Two figures of merit are used to simultaneously optimise the fraction of
2797 signal events in the data and the absolute number of signal events. These
2798 metrics are the S/B or purity and the signal significance.

2799 **Purity** : The purity of a process is defined as the ratio between the event
2800 yields of the target process and the total yields. Usually, for the signal, the
2801 signal to background ratio (S/B) is used instead of the purity.

2802 **Significance** : This metric does not only account to the relative fraction
2803 of the process of interest but also to the total amount events. Using the
2804 significance as metric enhances the importance of keeping enough statistics.

Process	SS	OS	SS + OS
tHq	0.9	1.2	2.1
tZq (with $Z \rightarrow \ell\ell$)	6.2	32.9	39.1
$t\bar{t}$	47.9	2965.0	3012.9
tW	2.3	118.9	121.2
W + jets	1.9	0.5	2.4
Z + jets	6.7	1956.2	1962.9
VV + jets ($V = W/Z$)	8.9	121.6	130.5
$t\bar{t}W$	21.0	43.4	64.4
$t\bar{t}Z$	17.5	101.2	118.7
$t\bar{t}H$	17.8	43.2	61.0
tWZ (with $Z \rightarrow \ell\ell$)	3.1	16.4	19.5
tWH	0.6	1.5	2.1
Other	1.9	9.3	11.2
Total	136.7	5411.3	5548.0
S/B (%)	0.6627	0.0222	0.0379
Significance	0.0771	0.0163	0.0282

Table 6.2: Event yields at preselection level for SS, OS and SS+OS combination. **The W and Z MC only feature leptonic decays**

The definition of the significance estimator used in this work is the one given in reference [169]

$$\text{Significance} = \sqrt{2[(s+b)\ln(1+s/b) - s]}, \quad (6.1)$$

where s is the number of events of the target process and b is the number of yields for the rest of processes combined. This can be used not only to evaluate the signal significance but also the significance of the background processes in the dedicated CRs.

6.6.1 Preselection

Refer to chapter 2 and the geometrical acceptance of the detector to justify the PR cuts

Preselection requirements

2813 6.6.2 Discriminant variables

2814 To enhance the capability of discrimination between processes, new vari-
2815 ables are build out of several others. Some of these are useful to improve
2816 the separation. The first task in this regard is to substitute the classifica-
2817 tion of the light leptons from leading (ℓ_1) and subleading (ℓ_2) lepton to ℓ_{top}
2818 and ℓ_{Higgs} . The variables using the light-lepton origin are more discriminant
2819 than the ones that classify them by the the p_{T} . **Aportar un figura donde**
2820 **se vea la diferencia entre emplear (ℓ_1 , ℓ_2) y (ℓ_{top} , ℓ_{Higgs})**

2821 6.6.3 BDT

2822 Since a BDT is going to be used for both the lepton assign-
2823 ment and region definition, it may be interesting to describe the
2824 technicalities of the BDT in an appendix

2825 Maybe, it can also be a good idea to explain the generalities of
2826 the BDT for region definition here and then put the BDT results
2827 into "Signal Region" and "Control Regions" section.

2828 6.6.3.1 Performance**2829 6.6.3.2 Ranking of variables****2830 6.6.3.3 Hyperparameter optimisation****2831 Grid search****2832 Genetic algorithm**

2833 **6.6.3.4 Negative-weights strategy**

2834 **6.6.3.5 k-Folding**

2835 **6.6.4 Signal Region**

2836 **6.6.4.1 Same Sign channel**

2837 **6.6.4.2 Opposite Sign channel**

2838 Here I shall explain the problem with some variables such us
2839 MET that, despite having great separation power, produce the
2840 effect of not differentiating the tHq signal from the $t\bar{t}$ contribu-
2841 tions.

2842 **6.6.5 Control Regions**

2843 **6.6.5.1 Same Sign channel**

2844 $t\bar{t}$

2845 $t\bar{t}W$

2846 $t\bar{t}Z$

2847 $t\bar{t}H$

2848 **6.6.5.2 Opposite Sign channel**

2849 $t\bar{t}$

2850 $Z +\text{jets}$

2851 **Diboson**

2852 tW

2853 6.7 Systematic uncertainties

2854 Particle collision physics distinguish two types of uncertainties, the statis-
 2855 tical uncertainty and the systematic uncertainty. The statistical uncer-
 2856 tainty is the result of stochastic fluctuations in data and is the result of a
 2857 limited size of analysed dataset. It is fully uncorrelated between subsequent
 2858 measurements. On the other hand there are the systematic uncertainties,
 2859 which are defined as everything that is not a statistical error. These are
 2860 fully correlated between subsequent measurements and are associated with
 2861 all sort of sources such us the measurement apparatus, the assumptions
 2862 made, the model used, the MC generator and many others.

2863 While the statistical uncertainty is usually intrinsically added in the
 2864 inference method, the inclusion of the systematic uncertainties and its
 2865 propagation through the statistical analysis are not trivial.

2866 Alternative samples are produced to evaluate the systematics: - Herwig7
 2867 -> parton shower
 2868 - asdfas. -> modelling

2869

2870 6.7.1 Theoretical uncertainties

2871 6.7.2 Modelling uncertainties

2872 6.7.3 Experimental uncertainties

2873 6.8 Fit results

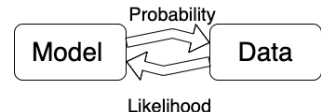
2874 6.8.1 Likelihood fit

2875 **Maybe I move the statistics description to an appendix** The
 2876 likelihood fit....

2877 The likelihood function is defined as the probability of observing a cer-
 2878 tain set of data (\vec{x}) given a model or hypothesis with certain parameter
 2879 values ($\vec{\theta}$). It is given by

2880

$$L(\vec{\theta}) = \mathcal{P}(\vec{x}|\vec{\theta}) = \prod_i \mathcal{P}(x_i|\vec{\theta})$$



where i runs over the data points. By maximising the likelihood function, the parameters $\vec{\theta}$ of the model that better fit the data are obtained. These are known as estimated values. The fit is the parameter estimation via the Likelihood maximisation, $\vec{\theta}_{estimated} = \text{argmax}_{\vec{\theta}} L(\vec{\theta})$.

For binned distributions the likelihood function can be written as

$$L(\vec{n}|\vec{\theta}) = \prod_{i \in bins} \mathcal{P}(n_i^{obs}|n_i^{exp}(\vec{\theta})) = \prod_{i \in bins} \mathcal{P}(n_i^{obs}|S_i^{exp}(\vec{\theta}) + B_i^{exp}(\vec{\theta}))$$

Here, i runs over the bins of the histogram, n_i^{obs} and n_i^{exp} are the observed and expected number of entries in the bin i . The predicted signal and background entries in the bin i are S_i and B_i .

Since particle physics experiments are counting experiments, the distribution follows the poissonian statistics. The Poisson distribution is a discrete probability distribution that expresses the probability of a given number of events occurring in a fixed interval of time or space if these events occur with a known constant mean rate and independently of the time since the last event

From the frequentist point of view the probability is defined as the fraction of times an event occurs, in the limit of very large number ($N \rightarrow \infty$) of repeated trials

$$\mathcal{P} = \lim_{N \rightarrow \infty} \frac{\text{Number of favorable cases}}{N}$$

where N is the number of trials. Even though this infinity can be conceptually unpleasant, for LHC experiments, the amount of events is so large that this \mathcal{P} definition becomes acceptable [170].

In contrast, for the Bayesian (or subjective) probability expresses the degree of belief that a claim is true. Starting from a prior probability, following some observation, the probability can be modified into a posterior probability. The more information an individual receives, the more Bayesian probability is insensitive on prior probability [170].

The Bayes theorem [171] states that considering two events A and B , the probability of A to happen given that B takes places is

$$\mathcal{P}(A|B) = \frac{\mathcal{P}(B|A)\mathcal{P}(A)}{\mathcal{P}(B)}$$

where $\mathcal{P}(B|A)$ is the conditional probability of B given A and $\mathcal{P}(B)$ the probability of the event B to happen. Here, $\mathcal{P}(A)$ has the role of prior probability while $\mathcal{P}(A|B)$ is known as posterior probability.

²⁹⁰⁵ **6.8.2 Strategy**

²⁹⁰⁶ **6.8.3 Fit with Asimov data**

²⁹⁰⁷ **6.8.3.1 Post-fit**

²⁹⁰⁸ **6.8.3.2 Pruning**

²⁹⁰⁹ **6.8.3.3 Nuisance Parameters**

²⁹¹⁰ **6.8.3.4 Correlation matrix**

²⁹¹¹ **6.8.3.5 Ranking**

²⁹¹² **6.8.4 Fit to data**

²⁹¹³ **6.8.4.1 Post-fit**

²⁹¹⁴ **6.8.4.2 Pruning**

²⁹¹⁵ **6.8.4.3 Nuisance Parameters**

²⁹¹⁶ **6.8.4.4 Correlation matrix**

²⁹¹⁷ **6.8.4.5 Ranking**

²⁹¹⁸ **6.8.5 Results**

The signal strength μ is defined as the ratio of the measured Higgs boson rate to its SM prediction. For the tHq , the signal strength production is:

$$\mu_{tHq} = \frac{\sigma_{tHq}}{(\sigma_{tHq})_{SM}}.$$

For particular desintegration mode f the decay signal strength is:

$$\mu^f = \frac{BR^f}{(BR^f)_{SM}},$$

being BR^f the branching ratio for the f decay mode. Since cross-section and the BR cannot be separated without further assumptions, only the product can measured experimentally, leading to the combined signal strength:

$$\mu_{tHq}^f = \frac{\sigma_{tHq} \cdot BR^f}{(\sigma_{tHq})_{SM} \cdot (BR^f)_{SM}} = \mu_{tHq} \cdot \mu^f.$$

2919 In our particular case f is $2\ell \text{ OS} + 1\tau_{\text{had}}$ or $2\ell \text{ SS} + 1\tau_{\text{had}}$.

2920 **6.8.6 Data fit**

2921 **6.9 Combination results**

2922 **Discuss results, compare them with CMS, future perspectives**
2923 ...

2924 **6.10 Conclusions**

²⁹²⁵ Chapter 7

²⁹²⁶ Conclusion

2927 **Appendix A**

2928 **Effect of negative weights**

2929 **A.1 Negative weights uncertainties**

- 2930 • What is a weight in a MC event?
- 2931 • Why are there negatively weighted events?
- 2932 • Why are negative weights problematic?

2933 **A.2 Statistical uncertainty of negative
2934 weights**

2935 Assume that there is a sample of N Monte Carlo simulated events. Of
2936 these, a fraction x have negative weights and, therefore, a fraction $(1 - x)$
2937 has a positive weight. The effective number of events is $(N_+ - N_-)$, being
2938 $N_+ = (1 - x)N$ the amount of positively weighted events and $N_- = xN$ the
2939 same for the negative weights.

2940 The statistical fluctuations are calculated in terms of x and the standard
2941 deviation ($\sigma_N = \sqrt{N}$). The number of positive and negative events can
2942 fluctuate randomly between $\pm\sigma_-$ for the later and $\pm\sigma_+$ for the former.
2943 Here, $\sigma_- = \sqrt{xN} = \sqrt{x}N$ and $\sigma_+ = \sqrt{1-x}N$

The variance ($V = \sigma^2$) of the sample is then

$$V(N_+ - N_-) = xV(N) + (1 - x)V(N) = V(N)$$

and the fractional uncertainty

$$\frac{\sigma(N_+ - N_-)}{N_+ - N_-} = \frac{\sigma_N}{(1 - x)N - xN} = \frac{1}{1 - 2x} \frac{\sigma_n}{N}$$

2944 When the fraction of negative events is $x = 0$, $\frac{\sigma(N_+ - N_-)}{N_+ - N_-} = \frac{\sigma_n}{N}$ as expected.
 2945 In contrast, if $x = 0.5$ the fractional uncertainty is infinite, as expected.

2946 For the signal tHq $2\ell + 1\tau_{\text{had}}$ MC signal sample the fraction of negative
 2947 weights is between 0.3 and 0.4 depending on the production used.

$$2948 \quad \bullet \quad x = 0.3 \rightarrow \frac{\sigma(N_+ - N_-)}{N_+ - N_-} = \frac{1}{0.2} \frac{\sigma_n}{N} = 5.0 \frac{\sigma_n}{N}$$

$$2949 \quad \bullet \quad x = 0.4 \rightarrow \frac{\sigma(N_+ - N_-)}{N_+ - N_-} = \frac{1}{0.4} \frac{\sigma_n}{N} = 2.5 \frac{\sigma_n}{N}$$

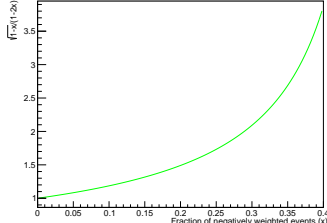
2950 The uncertainty of the effective number of events can be compared to
 2951 that of using only the positively weighted events. If the two fractional
 2952 uncertainties are divided:

$$\frac{\frac{\sigma(N_+ - N_-)}{N_+ - N_-}}{\frac{\sigma(N_+)}{N_x}} = \frac{\frac{1}{1-2x} \frac{\sigma_n}{N}}{\frac{1}{\sqrt{(1-x)N}}} = \frac{\sqrt{1-x} \sigma_n}{1-2x} \frac{1}{N} = \frac{\sqrt{1-x}}{1-2x}$$

2953 In the range of x values for the $2\ell + 1\tau_{\text{had}}$ simulated signal events.

$$2954 \quad \bullet \quad x = 0.3 \rightarrow \frac{\frac{\sigma(N_+ - N_-)}{N_+ - N_-}}{\frac{\sigma(N_+)}{N_x}} = 2.09$$

$$2955 \quad \bullet \quad x = 0.4 \rightarrow \frac{\frac{\sigma(N_+ - N_-)}{N_+ - N_-}}{\frac{\sigma(N_+)}{N_x}} = 3.87$$



2955 In Figure A.1, several ΔR distributions generated using all the events
 2956 and just the positively weighted ones. As expected, the uncertainty bands
 2957 are bigger for the 'All events' than for the 'Positive events'. These his-
 2958 tograms were produced to verify that using only the events with positive
 2959 weights in the training of the BDT for lepton assignment in the SS scenario
 2960 (Section 6.4.3) was not biasing the result. The size of the error bands is
 2961 calculated by ROOT as the square root of the quadratic sum of the weights,
 2962 as explained below.

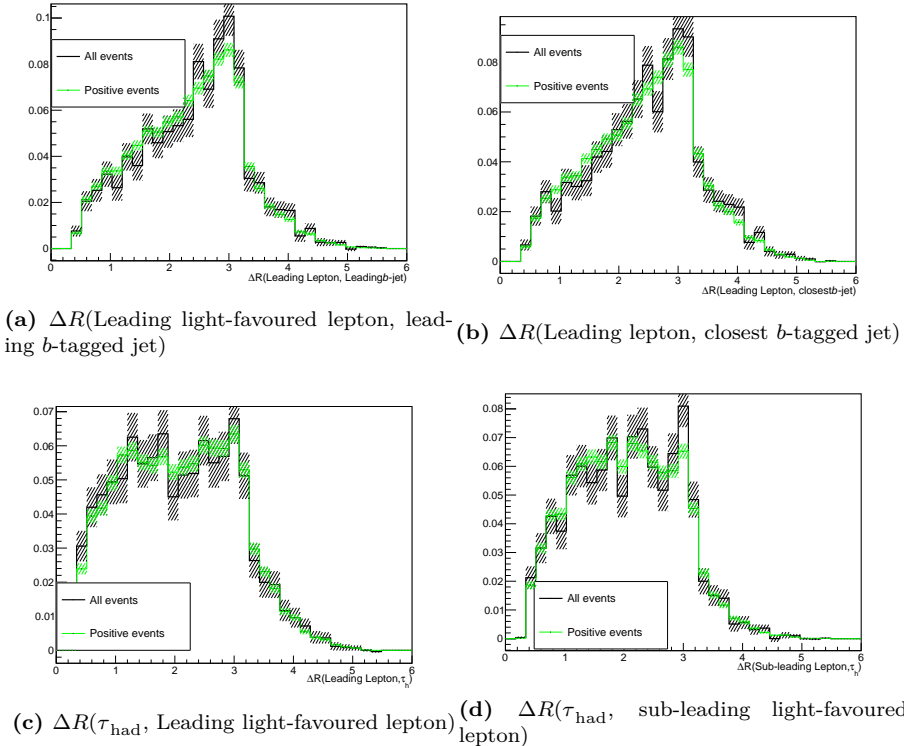


Figure A.1: Some normalised distributions for all the signal events in the $2\ell \text{SS} + 1\tau_{\text{had}}$ (black) and just the positively weighted events (green). For each bin, the error band is calculated as the square root of the quadratic sum of the weights.

2963 A.2.1 Errors in binned histograms

If a bin of a histogram has n entries of weighted events w_i with $i = 1, 2, \dots, n$, the size of the bar is $\sum_{i=1}^n w_i$. Therefore, the error of that bar is

$$\sqrt{\sum_{i=1}^n w_i^2} \quad (\text{A.1})$$

This expression for the error of a bin in a histogram is based on error propagation and intrinsic poissonian statistics only. The variance, i.e. the error on the weighted number of events" in that bin, is given by error propagation:

$$V\left(\sum_{i=1}^n w_i\right) = \sqrt{\left(\sum_{i=1}^n w_i^2\right)^2} = \sum_{i=1}^n w_i^2 = \sum_{i=1}^n V(w_i)$$

2964 The variance of the weight w_i , $V(w_i)$, is determined only by the statistical
2965 fluctuation of the number of events considered: $V(w_i) = w_i^2$.

2966 A.3 Negative weights in MVA methods

2967 Events coming from the MC generator can be produced with (unphys-
2968 ical) negative weights in some phase-space regions. Such occurrences are
2969 frequently inconvenient to deal with, and whether or not they are handled ef-
2970 fectively is dependent on the MVA method's actual implementation. Within
2971 the ROOT TMVA library, probability and multi-dimensional probability
2972 density estimators, as well as BDTs, are among the methods that correctly
2973 include occurrences with negative weights. In cases where a method does
2974 not properly treat events with negative weights, it is advisable to ignore such
2975 events for the training but to include them in the performance evaluation
2976 to not bias the results.

2977 **Appendix B**

2978 **Boosted Decision Trees**

2979 A boosted decision tree, typically referred just by its acronym BDT, is
2980 a supervised¹ machine learning (ML) technique used for classification. The
2981 analysis presented in this thesis uses several BDTs. Both the light lepton
2982 origin assignment (Section 6.4.3) and the signal to background separation
2983 (Section 6.6.3) are based on a BDT. This tool is applied in more scenarios
2984 within within ATLAS. In the b -tagging, for instance, a BDT is trained to
2985 discriminate b -jets from light-jets [172].

2986 **B.1 How does a BDT work?**

2987 A BDT is an ensamble of decision trees. Each decision tree is a map
2988 of possible results of related decisions. A decision tree takes a set of input
2989 features and splits input data recursively based on those features. This
2990 results in a tree structure that resembles that of a flow charts with a decision
2991 or split at each node. The last level of the trees are the so called leaves and
2992 each represents a class. An example of a tree can be seen on Figure B.1,
2993 where an event is classified in one of the two categories following a set of
2994 yes-no questions. In this work the BDTs employed are binary, i.e. separates
2995 into two categories, but multiclassifier BDTs could be used as well².

Boosting is a technique for turning numerous weak classifiers (trees in this case) into a powerful one. Each tree is created iteratively depending on the prior ones. The output of each tree, $h_t(\mathbf{x})$, is given a weight, w_t ,

¹Supervised learning means that the data used in the training is labeled.

²For the signal to background discrimination, multiclassifier BDTs were tested but the result was not satisfactory.

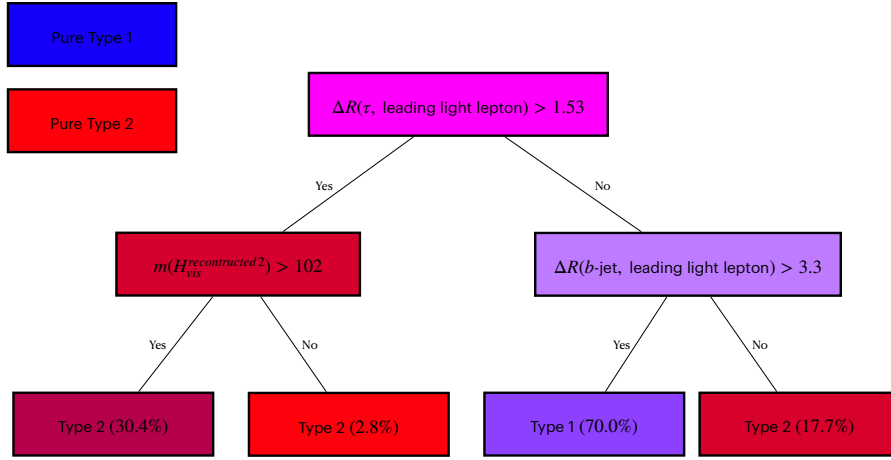


Figure B.1: Example of a decision tree with three nodes. This particular example corresponds to one of the trees in the BDT for the light lepton origin assignment (see Section 6.4.3). The color of the boxes represents the purity on Type 1 or Type 2 events that arrive to each node. Repeated left/right (yes/no) decisions are taken on one single variable at a time until the classification takes place.

relative to its accuracy. The ensamble output is the weighted sum

$$\hat{y}(\mathbf{x}) = \sum_t w_t h_t(\mathbf{x})$$

where t run over the trees. The goal of the boosting is to minimise a regularised objective function

$$L(x) = \sum_i l(\hat{y}_i, y_i) + \sum_t \Omega(f_t) \quad (\text{B.1})$$

where $l(\hat{y}_i, y_i) = l(f(\mathbf{x}_i|\theta), y_i)$ is a differentiable convex loss function (the distance between the truth and the prediction of the i^{th} sample) and $\Omega(f_t)$ is the regularisation function (penalises the complexity of the t^{th} tree, f_t). The θ in $f(\mathbf{x}_i|\theta)$ are the model parameters for a BDT these would be the weights and biases. The \mathbf{x}_i are values fo the input variables for the i^{th} sample and y_i the target variable real value.

The $\Omega(f_t)$ term helps to smooth the final learnt weights to avoid overfitting.

The tree ensemble model in Eq. B.1 cannot be optimised using traditional optimisation methods in Euclidean space. The model is trained instead in an additive way so that the the objective function to minimise is:

$$L^{(t)} = \sum_i^n l(y_i, \hat{y}_i^{(t-1)} + f_t(\mathbf{x}_i)) + \Omega(f_t). \quad (\text{B.2})$$

3004 There are several types of boosting for BDTs. Some of the most common
 3005 are AdaBoost, Gradient Boosting and XGBoost. The later, which stands
 3006 for “eXtreme Gradient Boosting”, is the used in this work and its details can
 3007 be found in reference [173]. Boosting can significantly improve performance
 3008 compared to that of a single tree and stabilise the response of the decision
 3009 trees to fluctuations in the training sample.

3010 **B.1.1 Training**

3011 For a ML algorithm, to train means to learn or determine good values
 3012 for all the weights within that model. To do so, the algorithm takes the
 3013 labelled data and fits the model. For instance, for the signal discrimination,
 3014 the ML model takes the MC samples, where all the events are labeled either
 3015 as signal or background events. A renormalisation can take place if needed.
 3016 With the data, the model also needs a set of variables that have some power
 3017 to discriminate between our categories. A condition on one discriminant
 3018 variable is set on each node of the BDT to split the phase space into two
 3019 parts. The aim of the training is to find the optimal cut in each node so that
 3020 after it the separation between the categories is maximised, in our example
 3021 one category is enriched in background and the other in signal. This is
 3022 done in a loop over all discriminating variables and trying to test as many
 3023 as possible values for each cut (the default in TMVA is trying 20 values for
 3024 each variable). The best splitting is defined on the basis of the splitting
 3025 index, which works as a measure of inequality because we want to measure the
 3026 inequality between the two categories in each split node. A low splitting
 3027 index value means a high inequality between the classes, i.e. high purity.
 3028 The best cut is defined as the one that yields the highest splitting
 3029 index difference between the parent node and the two children node (each
 3030 weighted by the total number of events in the corresponding block). Then
 3031 it is possible keep splitting blocks until a stopping requirement is satisfied.

3032 **Internal reweight of events in training sample**

3033 Sometimes, MC generators may provide event weights which may turn out
 3034 to be extremely small or very high. To avoid artefacts, TMVA can renor-
 3035 malise the signal and background training weights internally so that their
 3036 respective sums of effective (weighted) events are equal. By doing this,
 3037 the performance of the BDT can be improved since some classifiers are
 3038 sensitive to the relative amount of each category (Type1/Type2 or sig-
 3039 nal/background) in the training data. While for the lepton assignment
 3040 this renormalisation does not play an important role (the amount of Type1

3041 and Type2 signal events is similar), for the the tHq signal discrimination
 3042 the signal sample in the training test has to be reweighted.

3043 **B.1.1.1 Loss function**

3044 Sometimes called error function, the loss function is used to define what
 3045 is a good prediction and what is not by assessing how far an estimated value
 3046 is from its true value for a particular model iteration and penalising errors
 3047 in the prediction. Therefore, it is crucial to any supervised ML model.
 3048 Depending on whether the model is for a regression or for classification, the
 3049 way $l(y_n, f(\mathbf{x}_n|\theta))$ is defined may vary and, for the analysis, only binary
 3050 classification BDTs have been used.

3051 Classification problems include foreseeing a discrete class output. It
 3052 entails categorising the dataset into distinct categories based on various
 3053 factors (variables) so that when new and unseen data appears it can be
 3054 classified as well.

3055 **XGBoost loss functions**

3056 The loss function that have been used for predicting probabilities for the
 3057 binary classification in the signal selection is “binary:logistic” but there are
 3058 other available options such as “binary:logitraw” and “binary:hinge”. Some
 3059 tests were carried using a multiclass BDT, for those the “multi:softprob”
 3060 loss function was used.

When using the binary logistic loss function of XGBoost, the l in Eq B.2 is the logarithmic likelihood of the Bernoulli distribution and it takes the form

$$l = y_i \log[\text{logistic}(\hat{y}_i^{(t-1)} + f_t(\mathbf{x}_i))] + (1 - y_i) \log[1 - \text{logistic}(\hat{y}_i^{(t-1)} + f_t(\mathbf{x}_i))] \quad (\text{B.3})$$

where $\text{logistic}(\hat{y}_i^{(t-1)} + f_t(\mathbf{x}_i))$ is the probability. In an algebraically equivalent manner, it can be written as:

$$l = y_i[\hat{y}_i^{t-1} + f_t(\mathbf{x}_i)] - \log(1 + \exp(\hat{y}_i^{t-1} + f_t(\mathbf{x}_i))) \quad (\text{B.4})$$

3061 Other loss functions

- 3062 • **binary:logistic:** Logistic regression for binary classification, output
 3063 probability
- 3064 • **binary:logitraw:** Logistic regression for binary classification, output
 3065 score before logistic transformation

- **binary:hinge**: Hinge loss for binary classification. This makes predictions of 0 or 1, rather than producing probabilities.

$$l(f(x_i|\theta), y_i) = \max(0, 1 - f(x_i|\theta)y_i) \quad (\text{B.5})$$

3066 **B.1.1.2 Overtraining**

3067 Let's consider a ML model $f(\mathbf{x}|\theta)$, where x are the data points used as
 3068 input and θ the tuneable parameters of the model. The function $f(\mathbf{x}|\theta)$
 3069 outputs the prediction of the model. The parameters θ of the model are
 3070 tuned during the training process using a training set (\mathcal{T}). The true output
 3071 (y) of the elements in \mathcal{T} . When successful, the training finds the θ that
 3072 performs as good as possible on new, unseen, data.

For a given $f(\mathbf{x}|\theta)$ model, the training error, $\text{err}(\mathcal{T})$, is defined by [174]:

$$\text{err}(\mathcal{T}) = \frac{1}{N_t} \sum_{n=1}^{N_t} l(y_n, f(\mathbf{x}_n|\theta)) \quad (\text{B.6})$$

3073 where N_t is the number of events used for the training and l the chosen loss
 3074 function and \mathbf{x}_n and y_n the points in the training set. So, the error function
 3075 measures the model's error on a group of objects, whereas the loss function
 3076 deals with a single data instance.

3077 The $\text{err}(\mathcal{T})$ is a poor estimator of the model's performance on new data.
 3078 It usually decreases as the number of training cycles increases, and it can
 3079 begin to adapt to noise in the training data. When this happens the training
 3080 error continues to decrease but the error on the data outside of the training
 3081 set starts increasing, jeopardising the general performance of the model.
 3082 This effect is the so called overfitting or overtraining.

3083 Overtraining occurs when a ML model can accurately predict training
 3084 examples but is unable to generalise³ to new data. When overtraining takes
 3085 place, the ML model has learnt the details of the training data to an extent
 3086 in which these knowledge do not reflect the behaviour of the test sample.
 3087 This results in poor field performance.

3088 Figure B.2 shows how an overtrained BDT evolves. In Figure B.2a can
 3089 be seen that as the training of the BDT continues, the ability of the model
 3090 to classify the events in \mathcal{T} (blue) improves while for the data in the test
 3091 sample (orange) it doesn't. This means that the model is not generalising
 3092 properly. With the plot of the loss function (Figure B.2b) can be seen how
 3093 the error of the test data slightly increases while for the training samples is
 3094 strongly reduced.

³By generalise is meant that the model recognises only those characteristics of the data that are general enough to also apply to some unseen data.

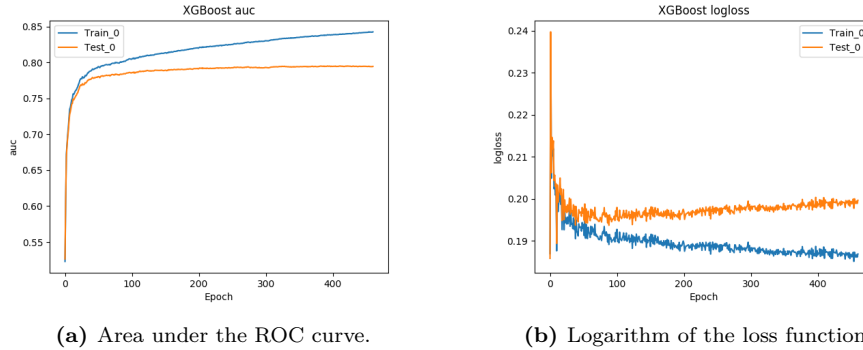


Figure B.2: Example of the evolution of the BDT metrics when overtraining occurs. The x-axis shows the training iteration.

When tested on the training sample, overtraining results in an apparent improvement in classification or regression performance over the objectively achievable one, but an effective performance loss when measured on an independent test sample (even though, there is a risk that it can still happen even if we use separate test data). Until deployed to real unseen data, there is a danger that overtraining will go unnoticed. This makes of overtraining one of the greatest dangers in ML. Other names for this phenomenon are overfitting and type III error.

Usually, this is a result of too little data or data that is too homogenous. Overtraining arises when there are too few degrees of freedom, because too many model parameters of an algorithm were adjusted to too few data points. Not all MVA methods are equally sensible to overtraining. While Fisher discriminant hardly suffers from it, BDTs usually suffer from at least partial overtraining, owing to their large number of nodes. Nevertheless, for the BDTs some countermeasures can be applied to preserve the ability to generalise:

- Never test the model on the data used for the training.
- The number of nodes in boosted decision trees can be reduced by removing insignificant ones (“tree pruning”). There are two types, pre-pruning and post-pruning
 - Pre-pruning: Refers to the early stopping of the growth of the decision tree
 - Post-pruning: Allows the decision tree model to grow to its full depth, then removes the tree branches to prevent the model from overfitting

- 3120 • Cross validation is a powerful technique to use all the data for training
 3121 at the same time that all the data for testing is employed while
 3122 avoiding overfitting. This method is based in cleverly iterating the
 3123 test and training split around and it is described in Section B.3.

3124 **B.1.2 Evaluation / Validation**

3125 **B.1.3 Application**

3126 **B.2 Treatment of negative weights**

3127 **B.3 Cross validation and k -folding**

3128 Cross validation is a technique consisting in training several ML models
 3129 on different subsets of the input data and evaluated on the complementary
 3130 subset of the data. The goal cross validation is to estimate the performance
 3131 of a machine learning model. It can identify overfitting or recognise the
 3132 failure of the model to generalise a pattern.

3133 One particular method to do this is the k -folding. It consists on splitting
 3134 the input data into $k \in \mathcal{N}$ equally-sized subsets. Each of these is known
 3135 as fold. With this procedure the ML model is trained k times. For each
 3136 train $k - 1$ folds are used as training set and the non-used fold is the subset
 3137 of date where the evaluation takes place. All folds are used once as test
 3138 sample and $k - 1$ times in the train sample.

3139 k -folding cross validation resample is of particular interest when the data
 3140 available is limited because, by using it, all events are used in the training
 3141 phase. It generally results in a less biased or less optimistic estimate of the
 3142 model skill than other methods, such as a simple train/test split.

3143 Note that when the score of the model is applied, each event gets the
 3144 score that was assigned when it was used as test event. Not doing this
 3145 would bias the model.

The expected error for a $f(x|\theta)$ trained using k -folding is:

$$\text{err}(\mathcal{T}) = \frac{1}{k} \sum_k \text{err}(\mathcal{T}_k), \quad (\text{B.7})$$

3146 where $\text{err}(\mathcal{T}_k)$ is the error as described in Eq. B.6 for each splits test. As
 3147 Eq. B.7 shows, an increase on the number of folds would imply more models
 3148 to average over and, hence, implying an improvement on the confidence of

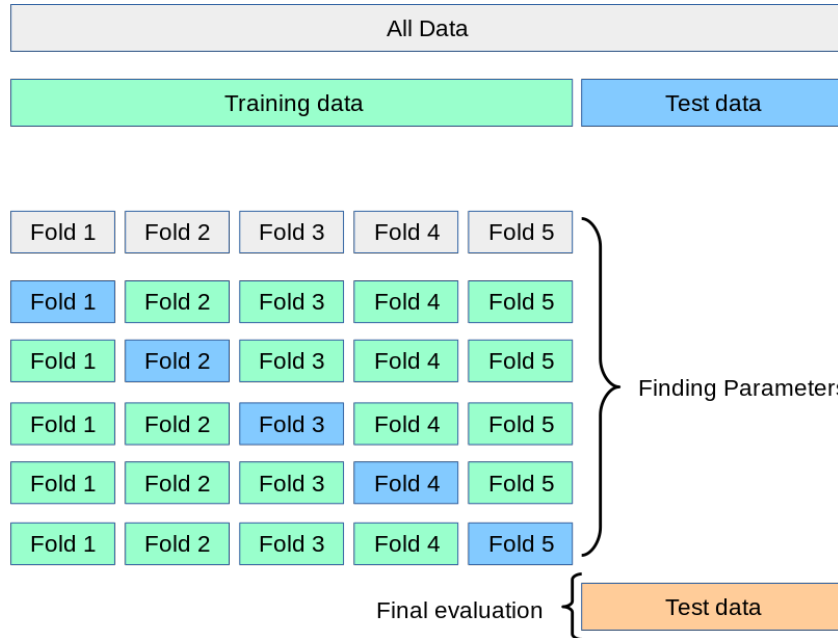


Figure B.3: Illustration of k -folding cross validation using 5 folds.

3149 how consistent the $f(x|\theta)$ achieves a given level of performance. However,
 3150 a larger k would also reduce the statistical strength of each fold.

3151 **Should I comment that the event number is the variable used
 3152 to split the samples into different folds so that we can later assign
 3153 the score properly?**

3154 B.4 Other considerations about BDTs

3155 Binary splits

3156 Rather than splitting into two groups at each node, one could consider
 3157 several splits at each stage. Although this has its benefits, it is not a wise
 3158 general course of action. Multiway splits cause the data to fragment too
 3159 quickly, leaving the next level below with insufficient data. At the end,
 3160 binary splits are favoured because they can also be used to create multiclass
 3161 divides.

3162 Instability of trees

3163 The large variance of trees is one of their main issues. A little modification
 3164 in the data can frequently lead to very different results. This is mainly
 3165 caused by the hierarchical structure of the trees, which causes errors in
 3166 the top split to cascade down to all splits below it. By attempting to

3167 employ a more stable split criterion, this can be somewhat mitigated, but
3168 the fundamental instability remains. It is the cost of using the data to infer
3169 a straightforward, tree-based structure.

3170 **Receiver operating characteristic curve**

3171 The receiver operating characteristic curve (ROC) is graphical plot used
3172 that is used to illustrate the ability of a binary classifier. It assesses the
3173 tradeoff between true positive (TP) and false negative (FP) rates as the
3174 parameters of the classification vary. This is depicted in Figure B.4a.

- 3175 • **True positive rate:** Also known as sensitivity. It is the possibility of
3176 a positive test conditioned on truly being positive. For instance, it's
3177 the probability for the BDT in Section 6.6.3 to identify a tHq event
3178 as such.
- 3179 • **False positivity rate:** It can be calculated as 1 - sensitivity. It refers
3180 to the possibility of a negative test given that it's truly positive. In
3181 the Section 6.6.3 BDT scenario it would be the ability to classify a
3182 background event as if it was tHq signal event.

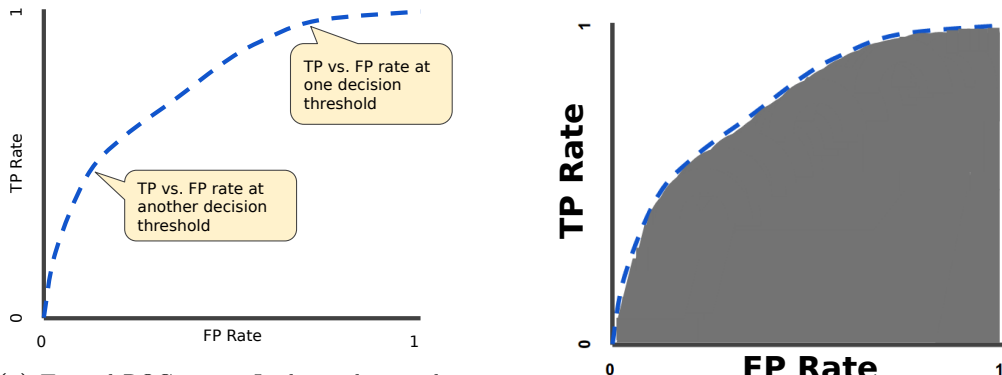
3183 The area under the curve (AUC) is a commonly used quantitative sum-
3184 mary, it measures the bidimensional area under the ROC from (0,0) to (1,1)
3185 as Figure B.4b shows. The use of the AUC is convenient for several two
3186 reasons. Firstly, it is invariant with the scale because it does not meas-
3187 ure absolute values but rates. Secondly, it is invariant with respect to the
3188 classification threshold and, hence, it evaluates quality of the classification
3189 model.

3190 **B.4.1 Hyperparameters**

3191 Hyperparameters is the term used to refer to the specifications that
3192 control⁴ the learning process of a ML algorithm.

3193 A ML model is defined by its model parameters, which are set by the
3194 process of training. In order to reach some level of intelligence, the process
3195 of training a model involves selecting the optimal hyperparameters that
3196 the learning algorithm will use to learn the ideal model parameters that
3197 accurately map the input variables (\mathbf{x}) to the labels (y). The learning
3198 algorithm uses hyperparameters when learning, but these are not included
3199 in the resulting model.

⁴The prefix “hyper” suggest that these parameters are on a higher level that modulates the training process.



(a) Typical ROC curve. It shows that as the classification threshold decreases, more events are classified as positive, causing both the FP and FN rates to increase.

(b) The AUC varies from 0 to 1. While 0.0 corresponds to a model that always fails, a 1.0 means that the model is right a 100% of times.

Figure B.4: The ROC presents the TP vs the FN rate. The ROC analysis is related to cost/benefit interpretation of decision making.

3200 B.4.1.1 XGBoost

3201 In XGBoost, the hyperparameters are classified in three categories: gen-
 3202 eral, booster and task hyperparameters. For the work developed in this
 3203 thesis, the parameters related to the boosting of the trees are the ones that
 3204 have been optimised. The process of finding the optimal set of hyperpara-
 3205 meters for each model is crucial to achieve success.

- 3206 • General parameters: Refers to which booster has been used (typically
 3207 a tree or linear model) and the number of parallel threads to be used
 3208 (set to the maximum in our case).
- 3209 • Booster parameters: Control the performance of the selected booster.
 3210 For trees, the most relevant are:
 - 3211 – **Learning rate:** This tuning parameter in an optimisation al-
 3212 gorithm determines the step size at each iteration while moving
 3213 toward a minimum of a loss function. Figure B.5 shows the evolu-
 3214 tion per epoch for the loss function depending on the learning
 3215 rate. This hyperparameter is also known as eta and ranges from
 3216 0 to 1.
 - 3217 – **Minimum split loss:** Also known as gamma or Lagrangian mul-
 3218 tiplier. it is the A node is split only when the resulting split gives
 3219 a positive reduction in the loss function and the gamma gives the
 3220 minimum loss reduction required to make a further partition on
 3221 a leaf node of the tree. Therefore, the higher the gamma, the
 3222 more conservative the algorithm will be. The minimum split loss

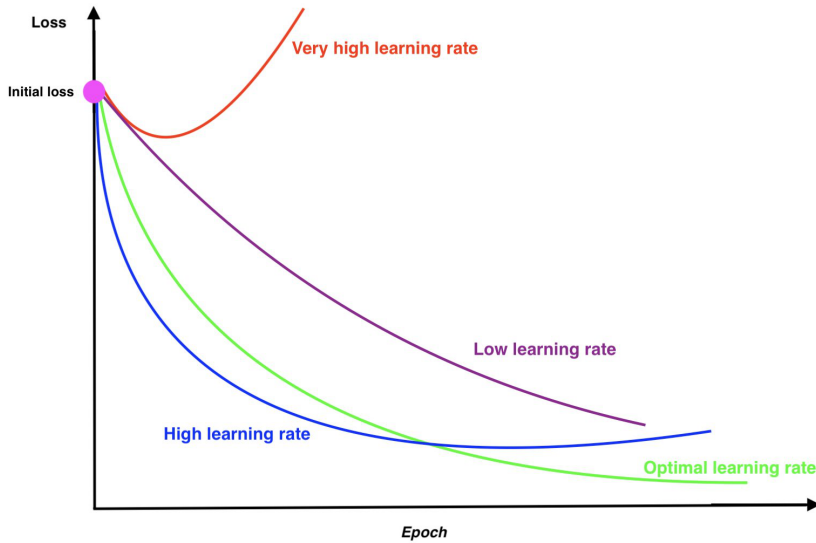


Figure B.5: Different loss-function curves versus iteration. Learning rate is one of the most important hyperparameters to adjust well during the ML model training. If it's high, it can cause the model to diverge. If it's too low it can slow down the training.

3223 ranges from 0 to inf. **We are not optimising this parameter**
 3224 **but using the default (not constrained).** Nevertheless,
 3225 **values between 1 and 10 have been tested.**

- 3226 – **Minimum child weight:** It defines the minimum sum of
 3227 weights of all observations required in a child. When the tree par-
 3228 tition results in a leaf node with the sum of instance weight less
 3229 than the value of this hyperparameter, the tree stops partition-
 3230 ing. Higher min_child_weight prevent the model from learning
 3231 too specific relation. So, this is done to prevent overfitting. This
 3232 tuneable parameter ranges from 0 to inf.
- 3233 – **Maximum depth:** It refers to the number of splits in each tree,
 3234 which controls the complexity of the boosted ensamble. The
 3235 maximum depth of a tree is an integer ranging from 1 to inf but
 3236 is rare to have trees with depth higher than 10 since XGBoost
 3237 aggressively consumes memory when training a deep tree. In our
 3238 trees this hyperparameter is 4 or 5.
- 3239 – **Scale of positive weight:** When the categories are imbalanced
 3240 as it is the case for the signal and background categories in this
 3241 analysis, the signal sample can be reweighted by this value to
 3242 have a larger impact. The typical value to consider is the frac-
 3243 tion between positive instances (signal) and negative instances
 3244 (background). When the BDT is targeting the identification of
 3245 background processes this hyperparameter is also used although
 3246 it does not take such extreme values.

- 3247 – Maximum delta step:
- 3248 – **Tree method:** It alludes to the tree construction algorithm
3249 used in XGBoost. Since the training of the BDTs takes place
3250 in ARTEMISA⁵ facility [175], the method used here is the GPU
3251 implementation of the faster histogram optimised approximate
3252 greedy algorithm.
- 3253 • Learning task parameters: Decide on the learning scenario. Specify
3254 the learning task and the corresponding learning objective.

⁵ARTEMISA (ARTificial Environment for Machine learning and Innovation in Scientific Advanced computing) is a ML dedicated facility at IFIC. It is composed of several Intel Xeon Platinum CPUs and Tesla Volta GPUs that help to find the optimal configuration for ML algorithms.

³²⁵⁵ Abbreviations

³²⁵⁶

Acronym	Meaning
AD	Antiproton Decelerator
ALICE	A Large Ion Collider Experiment
ATLAS	A Toroidal LArge AparatuS
AWAKE	Advanced Proton Driven Plasma Wakefield Acceleration Experiment
CERN	European Organization for Nuclear Research
CMS	Compact Muon Solenoid
CP	Charge conjugation Parity
CSC	Cathode-Strip Chambers
DAQ	Data Acquisition
ECAL	Electromagnetic Calorimeter
EF	Event Filter
EM	Electromagnetic
EW	Electro Weak
EWSB	Electroweak Symmetry Breaking
FASER	ForwArd Search ExpeRiment
FCAL	Forward calorimeter
FTK	Fast TracKer
GR	General Relativity
HCAL	Hadronic Calorimeter
HLT	High Level Trigger
IBL	Insertable B-Layer
IP	Interaction Point

Acronym	Meaning
IR	Insertion Regions
ISOLDE	On-Line Isotope Mass Separator
ITk	Inner Tracker
LAr	Liquid Argon
LCG	LHC Computing Grid
LEIR	Low Energy Ion Ring
LEP	Large Electron-Positron
LHC	Large Hadron Collider
LHCb	The Large Hadron Collider Beauty
LHCf	Large Hadron Collider forward
LINAC2	Linear Accelerator 2
LINAC3	Linear Accelerator 3
LINAC4	Linear Accelerator 4
3257	LO
	Leading Order
	LVL1
	Level-1 Trigger
	LVL2
	Level-2 Trigger
MATHUSLA	Massive Timing Hodoscope for Ultra Stable neutrAL pArticles
MDT	Monitored Drift Tube
MoEDAL	Monopole and exotic particle detector at the LHC
MS	Muon Spectrometer
NLO	Next-to-Leading Order
NNLO	Next-to-Next-to-Leading Order
PDF	Parton Distribution Function
PS	Proton Synchrotron
PSB	Proton Synchrotron Booster
QCD	Quantum Chromodynamics
QED	Quantum Electrodynamics
QFT	Quantum Field Theory

3258

Acronym	Meaning
RF	Radio Frequency
ROD	ReadOut Drivers
RoI	Regions of interest
ROS	ReadOut Systems
RPC	Resistive Plate Chambers
SCT	Semiconductor Tracker
SFO	Sub-Farm Output
SM	Standar Model
SPS	Super Proton Synchrotron
SSB	Spontaneus Symmetry Breakin
SSC	Superconducting Super Collider
SUSY	Supersimmetry
TGC	Thin Gap Chambers
TI	Transfer Injection

3259 Bibliography

- 3260 ¹G. Aad et al., *Observation of a new particle in the search for the*
3261 *Standard Model Higgs boson with the ATLAS detector at the LHC,*
3262 *Phys. Lett. B* **716** (2012) 1–29 (2012) (cit. on pp. v, 46, 58).
- 3263 ²S. Chatrchyan et al., *Observation of a New Boson at a Mass of 125*
3264 *GeV with the CMS Experiment at the LHC,*
3265 *Phys. Lett. B* **716** (2012) 30–61 (2012) (cit. on pp. v, 46, 58).
- 3266 ³F. Demartin, F. Maltoni, K. Mawatari and M. Zaro,
3267 *Higgs production in association with a single top quark at the LHC,*
3268 *Eur. Phys. J. C* **75** (2015) 267 (2015) (cit. on pp. v, 52, 54–56).
- 3269 ⁴D. de Florian et al., *Handbook of LHC Higgs Cross Sections: 4.*
3270 *Deciphering the Nature of the Higgs Sector*, **2/2017** (2016) (2016)
3271 (cit. on pp. vi, 48–50).
- 3272 ⁵Online Etymology Dictionary, "Physics", (2022)
3273 <https://www.etymonline.com/word/physics> (visited on 20/01/2022)
3274 (cit. on p. 1).
- 3275 ⁶Perseus Digital Library, "fusiko", (2022)
3276 <https://www.perseus.tufts.edu/hopper/text?doc=Perseus:text:1999.04.0057:entry=fusiko/s> (visited on 20/01/2022) (cit. on p. 1).
- 3278 ⁷C Singer, *A Short History of Science to the Nineteenth Century*, p. 35.
3279 (Streeter Press, 2008) (cit. on p. 1).
- 3280 ⁸C. C. W. Taylor et al., *The atomists, leucippus and democritus:*
3281 *fragments: a text and translation with a commentary*, Vol. 5
3282 (University of Toronto Press, 2010) (cit. on p. 2).
- 3283 ⁹O. Leaman, *Key concepts in eastern philosophy* (Routledge, 2002)
3284 (cit. on p. 2).
- 3285 ¹⁰A. Purcell, *Go on a particle quest at the first CERN webfest. Le premier*
3286 *webfest du CERN se lance à la conquête des particules*, (2012) 10 (2012)
3287 (cit. on p. 3).

- ³²⁸⁸¹¹A. Einstein, *The Foundation of the General Theory of Relativity*,
³²⁸⁹*Annalen Phys.* **49** (1916) 769–822, edited by J.-P. Hsu and D. Fine
³²⁹⁰(1916) (cit. on p. 2).
- ³²⁹¹¹²M. Aaboud et al., *Measurement of the W -boson mass in pp collisions at*
³²⁹² $\sqrt{s} = 7$ TeV *with the ATLAS detector*,
³²⁹³*Eur. Phys. J. C* **78** (2018) 110, [Erratum: *Eur.Phys.J.C* 78, 898 (2018)]
³²⁹⁴(2018) (cit. on p. 2).
- ³²⁹⁵¹³S. Schael et al.,
³²⁹⁶*Precision electroweak measurements on the Z resonance*,
³²⁹⁷*Phys. Rept.* **427** (2006) 257–454 (2006) (cit. on p. 2).
- ³²⁹⁸¹⁴F. Englert and R. Brout,
³²⁹⁹*Broken Symmetry and the Mass of Gauge Vector Mesons*,
³³⁰⁰*Phys. Rev. Lett.* **13** (1964) 321–323, edited by J. C. Taylor (1964)
³³⁰¹(cit. on p. 3).
- ³³⁰²¹⁵P. W. Higgs, *Broken Symmetries and the Masses of Gauge Bosons*,
³³⁰³*Phys. Rev. Lett.* **13** (1964) 508–509, edited by J. C. Taylor (1964)
³³⁰⁴(cit. on p. 3).
- ³³⁰⁵¹⁶P. A. M. Dirac, *On the theory of quantum mechanics*,
³³⁰⁶*Proceedings of the Royal Society of London. Series A, Containing*
³³⁰⁷*Papers of a Mathematical and Physical Character* **112** (1926) 661–677
³³⁰⁸(1926) (cit. on p. 3).
- ³³⁰⁹¹⁷R. Aaij et al., *Observation of a narrow pentaquark state, $P_c(4312)^+$, and*
³³¹⁰*of two-peak structure of the $P_c(4450)^+$* ,
³³¹¹*Phys. Rev. Lett.* **122** (2019) 222001 (2019) (cit. on p. 4).
- ³³¹²¹⁸A. Pich, ‘The Standard model of electroweak interactions’,
³³¹³2006 European School of High-Energy Physics (2007) 1
³³¹⁴(cit. on pp. 4, 16).
- ³³¹⁵¹⁹E. Noether, *Invariante variationsprobleme*, ger,
³³¹⁶*Nachrichten von der Gesellschaft der Wissenschaften zu Göttingen*,
³³¹⁷*Mathematisch-Physikalische Klasse* **1918** (1918) 235–257 (1918)
³³¹⁸(cit. on p. 6).
- ³³¹⁹²⁰C. A. Moura and F. Rossi-Torres, *Searches for Violation of CPT*
³³²⁰*Symmetry and Lorentz Invariance with Astrophysical Neutrinos*,
³³²¹*Universe* **8** (2022) 42 (2022) (cit. on p. 9).
- ³³²²²¹J. S. Bell, *Time reversal in field theory*,
³³²³*Proc. Roy. Soc. Lond. A* **231** (1955) 479–495 (1955) (cit. on p. 9).
- ³³²⁴²²R. F. Streater and A. S. Wightman,
³³²⁵*PCT, spin and statistics, and all that* (1989) (cit. on p. 9).

- ³³²⁶²³T. D. Lee and C.-N. Yang,
Question of Parity Conservation in Weak Interactions,
Phys. Rev. **104** (1956) 254–258 (1956) (cit. on p. 10).
- ³³²⁹²⁴C. S. Wu, E. Ambler, R. W. Hayward, D. D. Hoppes and R. P. Hudson,
Experimental Test of Parity Conservation in β Decay,
Phys. Rev. **105** (1957) 1413–1414 (1957) (cit. on p. 10).
- ³³³²²⁵J. H. Christenson, J. W. Cronin, V. L. Fitch and R. Turlay,
Evidence for the 2π Decay of the K_2^0 Meson,
Phys. Rev. Lett. **13** (1964) 138–140 (1964) (cit. on p. 10).
- ³³³⁵²⁶L.-L. Chau and W.-Y. Keung,
Comments on the Parametrization of the Kobayashi-Maskawa Matrix,
Phys. Rev. Lett. **53** (1984) 1802 (1984) (cit. on p. 11).
- ³³³⁸²⁷P. A. Zyla et al., *Review of Particle Physics*,
PTEP **2020** (2020) 083C01 (2020) (cit. on p. 12).
- ³³⁴⁰²⁸A. M. Sirunyan et al.,
*Measurement of the weak mixing angle using the forward-backward
asymmetry of Drell-Yan events in pp collisions at 8 TeV*,
Eur. Phys. J. C **78** (2018) 701 (2018) (cit. on p. 14).
- ³³⁴⁴²⁹O. W. Greenberg, *Spin and Unitary Spin Independence in a Paraquark
Model of Baryons and Mesons*, Phys. Rev. Lett. **13** (1964) 598–602
(1964) (cit. on p. 15).
- ³³⁴⁷³⁰D. D. Ryutov, *Using Plasma Physics to Weigh the Photon*,
Plasma Phys. Control. Fusion **49** (2007) B429 (2007) (cit. on p. 19).
- ³³⁴⁹³¹F. J. Yndurain, *Limits on the mass of the gluon*,
Phys. Lett. B **345** (1995) 524–526 (1995) (cit. on p. 19).
- ³³⁵¹³²J. Goldstone, A. Salam and S. Weinberg, *Broken Symmetries*,
Phys. Rev. **127** (1962) 965–970 (1962) (cit. on p. 21).
- ³³⁵³³³D. M. Webber et al., *Measurement of the Positive Muon Lifetime and
Determination of the Fermi Constant to Part-per-Million Precision*,
Phys. Rev. Lett. **106** (2011) 041803 (2011) (cit. on p. 25).
- ³³⁵⁶³⁴M. Aker et al.,
Direct neutrino-mass measurement with sub-electronvolt sensitivity,
Nature Phys. **18** (2022) 160–166 (2022) (cit. on p. 26).
- ³³⁵⁹³⁵N. Aghanim et al., *Planck 2018 results. VI. Cosmological parameters*,
Astron. Astrophys. **641** (2020) A6, [Erratum: Astron. Astrophys. 652,
C4 (2021)] (2020) (cit. on p. 28).
- ³³⁶²³⁶S. Weinberg, *A New Light Boson?*, Phys. Rev. Lett. **40** (1978) 223–226
(1978) (cit. on p. 29).

- ³³⁶⁴³⁷F. Wilczek,
³³⁶⁵*Problem of Strong P and T Invariance in the Presence of Instantons,*
³³⁶⁶*Phys. Rev. Lett.* **40** (1978) 279–282 (1978) (cit. on p. 29).
- ³³⁶⁷³⁸V. C. Rubin and W. K. Ford Jr., *Rotation of the Andromeda Nebula*
³³⁶⁸*from a Spectroscopic Survey of Emission Regions,*
³³⁶⁹*Astrophys. J.* **159** (1970) 379–403 (1970) (cit. on p. 29).
- ³³⁷⁰³⁹A. N. Taylor, S. Dye, T. J. Broadhurst, N. Benitez and E. van Kampen,
³³⁷¹*Gravitational lens magnification and the mass of abell 1689,*
³³⁷²*Astrophys. J.* **501** (1998) 539 (1998) (cit. on pp. 29, 31).
- ³³⁷³⁴⁰P. A. R. Ade et al., *Planck 2015 results. XIII. Cosmological parameters,*
³³⁷⁴*Astron. Astrophys.* **594** (2016) A13 (2016) (cit. on p. 29).
- ³³⁷⁵⁴¹M. Banner et al., *Observation of Single Isolated Electrons of High*
³³⁷⁶*Transverse Momentum in Events with Missing Transverse Energy at the*
³³⁷⁷*CERN anti-p p Collider*, *Phys. Lett. B* **122** (1983) 476–485 (1983)
³³⁷⁸(cit. on p. 30).
- ³³⁷⁹⁴²G. Arnison et al., *Experimental Observation of Lepton Pairs of*
³³⁸⁰*Invariant Mass Around 95-GeV/c**2 at the CERN SPS Collider,*
³³⁸¹*Phys. Lett. B* **126** (1983) 398–410 (1983) (cit. on p. 30).
- ³³⁸²⁴³I. Zurbano Fernandez et al., *High-Luminosity Large Hadron Collider*
³³⁸³*(HL-LHC): Technical design report,*
³³⁸⁴*10/2020* (2020), edited by I. Béjar Alonso et al. (2020) (cit. on p. 30).
- ³³⁸⁵⁴⁴M. Kobayashi and T. Maskawa,
³³⁸⁶*CP Violation in the Renormalizable Theory of Weak Interaction,*
³³⁸⁷*Prog. Theor. Phys.* **49** (1973) 652–657 (1973) (cit. on p. 32).
- ³³⁸⁸⁴⁵S. L. Glashow, J. Iliopoulos and L. Maiani,
³³⁸⁹*Weak Interactions with Lepton-Hadron Symmetry,*
³³⁹⁰*Phys. Rev. D* **2** (1970) 1285–1292 (1970) (cit. on p. 32).
- ³³⁹¹⁴⁶J. E. Augustin et al.,
³³⁹²*Discovery of a Narrow Resonance in e^+e^- Annihilation,*
³³⁹³*Phys. Rev. Lett.* **33** (1974) 1406–1408 (1974) (cit. on p. 32).
- ³³⁹⁴⁴⁷S. W. Herb et al., *Observation of a Dimuon Resonance at 9.5-GeV in*
³³⁹⁵*400-GeV Proton-Nucleus Collisions,*
³³⁹⁶*Phys. Rev. Lett.* **39** (1977) 252–255 (1977) (cit. on p. 32).
- ³³⁹⁷⁴⁸F. Abe et al., *Observation of top quark production in $\bar{p}p$ collisions,*
³³⁹⁸*Phys. Rev. Lett.* **74** (1995) 2626–2631 (1995) (cit. on p. 32).
- ³³⁹⁹⁴⁹S. Abachi et al., *Observation of the top quark,*
³⁴⁰⁰*Phys. Rev. Lett.* **74** (1995) 2632–2637 (1995) (cit. on p. 32).

- ³⁴⁰¹⁵⁰S. Amoroso et al.,
³⁴⁰²*Strategy for ATLAS top quark mass measurements: 2021-2023,*
³⁴⁰³tech. rep., CERN, 2020 (cit. on pp. 32, 33).
- ³⁴⁰⁴⁵¹Particle Data Group Web Page, *top-quark Mass (Direct Measurements)*,
³⁴⁰⁵(2022) <https://pdglive.lbl.gov/DataBlock.action?node=Q007TP>
³⁴⁰⁶(visited on 22/01/2022) (cit. on p. 33).
- ³⁴⁰⁷⁵²M. Aaboud et al.,
³⁴⁰⁸*Measurement of the top quark mass in the $t\bar{t} \rightarrow \text{lepton+jets}$ channel*
³⁴⁰⁹*from $\sqrt{s} = 8$ TeV ATLAS data and combination with previous results,*
³⁴¹⁰*Eur. Phys. J. C* **79** (2019) 290 (2019) (cit. on p. 33).
- ³⁴¹¹⁵³A. M. Sirunyan et al.,
³⁴¹²*Measurement of the Jet Mass Distribution and Top Quark Mass in*
³⁴¹³*Hadronic Decays of Boosted Top Quarks in pp Collisions at $\sqrt{s} = 13$ TeV,*
³⁴¹⁴*Phys. Rev. Lett.* **124** (2020) 202001 (2020) (cit. on p. 33).
- ³⁴¹⁵⁵⁴*Combination of CDF and D0 results on the mass of the top quark using*
³⁴¹⁶*up 9.7 fb^{-1} at the Tevatron,* (2016) (2016) (cit. on p. 33).
- ³⁴¹⁷⁵⁵J. Jimenez Pena and C. Nellist,
³⁴¹⁸*Top quark mass summary plots June 2022*, tech. rep.,
³⁴¹⁹All figures including auxiliary figures are available at
³⁴²⁰<https://atlas.web.cern.ch/Atlas/GROUPS/PHYSICS/PUBNOTES/ATL-PHYS-PUB-2022-032>: CERN, 2022 (cit. on p. 34).
- ³⁴²²⁵⁶M. Czakon and A. Ferroglio, *Top quark pair production at complete*
³⁴²³*NLO accuracy with NNLO +NNLL corrections in QCD,*
³⁴²⁴*Chinese Physics C* **44** (2020) 083104 (2020) (cit. on p. 34).
- ³⁴²⁵⁵⁷P. Kant et al., *HatHor for single top-quark production: Updated*
³⁴²⁶*predictions and uncertainty estimates for single top-quark production in*
³⁴²⁷*hadronic collisions,* *Comput. Phys. Commun.* **191** (2015) 74–89 (2015)
³⁴²⁸(cit. on p. 37).
- ³⁴²⁹⁵⁸M. Aliev et al.,
³⁴³⁰*HATHOR – HAdronic Top and Heavy quarks crOss section calculatoR,*
³⁴³¹*Comput. Phys. Commun.* **182** (2011) 1034–1046 (2011) (cit. on p. 37).
- ³⁴³²⁵⁹J. A. Aguilar-Saavedra,
³⁴³³*Single top quark production at LHC with anomalous Wtb couplings,*
³⁴³⁴*Nucl. Phys. B* **804** (2008) 160–192 (2008) (cit. on p. 38).
- ³⁴³⁵⁶⁰J. Butterworth et al., *PDF4LHC recommendations for LHC Run II,*
³⁴³⁶*J. Phys. G* **43** (2016) 023001 (2016) (cit. on pp. 39, 75).
- ³⁴³⁷⁶¹A. D. Martin, W. J. Stirling, R. S. Thorne and G. Watt,
³⁴³⁸*Parton distributions for the LHC,* *Eur. Phys. J. C* **63** (2009) 189 (2009)
³⁴³⁹(cit. on pp. 39, 76).

- ³⁴⁴⁰⁶²A. D. Martin, W. J. Stirling, R. S. Thorne and G. Watt,
³⁴⁴¹*Uncertainties on α_S in global PDF analyses and implications for*
³⁴⁴²*predicted hadronic cross sections*, Eur. Phys. J. C **64** (2009) 653–680
³⁴⁴³(2009) (cit. on p. 39).
- ³⁴⁴⁴⁶³H.-L. Lai et al., *New parton distributions for collider physics*,
³⁴⁴⁵Phys. Rev. D **82** (2010) 074024 (2010) (cit. on p. 39).
- ³⁴⁴⁶⁶⁴R. D. Ball et al., *Parton distributions with QED corrections*,
³⁴⁴⁷Nucl. Phys. B **877** (2013) 290–320 (2013) (cit. on p. 39).
- ³⁴⁴⁸⁶⁵M. Komm, ‘Measurement of Top-Quark Polarization in t-channel
³⁴⁴⁹Single-Top Production’,
³⁴⁵⁰7th International Workshop on Top Quark Physics (2014)
³⁴⁵¹(cit. on p. 44).
- ³⁴⁵²⁶⁶P. Martínez-Agulló,
³⁴⁵³*Optimisation of selection criteria of t-channel single-top-quark events at*
³⁴⁵⁴ $\sqrt{s}=13$ TeV *for studies of anomalous couplings in the Wtb vertex*,
³⁴⁵⁵MA thesis: Valencia U., 2017 (cit. on p. 44).
- ³⁴⁵⁶⁶⁷G. Aad et al., *Measurement of the polarisation of single top quarks and*
³⁴⁵⁷*antiquarks produced in the t-channel at $\sqrt{s} = 13$ TeV and bounds on the*
³⁴⁵⁸ *tWb dipole operator from the ATLAS experiment*, JHEP **11** (2022) 040
³⁴⁵⁹(2022) (cit. on p. 44).
- ³⁴⁶⁰⁶⁸Particle Data Group Web Page, *Higgs-boson Mass*, (2022)
³⁴⁶¹<https://pdglive.lbl.gov/DataBlock.action?node=S126M> (visited
³⁴⁶²on 22/01/2022) (cit. on p. 46).
- ³⁴⁶³⁶⁹M. Aaboud et al., *Measurement of the Higgs boson mass in the*
³⁴⁶⁴ *$H \rightarrow ZZ^*$ → 4ℓ and $H \rightarrow \gamma\gamma$ channels with $\sqrt{s} = 13$ TeV pp collisions*
³⁴⁶⁵*using the ATLAS detector*, Phys. Lett. B **784** (2018) 345–366 (2018)
³⁴⁶⁶(cit. on p. 46).
- ³⁴⁶⁷⁷⁰A. M. Sirunyan et al.,
³⁴⁶⁸*A measurement of the Higgs boson mass in the diphoton decay channel*,
³⁴⁶⁹Phys. Lett. B **805** (2020) 135425 (2020) (cit. on p. 46).
- ³⁴⁷⁰⁷¹F. Englert and R. Brout,
³⁴⁷¹*Broken symmetry and the mass of gauge vector mesons*,
³⁴⁷²Phys. Rev. Lett. **13** (9 1964) 321–323 (1964) (cit. on p. 46).
- ³⁴⁷³⁷²P. W. Higgs, *Broken symmetries and the masses of gauge bosons*,
³⁴⁷⁴Phys. Rev. Lett. **13** (16 1964) 508–509 (1964) (cit. on p. 46).
- ³⁴⁷⁵⁷³G. S. Guralnik, C. R. Hagen and T. W. B. Kibble,
³⁴⁷⁶*Global conservation laws and massless particles*,
³⁴⁷⁷Phys. Rev. Lett. **13** (20 1964) 585–587 (1964) (cit. on p. 46).

- ³⁴⁷⁸⁷⁴T. Aaltonen et al., *Combined search for the standard model Higgs boson*
³⁴⁷⁹*decaying to a $b\bar{b}$ pair using the full CDF data set,*
³⁴⁸⁰*Phys. Rev. Lett.* **109** (2012) 111802 (2012) (cit. on p. 46).
- ³⁴⁸¹⁷⁵V. M. Abazov et al., *Combined Search for the Standard Model Higgs*
³⁴⁸²*Boson Decaying to $b\bar{b}$ Using the D0 Run II Data Set,*
³⁴⁸³*Phys. Rev. Lett.* **109** (2012) 121802 (2012) (cit. on p. 46).
- ³⁴⁸⁴⁷⁶B. Mellado Garcia, P. Musella, M. Grazzini and R. Harlander,
³⁴⁸⁵*CERN Report 4: Part I Standard Model Predictions*, (2016) (2016)
³⁴⁸⁶(cit. on p. 49).
- ³⁴⁸⁷⁷⁷M. Farina, C. Grojean, F. Maltoni, E. Salvioni and A. Thamm,
³⁴⁸⁸*Lifting degeneracies in Higgs couplings using single top production in*
³⁴⁸⁹*association with a Higgs boson*, *JHEP* **05** (2013) 022 (2013)
³⁴⁹⁰(cit. on p. 51).
- ³⁴⁹¹⁷⁸S. Biswas, E. Gabrielli and B. Mele, *Single top and Higgs associated*
³⁴⁹²*production as a probe of the Htt coupling sign at the LHC*,
³⁴⁹³*JHEP* **01** (2013) 088 (2013) (cit. on p. 51).
- ³⁴⁹⁴⁷⁹T. Appelquist and M. S. Chanowitz,
³⁴⁹⁵*Unitarity Bound on the Scale of Fermion Mass Generation*, *Phys. Rev.*
³⁴⁹⁶*Lett.* **59** (1987) 2405, [Erratum: *Phys. Rev. Lett.* **60**, 1589 (1988)] (1987)
³⁴⁹⁷(cit. on p. 51).
- ³⁴⁹⁸⁸⁰M. Aaboud et al., *Observation of Higgs boson production in association*
³⁴⁹⁹*with a top quark pair at the LHC with the ATLAS detector*,
³⁵⁰⁰*Phys. Lett. B* **784** (2018) 173–191 (2018) (cit. on p. 52).
- ³⁵⁰¹⁸¹K. Skovpen, ‘First observation of the $t\bar{t}H$ process at CMS’,
³⁵⁰²11th International Workshop on Top Quark Physics (2018)
³⁵⁰³(cit. on p. 52).
- ³⁵⁰⁴⁸²G. Aad et al.,
³⁵⁰⁵*Search for $H \rightarrow \gamma\gamma$ produced in association with top quarks and*
³⁵⁰⁶*constraints on the Yukawa coupling between the top quark and the Higgs*
³⁵⁰⁷*boson using data taken at 7 TeV and 8 TeV with the ATLAS detector*,
³⁵⁰⁸*Phys. Lett. B* **740** (2015) 222–242 (2015) (cit. on p. 53).
- ³⁵⁰⁹⁸³V. Khachatryan et al., *Search for the associated production of the Higgs*
³⁵¹⁰*boson with a top-quark pair*,
³⁵¹¹*JHEP* **09** (2014) 087, [Erratum: *JHEP* 10, 106 (2014)] (2014)
³⁵¹²(cit. on p. 53).
- ³⁵¹³⁸⁴T. M. P. Tait and C. P. Yuan, *Single top quark production as a window*
³⁵¹⁴*to physics beyond the standard model*, *Phys. Rev. D* **63** (2000) 014018
³⁵¹⁵(2000) (cit. on p. 56).

- ³⁵¹⁶⁸⁵S. Biswas, E. Gabrielli, F. Margaroli and B. Mele,
³⁵¹⁷*Direct constraints on the top-Higgs coupling from the 8 TeV LHC data,*
³⁵¹⁸*JHEP* **07** (2013) 073 (2013) (cit. on p. 56).
- ³⁵¹⁹⁸⁶V. Khachatryan et al., *Search for the associated production of a Higgs*
³⁵²⁰*boson with a single top quark in proton-proton collisions at $\sqrt{s} = 8$ TeV,*
³⁵²¹*JHEP* **06** (2016) 177 (2016) (cit. on p. 56).
- ³⁵²²⁸⁷A. Airapetian et al., *ATLAS: Detector and physics performance*
³⁵²³*technical design report. Volume 2,* (1999) (1999) (cit. on pp. 57, 98).
- ³⁵²⁴⁸⁸CERN Web Page, *Our Member States*, (2022)
³⁵²⁵[https://home.web.cern.ch/about/who-we-are/our-](https://home.web.cern.ch/about/who-we-are/our-governance/member-states)
³⁵²⁶[governance/member-states](https://home.web.cern.ch/about/who-we-are/our-governance/member-states) (visited on 11/01/2022) (cit. on p. 58).
- ³⁵²⁷⁸⁹T. Fazzini, G. Fidecaro, A. W. Merrison, H. Paul and A. V. Tollestrup,
³⁵²⁸*Electron decay of the pion*, *Phys. Rev. Lett.* **1** (7 1958) 247–249 (1958)
³⁵²⁹(cit. on p. 58).
- ³⁵³⁰⁹⁰F. J. Hasert et al., *Observation of Neutrino Like Interactions Without*
³⁵³¹*Muon Or Electron in the Gargamelle Neutrino Experiment*,
³⁵³²*Phys. Lett. B* **46** (1973) 138–140 (1973) (cit. on p. 58).
- ³⁵³³⁹¹P. M. Watkins, *Discovery of the w and 2 bosons*,
³⁵³⁴*Contemporary Physics* **27** (1986) 291–324 (1986) (cit. on p. 58).
- ³⁵³⁵⁹²D. Decamp et al.,
³⁵³⁶*Determination of the Number of Light Neutrino Species*,
³⁵³⁷*Phys. Lett. B* **231** (1989) 519–529 (1989) (cit. on p. 58).
- ³⁵³⁸⁹³G. Baur et al., *Production of anti-hydrogen*,
³⁵³⁹*Phys. Lett. B* **368** (1996) 251–258 (1996) (cit. on p. 58).
- ³⁵⁴⁰⁹⁴G. D. Barr et al.,
³⁵⁴¹*A New measurement of direct CP violation in the neutral kaon system*,
³⁵⁴²*Phys. Lett. B* **317** (1993) 233–242 (1993) (cit. on p. 58).
- ³⁵⁴³⁹⁵V. Fanti et al., *A New measurement of direct CP violation in two pion*
³⁵⁴⁴*decays of the neutral kaon*, *Phys. Lett. B* **465** (1999) 335–348 (1999)
³⁵⁴⁵(cit. on p. 58).
- ³⁵⁴⁶⁹⁶R. Aaij et al., *Observation of $J/\psi p$ Resonances Consistent with*
³⁵⁴⁷*Pentaquark States in $\Lambda_b^0 \rightarrow J/\psi K^- p$ Decays*,
³⁵⁴⁸*Phys. Rev. Lett.* **115** (2015) 072001 (2015) (cit. on p. 58).
- ³⁵⁴⁹⁹⁷S. Maury, *The Antiproton Decelerator: AD*,
³⁵⁵⁰*Hyperfine Interact.* **109** (1997) 43–52 (1997) (cit. on p. 58).
- ³⁵⁵¹⁹⁸R. Alemany et al.,
³⁵⁵²*Summary Report of Physics Beyond Colliders at CERN*,
³⁵⁵³(2019), edited by J. Jaeckel, M. Lamont and C. Vallée (2019)
³⁵⁵⁴(cit. on p. 58).

- 3555 ⁹⁹R. Catherall et al., *The ISOLDE facility*, J. Phys. G **44** (2017) 094002
3556 (2017) (cit. on p. 58).
- 3557 ¹⁰⁰E. Gschwendtner et al., *AWAKE, The Advanced Proton Driven Plasma*
3558 *Wakefield Acceleration Experiment at CERN*,
3559 *Nucl. Instrum. Meth. A* **829** (2016) 76–82, edited by U. Dorda et al.
3560 (2016) (cit. on p. 58).
- 3561 ¹⁰¹M. Aguilar et al.,
3562 *The Alpha Magnetic Spectrometer (AMS) on the International Space*
3563 *Station. I: Results from the test flight on the space shuttle*, Phys. Rept.
3564 **366** (2002) 331–405, [Erratum: Phys.Rept. 380, 97–98 (2003)] (2002)
3565 (cit. on p. 59).
- 3566 ¹⁰²CERN Council holds special session on the Large Hadron Collider
3567 project, (1991) 3 p, Issued on 19 December 1991 (1991) (cit. on p. 59).
- 3568 ¹⁰³T. S. Pettersson and P Lefèvre,
3569 *The Large Hadron Collider: conceptual design*, tech. rep., 1995
3570 (cit. on pp. 59, 61, 62).
- 3571 ¹⁰⁴S. Myers,
3572 *The LEP Collider, from design to approval and commissioning*,
3573 John Adams' memorial lecture, Delivered at CERN, 26 Nov 1990
3574 (CERN, Geneva, 1991) (cit. on p. 60).
- 3575 ¹⁰⁵B. Müller, J. Schukraft and B. Wysłouch,
3576 *First Results from Pb+Pb Collisions at the LHC*,
3577 *Annual Review of Nuclear and Particle Science* **62** (2012) 361–386
3578 (2012) (cit. on p. 60).
- 3579 ¹⁰⁶CERN Web Page, *The Large Hadron Collider*, (2022)
3580 [https://home.cern/science/accelerators/large-hadron-](https://home.cern/science/accelerators/large-hadron-collider)
3581 *collider* (visited on 11/01/2022) (cit. on p. 60).
- 3582 ¹⁰⁷R. Steerenberg et al., ‘Operation and performance of the cern large
3583 hadron collider during proton run 2’,
3584 *10th international particle accelerator conference* (2019) MOPMP031
3585 (cit. on p. 60).
- 3586 ¹⁰⁸by Rende Steerenberg and A. Schaeffer, *LHC Report: The LHC is full!*,
3587 (2018) (2018) (cit. on p. 60).
- 3588 ¹⁰⁹*8th International Conference on High-Energy Accelerators*,
3589 CERN (CERN, Geneva, 1971) (cit. on p. 61).
- 3590 ¹¹⁰*LHC Machine*,
3591 *JINST* **3** (2008) S08001, edited by L. Evans and P. Bryant (2008)
3592 (cit. on pp. 61, 63).
- 3593 ¹¹¹*Radiofrequency cavities*, (2012) (2012) (cit. on p. 62).

- ³⁵⁹⁴ ¹¹²L Lari, H Gaillard and V Mertens,
³⁵⁹⁵ *Scheduling the installation of the LHC injection lines*, tech. rep.,
³⁵⁹⁶ CERN, 2004 (cit. on p. 63).
- ³⁵⁹⁷ ¹¹³G. Aad et al.,
³⁵⁹⁸ *The ATLAS Experiment at the CERN Large Hadron Collider*,
³⁵⁹⁹ *JINST* **3** (2008) S08003 (2008) (cit. on pp. 63, 81, 85, 86, 90, 91).
- ³⁶⁰⁰ ¹¹⁴S. Chatrchyan et al., *The CMS Experiment at the CERN LHC*,
³⁶⁰¹ *JINST* **3** (2008) S08004 (2008) (cit. on p. 64).
- ³⁶⁰² ¹¹⁵A. A. Alves Jr. et al., *The LHCb Detector at the LHC*,
³⁶⁰³ *JINST* **3** (2008) S08005 (2008) (cit. on p. 65).
- ³⁶⁰⁴ ¹¹⁶K. Aamodt et al., *The ALICE experiment at the CERN LHC*,
³⁶⁰⁵ *JINST* **3** (2008) S08002 (2008) (cit. on p. 65).
- ³⁶⁰⁶ ¹¹⁷O. Adriani et al.,
³⁶⁰⁷ *The LHCf detector at the CERN Large Hadron Collider*,
³⁶⁰⁸ *JINST* **3** (2008) S08006 (2008) (cit. on p. 65).
- ³⁶⁰⁹ ¹¹⁸C. Alpigiani et al., *A Letter of Intent for MATHUSLA: A Dedicated
³⁶¹⁰ Displaced Vertex Detector above ATLAS or CMS.*, (2018) (2018)
³⁶¹¹ (cit. on p. 65).
- ³⁶¹² ¹¹⁹J. H. Yoo, *The milliQan Experiment: Search for milli-charged Particles
³⁶¹³ at the LHC*, *PoS ICHEP2018* (2018) 520. 4 p, proceeding for ICHEP
³⁶¹⁴ 2018 SEOUL, International Conference on High Energy Physics, 4-11
³⁶¹⁵ July 2018, SEOUL, KOREA (2018) (cit. on p. 65).
- ³⁶¹⁶ ¹²⁰V. A. Mitsou, *The MoEDAL experiment at the LHC: status and results*,
³⁶¹⁷ *J. Phys. Conf. Ser.* **873** (2017) 012010, edited by B. Grzadkowski,
³⁶¹⁸ J. Kalinowski and M. Krawczyk (2017) (cit. on p. 65).
- ³⁶¹⁹ ¹²¹G. Anelli et al.,
³⁶²⁰ *The TOTEM experiment at the CERN Large Hadron Collider*,
³⁶²¹ *JINST* **3** (2008) S08007 (2008) (cit. on p. 65).
- ³⁶²² ¹²²A. Ariga et al.,
³⁶²³ *Letter of Intent for FASER: ForwArd Search ExpeRiment at the LHC*,
³⁶²⁴ (2018) (2018) (cit. on p. 65).
- ³⁶²⁵ ¹²³*LHC computing Grid. Technical design report*,
³⁶²⁶ (2005), edited by I. Bird et al. (2005) (cit. on p. 66).
- ³⁶²⁷ ¹²⁴WLCG Web Page, *Resources*, (2022)
³⁶²⁸ <https://wlcg-public.web.cern.ch/resources> (visited on
³⁶²⁹ 31/01/2022) (cit. on p. 67).
- ³⁶³⁰ ¹²⁵*ATLAS computing: Technical design report*,
³⁶³¹ (2005), edited by G. Duckeck et al. (2005) (cit. on pp. 66, 103).

- 3632 ¹²⁶WLCG Web Page, *Tier centres*, (2022)
3633 <https://wlcg-public.web.cern.ch/tier-centres> (visited on
3634 31/01/2022) (cit. on pp. 66, 68).
- 3635 ¹²⁷W. Herr and B Muratori, *Concept of luminosity*, (2006) (2006)
3636 (cit. on pp. 69, 70).
- 3637 ¹²⁸A. Hoecker, ‘Physics at the LHC Run-2 and Beyond’,
3638 2016 European School of High-Energy Physics (2016)
3639 (cit. on pp. 69, 70, 77).
- 3640 ¹²⁹M. Aaboud et al., *Luminosity determination in pp collisions at $\sqrt{s} = 8$ TeV using the ATLAS detector at the LHC*,
3641 *Eur. Phys. J. C* **76** (2016) 653 (2016) (cit. on p. 69).
- 3643 ¹³⁰G. Aad et al., *ATLAS data quality operations and performance for 2015–2018 data-taking*, *JINST* **15** (2020) P04003 (2020) (cit. on p. 71).
- 3645 ¹³¹*Luminosity determination in pp collisions at $\sqrt{s} = 13$ TeV using the ATLAS detector at the LHC*, tech. rep., CERN, 2019 (cit. on p. 71).
- 3647 ¹³²F. S. Cafagna, *Latest results for Proton-proton Cross Section Measurements with the TOTEM experiment at LHC*,
3648 *PoS ICRC2019* (2021) 207 (2021) (cit. on p. 74).
- 3650 ¹³³Particle Data Group Web Page,
3651 *Data files and plots of cross-sections and related quantities for hadrons*,
3652 (2022) <https://pdg.lbl.gov/2021/hadronic-xsections/> (visited on
3653 08/02/2022) (cit. on p. 74).
- 3654 ¹³⁴*Shrek*, 2001 (cit. on p. 79).
- 3655 ¹³⁵G. Aad et al., *Measurements of the Higgs boson production and decay rates and constraints on its couplings from a combined ATLAS and CMS analysis of the LHC pp collision data at $\sqrt{s} = 7$ and 8 TeV*,
3656 *JHEP* **08** (2016) 045 (2016) (cit. on p. 78).
- 3659 ¹³⁶G. Aad et al., *Measurement of the top quark-pair production cross section with ATLAS in pp collisions at $\sqrt{s} = 7$ TeV*,
3660 *Eur. Phys. J. C* **71** (2011) 1577 (2011) (cit. on p. 78).
- 3662 ¹³⁷G. Aad et al., *Evidence for Electroweak Production of $W^\pm W^\pm jj$ in pp Collisions at $\sqrt{s} = 8$ TeV with the ATLAS Detector*,
3663 *Phys. Rev. Lett.* **113** (2014) 141803 (2014) (cit. on p. 78).
- 3665 ¹³⁸M. Aaboud et al., *Evidence for light-by-light scattering in heavy-ion collisions with the ATLAS detector at the LHC*,
3666 *Nature Phys.* **13** (2017) 852–858 (2017) (cit. on p. 78).

- 3668 ¹³⁹M. Aaboud et al., *Search for the standard model Higgs boson produced*
- 3669 in association with top quarks and decaying into a $b\bar{b}$ pair in pp
- 3670 collisions at $\sqrt{s} = 13$ TeV with the ATLAS detector,
- 3671 Phys. Rev. D **97** (2018) 072016 (2018) (cit. on p. 78).
- 3672 ¹⁴⁰M. Aaboud et al., *Observation of $H \rightarrow b\bar{b}$ decays and VH production*
- 3673 *with the ATLAS detector*, Phys. Lett. B **786** (2018) 59–86 (2018)
- 3674 (cit. on p. 78).
- 3675 ¹⁴¹S. Amoroso, *Precision measurements at the LHC*, tech. rep.,
- 3676 CERN, 2020 (cit. on p. 80).
- 3677 ¹⁴²H. Pacey, *EW SUSY Production at the LHC*, tech. rep., CERN, 2021
- 3678 (cit. on p. 80).
- 3679 ¹⁴³S. Das Bakshi, J. Chakrabortty, C. Englert, M. Spannowsky and
- 3680 P. Stylianou, *CP Violation at atlas in effective field theory*,
- 3681 Phys. Rev. D **103** (5 2021) 055008 (2021) (cit. on p. 80).
- 3682 ¹⁴⁴B. T. Carlson, *Dark Matter searches with the ATLAS detector*, (2020)
- 3683 (2020) (cit. on p. 80).
- 3684 ¹⁴⁵J. L. Pinfold, *ATLAS and astroparticle physics*, Nucl. Phys. B Proc.
- 3685 Suppl. **175-176** (2008) 25–32, edited by K. S. Cheng et al. (2008)
- 3686 (cit. on p. 80).
- 3687 ¹⁴⁶N. D. Brett et al., *Discovery Reach for Black Hole Production*, (2009)
- 3688 (2009) (cit. on p. 80).
- 3689 ¹⁴⁷*ATLAS inner detector: Technical Design Report*, 1,
- 3690 Technical design report. ATLAS (CERN, Geneva, 1997) (cit. on p. 81).
- 3691 ¹⁴⁸G. Aad et al.,
- 3692 *The ATLAS Inner Detector commissioning and calibration*,
- 3693 Eur. Phys. J. C **70** (2010) 787–821 (2010) (cit. on p. 81).
- 3694 ¹⁴⁹M Capeans et al., *ATLAS Insertable B-Layer Technical Design Report*,
- 3695 tech. rep., 2010 (cit. on pp. 83, 84).
- 3696 ¹⁵⁰*Technical Design Report for the ATLAS Inner Tracker Pixel Detector*,
- 3697 tech. rep., CERN, 2017 (cit. on pp. 84, 86).
- 3698 ¹⁵¹ATLAS Experiment Web Page, *Detector and Technology*, (2022)
- 3699 <https://atlas.cern/discover/detector> (visited on 02/02/2022)
- 3700 (cit. on pp. 84, 87, 90, 94, 95).
- 3701 ¹⁵²F. Cavallari, *Performance of calorimeters at the LHC*,
- 3702 Journal of Physics: Conference Series **293** (2011) 012001 (2011)
- 3703 (cit. on pp. 86, 89, 90).
- 3704 ¹⁵³C. Grupen and B. Shwartz, ‘Calorimetry’, *Particle detectors*, 2nd ed.,
- 3705 Cambridge Monographs on Particle Physics, Nuclear Physics and
- 3706 Cosmology (Cambridge University Press, 2008) 230–272 (cit. on p. 88).

- 3707 ¹⁵⁴Particle Data Group Web Page, *π^0 Decay Modes*, (2022)
3708 <https://pdglive.lbl.gov/DataBlock.action?node=Q007TP> (visited
3709 on 02/02/2022) (cit. on p. 89).
- 3710 ¹⁵⁵A. Tarek Abouelfadl Mohamed, ‘The lhc and the atlas experiment’,
3711 *Measurement of higgs boson production cross sections in the diphoton*
3712 *channel: with the full atlas run-2 data and constraints on anomalous*
3713 *higgs boson interactions*
3714 (Springer International Publishing, Cham, 2020) 61 (cit. on pp. 90, 91).
- 3715 ¹⁵⁶*ATLAS muon spectrometer: Technical design report*, (1997) (1997)
3716 (cit. on p. 91).
- 3717 ¹⁵⁷K. Ishii, *The ATLAS muon spectrometer*, PoS **HEP2001** (2001) 253,
3718 edited by D. o. Horváth, P. Lévai and A. Patkós (2001) (cit. on p. 92).
- 3719 ¹⁵⁸M Livan, *Monitored drift tubes in ATLAS*, tech. rep., CERN, 1996
3720 (cit. on p. 92).
- 3721 ¹⁵⁹G. Cattani, *The resistive plate chambers of the ATLAS experiment:*
3722 *performance studies*,
3723 *Journal of Physics: Conference Series* **280** (2011) 012001 (2011)
3724 (cit. on p. 93).
- 3725 ¹⁶⁰K. Nagai, *Thin gap chambers in ATLAS*, Nucl. Instrum. Meth. A **384**
3726 (1996) 219–221, edited by F. Ferroni and P. Schlein (1996)
3727 (cit. on p. 93).
- 3728 ¹⁶¹*ATLAS magnet system: Technical Design Report, 1*,
3729 Technical design report. ATLAS (CERN, Geneva, 1997)
3730 (cit. on pp. 94, 95).
- 3731 ¹⁶²*ATLAS high-level trigger, data acquisition and controls: Technical*
3732 *design report*, (2003) (2003) (cit. on pp. 96, 97).
- 3733 ¹⁶³G. Aad et al., *Performance of the ATLAS Trigger System in 2010*,
3734 *Eur. Phys. J. C* **72** (2012) 1849 (2012) (cit. on p. 96).
- 3735 ¹⁶⁴G. Aad et al., *Alignment of the ATLAS Inner Detector in Run-2*,
3736 *Eur. Phys. J. C* **80** (2020) 1194 (2020) (cit. on pp. 97, 99, 100).
- 3737 ¹⁶⁵P. Mato, *GAUDI-Architecture design document*, (1998) (1998)
3738 (cit. on pp. 103, 114).
- 3739 ¹⁶⁶CherryPy Team, *CherryPy Documentation* (2'17) (cit. on p. 104).
- 3740 ¹⁶⁷G. Aad et al., *The ATLAS Simulation Infrastructure*,
3741 *Eur. Phys. J. C* **70** (2010) 823–874 (2010) (cit. on p. 108).
- 3742 ¹⁶⁸T. Gleisberg et al., *Event generation with SHERPA 1.1*,
3743 *JHEP* **02** (2009) 007 (2009) (cit. on p. 111).

- 3744 ¹⁶⁹G. Cowan, K. Cranmer, E. Gross and O. Vitells,
3745 *Asymptotic formulae for likelihood-based tests of new physics*,
3746 *Eur. Phys. J. C* **71** (2011) 1554 (2011) (cit. on p. 128).
- 3747 ¹⁷⁰L. Lista, ‘Practical Statistics for Particle Physicists’,
3748 *2016 European School of High-Energy Physics* (2017) 213
3749 (cit. on p. 132).
- 3750 ¹⁷¹T. Bayes Rev.,
3751 *An essay toward solving a problem in the doctrine of chances*,
3752 *Phil. Trans. Roy. Soc. Lond.* **53** (1764) 370–418 (1764) (cit. on p. 132).
- 3753 ¹⁷²I. Connelly, *Performance and calibration of b-tagging with the ATLAS*
3754 *experiment at LHC Run-2*, *EPJ Web Conf.* **164** (2017) 07025, edited by
3755 L. Bravina, Y. Foka and S. Kabana (2017) (cit. on p. 141).
- 3756 ¹⁷³T. Chen and C. Guestrin, ‘XGBoost’,
3757 *Proceedings of the 22nd ACM SIGKDD international conference on*
3758 *knowledge discovery and data mining* (2016) (cit. on p. 143).
- 3759 ¹⁷⁴J Zimmermann,
3760 *Statistical learning methods: basics, control and performance*,
3761 *Nuclear Instruments and Methods in Physics Research Section A:*
3762 *Accelerators, Spectrometers, Detectors and Associated Equipment* **559**
3763 (2006) 106–114 (2006) (cit. on p. 145).
- 3764 ¹⁷⁵Artemisa, *ARTificial Environment for ML and Innovation in Scientific*
3765 *Advanced Computing*, (2023)
3766 <https://artemisa.ific.uv.es/web/> (visited on 03/01/2023)
3767 (cit. on p. 152).

³⁷⁶⁸ Summary of the results

3769 **Recerca de la producció
3770 associada de bosó de Higgs i
3771 un quark top amb dos leptons i
3772 tau hadrònic a l'estat final**

3773 **1 Marc teòric**

3774 **1.1 El Model Estàndard**

3775 Maybe, I could translate this for the SM summary:
3776 <https://www.quantamagazine.org/a-new-map-of-the-standard-model->
3777 [of-particle-physics-20201022/](#)

3778 **1.2 La física del quark top**

3779 **1.3 La física del bosó de Higgs**

3780 **2 Dispositiu experimental**

3781 El treball desenvolupat al doctorat s'emmarca dins del detector ATLAS,
3782 que opera registrant les dades de les col·lisions del gran col·lisionador
3783 d'hadrons (LHC). El nom ATLAS prové de l'acronim angles d'un aparell
3784 toroidal del LHC.

3785 Aquestes eines pertanyen al centre europeu de recerca en física de
3786 partícules, popularment conegut com a CERN.

3787 **3 L'experiment ATLAS del LHC al CERN**

3788 **3.1 El gran col·lisionador d'hadrons**

3789 **3.2 El detector ATLAS**

3790 **4 Mesura de la polarització del quark top al**
3791 **canal-*t***

3792 Mesura d'observables sensibles a la polarització del quark top

3793 **4.1 Selecció d'esdeveniments**

3794 **4.2 Estimació del fons**

3795 **4.3 Fonts d'incertesa**

3796 **4.4 Resultats**

3797 **5 Recerca de processos tH amb un estat fi-**
3798 **final $2\ell + 1\tau_{\text{had}}$**

3799 **5.1 Selecció d'esdeveniments**

3800 **5.2 Estimació del fons**

3801 **5.3 Fonts d'incertesa**

3802 **5.4 Resultats**

3803 **6 Conclusions**

3805 Contraportada

3806 The discovery of a Higgs boson by the ATLAS and CMS experiments
3807 in 2012 opened a new field for exploration in the realm of particle physics.
3808 In order to better understand the Standard Model (SM) of particle physics,
3809 it is imperative to study the Yukawa coupling between this new particle
3810 and the rest of the SM components. Among these, of prominent interest is
3811 the coupling of the Higgs boson to the top quark (y_t), which is the most
3812 massive fundamental particle and, consequently, the one with the strongest
3813 coupling to the Higgs

3814 The direct measurement of y_t is only possible at LHC via two associated
3815 Higgs productions; with a pair of top quarks ($t\bar{t}H$) and with single-top
3816 quark (tHq). While the $t\bar{t}H$ permits a model-independent determination of
3817 the magnitude of y_t , the only way of directly measuring its sign is through
3818 the tHq production. This is due to the fact that the two leading-order
3819 Feynman diagrams for tHq production interfere with each other depending
3820 on y_t sign. Current experimental constraints on y_t favour the SM predictions,
3821 even though an opposite sign with respect to the SM expectations is not
3822 completely excluded yet.

3823 In this work it is presented a search for the production of a Higgs boson in
3824 association with a single-top quark in a final state with two light-floavoured-
3825 charged leptons and one hadronically decaying tau lepton (named $2\ell + 1\tau_{\text{had}}$
3826 channel). This analysis uses an integrated luminosity of 139 fb^{-1} of proton-
3827 proton collision data at centre-of-mass energy of 13 TeV collected by ATLAS
3828 during LHC Run 2.

3829 This search is exceptionally challenging due to the extremely small cross
3830 section of the tHq process (70 fb^{-1}) in general and, more particularly, the
3831 the $2\ell + 1\tau_{\text{had}}$ final-state channel, which only accounts for a 3.5% of the
3832 total tHq production.

3833 Because of this, the separation of the tHq signal events from background
3834 events is done by means of machine-learning (ML) techniques using boosted-
3835 decision trees (BDT) to define both signal and control regions. The most
3836 most relevant background processes are those related to top-pairs produc-

3837 tion (such as $t\bar{t}$, $t\bar{t}H$, $t\bar{t}Z$ and $t\bar{t}W$), Z -boson plus jets and single-top
3838 processes.

3839 Significant suppression of the background events with jets wrongly selec-
3840 ted as leptons is achieved by demanding electrons and muons to pass strict
3841 isolation requirements. Simultaneously, hadronic-tau leptons are demanded
3842 to pass the requirement of the recurrent-neural-network-based discriminator
3843 to reduce misidentifications from jets.

3844 The reconstruction of the events is also enhanced by similar ML methods
3845 since in the scenario in which the light-flavour leptons have the same sign,
3846 in principle, it is not possible to determine which lepton is originated from
3847 the Higgs boson and which from the top quark.

3848 The possible observation of an excess of signal events with respect to
3849 the SM predictions, would be a clear evidence of new physics in terms of
3850 \mathcal{CP} -violating y_t coupling.

3851 Additionally, the contribution to the single-top-quark polarisation first
3852 measurement is presented as well. In this other analysis the components of
3853 the full polarisation vector of the top quark are measured taking advantage
3854 of the peculiarities of the single-top-quark decay. Benefitting from the fact
3855 that the top quark lifetime is smaller than the depolarisation timescale, the
3856 decay products preserve the spin information of the top quark. Via angular
3857 distributions, it is measured in the top-quark rest frame.